

**High-stability differential frequency comparisons of optical
atomic clocks with correlated laser noise**

by

E.R. Clements

B.S., Miami University, 2014

M.S., Miami University, 2016

A thesis submitted to the
Faculty of the Graduate School of the
University of Colorado in partial fulfillment
of the requirements for the degree of
Doctor of Philosophy
Department of Physics

2022

Committee Members:

David R. Leibbrandt, Chair

Eric A. Cornell

Adam M. Kaufman

Svenja A. Knappe

Jun Ye

Clements, E.R. (Ph.D., Physics)

High-stability differential frequency comparisons of optical atomic clocks with correlated laser noise

Thesis directed by Prof. David R. Leibbrandt

Optical atomic clocks continue to reach higher levels of accuracy as a result of improved control of systematic effects. However, the ability to test the accuracy of these atomic clocks is often limited by local oscillator noise. The local oscillator noise limits the stability of optical frequency ratio measurements which thereby limits the speed and precision one can compare two atomic frequency standards. Limits set by the laser noise can be circumvented by using differential comparison techniques which utilize correlations in laser noise to increase the achievable interrogation time and thus increase the frequency comparison stability. In this thesis I discuss two differential measurement techniques, correlation and differential spectroscopy, which we have demonstrated in experiments. Correlation spectroscopy is a technique which uses a parity measurement following a synchronized Ramsey interrogation to measure the relative frequency of two similar frequency atomic clocks. With this technique we achieve a measurement instability of $2.8 \times 10^{-16}/\sqrt{\tau}$ using a $^{40}\text{Ca}^+ / ^{27}\text{Al}^+$ and $^{25}\text{Mg}^+ / ^{27}\text{Al}^+$ quantum-logic clock. Differential spectroscopy uses an atomic clock with low projection noise, here a ^{171}Yb lattice clock, to correct the phase noise of a second, higher frequency $^{27}\text{Al}^+$ clock's local oscillator, reducing the measurement instability by narrowing the phase noise distribution of the higher frequency local oscillator to the quantum projection noise level of the high stability clock. This can be further extended using two lattice clocks in a zero dead time configuration to correct the phase noise beyond the coherence time of a single Yb lattice clock. With these techniques we achieve measurement instabilities of $2.5 \times 10^{-16}/\sqrt{\tau}$ and $1.9 \times 10^{-16}/\sqrt{\tau}$ for a comparison between a single $^{27}\text{Al}^+$ ion clock and a ^{171}Yb lattice clock running as single clock and in a zero dead time configuration respectively. Additionally I will discuss improvements in the experimental system from the previous $^{27}\text{Al}^+$ quantum-logic clock and present progress toward evaluating the systematic shifts of the $^{40}\text{Ca}^+ / ^{27}\text{Al}^+$ quantum-logic clock.

Dedication

To Avery, for all the love and support she provides.

Acknowledgements

The results presented in this thesis were made possible by the effort and support of many people at NIST. I would like to thank my advisors David Hume and David Leibbrandt for their mentorship throughout the years. I am lucky to have been advised by two excellent scientists who have provided their deep technical experience on the many experiments I have been involved in. I would also like to thank James Chou for being so welcoming and for always being willing to lend an ear to laboratory issues. When I first joined the group Aaron Hankin and Sam Brewer quickly got me up to speed on the development of the new Ca/Al clock and helped me through the growing pains of the first years of graduate school. I will never forget the support you provided in the first few years and I truly appreciate all of your help. I would also like to thank and acknowledge May Kim, Jose Valencia, and Kaifeng Cui for being excellent lab partners, its was a lot of fun working with you and solving a plethora of experimental problems! The differential spectroscopy experiments would have been impossible without the great collaboration we have with the optical frequency measurements group. In this group I would like to particularly thank Andrew Ludlow, Tara Fortier, Will McGrew, Nick Nardelli, Youssef Hassan, and Xiaogang Zhang for the open and collaborative experiences. I also want to thank Matt Bohman for the help and camaraderie in the last year. I am disappointed I will not be working with you more but I wish you luck in the final steps of characterizing the systematics of the Ca/Al clock! I want to also thank all of the other members of the Ion Storage, past and present, for their help and inclusivity throughout the years, it has been a great work environment! Lastly I would like to thank my family and friends especially Avery, I would not have gotten here without your love and support. Thank you all!

Contents

Chapter	
1 Introduction	1
1.1 Optical frequency standards	1
1.1.1 What is a clock?	2
1.1.2 Towards redefinition of the SI second	5
1.1.3 Frequency Comparisons	8
1.2 Thesis Organization	11
2 Experimental Setup	12
2.1 Ion trapping background	13
2.2 $^{40}\text{Ca}^+ / ^{27}\text{Al}^+$ ion trap	21
2.2.1 Diamond wafer wheel trap	21
2.2.2 Meander line resonator	22
2.2.3 Titanium Vacuum system	25
2.3 $^{40}\text{Ca}^+$ -logic ion operations	27
2.3.1 $^{40}\text{Ca}^+$ Laser systems	35
2.4 $^{27}\text{Al}^+$ clock ion operations	39
2.4.1 $^{27}\text{Al}^+$ state preparation	41
2.4.2 $^{27}\text{Al}^+$ laser systems	43
2.5 Ablation Loading	46

2.6	Noise minimization setups	50
2.6.1	Active Magnetic Field Stabilization	50
2.6.2	Fiber Noise and Path Length Stabilization	53
2.7	Quantum logic spectroscopy	55
3	Correlation Spectroscopy	58
3.1	Limits in conventional frequency comparisons	59
3.2	Theoretical Discussion of Correlation Spectroscopy	64
3.3	Correlation spectroscopy experimental details	68
3.3.1	Differential phase noise stabilization	69
3.3.2	Differential magnetic field noise minimization	70
3.3.3	Experimental sequence	73
3.4	Experimental Results	75
4	Differential Spectroscopy	83
4.1	Theoretical Discussion	84
4.2	Differential spectroscopy experimental details	88
4.3	Experimental Results	92
5	Systematic Effects	98
5.1	Second order Doppler shift	99
5.1.1	Ground-state cooling	99
5.1.2	Micromotion minimization	103
5.2	Quadratic Zeeman shift	112
5.2.1	Resolved sideband method for measuring oscillating magnetic fields	112
5.2.2	Autler-Townes method for measuring oscillating magnetic fields	120
5.3	Black-body radiation shift	125
6	Conclusion	129

Bibliography	134
---------------------	------------

Appendix

A Optimization of the magnetic field servo	144
B Sphere cavity box temperature control	147
C Previous $^{27}\text{Al}^+$ clock uncertainty budget	149

Tables

Table

3.1	Percentage of the data used for different correlation spectroscopy probe durations . .	77
C.1	Systematic fractional frequency shifts ($\Delta\nu/\nu$) and associated uncertainties for the previous $^{27}\text{Al}^+$ quantum-logic.	149

Figures

Figure

1.1	Simplified schematic of the major components of an atomic clock	3
1.2	Level diagrams of ^{133}Cs , $^{40}\text{Ca}^+$, and $^{27}\text{Al}^+$	4
1.3	Historical trend of the systemic fractional uncertainty of atomic clocks.	6
1.4	Simplified diagram of a comparison of an $^{27}\text{Al}^+$ and ^{171}Yb optical clock.	10
2.1	Diagram of a standard RF Paul trap and details of the diamond wafer wheel trap and endcaps used to trap ions.	14
2.2	Diagram of the meander line resonator shield	24
2.3	CAD drawing of the grabber arms to connect trap electrodes.	25
2.4	CAD drawing of the titanium vacuum chamber.	27
2.5	Level structure of $^{40}\text{Ca}^+$ and relevant transitions labeled for different pulse sequences.	28
2.6	Doppler cooling and detection lineshapes using the $ 4^2S_{1/2}\rangle \leftrightarrow 4^2P_{1/2}\rangle$ transition.	30
2.7	Example sideband cooling and red and blue sideband thermometry pulse sequences	32
2.8	Relevant transitions strengths for $ 4^2S_{1/2}\rangle \leftrightarrow 3^2D_{5/2}\rangle$ for $ \Delta m = 0, 1,$ and 2 tran- sitions.	33
2.9	Laser distribution table.	36
2.10	Layout of the lasers locked to the optical sphere cavity.	37
2.11	Diagram of the doublepass towers used to scan the frequency, phase, and amplitude of our lasers before being sent to the ion trap.	38

2.12	Diagram of light send into the $^{40}\text{Ca}^+ / ^{27}\text{Al}^+$ vacuum system	40
2.13	$^{27}\text{Al}^+$ level diagram and state preparation diagrams.	42
2.14	Simulation of the inner manifold $^{27}\text{Al}^+$ state preparation procedure	44
2.15	Beampath for the 3P_1 laser on the $^{40}\text{Ca}^+ / ^{27}\text{Al}^+$ optical table.	45
2.16	Beampath for the 3P_0 laser on table.	47
2.17	Beampath for the 3P_1 and 3P_0 entering the vacuum system.	48
2.18	Ablation loading and $^{27}\text{Al}^+$ photoionization laser beamline.	49
2.19	Simplified diagram of magnetic field stabilization setup.	52
2.20	Differential path length noise test setup.	54
2.21	Quantum logic spectroscopy for the $^{40}\text{Ca}^+ / ^{27}\text{Al}^+$ system.	56
3.1	Overview of a similar frequency comparisons and pictures of the $^{40}\text{Ca}^+ / ^{27}\text{Al}^+$ and $^{25}\text{Mg}^+ / ^{27}\text{Al}^+$ setups.	60
3.2	Allan deviation of the Medusa laser noise	63
3.3	Dependence of the fringe contrast on the frequency ratio of the two clocks in correlation spectroscopy.	67
3.4	Schematic of the setups used in correlation spectroscopy	69
3.5	Representative magnetic field data for when the active magnetic field stabilization is engaged on both systems.	71
3.6	Results from a simulations to determine the impact of magnetic field noise on correlation spectroscopy using different transitions	72
3.7	Pulse sequence for correlation spectroscopy and a simplified diagram of the clock manifold	74
3.8	Parity fringes of data measured with the $ ^1S_0, m_F = 5/2\rangle \leftrightarrow ^3P_0, m_F = 5/2\rangle$ transition	77
3.9	Parity fringes of data measured with the $ ^1S_0, m_F = 3/2\rangle \leftrightarrow ^3P_0, m_F = 1/2\rangle$ transition	78

3.10	Experimental parity fringe contrast at a function of probe duration	79
3.11	Experimental stability vs. probe duration	80
3.12	Allan deviations of the parity measurement time series	81
4.1	Overview of the differential spectroscopy setup.	85
4.2	Pulse sequence for differential spectroscopy.	87
4.3	Pulse diagram for ZDT differential spectroscopy.	92
4.4	Test of phase feedforward.	93
4.5	Differential spectroscopy experimental results.	94
4.6	ZDT differential spectroscopy 36 hr. run.	96
4.7	Historical plot of the 1-sec. instability of interspecies frequency comparisons.	97
5.1	Sideband thermometry following Doppler cooling of single $^{40}\text{Ca}^+$	101
5.2	Sideband thermometry following sideband cooling of single $^{40}\text{Ca}^+$	102
5.3	Prior and possible mode structure for the $^{40}\text{Ca}^+ / ^{27}\text{Al}^+$ secular modes.	103
5.4	Heating rate measurements of the secular modes of the $^{40}\text{Ca}^+ / ^{27}\text{Al}^+$ crystal.	104
5.5	Rabi time scans of the carrier transition and micromotion sidebands along the pi, vertical, and axial directions.	107
5.6	Broad axial micromotion survey	108
5.7	Fine survey of the spatial axial micromotion minimum.	109
5.8	Survey of the low gradient position with axial RF compensation	110
5.9	Week long characterization of the EMM time dilation shift.	111
5.10	Energy level diagram showing the energy modulation from and AC magnetic field and a picture of a diamond wafer wheel trap where possible magnetic field sources are highlighted	114
5.11	Modulation index from AC magnetic field for different sensitivity transitions.	115

5.12 Comparison of the derivation of the resolved sideband method to measure the AC magnetic field and a simulation including micromotion and an oscillating magnetic field.	118
5.13 Experimental sideband based measurement of the quadratic Zeeman effect	119
5.14 Overview of the level structure for measuring the Autler-Townes effect and experimental setup for defining the quantization axes.	122
5.15 Example of the avoided crossing in the Autler-Townes effect measured in our system.	124
5.16 Measurement of Autler-Townes effect along three orthogonal quantization axes.	124
5.17 Measurement of Autler-Townes effect dependence on trap electrode parameters	126
5.18 Time series of temperature in the vacuum system.	128
A.1 Data showing the magnetic field measurements with ion and fluxgate magnetometers when feedback is disengaged where the fluxgate data is fit to the ion data to calibrate the magnetic field servo	144
A.2 Measurement of the magnetic field with the $^{40}\text{Ca}^+$ ion following calibration of the magnetic field servo	146
B.1 Temperature control box used to reduce drifts of the $^{40}\text{Ca}^+$ lasers.	148

Chapter 1

Introduction

With the advent of optical atomic clocks, higher accuracy and more stable frequency standards have become attainable. With these improved frequency standards it is possible to redefine the second in terms of an optical frequency as well as test physical models with higher precision. In this thesis, the focus is on one version of an optical atomic clock: an $^{27}\text{Al}^+$ quantum logic clock. One of the $^{27}\text{Al}^+$ quantum logic clocks in development at NIST is the $^{40}\text{Ca}^+ / ^{27}\text{Al}^+$ quantum logic clock which is the system which I have worked most with. During my time at NIST, I have performed experiments which used this atomic clock to demonstrate techniques that allow for comparison of frequency standards with stability beyond limits imposed by the local oscillator, and characterization of the systematic uncertainty of the $^{40}\text{Ca}^+ / ^{27}\text{Al}^+$ quantum logic clock. In this thesis I will describe my work building up the $^{40}\text{Ca}^+ / ^{27}\text{Al}^+$ quantum logic clock, two techniques called correlation and differential spectroscopy, and efforts towards characterizing the systematic shifts and uncertainties of this atomic clock. To provide context for this work I first provide a brief overview of current and future frequency standards in the SI system.

1.1 Optical frequency standards

It is important to understand the current status of frequency standards and the steps being taken to redefine the second based on an optical transition. There are many milestones that need to be reached before redefinition can take place, many of which involve comparisons between systems and tests of their performance. Presently, the second is defined by the unperturbed hyperfine atomic

transition in cesium which is interrogated via a microwave frequency of 9 192 631 770 Hz [1] and many realizations of these frequency standards are implemented in cesium fountain clocks [2, 3]. These atomic clocks already offer an excellent fractional frequency uncertainty of a few parts in 10^{16} which is already beyond the accuracy needed to enable many technologies such as GPS [4], telecommunications [5], and computer networks [6] but below the accuracy needed for relativistic geodesy [7], dark matter detection [8, 9, 10], and tests of Lorentz invariance [11, 12, 13]. However, with the development of higher accuracy atomic clocks based on optical atomic transitions, tests of these fundamental models are possible. Separately, there are also efforts to move toward redefining the second in terms of an optical atomic transition(s) [1, 14, 15]. Since the second is the base unit on which all other units depend [16], it will become important for it to not become a limiting factor in future definitions of fundamental constants. Another major technology which has enabled and motivated the push for redefinition of the second is the optical frequency comb. With the development of frequency combs, it is now possible to compare these systems directly and to synthesize microwave signals with higher accuracy [17, 18]. These systems have the potential to provide a more precise realization of the second due to their higher quality factor oscillators and ability to better control systematic frequency shifts and errors.

1.1.1 What is a clock?

The major components of a clock include a local oscillator which derives its stability from a microwave or optical cavity, an atomic frequency reference, and a control system which is used to lock the local oscillator to the atomic reference. Because the atoms which are providing the frequency reference of the clock are fundamentally the same, any clocks which are based on the same atomic species will have the same oscillator frequency. Therefore, comparisons of different systems or groups of systems based on the same standards allows for tests of systematic accuracy and reproducibility of atomic clocks allows independent standards to be developed. A simplified schematic of these systems can be seen in Fig. 1.1. By locking the local oscillator to the atomic standard, the accuracy of this standard becomes the accuracy of the local oscillator. At short

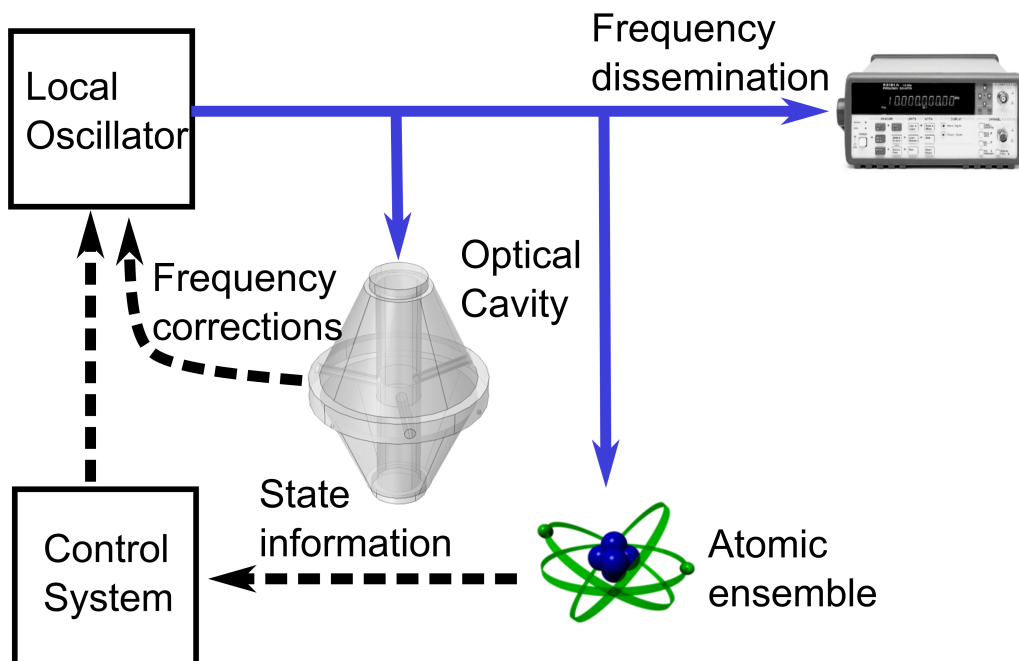


Figure 1.1: Simplified schematic of the major components of an atomic clock. A local oscillator which is a laser for optical atomic clocks or a microwave source for microwave atomic clocks is first locked to an optical cavity or a microwave cavity respectively. This stabilized light is sent to the clock to interrogate the atomic reference and following the interrogation the state is readout. This state information is then sent to a control system which will determine the proper correction to the local oscillator further stabilizing it to the atomic reference. A percentage of the stabilized light is picked off and sent to a frequency comb which measures the frequency of the atomic clock or uses the light to stabilize the frequency comb. The stabilized frequency comb then synthesizes a microwave signal for dissemination of the optical time standard.

times the stability is provided by the local oscillator and at times longer than the servo time constant the atomic reference provides the frequency stability. The frequency standard can then be disseminated by sending the stabilized light to other systems via optical networks or as an RF signal by conversion through a frequency comb [18]. These are the major components of atomic clocks but it is important to understand that each of these systems are major research projects on their own [19, 20, 21, 22, 23].

An important distinction between optical and microwave atomic clocks is how quickly a certain precision can be realized and the ultimate accuracy that the systems achieve. To understand this distinction, it is useful to look at what effects its accuracy and stability. The fundamental

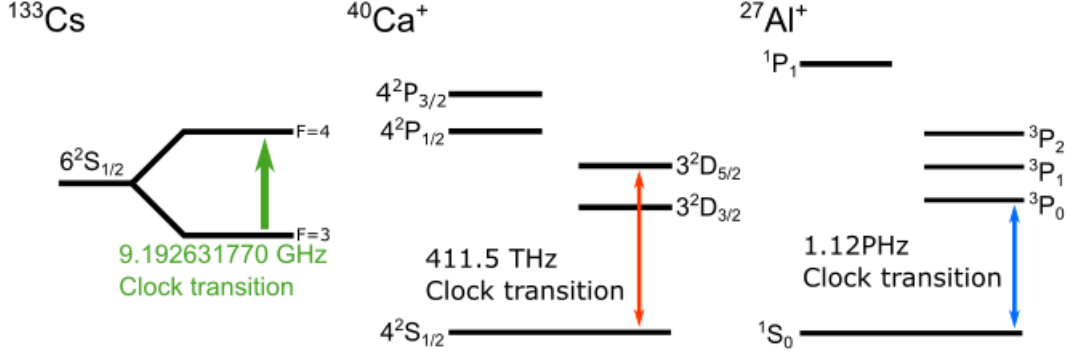


Figure 1.2: Different atomic clock species that represent different categories of atomic clocks. The second is defined by the 9.192 631 770 GHz transition in ^{133}Cs which can be compared to the 1.12 PHz and 411.5 THz transitions in $^{27}\text{Al}^+$ and $^{40}\text{Ca}^+$ respectively. With the higher oscillator frequency of optical atomic clocks the stability and fractional uncertainties surpasses what is currently possible with ^{133}Cs microwave clocks.

quantum limit to the precision of measurements of the oscillator frequency is given by the quantum projection noise limit. This limit describes the measurement instability which is used to quantify how quickly the statistical uncertainty of the average oscillator frequency $\langle \nu_i \rangle$ can be reduced. The quantum projection noise limited measurement instability [1] is given by

$$\sigma(\tau) = \kappa \frac{\Delta\omega}{\omega} \sqrt{\frac{T}{N\tau}}. \quad (1.1)$$

In this equation ω is the unperturbed oscillator frequency, $\Delta\omega$ is the linewidth at the interrogation time T , N is the number of atoms being interrogated, κ is a factor of order unity that depends on the type of interrogation used, and τ is the total averaging time. For example, when comparing the oscillator frequency of an $^{27}\text{Al}^+$ clock which is $\approx 1.12\text{PHz}$ against the microwave oscillator frequency of a cesium clock at $\approx 9.19\text{GHz}$, it can be seen that because the oscillator frequency is $\approx 10^5$ times larger the resulting measurement instability of an $^{27}\text{Al}^+$ clock will be $\approx 10^5$ lower than a cesium clock if the number of atoms being interrogated is identical. Fig 1.2 displays 3 species used as atomic clocks with ^{133}Cs representing a microwave atomic clock, $^{40}\text{Ca}^+$ representing a 1 valence electron optical clock species, and $^{27}\text{Al}^+$ representing a 2 valence electron optical clock species. The higher frequency for both of the optical clocks allows for higher measurement stabilities which will

make characterization of atomic clocks based on these species faster in comparison to microwave atomic clocks. Because of this difference in oscillator frequencies, optical atomic clocks require significantly fewer frequency measurements or alternatively less time to reach the same statistical uncertainty as a microwave atomic clock. In addition, the higher oscillator frequency results in a lower fractional frequency error $\delta\omega/\omega$ which can reduce the impact of frequency errors if the error $\delta\omega$ is commensurate when compared across systems. Many of these systems also offer the possibility to better control many systematic effects where one example, Doppler shifts, can be reduced by cooling the atoms to their motional quantum mechanical ground-states [24]. Fig. 1.3 presents a plot showing the historical trend of the fractional uncertainty of atomic clocks. With the ability to more quickly reach a lower statistical uncertainty and the potential for lower systematic frequency uncertainties in these systems the benefits of adopting an optical frequency standard to define the second becomes apparent.

1.1.2 Towards redefinition of the SI second

Despite a recent revision of the SI system, the second is still defined by a microwave transition in Cs, as it has been since 1967. While there is potential for optical atomic clocks to replace microwave standards, there are many technical challenges that need to be overcome. Milestones for these atomic clocks have been put forward by the International Committee of Weights and Measures (CIPM) which must be reached before the definition of the second can transition to an optical frequency reference [14]. These milestones are:

1. At least three different optical clocks (either in different laboratories, or of different species) have demonstrated validated uncertainties of about two orders of magnitude better than the best Cs atomic clocks of the time.
2. At least three independent measurements of at least one optical clock from milestone 1 have been compared in different institutes with, e.g., $\Delta\nu/\nu < 5 \times 10^{-18}$ either by transportable clocks advanced links, or frequency ratio closures.

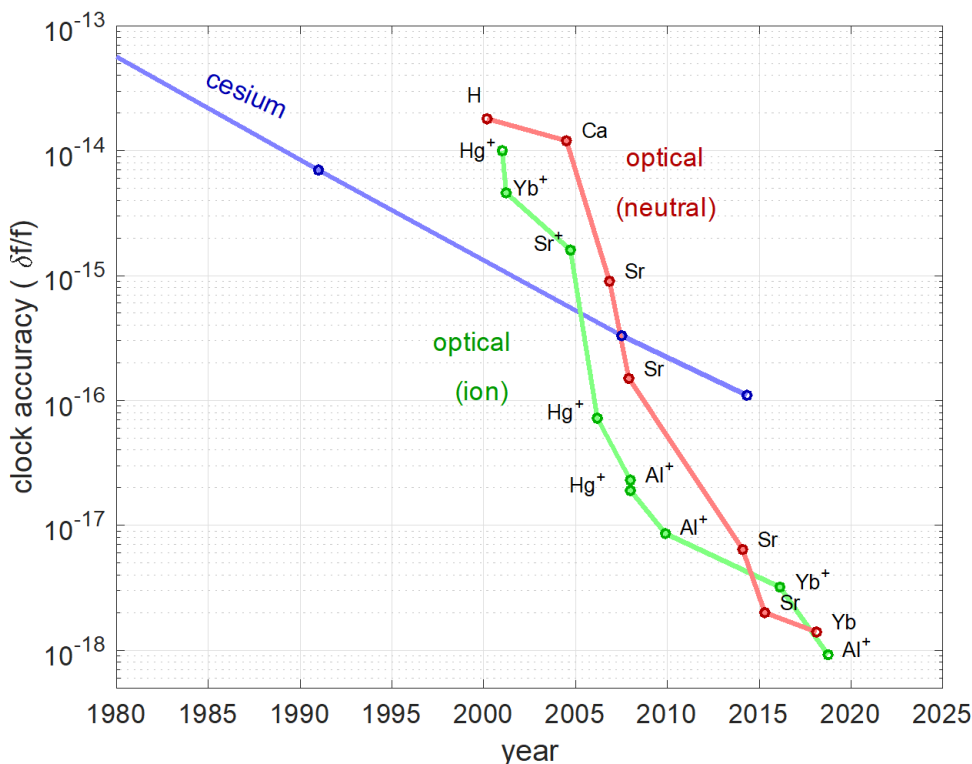


Figure 1.3: This figure shows the historical trend of the systematic fractional uncertainty in atomic clocks. The blue points describe the trend of cesium microwave clocks, the red points provide a sampling of the historical systematic uncertainty of various optical lattice clocks, and the green points provide a sampling of the historical systematic uncertainty of various ion based optical atomic clocks.

3. At least three independent measurements of the optical frequency standards of milestone 1 with three independent Cs primary clocks have been performed, where the measurements are limited essentially by the uncertainty of these Cs fountain clocks (with, e.g., $\Delta\nu/\nu < 3 \times 10^{-16}$).
4. Optical clocks, which are secondary representations of the second, contribute regularly to International Atomic Time (TAI).
5. Optical frequency ratios between a few (at least 5) other optical frequency standards have been performed; each ratio measured at least twice by independent laboratories and agreement was found to better than, e.g., $\Delta\nu/\nu < 5 \times 10^{-18}$.

At this current point, some of these milestones or a portion of these milestones have already been achieved. Item 1 has been demonstrated in many species which have realized a fractional uncertainty of $< 5 \times 10^{-18}$ [25, 26, 27, 28, 29] and more systems are approaching this criteria [30, 31, 32, 33]. Systems which have demonstrated this level of accuracy have been realized in RF Paul traps and optical lattices [15]. However, optical tweezers offer an additional platform where high accuracy atomic clocks could be achieved [34]. Item 2 has been partially demonstrated between ^{171}Yb , $^{27}\text{Al}^+$, and ^{88}Sr clocks located at NIST and JILA by utilizing separate frequency links between NIST and JILA [35]. These frequency links were implemented using a fiber network and free space optical two-way frequency transfer. Through this network the atomic clocks were compared with a fractional statistical uncertainty below 10^{-17} . A previous frequency comparison [36] between ^{88}Sr , ^{171}Yb and ^{199}Hg optical lattice clocks reached a ratio statistical uncertainty of $\approx 10^{-16}$. For Item 4 many atomic clocks have regularly contributed to TAI [37, 38, 39, 40]. For Item 5 two ratios which has been measured with systems located in different institutions are $^{199}\text{Hg}/^{88}\text{Sr}$ [36, 41] and $^{171}\text{Yb}/^{88}\text{Sr}$ [36, 42, 43]. With all of these examples we see great progress to meeting each of these criteria but much work is still needed.

In the criteria dictated by CIPM, many of the metrics require comparisons between different atomic clocks. One limit to reaching many of these milestones is the difficulty of comparing the existing systems with each other. Prior frequency comparisons have used measurements between the local oscillators of the corresponding systems to perform the comparisons. When using the local oscillators to perform the frequency comparison, the frequency ratio measurement stability is limited by the local oscillator stability. From Eq. 1.1, for a Ramsey experiment $\Delta\omega = 1/T\sqrt{N}$ [44], which when inserted into the equation for quantum projection noise shows that the instability is reduced as T is increased. In many optical atomic clocks the species used have transitions which have higher theoretical stability than the local oscillators locked to them due to the atomic coherence time, dictated by the excited state lifetime, being much longer than the local oscillator coherence time. Commonly, thermal noise in the mirror substrates of an optical cavity limits the coherence of the local oscillator preventing them from measuring the optical transition with the lifetime limited

stability. An additional complication to comparisons between different systems is that many of the atomic clocks are located in many different countries so either establishing phase noise stabilized optical fiber connections between these laboratories or development of transportable atomic clocks is required. Efforts towards these technologies are being developed in the form of phase stabilized fiber backbones [45] and development of transportable optical lattice [46, 47, 48] and ion trap based clocks [31, 32]. The issue still remains however, that local oscillator noise limits the speed at which these systems can be compared. In this thesis two techniques will be described, correlation and differential spectroscopy, which utilize correlations in the local oscillator noise to provide differential atom-atom comparisons that offer the possibility to compare these systems at their fundamental stabilities without the need for a high stability local oscillator.

1.1.3 Frequency Comparisons

Comparisons between optical atomic clocks also offer platforms to test fundamental physical models and place constraints on models of dark matter and test new physics. Frequency comparisons between atomic clocks are useful in a wide variety of applications. Some of these applications include relativistic geodesy [7], dark matter detection [8, 9, 10], and tests of Lorentz invariance [11, 12, 13]. These experiments in many cases can be realized with traditional comparison techniques but differential measurements detailed later in this thesis can improve the ability to test various models. In a recent demonstration, subsections of a strontium optical lattice clock which is vertically oriented were compared to observe a gravitational redshift at the mm scale [49]. This demonstration shows the possibility of using optical clocks to perform gravitational measurements at a much higher spatial and temporal resolution. Experiments like this showcase the potential to perform tests of relativity and perform geodesy with higher spatial and temporal resolution. In some dark matter models, particularly ultralight scalar dark matter, the scalar dark matter field can couple to different atomic transitions with different magnitudes [10]. By performing frequency comparisons between species with different sensitivities to the scalar dark matter field, these models of dark matter could be tested or constrained. Another avenue to test the existence of this

scalar field is to perform frequency comparisons between atomic clocks located across the globe to look for a time delayed frequency variation between these systems due to the length scale of the scalar field being on the order of the size of the earth [8, 50]. These measurements could be realized by performing comparisons between atomic clocks over free-space or fiber connections or alternatively be performed between atomic clocks in separated areas by comparing closed ratios of these systems [43, 35]. Recent measurements with $^{171}\text{Yb}^+$ optical clocks were able to perform tests of Lorentz invariance and constrain Lorentz invariance violating parameters 2 orders of magnitude further than previous tests [13, 11]. These tests are performed by comparing two $^{171}\text{Yb}^+$ optical atomic clocks which have their quantization axes oriented along non-parallel directions. By orienting the quantization axes in this way they can perform identical experiments in two inertial reference frames. In all of these examples comparisons between different atomic clocks or subsections of the same atomic clock are required. To better understand how these comparisons are performed an example comparison between an $^{27}\text{Al}^+$ clock and a ^{171}Yb is discussed.

In all of these applications a local oscillator, here a laser, is required to compare the systems with each other. A diagram of one realization of a frequency comparison between and $^{27}\text{Al}^+$ ion clock and a ^{171}Yb lattice clock via a frequency comb can be seen in Fig. 1.4. For both of the clocks an optical cavity is first used to pre-stabilize the clock laser which then interrogates the optical clock transition. From this interrogation the frequency error of the clock laser can be determined and used to further stabilize the light. Now that the laser light represents the frequency of the atomic transition a frequency comb is first locked to the ^{171}Yb lattice clock laser light by feeding back onto the frequency comb's repetition rate, thereby transferring the frequency information of the ^{171}Yb laser to the frequency comb. Now that the comb is stabilized to the ^{171}Yb clock laser the frequency components of the comb near the $^{27}\text{Al}^+$ oscillator frequency can be compared with the $^{27}\text{Al}^+$ clock laser light by generation of a beat-note which can then be measured with a high bandwidth photo-diode and frequency counter.

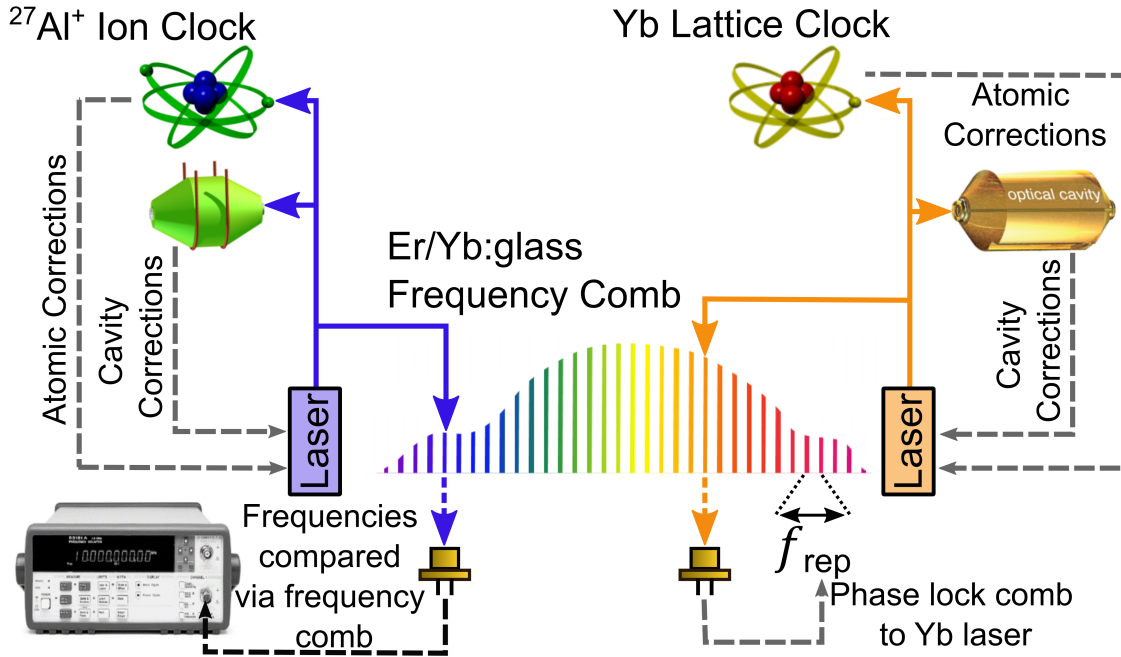


Figure 1.4: This figure provides a simplified diagram for a comparison between an $^{27}\text{Al}^+$ ion clock with a ^{171}Yb lattice clock mediated by a frequency comb.

As mentioned previously laser coherence limits the resolution of frequency measurements of each clock individually in traditional comparisons. In atomic clocks the local oscillator, here a laser, is often pre-stabilized to an optical cavity using Pound-Drever-Hall stabilization technique and then further stabilized using measurements of the optical atomic transition. Following pre-stabilization, the dominant type of laser noise is often flicker frequency noise and the source of this flicker frequency noise is thermo-mechanical noise in the mirrors or the spacer. This noise manifests itself as a limit to the coherence time of the local oscillator. Experiments are currently working on reducing this instability by utilizing crystalline mirrors [51], using crystalline mirror spacers [52], and cooling optical cavities to cryogenic temperatures [53]. Recently developed single crystalline silicon cryogenic optical cavities have enabled probe durations of a few seconds [53] and other cryogenic cavities based on sapphire are in the process of being developed. Developments in these technologies could allow for interrogation times approaching the intrinsic lifetime of some atomic optical transitions but developing complementary clock techniques that can make use of

correlations in laser noise to bypass technical limitations set by the coherence time of the laser can offer ways to compare these atomic systems without the need for a high stability local oscillator. These techniques will be further discussed in chapters 3 and 4.

1.2 Thesis Organization

This thesis will discuss the development of the NIST $^{40}\text{Ca}^+ / ^{27}\text{Al}^+$ quantum-logic atomic clock, detail methods used to avoid measurement stability limits imposed by the coherence of the local oscillator, and present the current status of the evaluation of the systematic uncertainty for the $^{40}\text{Ca}^+ / ^{27}\text{Al}^+$ quantum-logic atomic clock. In Chapter 2 I will discuss the development of the $^{40}\text{Ca}^+ / ^{27}\text{Al}^+$ quantum-logic atomic clock and the relevant sub-systems we use. In Chapter 3 I describe differential measurements used to measure the relative frequency of our two $^{27}\text{Al}^+$ clocks demonstrating a method called correlation spectroscopy. In this method we compare the two clocks using lasers with identical phase noise so we can probe at durations that exceed the coherence time of the laser. Similarly, in Chapter 4, I will present a second method, differential spectroscopy, which is another synchronous differential comparison technique in which the ratio of atomic phase evolution is estimated by Bayesian inference when the local oscillators of the two clocks have highly correlated phase noise. Following these discussions I will move to a discussion of the current status of the systematic uncertainty evaluation of the $^{40}\text{Ca}^+ / ^{27}\text{Al}^+$ quantum-logic atomic clock with a focus on systematic effects whose details differ from previous evaluation methods in the $^{25}\text{Mg}^+ / ^{27}\text{Al}^+$ system.

Chapter 2

Experimental Setup

In this chapter, I will describe the experimental setup of the $^{40}\text{Ca}^+ / ^{27}\text{Al}^+$ system that is used in experiments discussed in this thesis. To begin, I will discuss basics of ion traps which will be relevant for the discussion of sideband cooling and micromotion minimization needed to determine systematic shifts discussed in Chapter 5. Then, I will detail the hardware of our system which includes the vacuum system, ion trap, laser systems, and active noise stabilization setups. I will also discuss the laser systems used and detail laser pulse sequences used across experiments. Lastly, I will provide an overview of how quantum-logic spectroscopy is implemented in the $^{40}\text{Ca}^+ / ^{27}\text{Al}^+$ clock using the metastable transition in $^{40}\text{Ca}^+$.

When I joined the $^{27}\text{Al}^+$ clock experiment the group was finalizing the design of the new $^{27}\text{Al}^+$ quantum logic clock and the $^{40}\text{Ca}^+ / ^{27}\text{Al}^+$ side of the clock group was finishing up experiments with the capacitively coupled symmetrically driven wheel trap [54]. Spectroscopy had not yet been performed on $^{27}\text{Al}^+$ in the $^{40}\text{Ca}^+ / ^{27}\text{Al}^+$ experiment and many of the beam paths were still being assembled. Once the design work was finished we assembled the new system and installed it into the setup. We quickly trapped ions and began working toward building the remaining beam lines for the $^{40}\text{Ca}^+$ and $^{27}\text{Al}^+$ lasers. The vacuum pressure was measured and reorder rate measurements were performed for characterization of the background collision shift [55] and comparison to the previous $^{40}\text{Ca}^+ / ^{27}\text{Al}^+$ experiment. After these experiments we moved to driving the clock transition in the $^{40}\text{Ca}^+ / ^{27}\text{Al}^+$ experiment for the first time. Once this was accomplished we began the correlation spectroscopy experiments between the $^{40}\text{Ca}^+ / ^{27}\text{Al}^+$ and $^{25}\text{Mg}^+ / ^{27}\text{Al}^+$ quantum logic

clocks [56]. We continued our study of differential comparison techniques and performed differential spectroscopy with the ^{171}Yb lattice clock at NIST [57]. Now we are in the process of characterizing the systematic uncertainty of the $^{40}\text{Ca}^+ / ^{27}\text{Al}^+$ system. In this section I will detail the major components of the newest version of the $^{40}\text{Ca}^+ / ^{27}\text{Al}^+$ quantum logic clock and the experimental sequences used for measurements with $^{40}\text{Ca}^+$ and $^{27}\text{Al}^+$.

2.1 Ion trapping background

In the $^{40}\text{Ca}^+ / ^{27}\text{Al}^+$ apparatus we use a variation of a linear RF Paul trap to trap our ions. Radio frequency (RF) electric fields are applied to the Linear RF Paul trap to generate an RF pseudo-potential to trap ions in two directions typically referred to as the radial directions, and two electrodes which are perpendicular to the RF electrodes which apply a DC electric field to confine ions along what is called the axial direction. The standard 4 rod RF Paul trap can be seen in Fig 2.1 (a) where there are an additional two electrodes to displace the ion in the RF potential for micromotion minimization. Two of the radial electrodes are grounded and an oscillating voltage $V_0 \cos(\Omega_{RF}t) + U_r$ is applied to the second pair where a static voltage U_r applied to one pair of RF electrodes to break the mode degeneracy, the amplitude of the oscillating signal is represented by V_0 , and Ω_{RF} is the frequency of the RF signal used to trap the ions. The oscillating RF on the electrodes generates a potential in the x and y directions [58, 59] which is approximated for small displacements from $x = y = 0$ as

$$\Phi \simeq \frac{V_0 \cos(\Omega_{RF}t) + U_r}{2} \left(1 + \frac{x^2 - y^2}{R^2}\right), \quad (2.1)$$

where R is the approximate ion to electrode distance. To confine the ions along the axial (z) direction a static voltage is applied to the endcaps resulting in a harmonic potential described by the equation

$$\Phi_s = \kappa U_0 \left[z^2 - \frac{1}{2}(x^2 + y^2) \right] = \frac{m\omega_z^2}{2q} \left[z^2 - \frac{1}{2}(x^2 + y^2) \right], \quad (2.2)$$

where m is the mass of the ion, q is the charge of the ion, κ is a dimensionless geometric factor relating to the trap geometry which can be experimentally measured and d is the axial trap length [58].

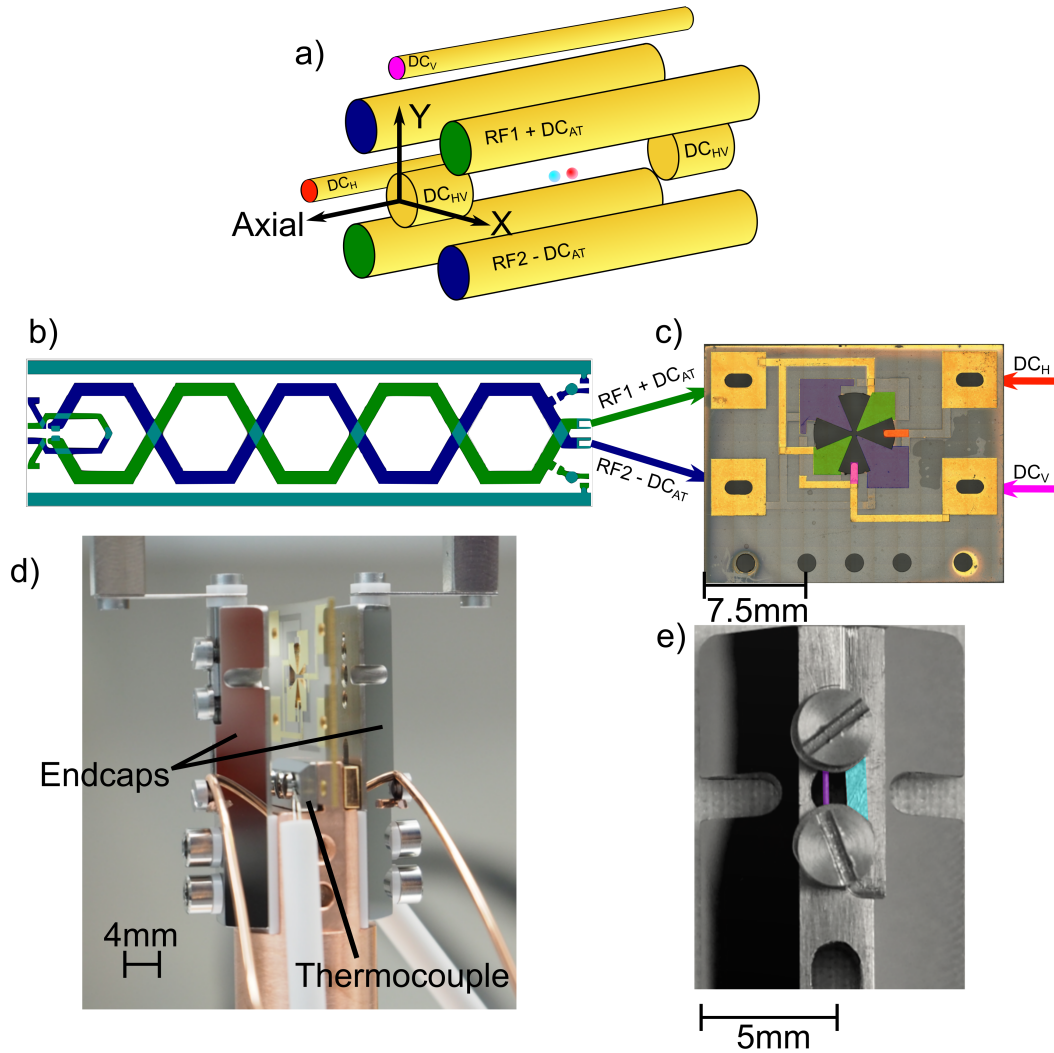


Figure 2.1: Overview of the major components used to trap ions in the $^{40}\text{Ca}^+ / ^{27}\text{Al}^+$ system. a) Diagram of a 4-rod RF Paul trap from which the wheel trap design is derived. The static confinement used to trap ions in the axial direction is applied with endcaps labeled DC_{HV} , the differentially driven radial electrodes used to generate the RF pseudo-potential are labeled $\text{RF1} + \text{DC}_{\text{AT}}$ and $\text{RF1} - \text{DC}_{\text{AT}}$, and the compensation electrodes used to move the ion in the RF pseudo-potential are labeled DC_{V} and DC_{H} which move the ion vertically and horizontally respectively. b) Meander line resonator with a hexagonal periodic pattern is used to filter and amplify the RF signal applied to the radial electrodes. c) Diamond wafer wheel trap used to trap ions. This trap design resembles a linear RF Paul trap but allows for a monolithic trap to better control design tolerances. Electrodes are color coded to match the corresponding electrodes displayed in the diagram of the linear RF Paul trap. d) Picture of the assembled ion trap which shows the diamond wafer wheel trap, the titanium endcaps, and mounted thermocouples. e) One of the titanium endcaps where the sides have been polished to use as retro-reflectors and a center region where ablation targets are mounted. The targets include a Ca/Al alloy (Blue) and a Mg wire (Purple) which are falsely colored to highlight the targets.

The ion also oscillates in the radial direction due to the pseudo-potential at frequencies ω_x and ω_y . Together these frequencies are referred to as secular frequencies. We use the combination of the static and RF potential to solve for the values of the x and y secular frequencies. The equations of motion along the radial directions take the form of the Mathieu equations

$$\frac{d^2 u_x}{d^2 t} + [a_x + 2q_x \cos(\Omega_{RF} t)] \frac{\Omega_{RF}^2}{4} u_x = 0 \quad (2.3)$$

$$\frac{d^2 u_y}{d^2 t} + [a_y + 2q_y \cos(\Omega_{RF} t)] \frac{\Omega_{RF}^2}{4} u_y = 0, \quad (2.4)$$

where the physical trap parameters are redefined as

$$a_x \equiv (4q/m\Omega_{RF}^2)(U_r/R^2 - \kappa U_0) \quad (2.5)$$

$$a_y \equiv -(4q/m\Omega_{RF}^2)(U_r/R^2 + \kappa U_0) \quad (2.6)$$

$$q_x = -q_y = 2qV_0/(\Omega_{RF}^2 m R^2) \quad (2.7)$$

to simplify solving for the equations of motion. The equation of motion for the axial direction is described by

$$\frac{d^2 u_z}{d^2 t} + \frac{q\kappa U_0}{m} u_z = 0 \quad (2.8)$$

which has no dependence on the RF electric field under ideal conditions. A static electric field applied along the radial direction will displace the ion from the center of the potential to a position of $\vec{u}_0 \cong u_{0,x}\hat{x} + u_{0,y}\hat{y} + u_{0,z}\hat{z}$. The resulting acceleration is described by $\ddot{u}_i = \frac{q\vec{E}_{DC} \cdot \hat{u}_i}{m}$ and modifies the equations of motion which are rewritten as

$$\frac{d^2 u_x}{d^2 t} + [a_x + 2q_x \cos(\Omega_{RF} t)] \frac{\Omega_{RF}^2}{4} u_x = \frac{q\vec{E}_{DC} \cdot \hat{u}_x}{m} \quad (2.9)$$

$$\frac{d^2 u_y}{d^2 t} + [a_y + 2q_y \cos(\Omega_{RF} t)] \frac{\Omega_{RF}^2}{4} u_y = \frac{q\vec{E}_{DC} \cdot \hat{u}_y}{m}, \quad (2.10)$$

for the radial directions and

$$\frac{d^2 u_z}{d^2 t} + \frac{q\kappa U_0}{m} u_z = \frac{q\vec{E}_{DC} \cdot \hat{u}_z}{m}. \quad (2.11)$$

for the axial direction. The Mathieu equation can be solved, in general, using Floquet solutions and when considering the adiabatic approximation which is valid in this system, the equations of

motion can be taken to first order in the parameters a_i and q_i because we are working in a regime such that $a_i < q_i^2 \ll 1, i \in \{x, y\}$. The Floquet solutions when solved to first order in a_i, q_i^2 are

$$u_i(t) = u_{0,i} + u_{1,i} \cos(\omega_i t + \phi_i) \left[1 + \frac{q_i}{2} \cos(\Omega_{RF} t) \right], \quad (2.12)$$

for the radial directions and

$$u_z(t) = u_{0,z} + u_{1,z} \cos(\omega_z t + \phi_i) \quad (2.13)$$

for the axial direction where $u_{0,i}$ is the ion position in direction i and $u_{1,i}$ is the secular motion amplitude in direction i . In this simplified version of the equations of motion there are terms dependent on the secular frequencies ω_i and the trap drive frequency Ω_{RF} with the z -direction only being dependent on the axial secular frequency ω_z . In our system there is a residual trap RF electric field along the axial direction due to a small misalignment between the trap wafer and the endcaps. The residual RF causes the equations of motion for the axial direction to follow the same form as the radial equations of motion. The modified axial equation of motion can be written as

$$u_z(t) = u_{0,z} + u_{1,z} \cos(\omega_z t + \phi_i) \left[1 + \frac{q_z}{2} \cos(\Omega_{RF} t) \right], \quad (2.14)$$

where q_z is still dependent on the RF voltage V_0 but will depend on a different geometric factor and $|q_z| < |q_i| \ll 1$. This is the regime where our trap operates. As $q_z \rightarrow 0$ the equation returns to its original form. From these equations of motion, the harmonic pseudo-potential can be rewritten in terms of the secular frequencies in the radial directions and is given by

$$\Phi_P = \frac{m\omega_r^2}{2q} (x^2 + y^2). \quad (2.15)$$

From the static and RF potentials the secular frequencies can be described by

$$\omega_p = \omega_x = \omega_y = \frac{qV_0}{\sqrt{2}\Omega_{RF}mR^2} = q_x\Omega_{RF}/2\sqrt{2}, \quad (2.16)$$

$$\text{and } \omega_z = \sqrt{\frac{2\kappa qU_0}{m}}. \quad (2.17)$$

In this equation $\omega_x = \omega_y$ is only true in the case that $U_r = 0$ but the degeneracy of secular frequencies is lifted by applying a static voltage U_r to a pair of radial electrodes. The resulting

secular frequencies are given by Ref. [59]. In Fig. 2.1 we label this anti-trapping voltage as DC_{AT} .

These modified secular frequencies are written as

$$\omega'_x = \sqrt{\omega_p^2 - \alpha\omega_z^2} = \sqrt{\epsilon^2 - \alpha}\omega_z, \quad (2.18)$$

$$\omega'_y = \sqrt{\omega_p^2 - (1 - \alpha)\omega_z^2} = \sqrt{\epsilon^2 - (1 - \alpha)}\omega_z, \quad (2.19)$$

with $0 > \alpha > 1$ being the anti-trapping factor which indicates the strength of the radial asymmetry. Often the anti-trapping factor α is determined by measuring the secular mode frequencies. The parameter $\epsilon = \omega_p/\omega_z$ is the ratio of the unbiased radial secular frequency and axial secular frequency. Representing the secular frequencies in terms of ϵ and α will be useful in simplifying the equations when extending the discussion to a two ion crystal.

For a two ion crystal there are 6 motional modes where there is an in-phase and out-of-phase mode for each radial direction. We describe the mass ratio of the two ions in the crystal as $\mu = m_2/m_1$ and the two modes for each direction can be further classified as an in phase center of mass (COM) mode and an out-of-phase stretch (STR) mode. The in-phase (I) and out-of-phase (O) modes are described by the equations from Ref. [59]

$$\omega_{I,z} = \sqrt{\frac{1 + \mu - \sqrt{1 - \mu + \mu^2}}{\mu}}\omega_z, \quad (2.20)$$

$$\omega_{O,z} = \sqrt{\frac{1 + \mu + \sqrt{1 - \mu + \mu^2}}{\mu}}\omega_z, \quad (2.21)$$

$$\omega_{I,x,y} = \sqrt{-\frac{\mu + \mu^2 - \epsilon^2(1 + \mu^2) - a}{2\mu^2}}\omega_z, \quad (2.22)$$

$$\omega_{O,x,yp} = \sqrt{-\frac{\mu + \mu^2 - \epsilon^2(1 + \mu^2) + a}{2\mu^2}}\omega_z, \quad (2.23)$$

$$a = \sqrt{\epsilon^4(\mu^2 - 1)^2 - 2\epsilon^2(\mu - 1)^2\mu(1 + \mu) + \mu^2[1 + (\mu - 1)\mu]}. \quad (2.24)$$

where the in-phase and out-of-phase frequencies for the two radial directions are degenerate in this derivation. We set the mode frequencies experimentally by applying an anti-trapping voltage and measuring the frequencies. When characterizing the cooling of these motional modes it is necessary to determine the mode amplitude or mode participation for each ion. In Ref. [59], the

mode amplitude is solved analytically but for our experiments we determine the secular mode amplitude by solving the equations of motion numerically. In addition, the mode amplitude can be experimentally determined by taking the ratio of the Rabi rate of the “carrier” transition used and the secular frequency sideband Rabi rate. The Rabi rate is a measure of the rate of driving the population from the ground to the excited state of the electronic transition and is dependent on the laser intensity, laser direction, and the quadrupole transition strength for $^{40}\text{Ca}^+$. A Rabi oscillation between two states with energy difference $\hbar\omega_0 = E_e - E_g$ is described by the time dependent probability and the Rabi oscillation rate which are written as

$$P_{g \rightarrow e}(t) = \left(\frac{\Omega_0}{\Omega}\right)^2 \sin^2\left(\frac{\Omega t}{2}\right), \Omega = \sqrt{(\omega_L - \omega_0)^2 + \Omega_0^2}, \quad (2.25)$$

where ω_L is the interrogating laser frequency and Ω_0 is the Rabi rate for the specific transition.

In a $^{40}\text{Ca}^+ / ^{27}\text{Al}^+$ crystal the mode amplitudes for each of the ions motions will be different because of the mass difference of the two co-trapped ions [59]. This variation in the mode amplitudes for specific ions will result in slower Rabi rates for the radial $^{40}\text{Ca}^+$ in-phase modes but faster for the radial $^{40}\text{Ca}^+$ out-of-phase modes. This reduction in driving rate will become detrimental when performing sideband cooling or characterizing the temperature of the ion and will be further discussed in Chapter 5.

Micromotion and secular motion are measured using the sidebands of the atomic transition which appear in the spectrum of the laser interacting with the ion. In the reference frame of the ion, the motion of the ion will appear as a phase modulation of the incident laser light and cause sidebands in the frequency spectrum. The phase modulation to the laser relative to the ion is, $\phi(t) = \vec{k} \cdot \vec{u}(t)$, where $\vec{u}(t)$ the time dependent ion position and \vec{k} is the laser wave vector. The electric field seen by the ion is given by a term describing the phase modulation of the laser in the rest frame of the ion and a term describing the oscillating electric field of the laser, this is written as

$$\vec{E}(t) = \vec{E}_0 \times e^{i\phi(t)} \times e^{i(\omega_0 - \omega_L)t} = \vec{E}_0 \times e^{i(\vec{k} \cdot \vec{u}(t))} \times e^{i(\omega_0 - \omega_L)t}, \quad (2.26)$$

where ω_0 is the atomic transition frequency, and ω_L is the laser frequency. The phase modula-

tion term can be broken into three components resulting from the equations of motion of the ion (Eq. 2.12) which we label $\phi(t) = \phi_{\text{sec}}(t) + \phi_{\text{IMM}}(t) + \phi_{\text{EMM}}(t)$. The first phase modulation term arises from the secular motion which is only dependent on the secular frequency. The secular motion results in a phase modulation of

$$\phi_{\text{sec}}(t) = k_i u_{1,z} \cos(\theta) \cos(\omega_i t + \phi_i) \quad (2.27)$$

where θ is the angle between the wave-vector and the ion motion. The second term is referred to as the intrinsic micromotion (IMM) and is caused by motion at the frequencies Ω_{RF} and ω_i . This phase modulation is given by

$$\phi_{\text{IMM}}(t) = \frac{k_i u_{1,i} q_i}{2} \cos(\theta) \cos(\omega_i t + \phi_i) \cos(\Omega_{RF} t), \quad (2.28)$$

which, using trigonometric identities can be written as

$$= \frac{k_i u_{1,i} q_i}{4} \cos(\theta) (\cos((\Omega_{RF} - \omega_i)t + \phi_i) + \cos((\Omega_{RF} + \omega_i)t + \phi_i)). \quad (2.29)$$

where we identify two terms one at $\Omega_{RF} - \omega_i$ and another at $\Omega_{RF} + \omega_i$. If the ion is well centered in the trap, IMM will still be present due to the movement of the ion into the RF field from the secular oscillation. The last term is a consequence of the RF electric field and arises from a displacement of the ion away from the center of the trap where the RF electric field is zero. This modulation factor is referred to as excess micromotion (EMM) and is given by

$$\phi_{\text{EMM}}(t) = \frac{k_i u_{0,i} q_i \cos(\theta)}{2} \cos(\Omega_{RF} t). \quad (2.30)$$

The Jacobi-Anger expansion can then be used to write Eq. 2.26 in terms of Bessel functions. The Jacobi-Anger expansion is given by

$$e^{iz \cos(\phi)} = \sum_{n=-\infty}^{\infty} i^n J_n(z) e^{in\phi}. \quad (2.31)$$

Using this expansion the electric field of the laser can be written as

$$\begin{aligned} \vec{E}(t) = \vec{E}_0 e^{i(\omega_0 - \omega_L)t} & \left(\sum_{n=-\infty}^{\infty} i^n J_n(k_i u_{1,i} \cos(\theta)) e^{in(\omega_i t + \phi_i)} \right) \left(\sum_{n=-\infty}^{\infty} i^n J_n\left(\frac{k_i u_{0,i} q_i \cos(\theta)}{2}\right) e^{in(\Omega_{RF} t)} \right) \\ & \left(\sum_{n=-\infty}^{\infty} i^n J_n\left(\frac{k_i u_{1,i} q_i}{4} \cos(\theta)\right) e^{in((\Omega_{RF} - \omega_i)t + \phi_i)} \right) \left(\sum_{n=-\infty}^{\infty} i^n J_n\left(\frac{k_i u_{1,i} q_i}{4} \cos(\theta)\right) e^{in((\Omega_{RF} + \omega_i)t + \phi_i)} \right). \end{aligned} \quad (2.32)$$

To simplify this equation it is assumed that the Bessel function arguments are $\ll 1$ so only terms up to $n = 1$ need to be considered in the expansion. Additionally, the arguments of the Bessel functions can be relabeled as β_i which describes the modulation index from the phase modulation. The terms are relabeled as $\beta_{sec} = k_i u_{1,i} \cos(\theta)$, $\beta_{EMM} = \frac{k_i u_{0,i} q_i \cos(\theta)}{2}$, $\beta_{IMM} = \frac{k_i u_{1,i} q_i \cos(\theta)}{4}$. The electric field can then be written as

$$\begin{aligned} \vec{E}(t) = \vec{E}_0 e^{i(\omega_0 - \omega_L)t} & \left(J_0(\beta_{sec}) + iJ_1(\beta_{sec})e^{i(\omega_i t + \phi_i)} - iJ_{-1}(\beta_{sec})e^{-i(\omega_i t + \phi_i)} \right) \\ & \left(J_0(\beta_{EMM}) + iJ_1(\beta_{EMM})e^{i(\Omega_{RF}t)} - iJ_{-1}(\beta_{EMM})e^{-i(\Omega_{RF}t)} \right) \\ & \left(J_0(\beta_{IMM}) + iJ_1(\beta_{IMM})e^{i((\Omega_{RF} - \omega_i)t + \phi_i)} - iJ_{-1}(\beta_{IMM})e^{-i((\Omega_{RF} - \omega_i)t + \phi_i)} \right) \\ & \left(J_0(\beta_{IMM}) + iJ_1(\beta_{IMM})e^{i((\Omega_{RF} + \omega_i)t + \phi_i)} - iJ_{-1}(\beta_{IMM})e^{-i((\Omega_{RF} + \omega_i)t + \phi_i)} \right) \end{aligned} \quad (2.33)$$

When $\beta_i \ll 1$ these equations can be simplified again resulting in

$$\begin{aligned} \vec{E}(t) = \vec{E}_0 e^{i(\omega_0 - \omega_L)t} & \left(1 + \frac{\beta_{sec}}{2} e^{i(\omega_i t + \phi_i + \pi/2)} + \frac{\beta_{sec}}{2} e^{-i(\omega_i t + \phi_i + \pi/2)} \right) \\ & \left(1 + \frac{\beta_{EMM}}{2} e^{i(\Omega_{RF}t + \pi/2)} + \frac{\beta_{EMM}}{2} e^{-i(\Omega_{RF}t + \pi/2)} \right) \\ & \left(1 + \frac{\beta_{IMM}}{2} e^{i((\Omega_{RF} - \omega_i)t + \phi_i + \pi/2)} + \frac{\beta_{IMM}}{2} e^{-i((\Omega_{RF} - \omega_i)t + \phi_i + \pi/2)} \right) \\ & \left(1 + \frac{\beta_{IMM}}{2} e^{i((\Omega_{RF} + \omega_i)t + \phi_i + \pi/2)} + \frac{\beta_{IMM}}{2} e^{-i((\Omega_{RF} + \omega_i)t + \phi_i + \pi/2)} \right). \end{aligned} \quad (2.34)$$

If this is taken to first order in β_i and $\phi_i + \pi/2 = \phi'_i$ the resulting spectrum will follow the equation

$$\begin{aligned} \vec{E}(t) = \vec{E}_0 & \left(e^{i(\omega_0 - \omega_L)t} + \frac{\beta_{sec}}{2} e^{i((\omega_i + \omega_0 - \omega_L)t + \phi'_i)} + \frac{\beta_{EMM}}{2} e^{i((\Omega_{RF} + \omega_0 - \omega_L)t + \phi'_i)} \right. \\ & + \frac{\beta_{IMM}}{2} e^{i((\omega_{RF} - \omega_i + \omega_0 - \omega_L)t + \phi'_i)} + \frac{\beta_{IMM}}{2} e^{i((\omega_{RF} + \omega_i + \omega_0 - \omega_L)t + \phi'_i)} \\ & + \frac{\beta_{sec}}{2} e^{-i((\omega_i + \omega_0 - \omega_L)t + \phi'_i)} + \frac{\beta_{EMM}}{2} e^{-i((\Omega_{RF} + \omega_0 - \omega_L)t + \phi'_i)} \\ & \left. + \frac{\beta_{IMM}}{2} e^{-i((\omega_{RF} - \omega_i + \omega_0 - \omega_L)t + \phi'_i)} + \frac{\beta_{IMM}}{2} e^{-i((\omega_{RF} + \omega_i + \omega_0 - \omega_L)t + \phi'_i)} \right). \end{aligned} \quad (2.35)$$

This equation displays both the red and blue sidebands of the micromotion and secular frequency sidebands. When considering driving transitions at the carrier frequency and the micromotion sideband frequency we can use the ratio of the Rabi rates of these transitions to determine the modulation index, $\Omega_1 = \Omega_0 \beta_i / 2$, when measured at the specified sideband frequency $\omega_l = \omega_i$.

Therefore, when measuring the ratio $\Omega_{\pm 1}/\Omega_0 = \beta_i/2$ which is the blue or red (+/-) micromotion sideband Rabi rate to the carrier Rabi rate we can get a direct measurement of the modulation index. This expression will be used in later chapters to characterize the EMM in the $^{40}\text{Ca}^+ / ^{27}\text{Al}^+$ experiment.

2.2 $^{40}\text{Ca}^+ / ^{27}\text{Al}^+$ ion trap

The primary components which make up the apparatus are a type of linear RF Paul trap which we call the diamond wafer wheel trap, the Ti-vacuum system, and the meander line resonator. Each of these components will be discussed in detail and compared with what was used historically and in previous $^{27}\text{Al}^+$ -ion clocks at NIST.

2.2.1 Diamond wafer wheel trap

In this experiment a type of a linear RF-Paul trap referred to as the wheel trap is used. The derivation of the trapped ion behavior is identical in this case aside from a factor 2 increase in the trapping voltage from the RF synthesizer differentially driving the electrodes. Additionally, instead of using individual macroscopically machined rods to form the trap all of the electrodes are patterned on a single Diamond wafer. The diamond wafer used in this experiment is 500 μm thick and is laser cut to form the shape of the electrodes which will generate the trapping region. Previous versions of the wheel trap have used 300 μm thick diamond wafers but in this experiment the thickness was increased to improve the uniformity of the axial trapping region by making the RF “rods” longer. An added benefit of using a diamond wafer as the substrate for the RF trap is the high thermal conductivity of diamond which aids in the dissipation of heat created from dissipation of the RF voltage applied to the trap. It is important to have good heat dissipation to prevent large temperature gradients which can increase the uncertainty of the black body radiation shift. Measurements of the thermal gradients are discussed in Chapter 5. To form the trapping electrodes, a 5 μm thick gold layer is sputtered onto the diamond wafer using a shadow mask to define the shapes of the individual electrodes. This coating forms both the RF trapping electrodes to generate

the RF pseudo-potential and the DC electrodes which are used to displace the ions vertically and horizontally. The benefit to laser cutting and sputtering gold to fabricate the trap is the ability to produce a monolithic trap with electrode distances that have tight tolerances of a few μm . The precise spacing between electrodes reduces residual RF electric fields at the center of the pseudo-potential. The residual RF in the radial direction comes from a phase mismatch of the electric fields and the residual RF in the axial direction is caused by misalignment in the trap electrodes or an imbalance in the RF amplitude applied to the trapping electrodes. This residual RF field will cause excess micromotion (EMM), inducing a second order Doppler shift in the atomic clock. Previous versions of the diamond wafer trap have been used in other systems [28, 54] but these versions have had difficulties in minimizing the residual electric field along both the axial direction and the vertical directions due to an imbalance in the capacitance of different electrodes. To reduce the residual RF in the newest version of the wheel trap, the capacitance between electrodes on the wheel trap was increased to allow for easier balancing of the capacitance between electrodes and in some cases traces were made thinner to reduce coupling between some electrodes particularly those that overlap with each other on the two sides of the diamond wafer trap. With better balancing of capacitance between electrodes the ability to compensate the micromotion by applying RF along the axial and radial directions is possible because the compensation field will no longer asymmetrically couple to different electrodes. By controlling the phase and amplitude of this compensating electric field at the trap frequency Ω_{RF} the residual RF can be reduced through destructive interference with the compensation field.

2.2.2 Meander line resonator

We drive the trap using an amplified ≈ 72 MHz signal from a Holtzworth digital synthesizer and inject it into a meander line resonator connected to the ion trap electrodes. The meander line resonator filters noise from the source signal and amplifies the electric field sent to the RF electrodes. Previous versions of the meander line resonators used a semi-circle periodic copper pattern on two sides of Rogers board to create the RF resonator where here we use a semi-hexagonal periodic copper

pattern. In the previous design, a freestanding wire loop was used to couple RF into the resonator which made the coupling and impedance matching prone to drifting, affecting the stability of the ion secular frequencies. This version of the meander line resonator uses a balun and integrated coupling loop to couple RF into the resonator removing the possibility of mechanical drifts. The resonant frequency of the meander line resonator is determined by the number of loops used and an example of the hexagonal resonator can be seen in Fig. 2.1 and the hexagonal periodic pattern is used to control the size of the resonator while maintaining the value of the inductance needed for the desired resonant frequency. Additionally, we tested both Rogers and alumina as substrates for the PCB where limits to the quality factor are set by dielectric losses of these two materials. By switching to alumina the dielectric losses can be reduced thereby increasing the Q-factor by 5-10, with the additional benefit of alumina having a better thermal conductivity. Heat is dissipated on the wafer due to resistive and dielectric loss and if the thermal conductivity of the PCB is low the resonator will heat up. When alumina is used, the heat can be more efficiently dissipated through the PCB to the aluminum resonator shield. Better temperature stability ensures a more stable RF amplitude and subsequently an improvement in the secular frequency stability. With the updated resonator design and using Rogers boards as the PCB substrate Q-factors of 140 can be achieved, and by switching to Alumina Q-factors of 170 can be achieved.

To house the meander line resonator an aluminum resonator shield was designed. N-type and SMA connectors used as feedthroughs on this shield to apply the RF to the resonator board and to apply a bias voltage to the RF electrodes to break the secular frequency degeneracy. Copper pads on the edges of the meander line resonator are used to ensure good thermal contact between the resonator board and the shield. The resonator board is clamped between two aluminum mounting blocks then mounted to the resonator shield providing heatsinking of the resonator board through the aluminum shield. RF gaskets are used between the shield body and the shield lid to ensure a full RF seal preventing stray RF fields from coupling to the resonator board. RF fields detuned from the trap drive frequency by the secular frequency will induce motional heating if present in the system.

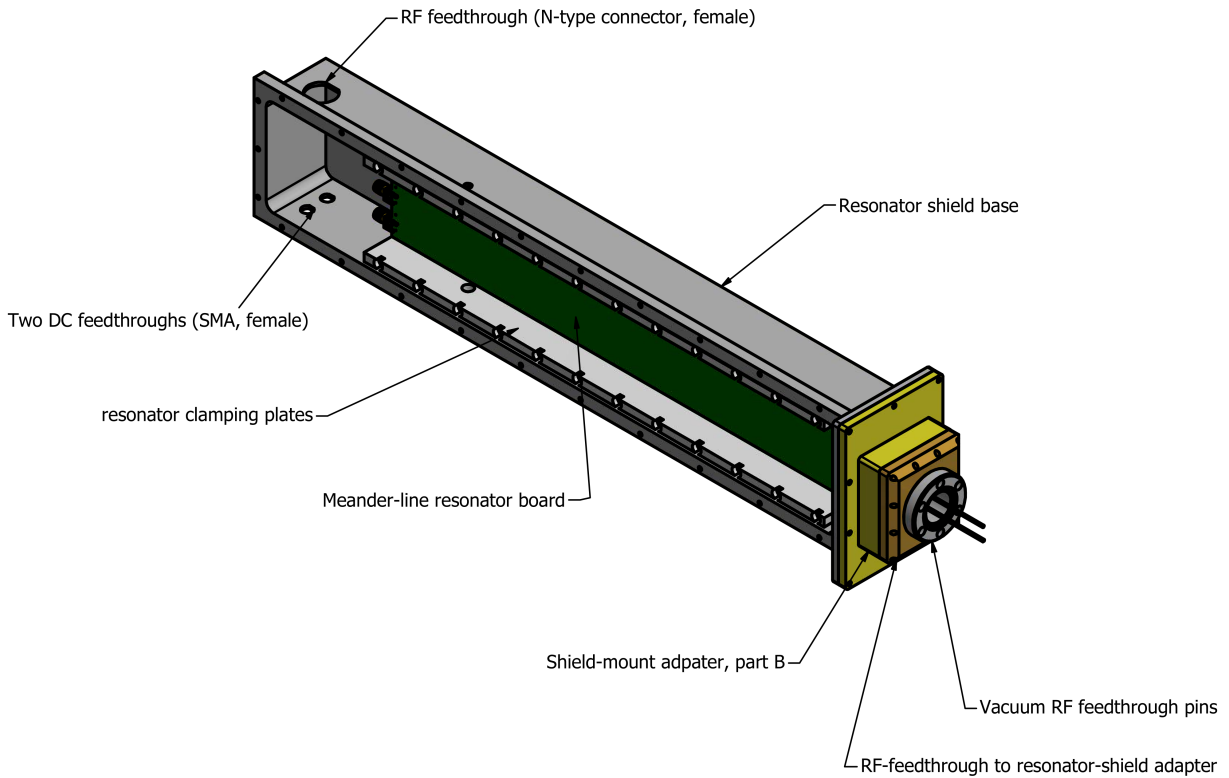


Figure 2.2: CAD drawing of the meander line resonator shield used in our experiment. This shield is used to prevent environmental noise from coupling directly to the resonator board which can cause motional heating if the noise at the motional sideband frequency. The lid is not pictured but covers the internal components seen in the picture.

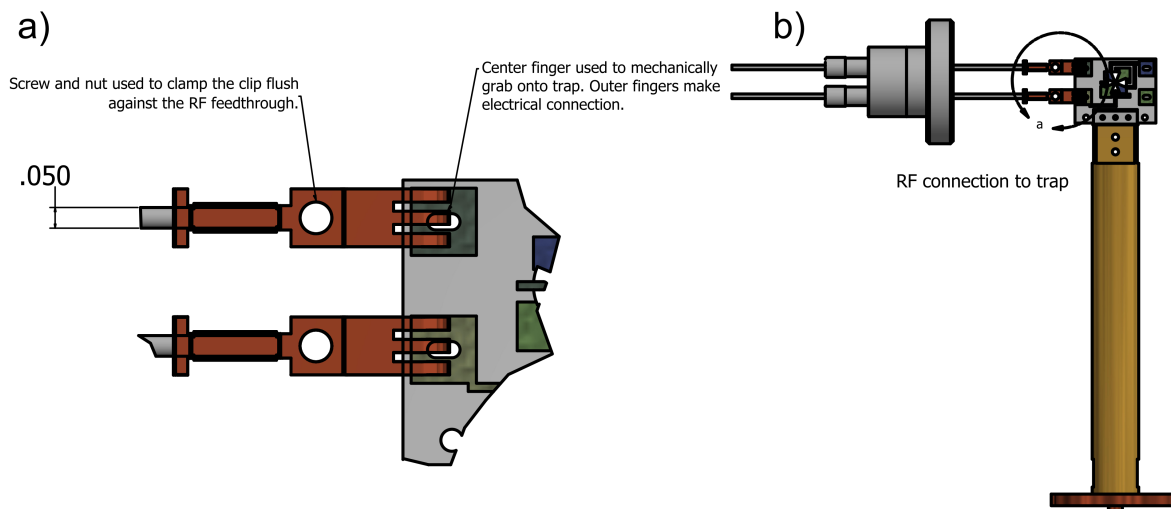


Figure 2.3: CAD drawing of the grabber arms to connect trap electrodes. a) Zoomed in picture of the grabber arms showing the connection between the vacuum feedthrough pins and the trap electrode pad. These grabber arms are folded metal and are gold coated to ensure a good electrical connection. b) Zoomed out picture of the grabber arms in reference to the trap mounted to the copper post bridging the electrical connection for the RF trapping voltage. An identical set of grabber arms are used on the other side of the trap to input the DC compensation voltages.

2.2.3 Titanium Vacuum system

We developed this new system to have vacuum components primarily made of titanium to reduce the hydrogen partial pressure in the system. The motivation for reducing the hydrogen partial pressure is to reduce the probability of Al-H^+ formation and to reduce the shift due to background gas collisions. Al-H^+ formation limited the up-time of the clock in previous comparisons [35] and the background gas collision shift uncertainty increases with increasing probe times [55]. We detail our efforts to reduce the hydrogen partial pressure in our system to eliminate these effects.

The vacuum system used in our system was designed to be compact and use only a few vacuum components. These components include: a 2.75" spherical octagon to provide enough optical access and electronic connections for the trap; a double spherical cube to provide enough space for BNC feedthroughs, a SAES D-100 combination ion and non-evaporable getter (NEG) pump, a feedthrough for thermistors for temperature monitoring, and copper pinch-off for the initial pump down. A picture of the vacuum system can be seen in Fig. 2.4. The BNC high voltage

feedthrough flange mounted to the double spherical cube is used to apply voltages to the titanium endcaps. We mount the ablation targets to one of the titanium endcaps on the face facing away from the wheel trap, seen in Fig. 2.1. One target mounted to the endcap is a Ca-Al alloy, that is 30% Ca and 70% Al, which is cut into a wafer and mounted in a groove on the endcap. Loading from an alloy removes the need to displace the ablation laser when loading the two species where in the previous system two separate targets were used for loading the logic ion and the aluminum ion. The other target is a natural abundance Mg wire which is fastened on the other side of the endcap facing away from the wheel trap. The Mg wire was included in our system in case we found it necessary to use $^{25}\text{Mg}^+$ for characterization of certain systematic shifts. On the octagon there are two feedthroughs each with two pins that enter perpendicular to the normal vector of the wheel trap. These feedthrough pins are used to apply DC and RF voltages to the electrodes to generate the RF pseudo-potential and displace the ion vertically and horizontally in the ion trap. To bridge the distance between the feedthrough pins and the diamond wafer, grabber arms are mounted to the feedthrough pins and connected to gold pads sputtered on the diamond wafer. These grabber arms are seen in Fig. 2.3

A major modification in this iteration of the $^{27}\text{Al}^+$ quantum-logic clock is that the vacuum system is primarily made of a titanium grade 5 alloy. The only stainless steel present in the vacuum system is the body and the con-flat connector of the SAES combination ion pump/NEG getter. The purpose for using titanium in place of 316 stainless steel is to reduce the hydrogen partial pressure in the vacuum chamber. Because of the crystalline structure of titanium, when baking the system much more of the hydrogen trapped in the bulk of the material can move along the grain boundaries and be pumped out of the system [60, 61]. This helps minimize the possible sources of hydrogen without going to cryogenic temperatures. In similar operating conditions stainless steel will still continue to have hydrogen trapped in the bulk of the material which can become a long term source of hydrogen outgassing [62]. When operating the clock and driving the $^{27}\text{Al}^+$ clock transition the $^{27}\text{Al}^+$ ion spends a portion of time in the $^3\text{P}_0$ excited state. If a H_2 molecule collides with the $^{27}\text{Al}^+$ ion while it is in the excited $^3\text{P}_0$ state, the H_2 molecules interacting with the ion

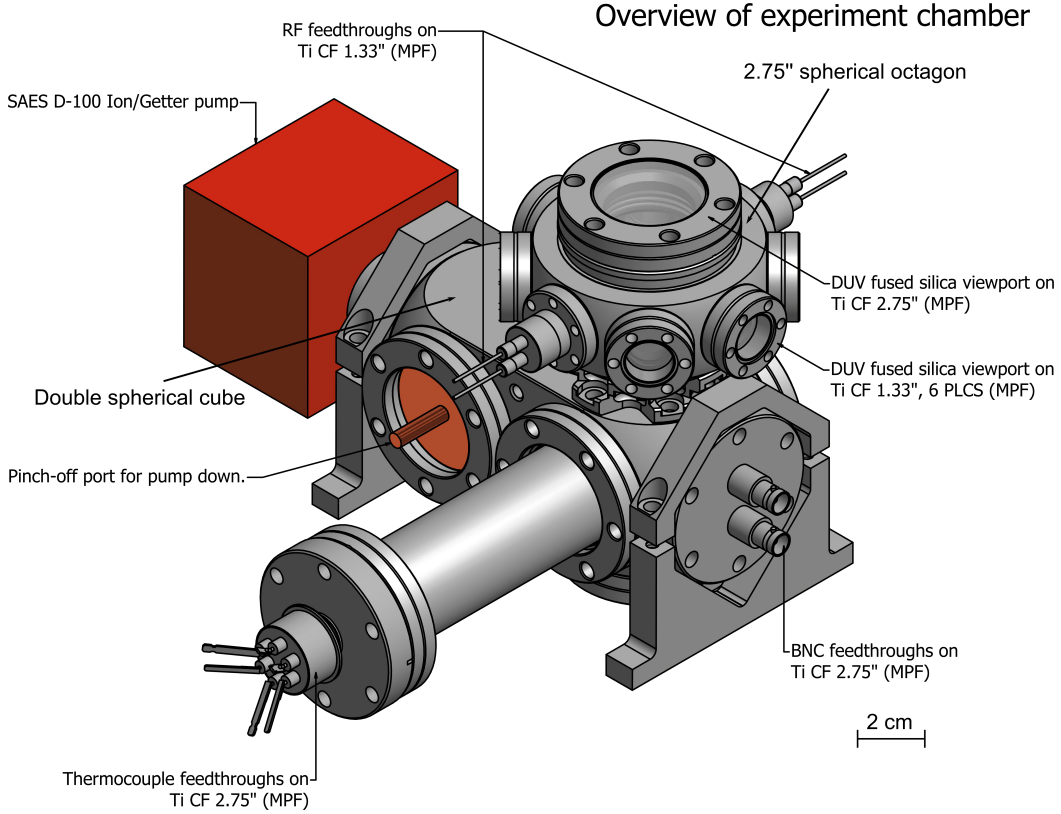


Figure 2.4: Overview of the titanium vacuum system used in our experiments. Relevant electrical connections for the ion trap and temperature sensors are labeled. When baking the system gas is pumped through the copper pinch-off tube into a larger ion-pump. The tube is pinched following the bake and the SEAS ion pump is used to maintain the vacuum pressure.

will have enough energy to overcome the reaction barrier with some probability, forming Al-H^+ .

2.3 $^{40}\text{Ca}^+$ -logic ion operations

The $^{40}\text{Ca}^+$ ion is a convenient ion to use in quantum information experiments and as a co-trapped ion for quantum-logic spectroscopy due to its transitions being easily accessible with diode based laser systems. Doppler cooling and fluorescence detection can be implemented using either the $|4^2S_{1/2}\rangle \leftrightarrow |4^2P_{1/2}\rangle$ or the $|4^2S_{1/2}\rangle \leftrightarrow |4^2P_{3/2}\rangle$ transitions, seen in Fig. 2.5 where we make use of the former. The transitions are driven with a wavelength of ≈ 397 nm and ≈ 393 nm respectively. The ion will $\approx 6\%$ of the time [63] into the $|3^2D_{3/2}\rangle$ metastable state so a repumper is applied simultaneously to drive the $|3^2D_{3/2}\rangle \leftrightarrow |4^2P_{1/2}\rangle$, $|3^2D_{3/2}\rangle \leftrightarrow |4^2P_{3/2}\rangle$, or $|3^2D_{5/2}\rangle \leftrightarrow |4^2P_{3/2}\rangle$ transition. The

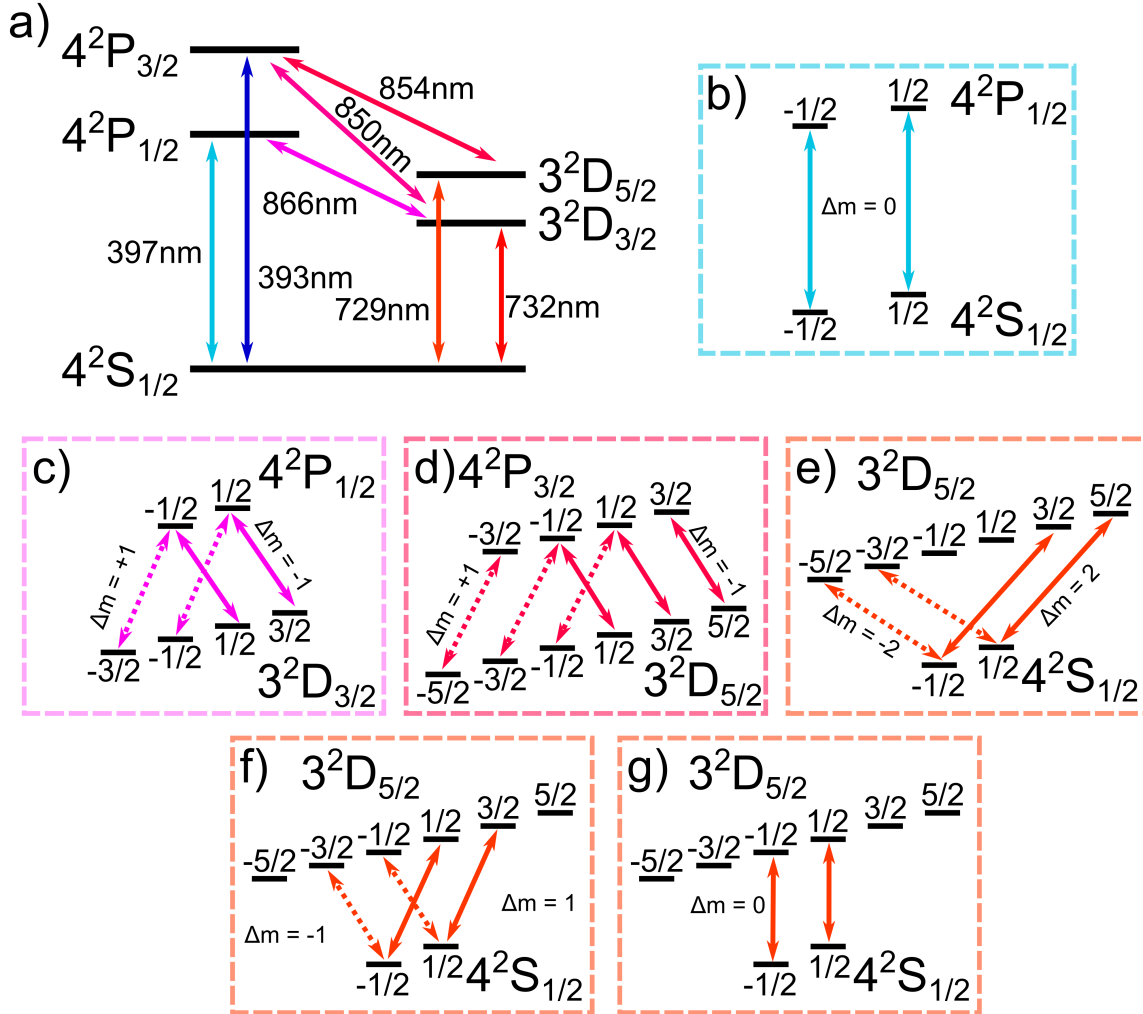


Figure 2.5: Level structure of $^{40}\text{Ca}^+$ with the Zeeman manifolds displayed for all of the states to describe the transitions driven in cooling (b), detection (b), repumping (c,d), and qubit operations (e-g)

wavelength used to drive these transitions are ≈ 866 nm, ≈ 850 nm and ≈ 854 nm respectively. Lastly, there are two qubit transitions $|4^2S_{1/2}\rangle \leftrightarrow |3^2D_{3/2}\rangle$ and $|4^2S_{1/2}\rangle \leftrightarrow |3^2D_{5/2}\rangle$ which can be driven with 732 nm and 729 nm wavelength lasers. The transitions which are used in this experiment are the $|4^2S_{1/2}\rangle \leftrightarrow |4^2P_{1/2}\rangle$, $|3^2D_{3/2}\rangle \leftrightarrow |4^2P_{1/2}\rangle$, $|3^2D_{5/2}\rangle \leftrightarrow |4^2P_{3/2}\rangle$, and $|4^2S_{1/2}\rangle \leftrightarrow |3^2D_{5/2}\rangle$ transitions. In these various manifolds different sequences are used to manipulate the state of the ion where these sequences require specific beam pointing and beam polarization to drive the required transitions. The $^{40}\text{Ca}^+$ transitions used in this system are labeled in Fig. 2.5.

For Doppler cooling and state detection, photons are scattered by the $^{40}\text{Ca}^+$ valence electron when driving the $|4^2S_{1/2}\rangle \leftrightarrow |4^2P_{1/2}\rangle$ transition. To prevent population from getting trapped in a metastable state the $|3^2D_{3/2}\rangle \leftrightarrow |4^2P_{1/2}\rangle$ transition is used to repump population back to the $|4^2P_{1/2}\rangle$ state. The $|4^2S_{1/2}\rangle \leftrightarrow |4^2P_{1/2}\rangle$ transition has a linewidth of ≈ 20.6 MHz. In the $|4^2S_{1/2}\rangle \leftrightarrow |4^2P_{1/2}\rangle$ manifold we choose to drive $\Delta m = 0$ transitions which uses π -polarized light to maximize the Rabi rate. Because of the small Zeeman splitting and the broad linewidth of the $|4^2S_{1/2}\rangle \leftrightarrow |4^2P_{1/2}\rangle$ transition, both Zeeman transitions are addressed. One issue with this transition is that since the repumper is applied at the same time as the cooling light a dark state can occur due to coherent effects between the two transitions [64]. This can effect the line shape of the cooling transitions impacting the scattering rate and cooling of different motional modes. This effect can also be used to increase the slope of the Doppler cooling lineshape by placing the dark resonance in the Doppler cooling line by adjusting the detuning of the 866 nm laser [65] allowing for a larger cooling rate. When applying the $|3^2D_{3/2}\rangle \leftrightarrow |4^2P_{1/2}\rangle$ repumper we choose to use $\pm\sigma$ polarized light which will clear all of the population out of the $|3^2D_{3/2}\rangle$ metastable state, which are separated by a applying a quantization field to the ion. Only one laser frequency is needed because the transitions are not frequency resolved and the polarization choice connects all the states as seen in Fig 2.5 (c). For detection experiments we observe an average of 18 counts during a detection time of 260 μs . Examples of the detection and Doppler cooling line shapes can be seen in Fig. 2.6. In Doppler cooling, we optimize the cooling rate experimentally by adjusting the amplitude and frequency of the 397 nm and 866 nm lasers. We use sideband thermometry to determine the temperature of the ion following Doppler cooling and results of this characterization will be presented in Chapter 5. To aid in loading the ions we use a far-detuned cooling beam. This cooling laser is also useful when cooling the ion after high energy background gas collisions. This laser is detuned to be on resonance with the third red micromotion sideband which will result in a high scattering rate if the ion is especially hot and de-localized in the RF-Paul trap. From the slope of this lineshape we expect the Doppler cooling to cool single $^{40}\text{Ca}^+$ to $\bar{n} = (3.9, 2.6, 2.8)$ for $(\omega_z, \omega_x, \omega_y)$.

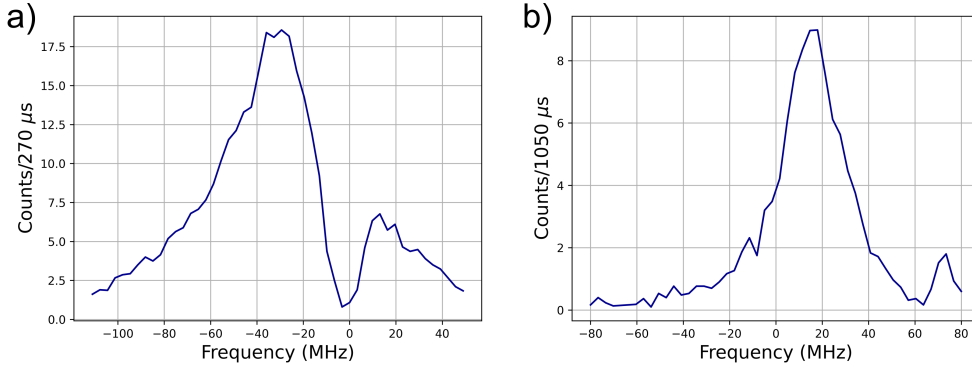


Figure 2.6: Experimentally optimized detection (a) and Doppler cooling (b) lineshapes using the $|4^2S_{1/2}\rangle \leftrightarrow |4^2P_{1/2}\rangle$ transition. The trace shows the background subtracted counts for the scan. The peak to the right of the scans is a result of the $|3^2D_{3/2}\rangle \leftrightarrow |4^2P_{1/2}\rangle$ dark resonance impacting the scattering rate. There is an offset in the center of the two peaks because of stark shifts from the high intensity used for detection.

For qubit operations, characterization of systematic shifts, and sideband cooling we use the $^{40}\text{Ca}^+ |4^2S_{1/2}\rangle \leftrightarrow |3^2D_{5/2}\rangle$ qubit transition. The qubit operations are used for quantum logic spectroscopy, magnetic field measurements, micromotion measurements, cooling characterization, and heating rate measurements. To separate the Zeeman manifold and define quantization axis we apply a magnetic field 1.7 G along the viewports of the vacuum chamber with a pair of Helmholtz coils. In later experiments we reduced this quantization field to 1 G to reduce the second-order Zeeman shift. When sideband cooling, the excited metastable state must be quenched in order to perform sideband cooling due to the metastable state lifetime of 1 s. The metastable $|3^2D_{5/2}\rangle$ state is repumped via the $|3^2D_{5/2}\rangle \leftrightarrow |4^2P_{3/2}\rangle$ 854 nm transition where the population is driven to the $|4^2P_{1/2}\rangle$ excited state which will decay quickly to the $|4^2S_{1/2}\rangle$ ground-state. The $|3^2D_{3/2}\rangle \leftrightarrow |4^2P_{3/2}\rangle$ laser is also applied in case any population decays into the $D_{3/2}$ state. The polarization of both of the lasers is again set to be $\pm\sigma$ polarized to address all of the metastable states since the Zeeman states are not frequency resolved due to the transitions broad linewidth. To perform sideband cooling, a sequence of motion subtracting $|4^2S_{1/2}\rangle \leftrightarrow |3^2D_{5/2}\rangle$ sideband transitions followed by a repumping pulse are driven multiple times to sequentially remove quanta of motion from a chosen secular mode. This

sequence is repeated for all of the secular frequencies for the ultimate goal of cooling the two ion crystal to the motional ground-state. For determination of the temperature of the ion following Doppler cooling we can apply independent sequences where following the cooling we apply a red or blue sideband pulse for a select motional frequency and use the probability of being in $|3^2D_{5/2}\rangle$ following these two transitions to measure the average motional mode occupation. Example pulse sequences for sideband cooling and sideband thermometry are shown in Fig. 2.7. The probability of being in the excited state following a red or blue sideband pulse of duration t are written as $P_{\uparrow}^{\text{RSB}}(t)$ and $P_{\uparrow}^{\text{BSB}}(t)$ and the average mode occupation \bar{n} is determined using [66]

$$\bar{n} = \frac{1}{P_{\uparrow}^{\text{BSB}}(t)/P_{\uparrow}^{\text{RSB}}(t) - 1}. \quad (2.36)$$

This method of thermometry works when evaluating the ion temperature following Doppler cooling but is not sufficiently accurate after sideband cooling because the Fock state distribution is no longer thermal. This procedure relies on the motional state distribution of the mode being thermal following cooling. This assumption is not necessarily the case after many sideband cooling pulses are applied where now the motional state distribution is a combination of a thermal and a non-thermal distribution. This limit in characterizing the ion temperature is avoided by instead fitting a Rabi time scan of the red and blue motional sidebands as described in Refs. [54, 66]. Fits to the Rabi lineshape when driving a Δn motional sideband pulse are performed using

$$P_{\uparrow}^{(\Delta n)}(t) = \sum_n \frac{1}{2} (1 - e^{-\gamma t} \cos(2\Omega_{n,n+\Delta n} t)) P_{th}(n) \quad (2.37)$$

where $P_{th}(n)$ describes the population in a Fock state $|n\rangle$ in thermal equilibrium, γ is a factor accounting for decoherence in the measurement, and $\Omega_{n,n+\Delta n}$ is the Rabi rate between two Fock states n and $n + \Delta n$ for a specific secular mode. The Rabi rate $\Omega_{n,n'}$ from n to n' is

$$\Omega_{n,n'} = \Omega e^{-\frac{\eta^2}{2}} \sqrt{\frac{n_{<}}{n_{>}}} \eta^{|n-n'|} L_{n_{<}}^{|n-n'|}(\eta^2) \quad (2.38)$$

where Ω is the Rabi rate of the carrier transition used and $\eta \equiv kz_0$ is the Lamb-Dicke parameter which quantifies the coupling between the motional states and the internal states of the ion where

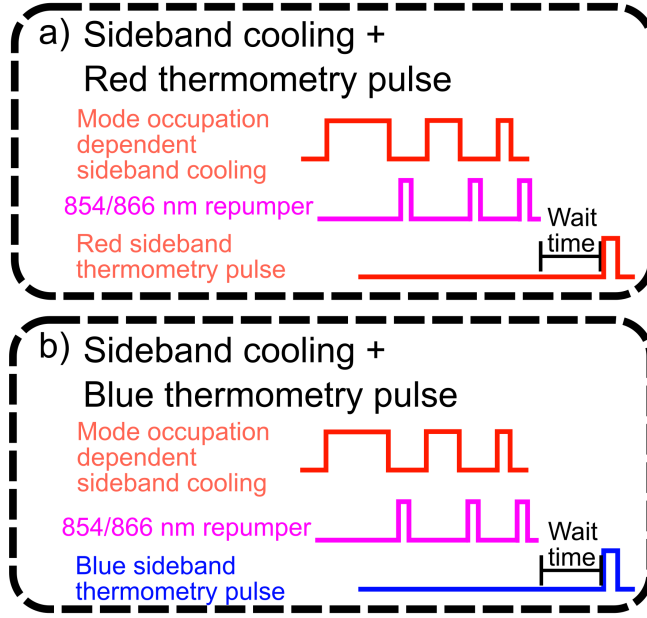


Figure 2.7: Example pulse sequences to clarify the sideband cooling pulses and the sideband thermometry pulses applied. In both (a) and (b) the mode occupation dependent sideband cooling pulses are described to show the changing Rabi rate of the sideband pulse as \bar{n} decreases throughout cooling. Additionally, the repumper pulses applied after each cooling pulse are shown. In (a) sideband cooling followed by red sideband thermometry pulse is shown and in (b) the same sideband cooling is applied but instead a blue sideband thermometry pulse is applied. The measurements from these two pulse sequences can be used to determine the ion mode occupation and by introducing a wait time the heating rates can be determined.

z_0 is the size of the $n = 0$ wavefunction and k is the wavenumber of the transition. The lesser and greater Fock states, $n_<$ and $n_>$ are replaced by n or n' depending on which of these are larger.

$L_n^\alpha(x)$ in this equation is the generalized Laguerre polynomial and is given by the equation

$$L_n^\alpha(x) = \sum_{m=0}^n (-1)^m \binom{n+\alpha}{n-m} \frac{x^m}{m!}. \quad (2.39)$$

By fitting to these time scans the motional distribution of the ions following sideband cooling can be better determined [24]. This will be used in later sections to quantify the results of sideband cooling in our system. These sideband thermometry methods assuming a thermal distribution are also used to characterize the heating rates of the motional modes in our system. By implementing a wait time between the thermometry and the cooling pulses we can measure the increase in motional occupation as a function of the wait period for each motional mode.

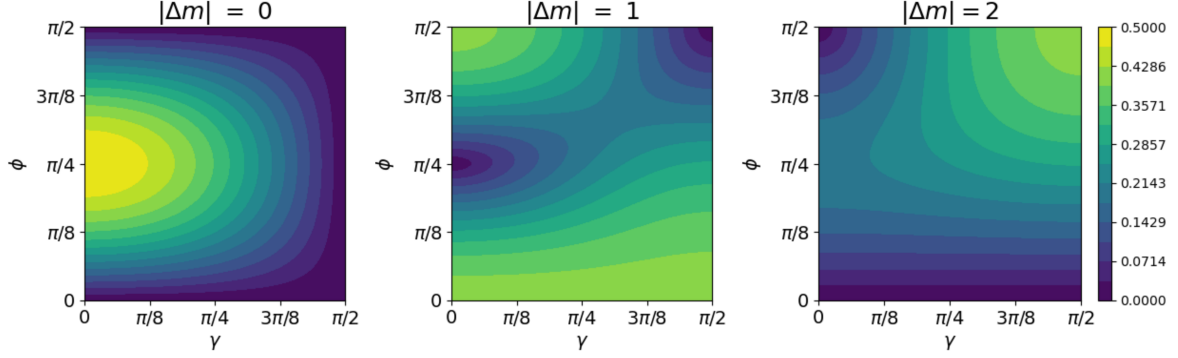


Figure 2.8: This figure displays the relative coupling strength for $|4^2S_{1/2}\rangle \leftrightarrow |3^2D_{5/2}\rangle$ transitions when $|\Delta m| = 0, 1,$ and 2 transition is applied. The coupling strength depends on γ the angle between the laser polarization and the quantization projected on the plane of incidence and also depends on ϕ the angle between the laser beam propagation direction and the quantization axis. Yellow shading indicated high coupling strength and blue shading indicates low coupling strength.

To characterize the micromotion in all three directions the micromotion sidebands of $|S_{1/2}\rangle \leftrightarrow |D_{5/2}\rangle$ transitions are probed along three directions with projections along the orthogonal axes. From Ref. [63] the carrier Rabi rate for a quadrupole transition is given by

$$\Omega_0 = \left| \frac{eE_0}{2\hbar} \langle S_{1/2}, m | (\vec{\epsilon} \cdot \vec{r}) (\vec{k} \vec{r}) | D_{5/2}, m' \rangle \right| \quad (2.40)$$

where e is the charge of the electron, E_0 is the laser electric field strength of the laser, $\vec{\epsilon}$ is the laser polarization vector, \vec{k} is the laser wave vector, \vec{r} is the operator describing the position operator of the valence electron with respect to the atomic center of mass, m is the ground-state magnetic quantum number, and m' is the excited state magnetic quantum number. In Ref. [63] they solve this equation to determine the relative coupling strength for different Δm transitions dependent on the angle of the laser polarization $\vec{\epsilon}$ with respect to the quantization axis labeled γ and the angle between the laser wave vector \vec{k} and the quantization axis labeled ϕ . The relative coupling strengths for a $|\Delta m|$ transition is given by $g^{|\Delta m|}$ which for the three $|\Delta m|$ values is given by the

equations

$$g^0 = \frac{1}{2} |\cos(\gamma) \sin(2\phi)| \quad (2.41)$$

$$g^1 = \frac{1}{\sqrt{6}} |\cos(\gamma) \cos(2\phi) + i \sin(\gamma) \cos(\phi)| \quad (2.42)$$

$$g^1 = \frac{1}{\sqrt{6}} \left| \frac{1}{2} \cos(\gamma) + \sin(2\phi) i \sin(\gamma) \sin(\phi) \right|. \quad (2.43)$$

The coupling strength for each of these terms as a function of ϕ and γ is plotted in Fig. 2.8. From time scans of the micromotion sidebands a Rabi rate of the micromotion transition can be determined which is used to measure the second order Doppler-shift of the $^{27}\text{Al}^+$ clock transition and associated uncertainty. Because the carrier Rabi rate is different for each of these beam directions it is optimal to use $\Delta m = 2$ transitions for measurements perpendicular to the quantization axis, $\Delta m = 1$ transitions for measurements along the vertical direction, and $\Delta m = 0$ transitions for measurements along the axial direction. The polarizations displayed in Fig. 2.12 for each of the 729 nm beam directions optimize the coupling rate for a given γ for each of the probe directions where we use Fig 2.8 to determine the optimum parameters. We also display the inverse of the decay rate given by $1/A_{i,j}$ where $A_{i,j}$ is the Einstein coefficient for states i and j and Lande g -factors for $^{40}\text{Ca}^+$ transitions. These are listed in Tables 2.3 and 2.3.

Lande g -factors for relevant energy levels [67]					
	$S_{1/2}$	$P_{1/2}$	$P_{3/2}$	$D_{3/2}$	$D_{5/2}$
g_J	2	2/3	4/3	4/5	6/5

$1/A_{i,j}$ for relevant states of $^{40}\text{Ca}^+$ [68]						
	$P_{1/2} \rightarrow S_{1/2}$	$P_{3/2} \rightarrow S_{1/2}$	$P_{3/2} \rightarrow D_{3/2}$	$P_{3/2} \rightarrow D_{5/2}$	$P_{1/2} \rightarrow D_{3/2}$	$D_{5/2} \rightarrow S_{1/2}$
$\tau(\text{ns})$	7.7(2)	7.4(3)	901	101	94.3	1.045×10^9

Experimental measurements of the g -factors for $|4^2S_{1/2}\rangle$ and $|3^2D_{5/2}\rangle$ are published in Refs. [69,

70]. For in-situ magnetic field measurements, different Zeeman states of the $|3^2D_{5/2}\rangle$ manifold are used. A pair of transitions are used to prevent errors in the measured magnetic field which can arise from frequency drifts of the laser. In practice any combination of Zeeman transitions can be used but typically the $\Delta m = 2$ transitions from the $|4^2S_{1/2}, m = -1/2\rangle$ ground-state are used because this maximizes the sensitivity of the magnetic field measurements.

2.3.1 $^{40}\text{Ca}^+$ Laser systems

In our experiments we use many diode based lasers for $^{40}\text{Ca}^+$. Fig. 2.9 shows a diagram of the lasers used in our experiments. For the 397, 866, and 422 nm lasers we use Toptica ECDL lasers, for 729 nm we use a combination ECDL/TA PRO laser from Toptica, for 854nm we use a distributed feedback (DFB) laser from Photodigm, and for 375nm we use an unstabilized diode laser from Toptica. These lasers are shared between the $^{40}\text{Ca}^+ / ^{27}\text{Al}^+$ experiment and a molecular ion experiment [71] and the 397, 729, 866, and 854 nm lasers are stabilized to an optical spherical cavity [21]. The spherical cavities were initially designed to be mobile reference cavities that are insensitive to accelerations and mounting orientation. In addition, to the low sensitivity cavity axis there is an additional cavity bore perpendicular to the main bore which is used for laser locks at different frequencies. Both of these bores have a length of 48 mm. Cavity mirrors are optically contacted and from cavity ring down measurements we observe a decay time of $\tau = 16.1 \mu\text{s}$. From $F = (\pi\tau c)/L$ we measure a cavity finesse of 3.16×10^5 . Fig. 2.10 displays a diagram of the sphere cavity table where the 397,866, and 854 nm lasers are locked to the lower finesse cavity direction and the 729 nm laser is locked to the higher finesse cavity direction. The 397 and 866 nm lasers use offset Pound-Drever-Hall (PDH) locks to lock the lasers to the cavity and the 854 and 729 nm laser are locked to the cavity using a PDH lock. The offset locks are required to offset the laser frequency to reach a cavity resonance and in the experiment we offset the frequencies using EOMs at 9.7 GHz and 1.3 GHz for the 866 and 397 nm lasers respectively [72]. The sidebands for the PDH locks are generated using EOMs and range from 13-30 MHz and are labeled in Fig. 2.10. Since the linewidths of the 397,866, and 854 nm transitions are on the order of 10s of MHz these lasers

Laser Dist. Table

422 nm	
375 nm	
397 nm	
729 nm	
854 nm	
866 nm	
PBS	
Mirror	
Dichroic	
Lens	
Grating	
AOM	

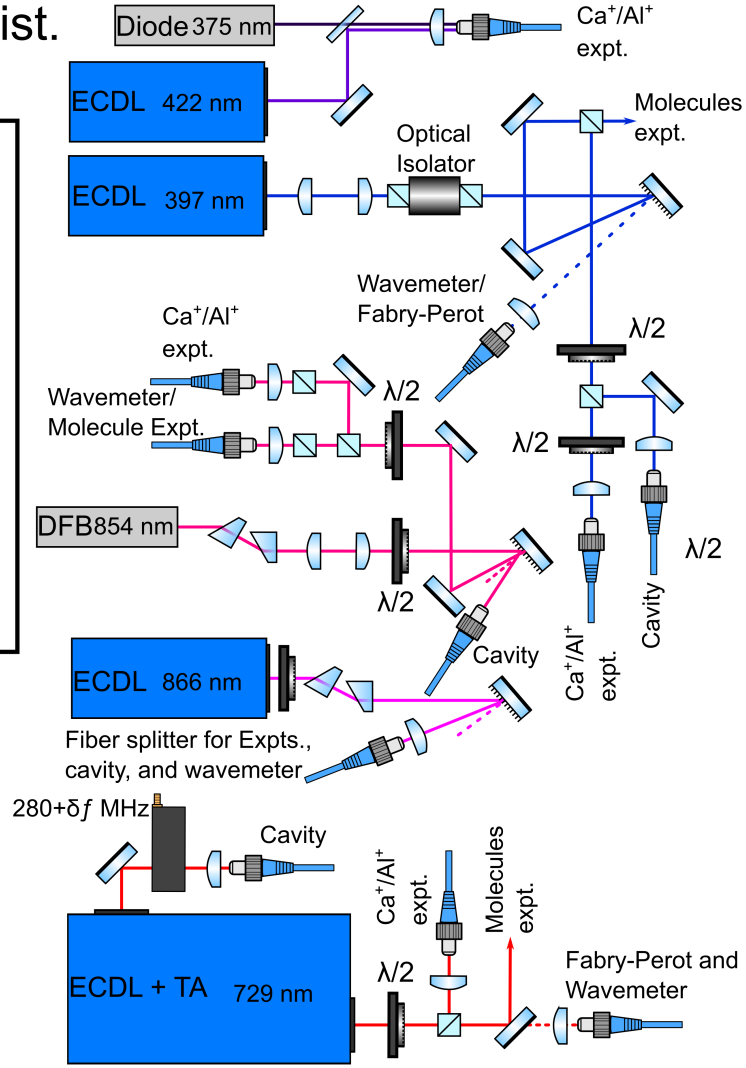


Figure 2.9: Overview of the laser distribution table which distributes the $^{40}\text{Ca}^+$ lasers to the $^{40}\text{Ca}^+ / ^{27}\text{Al}^+$ and molecule experiments. Light from this table is also sent to an optical sphere cavity to stabilize the laser light.

do not require a very narrow linewidth. However, the 729 nm transition has a natural linewidth of ≈ 1 Hz so having a narrow linewidth laser for driving the $|4^2S_{1/2}\rangle \leftrightarrow |3^2D_{5/2}\rangle$ transitions would allow higher precision measurements with $^{40}\text{Ca}^+$ in cases where we are limited by laser coherence times. A laser with linewidth approaching the natural linewidth of the laser would also allow for higher fidelity qubit operations in cases where operations are performed on motional sidebands with low Rabi frequencies. We achieve coherence times approaching 3 ms when Ramsey interrogations

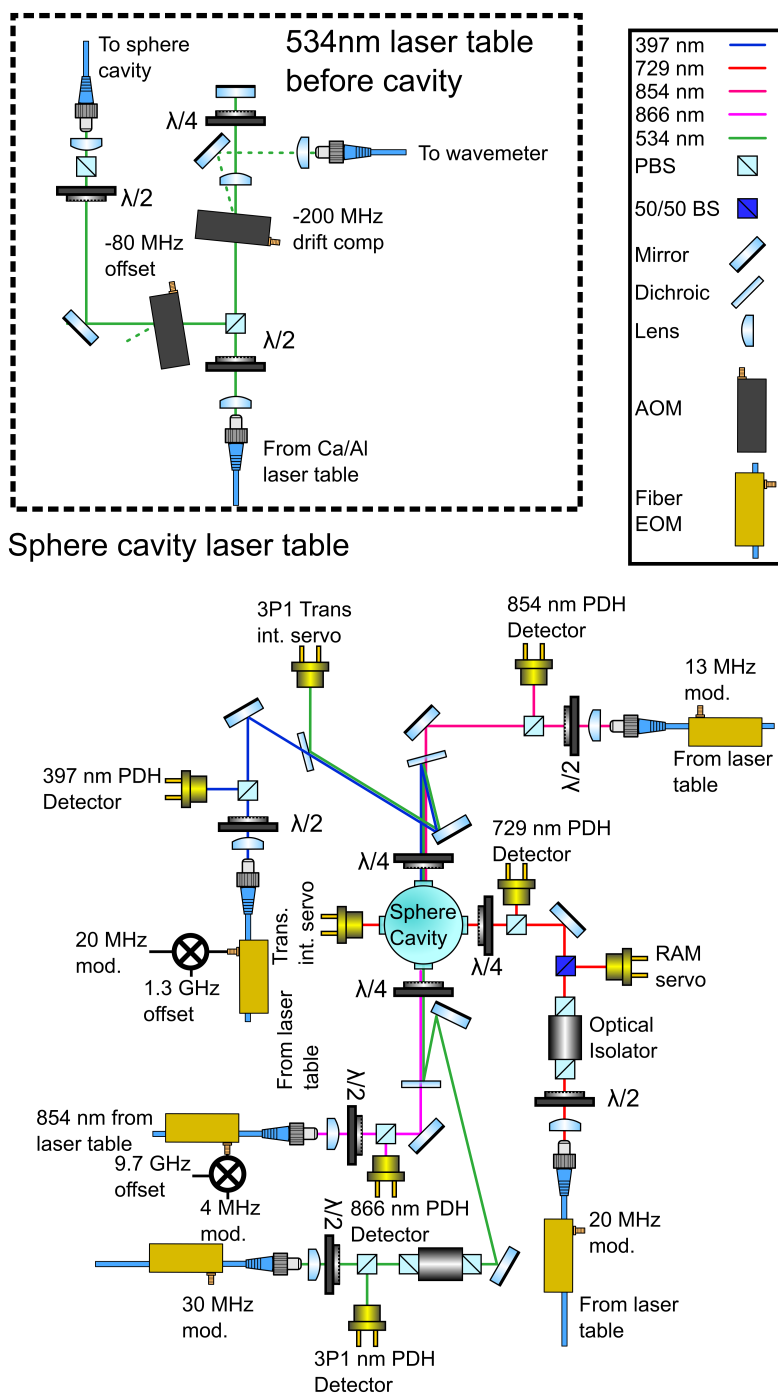


Figure 2.10: Diagram describing how light of various lasers are sent to the optical sphere cavity for stabilization. All of the lasers shown are locked to the cavity with PDH locks and for the 866 and 397 nm lasers a frequency offset is applied with a fiber EOM. Additionally we stabilize the cavity transmission of the 3P1 and 729 lasers to prevent laser instability from intensity fluctuations. A RAM servo is also used to minimize the residual amplitude modulation (RAM) from the 729 nm fiber EOM.

Ca lasers doublepass towers

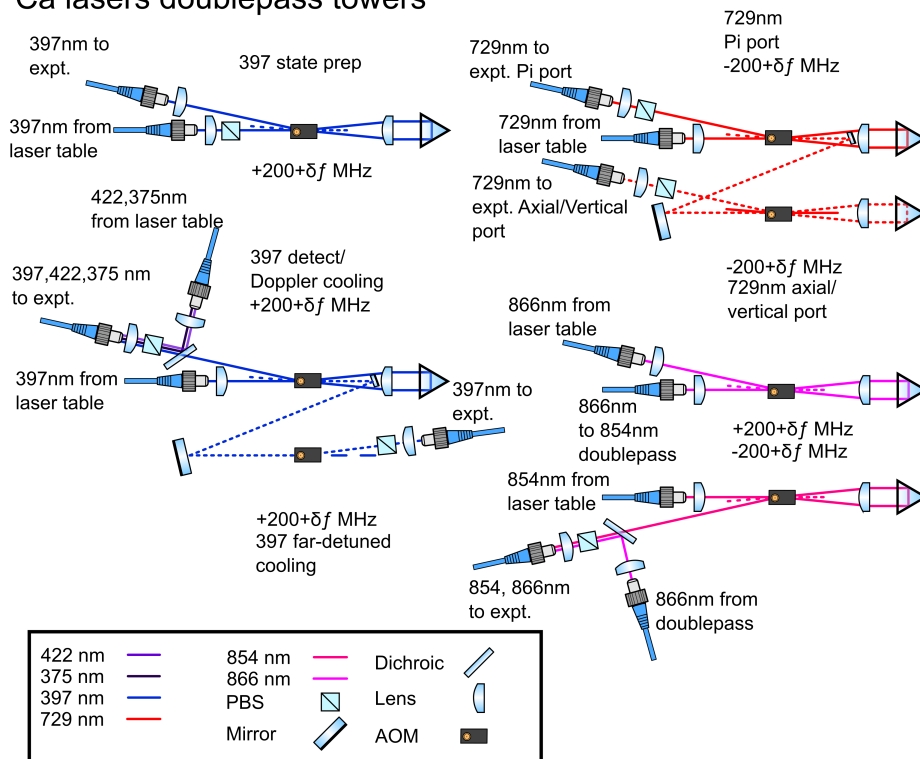


Figure 2.11: Diagram of the double-pass tower used for the $^{40}\text{Ca}^+$ lasers in our experiment and a signal pass tower used for the far-detuned cooling laser. All of the towers use AOMs centered at 200 MHz.

are performed with the 729 laser. It is likely at this time scale the coherence is limited equally by magnetic field noise modulating the $^{40}\text{Ca}^+$ energy levels and decoherence of the 729 nm laser. For the 729 nm laser we use a Toptica FALC to control the diode current for high bandwidth stabilization and a slow integrator controls the ECDL piezo to keep the laser centered in the mode hop free range. This slow integrator is implemented using a digital servo box [73] and these same digital servos are also used to lock the other lasers to the optical spherical cavity.

Light from the laser table is sent to vertically-oriented double-pass AOM towers which vary the frequency, phase, and amplitude of the lasers linearly before they are sent to the ions [74]. These double-pass towers are oriented vertically to reduced the footprint on our optical table. All of the double-pass towers use AOMs with a center frequency of 200 MHz and provide a scan range of ± 40 MHz with minimal intensity variation. Diagrams of these towers are seen in Fig 2.11 where

we also include a single pass setup used for our far-detuned 397 nm laser. After the double-pass towers, laser light is sent to the trapped ions. Fig 2.12 displays which vacuum ports the light is sent through to interact with the ion where we have three ports which we call the π -port, σ -port, and the vertical-port. The 397 state preparation and far detuned cooling are sent through opposite ports along the quantization axis. We also refer to these ports as the σ direction. The 729 nm π beam, 866 nm, 854 nm, and the 397 nm detection and cooling beam are sent into what we refer to as the π -port. A UV to NIR corrected triplet lens is used to focus light onto the ions on this port. This lens has minimal chromatic shift over a wavelength range of 193-1000nm. This triplet is necessary for this port because light in the range of 266-866 nm is used. The 266 nm light entering this port will be discussed in the next section. On the opposite side from these launchers the light is split with a dichroic and sent to through two detectors which are used to intensity servo the pulses. Along the axial direction which is perpendicular to the entry port for the RF resonator, we send the 729 nm axial beam which is used to measure the micromotion along the axial direction. A vertical beam is sent down through the imager and exits the chamber by reflecting off of a titanium vertical pick-off mirror with an angle of 17° between the normal vector of the mirror and the axial direction, seen in Fig. 2.12 (b). This probe is used to measure the micromotion along the vertical direction. The 729 nm π beam is used to measure the remaining micromotion direction since it has a vector component perpendicular to vertical and axial directions. This beam also has both $\lambda/2$ and $\lambda/4$ waveplates to have full control over the laser polarization.

2.4 $^{27}\text{Al}^+$ clock ion operations

In this apparatus, two optical transitions are used to manipulate the $^{27}\text{Al}^+$ ion. The $|^1S_0\rangle \leftrightarrow |^3P_1\rangle$ transition is used to prepare the internal state of the $^{27}\text{Al}^+$ ion and to drive motional sideband pulses for quantum logic spectroscopy. The $|^1S_0\rangle \leftrightarrow |^3P_0\rangle$ transition is the clock transition with a transition frequency of $\approx 1.121\text{PHz}$. The $|^1S_0\rangle \leftrightarrow |^3P_1\rangle$ transition has a resonant frequency of 266.92 nm and has a natural linewidth of 520 Hz [75]. This transition can also be used to measure the magnitude of micromotion directly on $^{27}\text{Al}^+$ [28, 54]. The clock transition is a $J =$

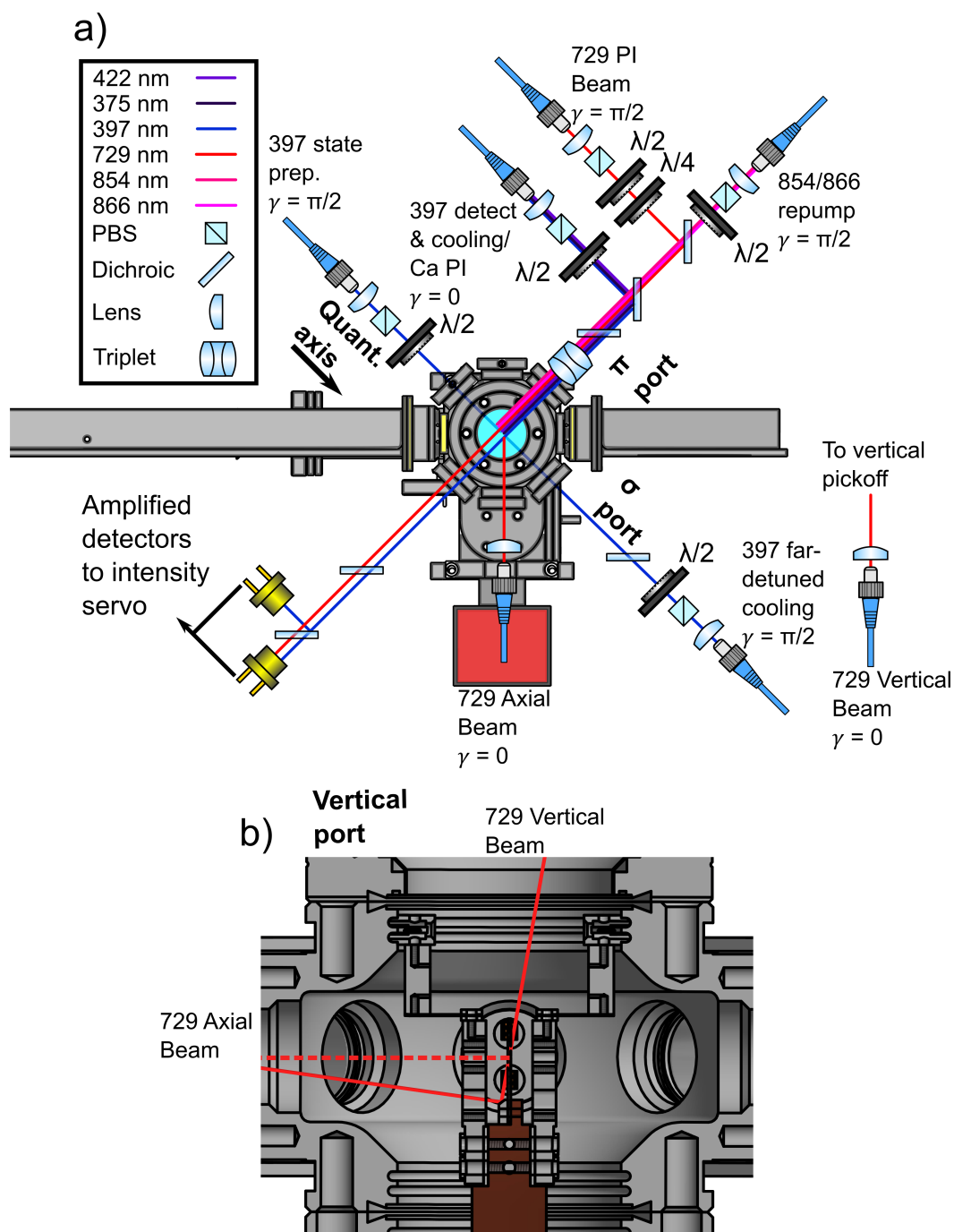


Figure 2.12: Diagram of the beam paths which are sent into the vacuum system and are incident on the trapped ions. a) This image displays the table layout from an overhead view. b) This figure displays how the 729 nm light enters and exits along the vertical and axial directions. This picture is a slice along the axial direction through the middle of the system.

$0 \leftrightarrow J' = 0$ transition which is strictly forbidden [76] but is allowed by hyperfine mixing with the $|^3P_1\rangle$ excited state [76]. This transition has many nice characteristics such as the high transition frequency of 1.121 PHz, a relatively narrow natural linewidth of ≈ 6 mHz which results in an excited state lifetime of 20.6 s, and very low sensitivity to electromagnetic fields which corresponds to the transition being highly insensitive to the black body radiation (BBR) shift and having a negligible electric quadrupole shift. In $^{27}\text{Al}^+$ laser pulse sequences discussed in this thesis two pairs of transitions are utilized. The first pair are the $|^1S_0, m_f = \pm 5/2\rangle \leftrightarrow |^3P_0, m_f = \pm 5/2\rangle$ transitions which have been used in previous implementations of the $^{27}\text{Al}^+$ -ion clock, and the other pair are the $|^1S_0, m_f = \pm 3/2\rangle \leftrightarrow |^3P_0, m_f = \pm 1/2\rangle$ transitions which have a smaller magnetic field sensitivity but require a different state preparation sequence than what was previously used.

2.4.1 $^{27}\text{Al}^+$ state preparation

Preparation of the $^{27}\text{Al}^+$ ground-state for the two versions of clock operation utilize two different pumping sequences. For the case where the clock transition is driven between $|^1S_0, m_f = \pm 5/2\rangle$ and $|^3P_0, m_f = \pm 5/2\rangle$ we use σ polarized light to pump the population to either side of the manifold. When driving to the $m_f = -5/2$ ground-state σ^- polarized laser light is used and when driving the $m_f = 5/2$ ground-state σ^+ polarized laser light is used. A pumping sequence where $m_f \rightarrow m'_f = m_f \pm 1$ transitions are driven is used where m_f and m'_f denote the initial and final magnetic sublevels. In each iteration of this preparation sequence all of the $|\Delta m| = 1$ pumping pulses are applied iteratively and a wait period of 600 μs is used after the pulses to allow for the population to decay from the 3P_1 excited state. This series of pulses is repeated multiple times to ensure a high probability of the ion being in the $|^1S_0, m_f = \pm 5/2\rangle$ ground-state. Transitions used for this state preparation sequence are shown in Fig 2.13 (b). This sequence will not move the population to the correct ground-state in a single iteration since it only has a small probability of decay and re-excitation in one iteration. Therefore, to have high state preparation fidelity the pulse sequence needs to be repeated multiple times, in our experiments we typically use ≈ 7 cycles of this preparation.

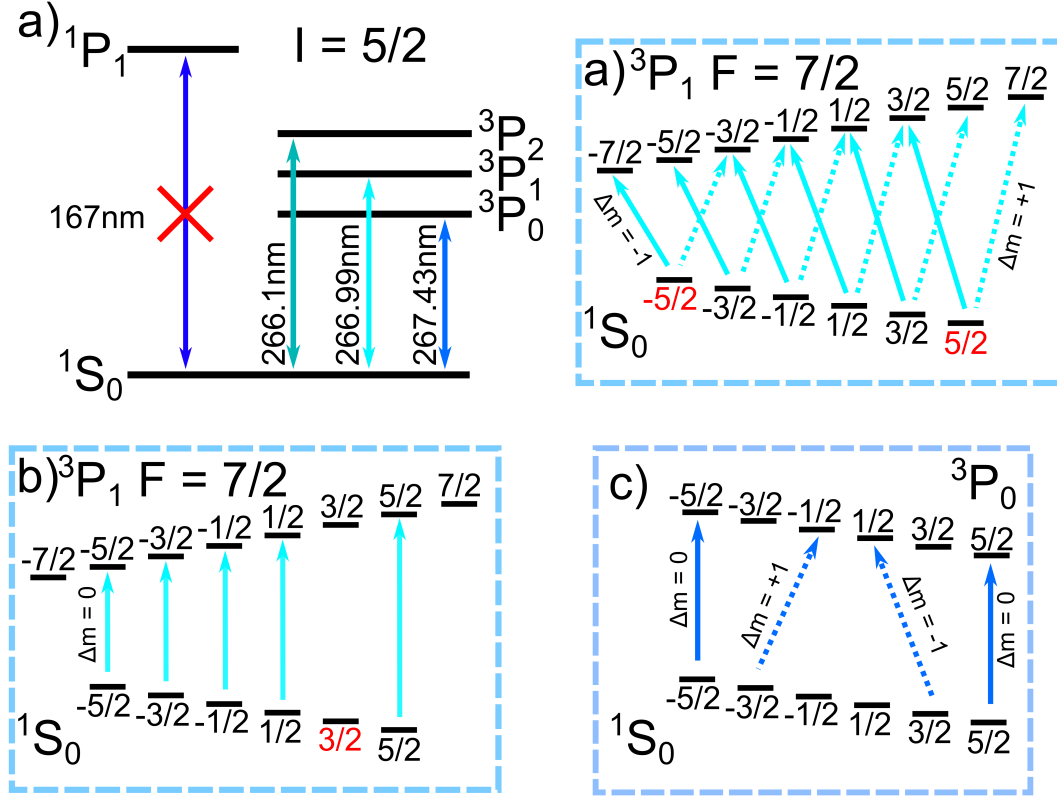


Figure 2.13: a) Level diagram of relevant states of $^{27}\text{Al}^+$. A red x is used to display the inaccessibility of the $|^1S_0\rangle \leftrightarrow |^1P_1\rangle$ transitions and the nuclear spin $I = 5/2$ shown. This inaccessibility is due to the deep UV wavelength needed to drive the transition. This inability to use this transition for cooling and state detection is the reason why QLS is used. b) The $|\Delta m| = 1$ transitions used for the preparing $^{27}\text{Al}^+$ in $|^1S_0, m_f = -5/2\rangle$ or $|^1S_0, m_f = 5/2\rangle$. c) The $|\Delta m| = 0$ transitions used for preparing $^{27}\text{Al}^+$ in $|^1S_0, m_f = 3/2\rangle$. This same sequence can be used to prepare the ion in $|^1S_0, m_f = -3/2\rangle$ but instead no pulse would be applied to on the $|^1S_0, m_f = -3/2\rangle \rightarrow |^3P_1, m_f = -3/2\rangle$ transition and a pulse would be applied on the $|^1S_0, m_f = 3/2\rangle \rightarrow |^3P_1, m_f = 3/2\rangle$ transition. For both (b) and (c) the red states are the target preparation state. d) Clock transitions used in experiments discussed in this thesis. It was found that magnetic field noise was limiting measurements that used the $|^1S_0, m_f = \pm 5/2\rangle \leftrightarrow |^3P_0, m_f = \pm 5/2\rangle$ transitions so we switched to the $|^1S_0, m_f = \pm 3/2\rangle \leftrightarrow |^3P_0, m_f = \pm 1/2\rangle$ transitions which have smaller sensitivity to magnetic fields.

The alternative pumping procedure to prepare the $^{27}\text{Al}^+$ ion in the $|^1S_0, m_f = \pm 3/2\rangle$ ground-state works by making the target states dark states in the pumping procedure where the population will collect. The $|^1S_0, m_f = 3/2\rangle$ initial state is prepared by applying a series of π -polarized laser pulses on the $|^1S_0, m_f = m\rangle \rightarrow |^3P_1, F = 7/2, m_f = m\rangle$ transitions, for

$m \in \{-5/2, -3/2, -1/2, 1/2, 5/2\}$ followed by a wait period of 300 μs . The transitions used for this procedure can be seen in Fig. 2.13 (c). Because the final decay channel of this sequence does not only link to the desired state like the previous preparation version more iterations are required to have a high probability of being in the $|^1S_0, m_f = \pm 3/2\rangle$ ground-state. This preparation process was modeled using a Monte-Carlo simulation to estimate the number of pumping iterations that are needed to reliably prepare the ion in the desired state. For this simulation we begin in an initial outer state ($|^3P_1, \pm 5/2\rangle$) and simulate the pulses by moving the ion to the corresponding $|^3P_1, m_f\rangle$ excited state. We use the branching ratios of the $|^3P_1, m_f\rangle$ Zeeman states to set the decay probability for the state then repeat this sequence until we arrive in our target state. Results from this simulation can be seen in Fig. 2.14 where we model the the number of pulses needed to move from $|^1S_0, m_f = -5/2\rangle$ to $|^1S_0, m_f = -3/2\rangle$ and $|^1S_0, m_f = 5/2\rangle$ to $|^1S_0, m_f = -3/2\rangle$. This simulation suggests that a combination of the two preparation methods is optimal, where we use σ polarized light to prepare in $|^1S_0, m_f = \pm 5/2\rangle$ and then follow this with π polarized light to prepare in the inner manifold target state. In the experiment we have low probability of driving off-resonant transitions because the $|^3P_1, F = 7/2\rangle$ manifold has $g_F \approx 3/7$ [77, 76], the splitting of the transition frequencies for adjacent Zeeman levels is near 1 MHz at typical operating magnetic fields of 1.0 to 1.7 G, and these optical pumping transitions (pulse durations $t_\pi > 50 \mu\text{s}$) are frequency-resolved. Because of this we did not include the possibility of off-resonant excitation into the simulation. When running the experiment, after the σ polarized pumping pulses are applied, the π -polarized laser pulses sequence is repeated twelve times to ensure a high fidelity of being in the target state. Once $|^1S_0, m_F = 3/2\rangle$ is prepared, we drive the $|^1S_0, m_F = 3/2\rangle \leftrightarrow |^3P_0, m_F = 1/2\rangle$ transition with a σ^+/σ^- -polarized laser beam for clock operation.

2.4.2 $^{27}\text{Al}^+$ laser systems

For both of the $^{27}\text{Al}^+$ laser systems “The Rock” fiber laser at $\approx 1068 \text{ nm}$ from NP photonics is used. These fiber lasers have a baseline linewidth of $> 5 \text{ kHz}$ and output power of $\approx 60 \text{ mW}$. For both laser systems the lasers are amplified with fiber amplifiers which can reach powers of $\approx 3 \text{ W}$

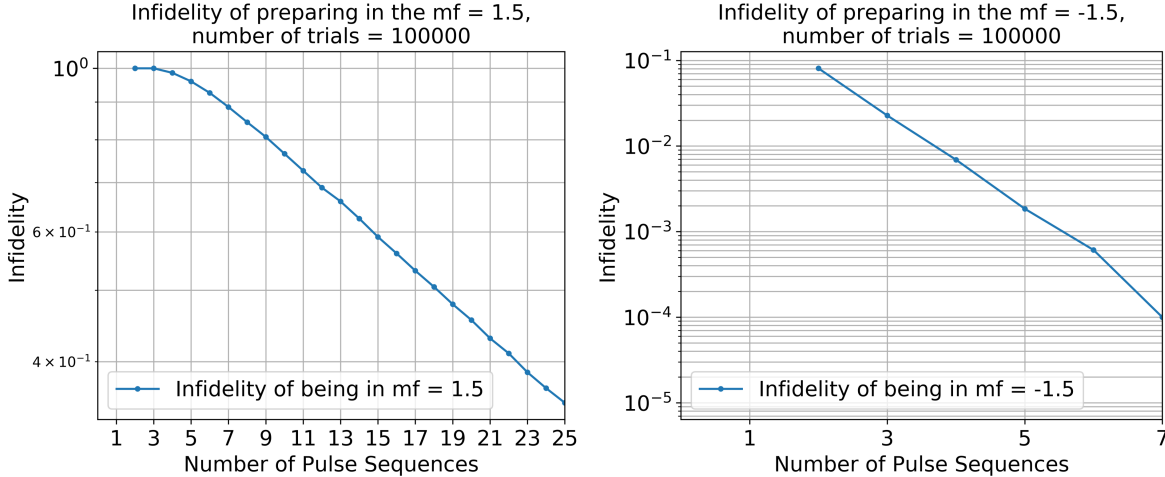


Figure 2.14: Results from a Monte-Carlo simulation used to determine the number of pulses needed to reliably prepare the ion state using the Π polarized pumping procedure. From these simulations we determine that a combination of σ polarized pumping and π polarized pumping is most efficient to move the $^{27}\text{Al}^+$ across manifold. More π polarized pulses are needed when driving the population across the manifold where here we assume the same starting state of $m_f = -5/2$.

but are operated with output powers of ≈ 1 W. The ≈ 1068 nm light is then fiber coupled into a periodically poled lithium niobate (PPLN) waveguide doubling module which converts this light to 534 nm with ≈ 300 mW of power. A small percentage of this light is then picked off in each of these laser lines and sent to their corresponding optical cavities. For the 3P_1 laser system, we generate the light on the $^{40}\text{Ca}^+ / ^{27}\text{Al}^+$ optical table, shown in Fig. 2.15 and send the light to the sphere cavity. The laser is stabilized to the same axis of the spherical cavity as the 397, 866, and 854 nm lasers using a PDH laser lock, seen in Fig. 2.10. The stabilized 534 nm 3P_1 laser light is sent to an M-squared doubling cavity based on a BBO doubling crystal to generate light at 266 nm. The UV light is then sent through a doublepass tower to control the frequency, amplitude, and phase of the laser and is directed to the different experimental ports using switch AOMs. The 3P_1 laser is then sent to the ion through either the σ -port which is where the σ polarized state preparation is applied or the π -port which is where the π polarized state preparation is applied. Before the σ -port we have a free space EOM which is used to switch the polarization between σ^+ and σ^- depending on which side of the manifold the ion state is prepared in. The 3P_0 laser light is generated on a

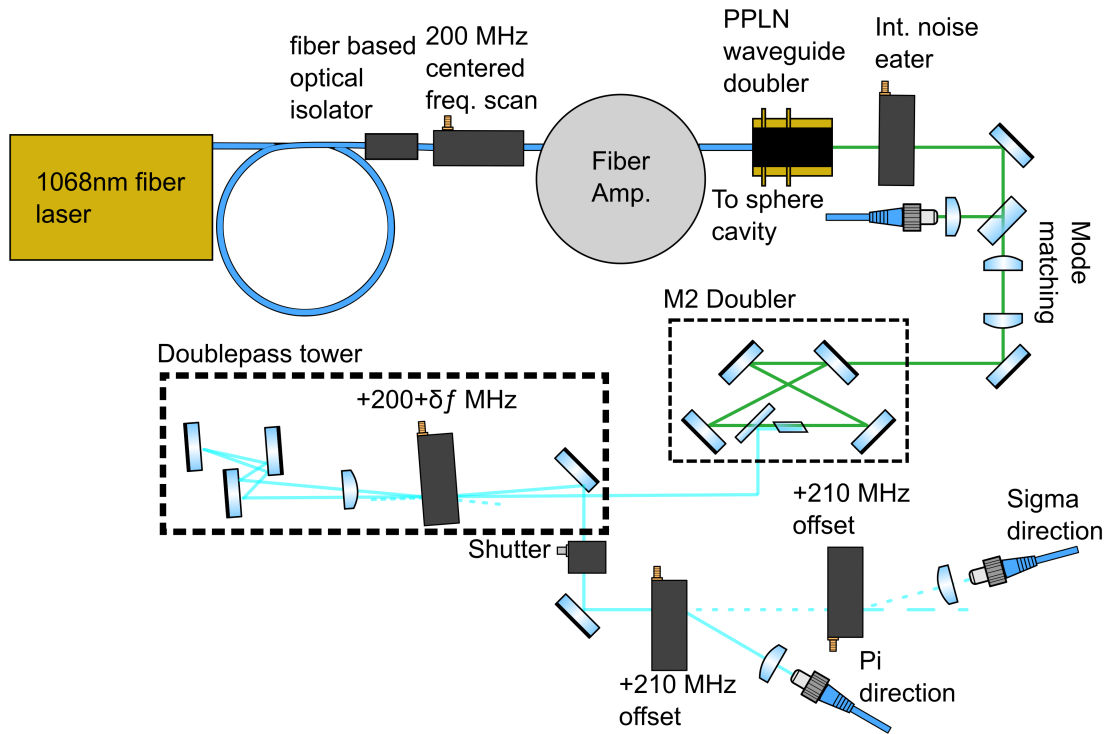


Figure 2.15: Simplified diagram of the 3P_1 beamline is displayed where we include the doubling stages and the doublepass tower used for laser control

separate laser table where the beam path is seen in Fig. 2.16. This table is used to distribute light to various experiments and is where the optical link to the comb lab is located. Light is sent to both the $^{40}\text{Ca}^+ / ^{27}\text{Al}^+$ table and to the optical cavity which we call “Medusa” [78]. The 3P_0 laser is stabilized to Medusa with a PDH (Pound-Drever-Hall) lock. Medusa is comprised of a 24 cm long ULE spacer and fused silica mirror substrates with dielectric coatings. The finesse of this optical cavity is 300,000 and stabilizing the laser to this optical cavity allows for a clock interrogation time of 150 ms. Phase noise compensation links are used to stabilize phase noise in the optical path length from just before Medusa all the way up to the $^{40}\text{Ca}^+ / ^{27}\text{Al}^+$ vacuum system. Phase stabilization of the lasers will be further discussed in Section 2.6.2 and the path length stabilization setups can be seen in Figs 2.16 and 2.17. The light sent to the $^{40}\text{Ca}^+ / ^{27}\text{Al}^+$ table is doubled to 267 nm using a M-squared bow-tie cavity based on a BBO doubling crystal and distributed to two counter propagating ports of the vacuum chamber to drive the clock transition of the $^{27}\text{Al}^+$

ion. The frequency is varied using the AOMs just before the vacuum system in Fig 2.17 and the zero order of this AOM is retro-reflected to generate the beatnote for the PNC. The waveplates just before the chamber in these two paths are used to switch between the polarizations needed to interrogate the two magnetic field sensitivity clock transitions used throughout experiments. The 3P_0 laser on the ablation side of the vacuum system is combined with the $^{40}\text{Ca}^+$ -lasers on this port using a dichroic.

2.5 Ablation Loading

We use laser ablation to load both $^{40}\text{Ca}^+$ and $^{27}\text{Al}^+$ by applying a high intensity laser pulse on a target made of a Ca-Al alloy. The ablation laser is a Cryatalaser Q-switched pulsed laser at 534 nm and has a pulse energy of ≈ 0.3 mJ with a 1 kHz repetition rate. The ablation laser is aligned to the axial direction of the trap and single pulses are applied followed by a wait period to see if an ion is loaded. We have found that just using the ablation laser to load $^{40}\text{Ca}^+$ is enough but we also have used 375 and 422 nm light aligned to the π -port to increase our $^{40}\text{Ca}^+$ loading efficiency. We have roughly 20 mW of 375 nm light and 5 mW of 422 nm light going into our vacuum system for photoionization. To determine if $^{40}\text{Ca}^+$ is loaded the detection sequence is run and photons are scattered by the ion once the ion crystallizes in the trap. The ablation laser is aligned to the target by first attenuating the laser and then measuring the light transmitted past the target with a CCD camera. The focus of this laser can also be set with a knife edge measurement of this target using the wire Mg target as a reference for the spot size. To load $^{27}\text{Al}^+$, the same ablation laser is used in combination with a Q-switched 266 nm pulsed laser from Crystalaser with a pulse energy of ≈ 0.1 mJ at 1 kHz repetition rate for photo-ionization of Al. To load $^{27}\text{Al}^+$ the ablation laser is pulsed followed by a delayed photo-ionization (PI) pulse to ionize the ablated Al atoms. The delay is included to account for the time it takes for the ablated cloud to reach the trapping volume. It is a bit harder to determine if $^{27}\text{Al}^+$ is loaded in the trap because photons cannot be directly scattered by $^{27}\text{Al}^+$ with a high enough rate. To determine if an $^{27}\text{Al}^+$ ion is loaded in the trap a CCD, position dependent fluorescence signal, or RF tickle are used. If a CCD is used, the position

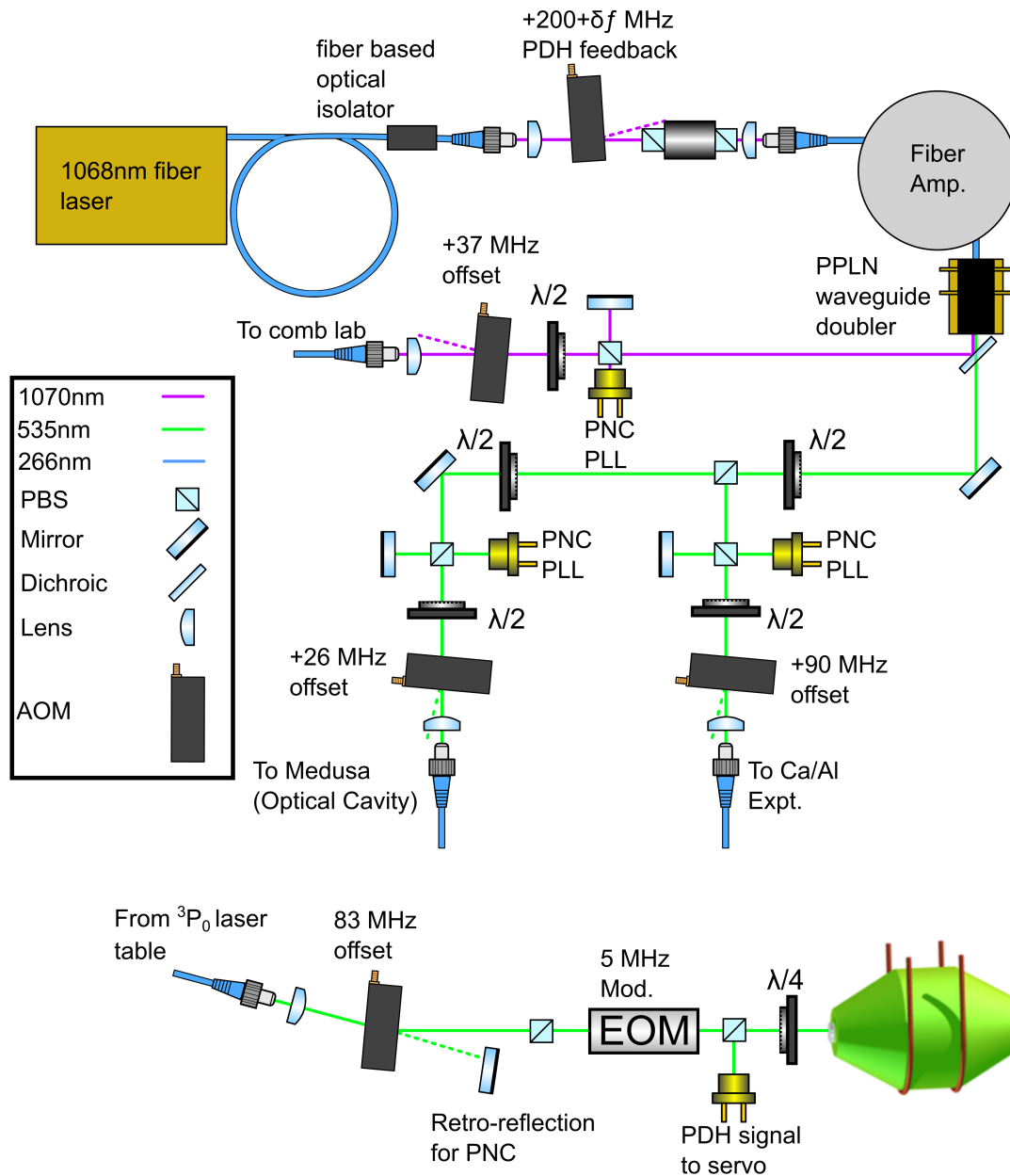


Figure 2.16: Simplified diagram of the laser distribution setup for the 3P_0 laser. We stabilize the laser to the optical cavity with feedback in the IR and the pathlength is stabilized from Medusa to the experimental setups with separate stabilization subsections. A path to the comb lab is labeled, where this path is used as an optical link to the ^{171}Yb laser system in later experiments.

of the $^{40}\text{Ca}^+$ ion can be marked on the CCD control software and the trapping voltages can be ramped to see if the ion crystal order switches from $^{40}\text{Ca}^+ / ^{27}\text{Al}^+$ to $^{27}\text{Al}^+ / ^{40}\text{Ca}^+$. For the position dependent detection, a sharply focused 729 nm laser is aligned such that the two crystal orders

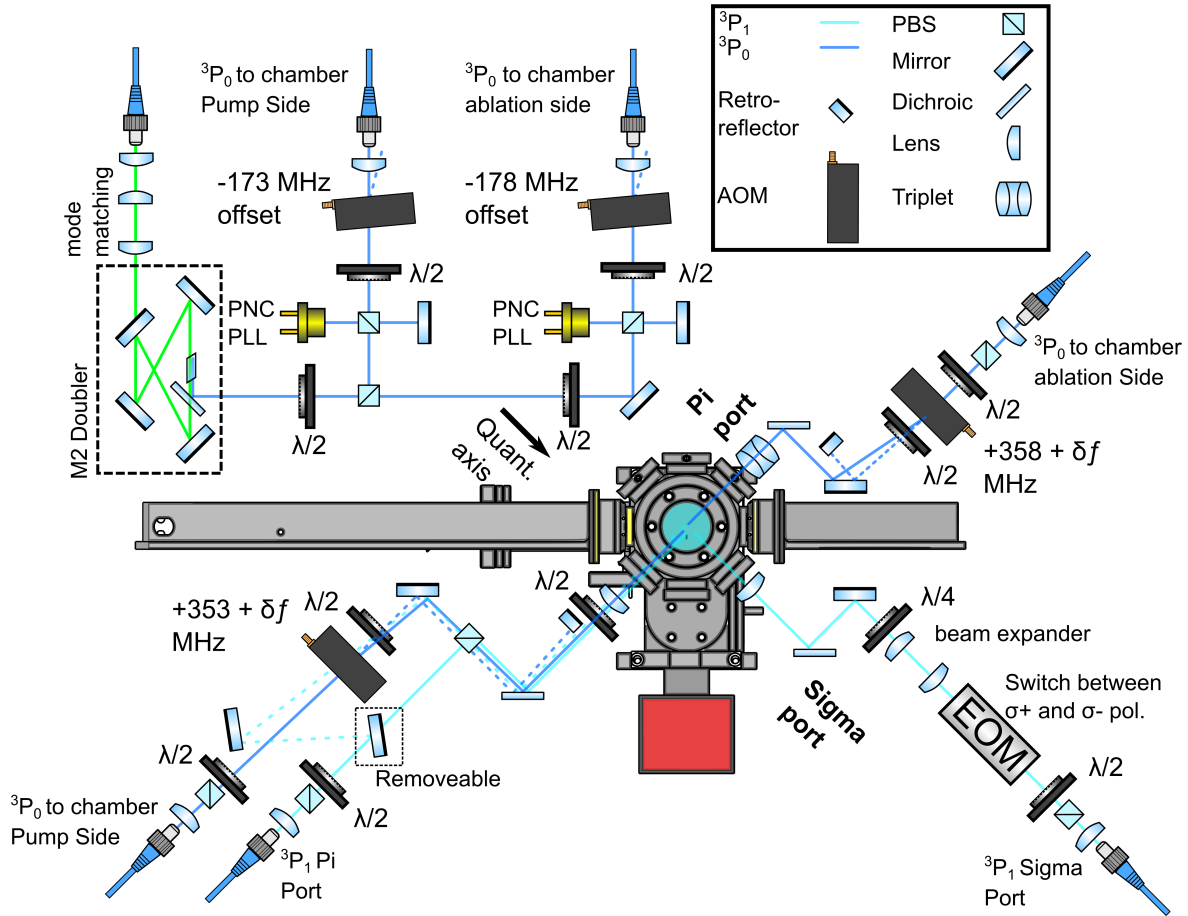


Figure 2.17: Simplified setup of the 3P_0 and 3P_1 beampaths to the $^{40}\text{Ca}^+ / ^{27}\text{Al}^+$ ions. An EOM is located just before the vacuum system to switch the laser polarization of the 3P_1 laser between σ^\pm . Along the Pi direction there is a removable mirror to switch beam direction when probing the inner manifold clock transition. This is included to allow for the beam to be π polarized when the clock laser polarization is rotated by 90° . Included in this figure is the distribution paths for the 3P_0 to send light to the counter propagating pump side and ablation side ports. Path length stabilization setups are used to stabilize the phase noise from the doubler to the vacuum system.

result in a position dependent Rabi rate for driving the $^{40}\text{Ca}^+$ ion from the $|S_{1/2}\rangle$ ground-state to the $|D_{5/2}\rangle$ metastable excited state. To detect the order dependence a 729 nm pulse is applied and then the state is detected with a 397 nm laser. If the ion crystal is in the $^{40}\text{Ca}^+ / ^{27}\text{Al}^+$ order the $^{40}\text{Ca}^+$ ion will scatter photons and if the ion crystal is in the $^{27}\text{Al}^+ / ^{40}\text{Ca}^+$ order then the $^{40}\text{Ca}^+$ ion will appear dark. Therefore if an ion is loaded the voltages can be ramped and the bright and dark states can be observed to determine if $^{27}\text{Al}^+$ is loaded. For the last case an RF signal can be

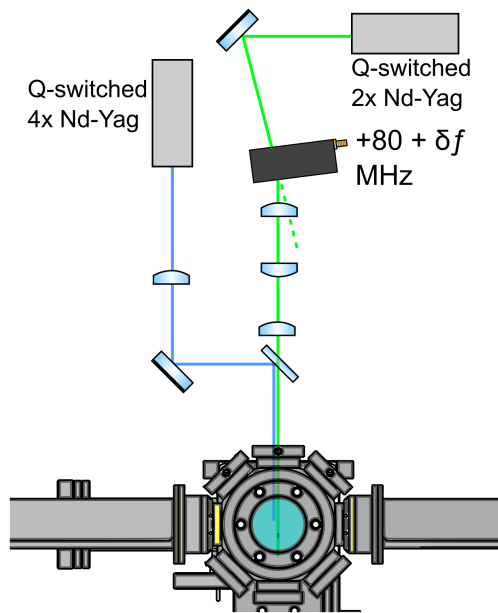


Figure 2.18: Diagram of the ablation and PI laser paths to the ablation target. The AOM in this picture is used to displace the beam position on the target and is randomly varied from shot to shot to reduce the likelihood of depleting spots of the ablation target unevenly.

applied via a trap electrode to excite the secular modes of the $^{40}\text{Ca}^+ / ^{27}\text{Al}^+$ crystal. To excite the ions motion, the RF signal frequency is set to the secular frequency of interest. If there is no $^{27}\text{Al}^+$ loaded in the trap the $^{40}\text{Ca}^+ / ^{27}\text{Al}^+$ secular mode won't be excited and the fluorescence signal will remain high. If $^{27}\text{Al}^+$ is loaded in the trap, the secular mode will be heated and the fluorescence signal will drop indicating that an $^{27}\text{Al}^+$ ion is loaded. To improve the loading efficiency we align the $^{27}\text{Al}^+$ PI beam to trapping region using a 397 nm guide beam. We first overlap the pulsed 266 nm laser with a near resonant 397 nm laser using a beam profiler such that the two beams are colinear. Then the 397 nm guide beam is aligned to $^{40}\text{Ca}^+$ by using a fluorescence signal. This helps to ensure that the PI light is well aligned with the trapping region. By following these sequences loading both $^{40}\text{Ca}^+$ and $^{27}\text{Al}^+$ can be performed reliably within ≈ 10 min.

2.6 Noise minimization setups

Two major sources of noise in this experiment are phase noise due to path length variations of the clock beam line which causes variations in the local oscillator phase and magnetic field noise which arises from the lab environment and results in variations of the energies of the $^{27}\text{Al}^+$ internal states. Both of these noise sources can create differential noise between atomic clocks used in experiments discussed in this thesis. The differential noise causes variations in the relative or measured frequency of the atomic clocks and cannot be corrected for in the measurements. The effect of the noise on measurements can be minimized by either passively reducing the measurements sensitivity to the noise which is done by driving a less magnetically sensitive clock transition or actively by stabilizing the phase noise by actively stabilizing the local magnetic field and path length.

2.6.1 Active Magnetic Field Stabilization

To implement magnetic field stabilization, we use magnetic field coils to manipulate the local field environment with large enough magnitude and high enough bandwidth. When implementing this control system we need to also measure the magnetic field to both characterize and optimize the stabilization setup. In this section we will discuss these two aspects of the magnetic field stabilization setup.

To generate the magnetic field, large coils that are close to a Helmholtz configuration are set up around the optical table to prevent obstruction of the optical ports. Each coil has 10 turns of wire and has an inductance of ≈ 2 mH and a resistance of 4Ω . With this low inductance the coil has a bandwidth of 1 kHz which is sufficient to cancel out 60 Hz line noise and stabilize the slowly drifting magnetic fields. The coil is driven by an Arryo laser diode driver which can drive currents up to 0.5 A. An error signal for the slowly varying environmental magnetic field is obtained from a set of Bartington Mag-03 fluxgate magnetometers which are aligned along the quantization axis because magnetic field noise along this direction effects the ion the most. Two sensors are aligned along the

quantization vector and a third is aligned counter to the quantization axis. This allows us to take into account variations in the magnetic field gradient. The compensation coil is aligned 45 degrees from the quantization axis so a component of the correction field is aligned along the quantization axis. The voltages from the three sensors are recorded by a Labjack analog to digital converter and are processed by the lab computer which takes a linear combination of this data and outputs it as a correction signal. This is summed with the lower frequency drift correction signal and sent to the Arryo current driver. The correction voltages are added in this way so both higher frequency corrections can be applied to correct for line noise and lower frequency signals can be applied for slower long term drifts. A schematic of the servo stabilization hardware can be seen in Fig. 2.19. An important aspect to making the magnetic field stabilization work is proper calibration of the coefficients used in the linear combination for determination of the correction signal. Calibration is achieved by fitting data from the fluxgate magnetometer to in-situ measurements of the local magnetic field with the $^{40}\text{Ca}^+$ ion. An example and further discussion of the calibration routine can be seen in Appendix A.

The magnetic field can be measured directly in the trapping region using two Zeeman transitions in $^{40}\text{Ca}^+$ with high sensitivity to magnetic fields. Two transitions are measured so laser frequency drifts can be canceled since the drift is common to both measurements. Measuring with these two transitions prevents an inaccurate measurement of the magnetic field. The most convenient and sensitive transitions that can be used in this experiment are the $|4^2S_{1/2}, m_f = -1/2\rangle \leftrightarrow |3^2D_{5/2}, m_f = -5/2\rangle$ and $|4^2S_{1/2}, m_f = -1/2\rangle \leftrightarrow |3^2D_{5/2}, m_f = 3/2\rangle$ transitions with transition frequencies which will be labeled as f_- and f_+ respectively. One method for tracking the long term magnetic field is to use individual frequency locks to track these transition frequencies. From these two frequency measurements the magnetic field drift can be determined from

$$B_{\text{mag}} = \frac{\hbar(f_+ - f_-)}{\mu_B g_{5/2} (m_{f,+} - m_{f,-})}, \quad (2.44)$$

where μ_B is the Bohr magneton, $g_{5/2}$ is the $D_{5/2}$ Lande g -factor, and $m_{f,[+,-]}$ are the $D_{5/2}$ Zeeman level quantum numbers used in the magnetic field measurement. Alternatively, the magnetic field

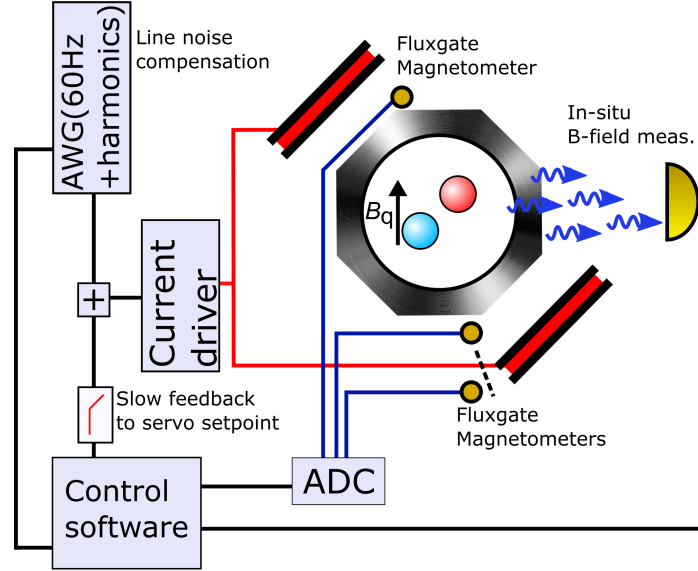


Figure 2.19: Schematic of the magnetic stabilization system. Three fluxgate magnetometers, labeled by the yellow circles, measure the magnetic field along the quantization axis where one sensor is anti-aligned to the quantization direction. The magnetic field measured by these sensors is measure by a Labjack analog to digital converter (ADC) and sent to the computer. A linear combination of these measurements is used to estimate the value of the magnetic field at the center of the ion trap where a correction signal corrects for the slow drifts. This is combined with a signal from an arbitrary waveform generator (AWG) which is used to null the line noise seen by the ion. In-situ measurements of the magnetic field are obtained with ion measurements which are used to calibrate the coefficients used in the linear combination of the fluxgate magnetometer measurements.

can be determined using a Ramsey phase measurement. This is achieved by using a Ramsey phase measurement where the Ramsey sequence is implemented between the $|3^2D_{5/2}, m_f = -5/2\rangle$ and the $|3^2D_{5/2}, m_f = 3/2\rangle$ states, the experimental sequence follows these steps:

- (1) To begin the sequence a $\pi/2$ -pulse is driven on the $|4^2S_{1/2}, m_f = -1/2\rangle \leftrightarrow |3^2D_{5/2}, m_f = -5/2\rangle$ transition to move half of the population to the $|3^2D_{5/2}\rangle$ state.
- (2) Then a π -pulse on the $|4^2S_{1/2}, m_f = -1/2\rangle \leftrightarrow |3^2D_{5/2}, m_f = 3/2\rangle$ transition is applied to move the remaining population to the $|3^2D_{5/2}, m_f = 3/2\rangle$ state.
- (3) This superposition freely evolves for a period T_R .
- (4) The phase is read out by reversing the initial pulses, a π -pulse on the $|4^2S_{1/2}, m_f = -1/2\rangle \leftrightarrow$

$|3^2D_{5/2}, m_f = 3/2\rangle$ transition is applied followed by a $\pi/2$ -pulse on the $|4^2S_{1/2}, m_f = -1/2\rangle \leftrightarrow |3^2D_{5/2}, m_f = -5/2\rangle$ transition.

- (5) Lastly, a fluorescence measurement is made. After this the state is detected and the phase is determined from repeated measurements.

The phase evolution can be converted in a change in the magnetic field using the equation

$$\delta B_{\text{mag}} = \delta\phi \frac{\hbar}{2\pi T_R \mu_B (m_{f,+} g_+ - m_{f,-} g_-)}. \quad (2.45)$$

An absolute measurement of the magnetic field can be determined with this technique by using the initial frequencies of the two transitions and calculating the initial magnetic field using Eq. 2.44. With these two magnetic field measurement techniques we can quantify the magnetic field noise and calibrate servos to actively stabilize the magnetic field local to the ions. By using the phase dependent measurement, the magnetic field noise can be measured with a higher bandwidth because fewer measurements are needed to determine the magnetic field. The higher measurement bandwidth aids in fitting the fluxgate measurements to in-situ data measured with the $^{40}\text{Ca}^+$ to determine the coefficients for the linear combination.

2.6.2 Fiber Noise and Path Length Stabilization

Another source of differential noise comes from air turbulence in the beam path and variations in the refractive index of fibers causing variations in the laser phase. There are many stages of phase noise compensation (PNC) for the clock beam path which are used to stabilize the phase noise from the optical cavity to the $^{27}\text{Al}^+$ ion. The basic setup for phase noise compensation requires two interferometer arms where one shorter arm provides a phase reference and the second longer interferometer arm is phase stabilized to the shorter path. Commonly the longer arm is frequency shifted from the reference to make it easier to measure the interference between the two paths. The relative phase between the two arms is measured using a high bandwidth photodetector which measures the beatnote generated between the two paths. This beatnote is mixed down and an

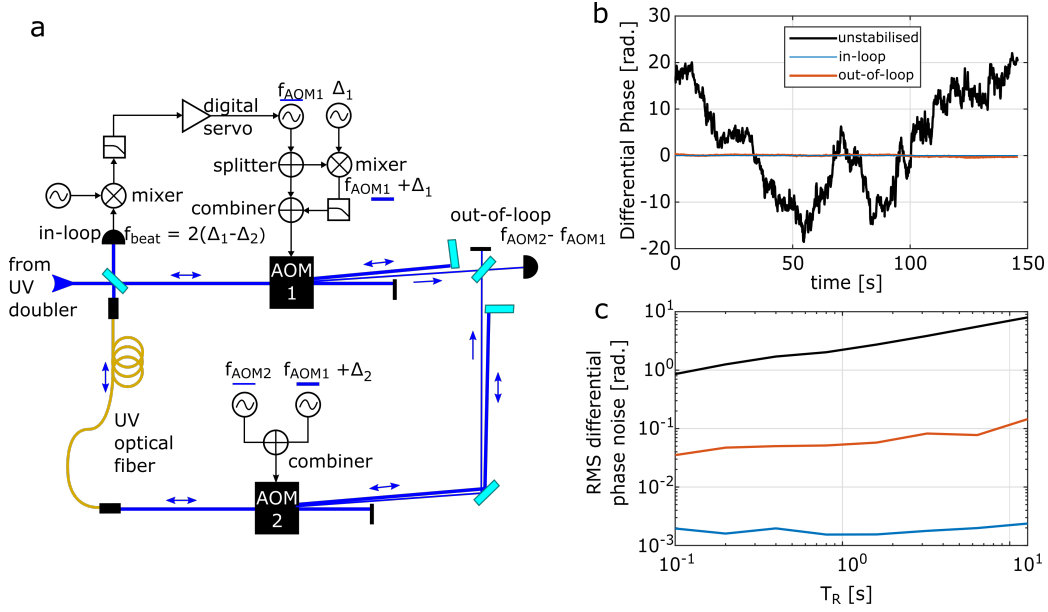


Figure 2.20: Measurement of differential path length noise in a test setup. (a) Diagram of the optical and electronic system for stabilizing and measuring differential phase noise between the two beam paths. This test setup is used to measure the differential phase noise at the position of the ions using a beam-splitter to form an out-of-loop beatnote. This beatnote will approximate the phase noise of the real experiment. (b) Time-series phase measurement of the out-of-loop and in-loop detectors (measured simultaneously) and the unstabilized phase noise observed on the out-of-loop detector immediately before the other measurements. (c) Root-mean-squared phase fluctuations for a simulated Ramsey experiment using the three time-series measurements from (b).

error signal is generated by comparing against a maser stabilized 10 MHz reference. The beatnote is then stabilized by feeding back to the the AOM which provides the offset to the long path. A test setup can be seen in Fig. 2.20 where the two beamlines were used to measure the phase noise of an implementation of a phase noise compensation setup against a nearly identical path. This setup is used for a UV laser and is able to provide an out of loop test of the stabilization setup. It can be seen that with the out of loop measurement the RMS differential phase noise below is 0.1 rad out to 10 s of averaging. PNC setups have been used in many experiments and further details about these setups can be found in Refs. [79, 80].

2.7 Quantum logic spectroscopy

The experiments in this thesis use an $^{27}\text{Al}^+$ quantum-logic clock to demonstrate differential comparison techniques. The use of quantum-logic spectroscopy (QLS) is not unique to clocks based on $^{27}\text{Al}^+$ and has been used to perform spectroscopy on $^{27}\text{Al}^+$ ions [77] as well as molecules [81, 71] and highly charged ions [82]. QLS is used in cases where the spectroscopic ion of interest is lacking electronic transitions needed for Doppler cooling and state detection. By co-trapping a logic ion with a spectroscopic ion, the accessible cooling and detection transitions of the logic ion can be used to sympathetically cool the coupled motional modes of the ion crystal and QLS can be used to readout the electronic state of spectroscopic ion using the logic ion. For experiments performed in this thesis we utilize $^{25}\text{Mg}^+$ and $^{40}\text{Ca}^+$ as the logic ions in our two $^{27}\text{Al}^+$ ion clocks. QLS is implemented by using a shared motional mode of the ion crystal as an information bus to transfer information about the internal state of the spectroscopy ion to the logic ion where the state can then be read out using fluorescence detection [77]. Efficient cooling and state detection can be realized with the co-trapped logic ion and in $^{27}\text{Al}^+$ a clock transition which has low sensitivity to certain systematic effects can be utilized.

The $^{27}\text{Al}^+$ ion provides an excellent clock transition because of its low sensitivity to external field shifts but it is limited in its ability to directly measure the ion's state using fluorescence detection. By applying motion adding and subtracting sideband pulses to the two ions the $|^3P_0\rangle$ and $|^1S_0\rangle$ states of the $^{27}\text{Al}^+$ ion can be mapped to the bright and dark state of the $^{40}\text{Ca}^+$ ion. The secular mode which is used as the bus in this system is the out-of-phase axial mode. This mode is chosen because both ions have similar mode participation and the out-of-phase mode is less susceptible to motional heating from electric field noise. A description of QLS is shown in Fig 2.21 and follows these steps:

- i. State preparation is applied to the $^{27}\text{Al}^+$ ion to prepare the ion in the desired $|^1S_0\rangle$ Zeeman sub-level using one of the state preparation procedures discussed previously. Additionally, the $^{40}\text{Ca}^+$ ion is prepared in the $|4^2S_{1/2}\rangle$ state. The axial out-of-phase axial mode (STR)

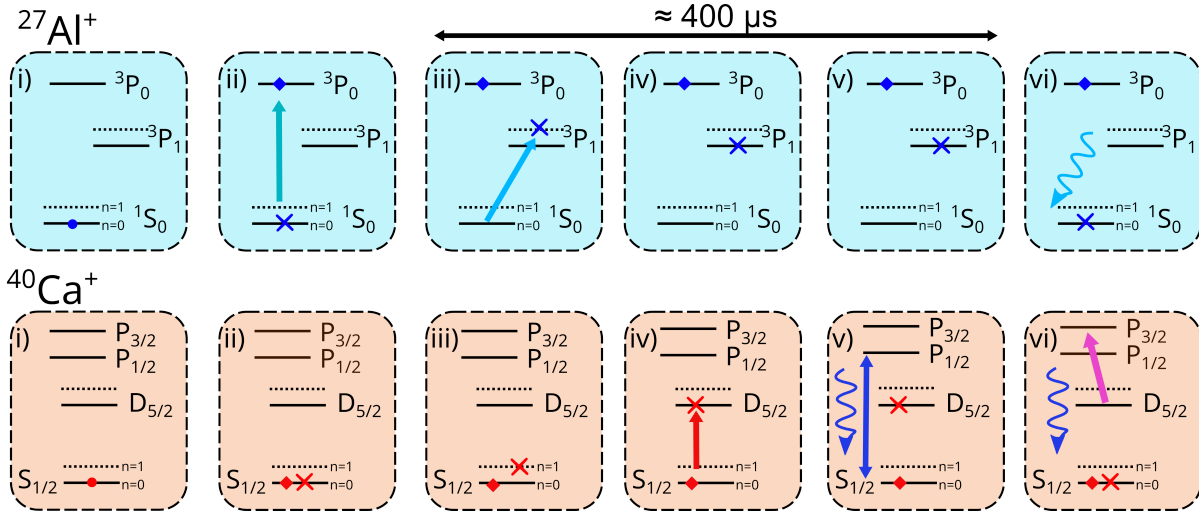


Figure 2.21: Simplified description of the QLS sequence. (i) The ions are prepared in their initial states. (ii) The clock transition is driven where the two possible final states are labeled by \times and \blacklozenge respectively. (iii) A blue motion adding sideband is driven on $^{27}\text{Al}^+$ which will add a quanta of motion if the clock pulse did not drive a transition. (iv) A motion subtracting red sideband pulse is driven on $^{40}\text{Ca}^+$ which will drive the ion to a metastable state if a clock transition is not driven or leave the ion in the ground-state if the clock transition is driven, thereby mapping the transition probability to $^{40}\text{Ca}^+$. (v) Fluorescence detection is then used to determine the $^{40}\text{Ca}^+$ state which will translate into a determination of the $^{27}\text{Al}^+$ state. (vi) The metastable state is quenched and the cycle repeats. Steps (iii-v) take $\approx 400\mu\text{s}$ so often the $|^3P_1\rangle$ state will decay requiring the the readout steps (iii-v) to be repeated when high fidelity state determination is needed.

mode is then cooled to the motional ground-state with sideband cooling. Both $^{27}\text{Al}^+$ and $^{40}\text{Ca}^+$ are now in the motional ground-state $n = 0$.

- ii. The clock pulse is applied which has some probability of driving the $^{27}\text{Al}^+$ ion to its excited clock state. The two possible final states after the clock transition is driven are labeled by \times and \blacklozenge respectively.
- iii. A motion adding blue STR sideband on the $|^1S_0, m_f = \pm 5/2\rangle \rightarrow |^3P_0 m_f = \pm 7/2\rangle$ transition is then driven which will add a quantum of motion if the $^{27}\text{Al}^+$ ion is in the ground-state following the clock pulse. Because the ions are coupled if this transition is driven then the $^{40}\text{Ca}^+$ ion will also have a motional quanta added to this mode
- iv. A motion subtracting red STR sideband of the $|4^2S_{1/2}\rangle \leftrightarrow |3^2D_{5/2}\rangle$ transition is then driven

which will drive the $^{40}\text{Ca}^+$ ion to be in its metastable D state if there is a quanta of motion present or will remain in the $|4^2S_{1/2}\rangle$ ground-state if there is no quantum of motion present.

- v. Fluorescence detection of the $^{40}\text{Ca}^+$ ion is then used to determine if the ion is in the metastable state thereby mapping $|^3P_0\rangle \rightarrow |\text{Bright}\rangle_{\text{Ca}}$ and $|^1S_0\rangle \rightarrow |\text{Dark}\rangle_{\text{Ca}}$.
- vi. The $^{40}\text{Ca}^+$ meta-stable state is then repumped by driving the $|3^2D_{5/2}\rangle \leftrightarrow |4^2P_{3/2}\rangle$ transition and steps (iii-vi) can be repeated to improve the state determination fidelity.

Because the outcome of the clock transition is preserved for some time due to the long lifetime of the $^{27}\text{Al}^+ \ ^3P_0$ state, multiple “non-demolition” measurements can be performed allowing for the state to be determined with higher fidelity than a destructive measurement. After step (vi) $^{27}\text{Al}^+$ can be re-prepared in its electronic ground-state or alternatively the population can be left in its final state and a successful clock excitation can be determine by if the $^{27}\text{Al}^+$ ion changes its state. Additionally if the ion remains in its excited state the ground-state does not need to be re-prepared. In the experiments discussed we use the change $^{27}\text{Al}^+$ ion state after a clock pulse is applied to determine if there was a successful clock excitation.

Using this information about the $^{40}\text{Ca}^+ / ^{27}\text{Al}^+$ experimental apparatus we can now move into discussing the experiments performed with this system. We will use the information detailed in this chapter as a basis for discussion on differential comparison techniques with the $^{40}\text{Ca}^+ / ^{27}\text{Al}^+$ system and discuss evaluation of systematic shifts of the $^{27}\text{Al}^+$ clock transition in the $^{40}\text{Ca}^+ / ^{27}\text{Al}^+$ experiment.

Chapter 3

Correlation Spectroscopy

In this chapter, details are provided on correlation spectroscopy, a high-stability differential frequency comparison technique that allows comparisons beyond the laser coherence time when comparing systems with similar oscillator frequencies. Here, I describe measurements that reach interrogation periods of a few seconds which result in an order of magnitude reduction in the frequency comparison instability when compared to previous Al-Al comparisons. These results differ from previous implementations of correlation spectroscopy where this technique was used to compare two or more ions [83, 84, 85, 86, 87, 88] or neutral atomic ensembles [89, 34, 90, 49] located in the same trap. In all of these experiments, aside from [84], the atoms were located in the same trap to minimize the impact of differential noise effects which can limit the viability of this technique. Common sources of differential noise in these experiments include optical path length fluctuations which vary the relative phase between the lasers interrogating the atomic ensembles and variations in magnetic fields local to the two atomic clocks. For the case of co-located atoms these effects are mostly common-mode to all atoms so the effect of these noise sources can be suppressed with correlation spectroscopy. Here, we implement this comparison technique in spatially separated optical clocks where differential noise can limit their relative coherence. To reach comparison times of a few seconds in spatially separated atomic clocks these differential noise sources must be suppressed. In this chapter I will contrast the standard frequency comparison stability with the comparison stability that can be achieved with correlation spectroscopy, describe how the primary differential noise sources are characterized and mitigated, and present correlation spectroscopy

measurements between two $^{27}\text{Al}^+$ clocks at the lifetime limit of this atomic species.

3.1 Limits in conventional frequency comparisons

Standard frequency comparisons between optical clocks are performed by first interrogating an atomic resonance using an ultrastable laser and stabilizing the laser frequency based on the measured atomic transition probabilities [15]. Following stabilization of the laser, the frequency of the atomic standard can be distributed and compared with a second, independent atomic clock. For clocks operating at similar oscillator frequencies the stabilized lasers can be compared directly by generating a beatnote between the two lasers which can be directly measured by a frequency counter. An example of this standard comparison method for similar frequency optical clocks can be seen in Fig. 3.1. For these standard comparisons techniques, the local oscillators are used as intermediaries to compare the two systems. Because the lasers are mediating this comparison, laser frequency noise is a major limiting factor in the comparisons. The laser frequency noise makes probing with long times impossible so we chose probe times which optimize the coherence and stability of the measurement [91, 92]. Laser noise can also affect the accuracy of comparisons through aliasing of noise due from the dead-time between measurements, also known as Dick effect noise [93]. Developments in cryogenic optical cavities have resulted in improvements to the stability of laser systems but the advances have yet to reach the stability required to probe many atomic species' clock transitions at their natural linewidths [19]. To illustrate how correlation spectroscopy can be used to improve the stability of frequency comparisons independent of limits set by laser instability, I will provide a discussion of the effect of laser noise on the ability to compare two frequency standards.

The ground and excited state of the clock transition can be described by a two level system and in this discussion will be labeled by $|\downarrow\rangle$ and $|\uparrow\rangle$ [44]. To simplify the discussion the initial state of the clock transition will begin in $|\downarrow\rangle$ and a Ramsey interrogation with a free evolution period of T_R will be used to measure the phase evolution of the frequency standard. Additionally, we assume that the duration of the $\pi/2$ -pulses is negligible compared to T_R , and the second $\pi/2$ pulse has a

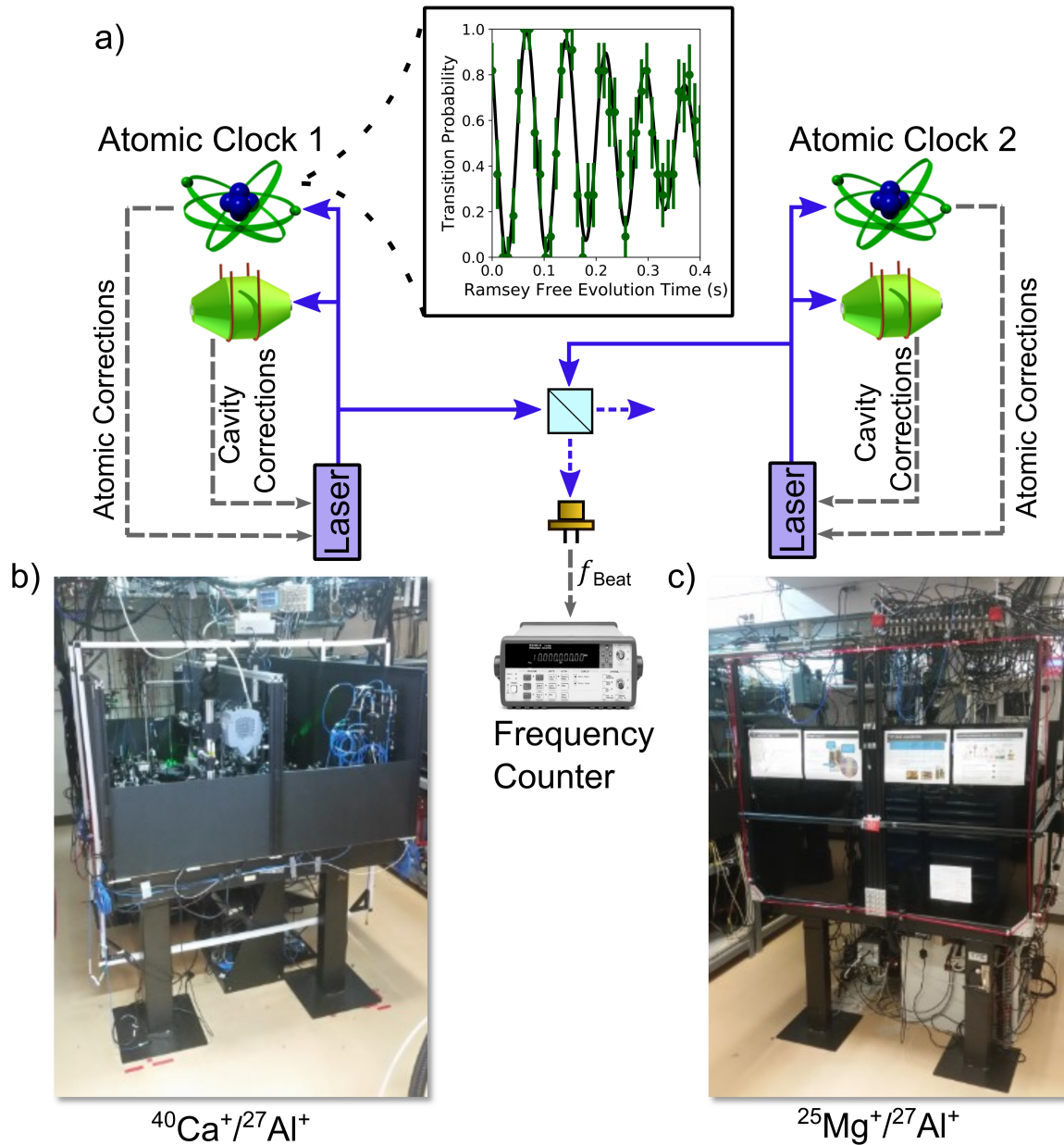


Figure 3.1: a) Scan of the Ramsey free evolution period when driving the $^1S_0 \leftrightarrow ^3P_0$ transition where the transition probability is plotted vs. the Ramsey free evolution period. The sinusoidal behavior of the scan is from detuning the interrogating laser by 13.14 Hz and the decaying contrast envelope is a consequence of the local oscillator noise. From fitting to this data a fractional laser noise floor of $\sigma_0 = 4.4(2) \times 10^{-16} / \sqrt{\tau/s}$ is determined. Also included is a simplified diagram of the components required to compare two similar frequency atomic clocks via their individually stabilized local oscillators. Pictures of the (b) $^{40}\text{Ca}^+ / ^{27}\text{Al}^+$ and (c) $^{25}\text{Mg}^+ / ^{27}\text{Al}^+$ quantum logic clocks used to demonstrate correlation spectroscopy. These clocks are contained in the same lab and are located ≈ 3 m apart.

controlled laser phase difference ϕ [94] relative to the phase of the first $\pi/2$ -pulse. The state of the ion following the first $\pi/2$ pulse is $|\Psi\rangle = \frac{1}{\sqrt{2}}(|\downarrow\rangle - |\uparrow\rangle)$. Over the Ramsey free evolution period the phase evolution of $|\downarrow\rangle$ and $|\uparrow\rangle$ results in the state

$$|\Psi\rangle = \frac{1}{\sqrt{2}}(e^{i(\Delta\phi/2)}|\downarrow\rangle - e^{-i(\Delta\phi/2)}|\uparrow\rangle) \quad (3.1)$$

where $\Delta\phi = (\omega_L - \omega_0)T_R + \phi$, $\omega_L/2\pi$ is the laser frequency, $\omega_0/2\pi$ is the atom frequency. A measurement of $\hat{\sigma}_z = |\uparrow\rangle\langle\uparrow| - |\downarrow\rangle\langle\downarrow|$ at the end of this sequence has expectation value

$$\langle\hat{\sigma}_z\rangle = \cos [(\omega_L - \omega_0) T_R + \phi] . \quad (3.2)$$

This is the measurement outcome for a Ramsey interrogation without any noise processes. To include noise we will substitute $\phi \rightarrow \phi + \phi_N$ with ϕ_N describing the laser phase noise. The effect of the laser noise ϕ_N in this measurement can be described by a Gaussian distribution with a standard deviation σ_N as

$$P(\phi_N) = \frac{1}{\sigma_N\sqrt{2\pi}}e^{-\phi_N^2/2\sigma_N^2} . \quad (3.3)$$

With flicker noise being described by a $1/f$ power spectral density, the phase noise standard deviation can be further described by $\sigma_N = \sigma_0\omega_L T_R$, where σ_0 is the fractional flicker noise floor of the Allan deviation. The effect of other noise processes can be added to this description of ϕ_N by modification of $P(\phi_N)$, but for simplicity we consider the case where there are no long term drifts in the frequency. We modify the expression for $\langle\hat{\sigma}_z\rangle$ to include the effect of laser noise. By multiplying Eq. 3.2 by the phase noise distribution and integrating over the phase,

$$\langle\hat{\sigma}_z\rangle = \int_{-\infty}^{\infty} P(\phi_N) \cos [(\omega_L - \omega_0) T_R + \phi_N + \phi] d\phi_N = e^{-\sigma_N^2/2} \cos [(\omega_L - \omega_0) T_R + \phi] \quad (3.4)$$

which provides an expression for Ramsey interrogation that is impacted by the laser phase. In Eq. 3.4 the term before the exponential shows how the fringe contrast is effected by the standard deviation of the phase noise and the probe duration T_R . This term can be rewritten as $C(T_R) = e^{-\sigma_N^2/2}$ to illustrate that it determines the contrast of the Ramsey fringe. We can now use this equation for the Ramsey fringe to calculate the measurement instability that would be obtained

considering the impact of laser phase noise. Measurement instability is characterized by the Allan deviation $\sigma_y = \delta\omega_L/\omega_L\sqrt{\frac{T}{N\tau}}$, where $\delta\omega_L$ is the single shot measurement uncertainty [44] and is given by

$$\delta\omega_L = \delta\langle\hat{\sigma}_z\rangle/|d\langle\hat{\sigma}_z\rangle/d\omega| \quad (3.5)$$

for Ramsey interrogation. Evaluating $|d\langle\hat{\sigma}_z\rangle/d\omega|$ at the maximum slope points of the Ramsey fringe $\phi = \pm\pi/2$, results in

$$\left|\frac{d\langle\hat{\sigma}_z\rangle}{d\omega_L}\right|_{\phi=\pi/2} = T_R e^{-(\sigma_0\omega_L T_R)^2/2}. \quad (3.6)$$

This equation does not yet consider the impact of the excited state lifetime but this will be added later by modifying $C(T_R)$. Combining this result with the expression for the projection-noise-limited measurement instability yields

$$\sigma_y(\tau) = \frac{\delta\omega_L}{\omega_L} \sqrt{\frac{T_R}{\tau}} = \frac{1}{\omega_L \sqrt{T_R \tau}} e^{(\sigma_0\omega_L T_R)^2/2}. \quad (3.7)$$

The measurement instability σ_y has a minimum at

$$T_{R,\text{opt}} = \frac{1}{\sqrt{2}\sigma_0\omega_0}, \quad (3.8)$$

which is the optimum Ramsey free evolution period for an interrogation limited by laser noise. This simple model results in a value close to the asymptotic optimum probe time reported in Ref. [92], in which a more accurate result is obtained by using a more realistic treatment of the laser noise. This consideration of more realistic noise sources causes the maximum probe time to be shorter than $T_{R,\text{opt}}$ to avoid Ramsey fringe hops which are detrimental.

We further study the effect of laser noise on Ramsey interrogation using a Monte-Carlo simulation of the phase noise in Ramsey interrogation. This simulation is used to study the effect laser decoherence has on the optimum Ramsey interrogation period. A representative measurement of the fractional noise floor σ_0 of the laser system is first obtained for use in the simulation to determine the interrogation limits for our atomic clock. To measure this, a Ramsey experiment is performed and a fit to the decay envelope is used to determine the experimental values of σ_0 . The resulting scan of the Ramsey free evolution period is plotted in Fig. 3.1 (a). From this fit we

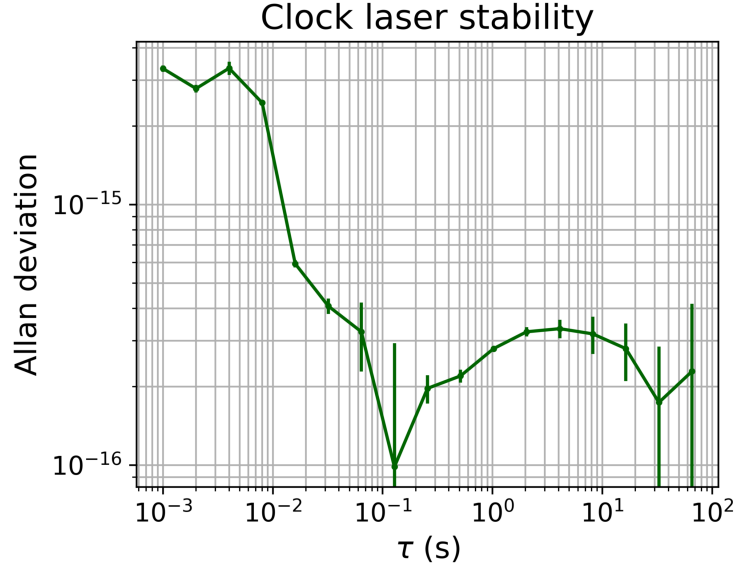


Figure 3.2: Allan deviation of the Medusa laser noise obtained from a 3 cornered hat comparison with two other laser systems. We can use this measurement to estimate the fractional noise floor σ_0 which we use to model the impact of laser noise on a laser lock to the atomic reference frequency.

can utilize the fitted fractional noise floor of $\sigma_0 = 4.4(2) \times 10^{-16} / \sqrt{\tau/s}$ for the Allan deviation of numerically-generated flicker frequency noise. Additionally, we also show an Allan deviation of the “Medusa” cavity laser stability in Fig. 3.2 obtained from a 3 cornered hat laser comparison [95] between three independent laser systems where we observe a noise floor of $\sigma_0 \approx 3 \times 10^{-16}$. The noise spectrum measurements are used to model the phase noise of a simulated interrogation. For this simulation 300,000 clock interrogation cycles are used and the probe duration is varied from 20 ms to 200 ms with a dead time equal to the average dead time of the $^{25}\text{Mg}^+ / ^{27}\text{Al}^+$ and $^{40}\text{Ca}^+ / ^{27}\text{Al}^+$ systems of 100 ms. There are two characteristics of the resulting Allan deviation of the simulated data. At short averaging times, the Allan deviation is described by flicker noise from the local oscillator and at averaging times beyond 100 s, the Allan deviation follows a slope of $1/\sqrt{\tau}$ which is expected from the white spectrum of quantum projection noise. As we vary the probe duration used in the simulation we fit to the section of the Allan deviation corresponding to the white frequency noise to determine the asymptotic 1 second instability. The results of the simulation

show a diverging instability beyond probe times of 0.18 s due to phase hops induced by the noise and the response of the lock to the fringe. The results of the simulation are shown as the red dots in Fig. 3.11. The discrepancy between the numerical estimate of the laser-limited instability and the analytical estimate displayed in Fig. 3.11 is likely caused but the non-linear error signal response at longer probe durations from the non-linear error signal slope near the turning points at the sinusoid. While this does not provide a complete picture of clock interrogation because I do not include additional sequences used to stabilize the system and other noise processes which occur in the system, it does provide a best case scenario for the laser-limited instability which can be used as a reference for the instability which is observed in correlation spectroscopy experiments.

Using the analytical and simulated models of the effect of laser noise in a Ramsey interrogation, a comparison against differential measurement techniques can now be made. If the laser phase noise of interrogations of two atomic clocks are correlated differential measurements can be used to remove this common source of noise and increase the Ramsey interrogation period.

3.2 Theoretical Discussion of Correlation Spectroscopy

In correlation spectroscopy, two atoms or atomic ensembles are probed simultaneously with the same laser and their frequency difference is determined by measurements of the parity operator, $\hat{\Pi} = \hat{\sigma}_{z,1} \otimes \hat{\sigma}_{z,2}$. The parity operator is described by

$$\begin{aligned} \hat{\Pi} = \hat{\sigma}_{z,1} \otimes \hat{\sigma}_{z,2} = & \\ & (|\uparrow\rangle_1 \langle\uparrow|_1 - |\downarrow\rangle_1 \langle\downarrow|_1)(|\uparrow\rangle_2 \langle\uparrow|_2 - |\downarrow\rangle_2 \langle\downarrow|_2) = \\ & (|\uparrow\uparrow\rangle \langle\uparrow\uparrow| + |\downarrow\downarrow\rangle \langle\downarrow\downarrow|) - (|\uparrow\downarrow\rangle \langle\uparrow\downarrow| + |\downarrow\uparrow\rangle \langle\downarrow\uparrow|). \end{aligned} \quad (3.9)$$

The expectation value of this operator for unentangled atoms can be found by replacing $\langle\hat{\sigma}_{z,i}\rangle$ with the result from Eq. 3.2

$$\langle\hat{\Pi}\rangle = \langle\hat{\sigma}_{z,1}\rangle\langle\hat{\sigma}_{z,2}\rangle = \cos(\Delta_1 T_R + \phi_1) \cos(\Delta_2 T_R + \phi_2) \quad (3.10)$$

where we have defined the laser frequency and phase relative to the atomic frequency as $\Delta_i \equiv \omega_L - \omega_{0,i}$ and $\phi_i = \phi_{L,i} - \phi_{0,i}$ where i is an index that refers to each atom. To simplify this expression and to observe how measurements beyond the laser coherence limit are performed, $\langle \hat{\Pi} \rangle$ can be separated into terms that depend on the sum and difference frequency detunings $\Delta_{\pm} \equiv \Delta_1 \pm \Delta_2$ and phases $\phi_{\pm} \equiv \phi_1 \pm \phi_2$ by using the identity $\cos(A) \cos(B) = \frac{1}{2}[\cos(A+B) + \cos(A-B)]$. Using this identity the parity expectation value can be rewritten as

$$\langle \hat{\Pi} \rangle = \frac{1}{2} [\cos(\Delta_+ T_R + \phi_+) + \cos(\Delta_- T_R + \phi_-)]. \quad (3.11)$$

At probe durations long compared to the laser coherence time ($T_R \gg T_{\text{coherence}}$), the argument of the first term in Eq. (3.11) will be a random value for each measurement which will result in the first term averaging to zero over many measurements. However, the second term has arguments that depend on the differential frequency and phase, and because $\phi_{L,1}$, $\phi_{L,2}$, and ω_L are equivalent for both systems, these terms will cancel leaving just a differential phase measurement that is independent of the laser phase noise,

$$\langle \hat{\Pi} \rangle = \frac{1}{2} \cos((\omega_{0,1} - \omega_{0,2})T_R + (\phi_1 - \phi_2)). \quad (3.12)$$

While correlation spectroscopy can reduce the impact of laser phase noise, some decoherence mechanisms can still limit the probe times.

One of these mechanisms is decoherence of the atomic reference from spontaneous decay of the excited state. This process limits the achievable measurement stability by effectively reducing the contrast of the averaged parity fringe. The spontaneous decay rate is described by Γ and if a spontaneous decay event occurs during the Ramsey probe duration the second Ramsey $\pi/2$ -pulse places the atom in an equal superposition of up and down. This can be described in the parity measurement by instead using Eq. 3.4 with Eq. 3.9 and using $C(T_R) = e^{-\Gamma T_R}$ to describe the lifetime of the excited state. Using the trigonometric identity to simplify the equation in the same way results in

$$\langle \hat{\Pi} \rangle = \frac{1}{2} e^{-\Gamma T_R} \cos(\Delta_- T_R + \phi_-). \quad (3.13)$$

The fractional instability of a frequency ratio measurement when considering limits set by the lifetime of the excited clock state can be determined using a method similar to what was discussed in the previous section in Eq. 3.5. To do this we instead find the single shot measurement uncertainty for the parity measurement by taking Eq. 3.5 and replacing $\delta\omega_L \rightarrow \delta\Delta_-$ and $\langle\hat{\sigma}_z\rangle \rightarrow \langle\hat{\Pi}\rangle$, resulting in $\delta\Delta_- = \delta\langle\hat{\Pi}\rangle/|d\langle\hat{\Pi}\rangle/d\Delta_-|$. Solving this results in a single shot frequency uncertainty of

$$\delta\Delta_- = \frac{2}{T_R} \frac{\sqrt{1 - \frac{1}{4}e^{-2\Gamma T_R} \cos^2(\Delta_- T_R + \phi_-)}}{|e^{-\Gamma T_R} \sin(\Delta_- T_R + \phi_-)|}. \quad (3.14)$$

This single shot measurement uncertainty can be minimized by probing at the maximum slope points of the correlation parity fringe. This is done by choosing to probe at $\Delta_- T_R + \phi_- = \pm\pi/2$. Inserting this value into the equation and calculating the fractional measurement instability yields the differential measurement instability

$$\sigma_D(\tau) = \frac{2}{\omega_0 \sqrt{T_R \tau}} e^{\Gamma T_R}, \quad (3.15)$$

where we have used $\omega_{0,i} \approx \omega_0$. The optimum probe duration for minimum instability with correlation spectroscopy comparison is $T_{R,\text{opt}} = 1/(2\Gamma)$. For $^{27}\text{Al}^+$ this results in a best case fractional measurement instability of $\sigma_{D,\text{opt}}(\tau) = 1.5 \times 10^{-16}/\sqrt{\tau/s}$ with $\omega_0 = 2\pi \times 1.121 \times 10^{15}$ and $\Gamma = 1/(20.6 \text{ s})$.

It is also interesting to consider how the frequency difference between the two oscillators impacts the attainable parity fringe contrast. The case of a Gaussian phase noise distribution can be considered in the same way as Eq. 3.4. By inserting the result of Eq. 3.4 into Eq. 3.9 and simplifying in the same way as before we obtain

$$\langle\hat{\Pi}\rangle = \frac{1}{2} \left[e^{-\sigma_+^2/2} \cos(\omega_+ T_R + \phi_+) + e^{-\sigma_-^2/2} \cos(\omega_- T_R + \phi_-) \right]. \quad (3.16)$$

This equation does not consider the effect of the finite excited state lifetime. In this equation we define $\sigma_{\pm} = \sigma_0(\omega_{L1} \pm \omega_{L2})T_R$ which are the sum(difference) of the phase noise distribution for the two lasers and $R = \omega_{L2}/\omega_{L1}$ is the ratio of the oscillator frequencies. For clock comparisons with the same species, the frequency difference between the two oscillators is typically at radio

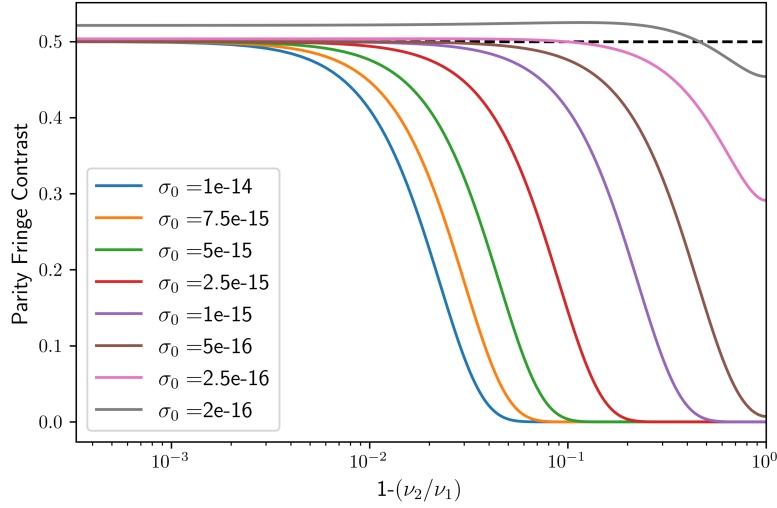


Figure 3.3: Dependence of the parity fringe contrast for correlation spectroscopy on $1 - (\nu_2/\nu_1)$ where ν_2/ν_1 is the frequency ratio R of the two oscillators and σ_0 is the fractional frequency noise floor of the laser where the laser noise is purely flicker. In this plot σ_0 is varied for each curve, but T_R is fixed at 1 s, and the resonance frequency of the higher frequency clock is 1 PHz. T_R can be thought of as a factor which scales the magnitude of σ_0 . For clocks with a large value of σ_0 maximum parity fringe contrast occurs when $\omega_1 \approx \omega_2$ but becomes less stringent as σ_0 is decreased.

frequencies and results in the condition $\sigma_-/\sigma_+ = \omega_{RF}/2\omega_L \ll 1$ which will result in Eq. 3.16 simplifying to Eq. 3.13 with $\Gamma = \infty$. However, in Fig. 3.3, a broader span of R is considered with different noise floor levels to illustrate what at what level of R correlation spectroscopy is still useful. The contrast in this plot approaches the maximum value $1/2$ as the laser noise becomes less significant. In these plots, the effect of T_R can be thought of as a factor scaling the value of σ_0 but real values are specified. Correlation spectroscopy is most useful when $R \approx 1$ but there may be cases or other considerations where this technique may still be useful to compare clocks at different frequencies. A possible future experiment which could use correlation spectroscopy to compare two different ion species is a comparison with $^{10}\text{B}^+$ and $^{27}\text{Al}^+$. The clock transition wavelength in $^{10}\text{B}^+$ is ≈ 277 nm [96] and when compared against $^{27}\text{Al}^+$, $R \approx .96$. Fig. 3.3 shows that the parity fringe contrast would be near unity for laser flicker noise floors of $\approx 2.5 \times 10^{-15}$. In the next section, the impact of differential atomic noise between the ions and its impact on correlation spectroscopy is discussed. Because correlation spectroscopy is based on a differential measurement of the laser

phase any differential phase noise will effectively scramble ϕ_- , which when averaged over many measurements will cause the fringe contrast to decrease. The two dominant sources of differential noise which we encounter in the experimental setup are differential magnetic field noise and path length noise which arise from air turbulence or variations in the refractive index of the fiber which connects the two systems.

3.3 Correlation spectroscopy experimental details

We demonstrate correlation spectroscopy between two separated atomic clocks, a $^{25}\text{Mg}^+ / ^{27}\text{Al}^+$ and a $^{40}\text{Ca}^+ / ^{27}\text{Al}^+$ quantum logic clock. Both of these atomic clocks utilize quantum logic spectroscopy to measure the state of the $^{27}\text{Al}^+$ ion following driving of the $^1S_0 \leftrightarrow ^3P_0$ clock transition. The primary difference between these two systems is the choice of qubit species used for sympathetic cooling and state readout [77]. The details of the $^{40}\text{Ca}^+ / ^{27}\text{Al}^+$ quantum logic clock are described in Chapter 2 while the $^{25}\text{Mg}^+ / ^{27}\text{Al}^+$ quantum logic clock uses hyperfine levels in the ground-state manifold of $^{25}\text{Mg}^+$ as a qubit for quantum logic spectroscopy. Further information about this setup can be found in Ref. [28]. During the correlation spectroscopy demonstration, the two atomic clocks were not operated in a high accuracy configuration. In what follows, we identify these two systems as $^{25}\text{Mg}^+ / ^{27}\text{Al}^+$ and $^{40}\text{Ca}^+ / ^{27}\text{Al}^+$, respectively.

Fig. 3.4 provides an overview of the setup which includes the two clocks that are on optical tables spaced roughly 3 m apart and the differential noise stabilization subsections used for phase noise compensation (PNC) and local magnetic field stabilization. All laser systems used for cooling and manipulation of the qubit ions are independent; however, the two systems share common lasers for the $^{27}\text{Al}^+$ transitions. The 267 nm laser light used to drive the $^1S_0 \leftrightarrow ^3P_0$ clock transition is generated on the $^{40}\text{Ca}^+ / ^{27}\text{Al}^+$ optical table and sent to the $^{25}\text{Mg}^+ / ^{27}\text{Al}^+$ table via a 6-m-long UV-cured photonic crystal fiber [97].

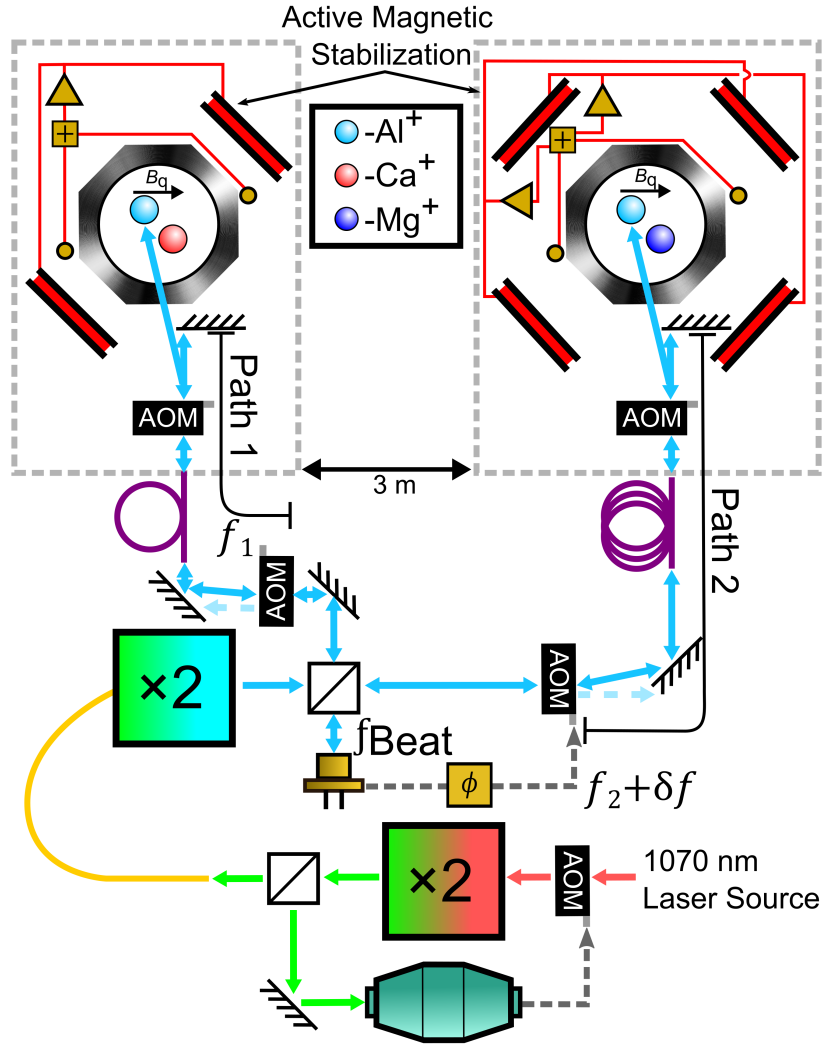


Figure 3.4: Schematic of the correlation spectroscopy experiment, including the laser path-length stabilization and active magnetic field stabilization setups. Here $f_{Beat} = 2(f_1 - f_2 - \delta f)$ is phase locked to a maser-referenced 10 MHz signal, and the relative phase is corrected by modulating the Path 2 AOM frequency, denoted by $f_2 + \delta f$. The magnetic field is stabilized using measurements from single-axis fluxgate sensors (shown as yellow circles) oriented along the quantization axis B_q . In the $^{25}Mg^+/^{27}Al^+$ clock two pairs of coils are used, while in the $^{40}Ca^+/^{27}Al^+$ system there is only one. Boxes labeled $\times 2$ denote frequency doubling of the input light where the final light sent to the atomic clocks is at 267.4 nm.

3.3.1 Differential phase noise stabilization

Using the same laser source for the two clocks allows for precise control of the differential phase in the probe pulses by active suppression of Doppler-noise in the optical fibers and free-space

optical paths [79, 80], although two independent laser systems could be used with the addition of a phase stabilization link through a frequency comb or via an interferometer. A diagram of the path-length stabilization setup is given in Fig. 3.4, where the total optical path length between the two ions is ≈ 10 m. The zeroth-order of the switch AOMs used to deflect light toward the ion is retro-reflected close to where the light enters each vacuum systems. This retro-reflected light forms a beatnote at a beamsplitter close to the UV frequency doubler which is used to measure the relative phase between the two paths. The relative phase noise in this beatnote is measured using a 400 MHz bandwidth avalanche photodiode and is stabilized by controlling an acousto-optic modulator (AOM) frequency in the $^{25}\text{Mg}^+ / ^{27}\text{Al}^+$ path. The $^{40}\text{Ca}^+ / ^{27}\text{Al}^+$ serves as the reference arm for the path length stabilization since it is the shorter distance of the two paths between the doubler and ions. In out-of-loop measurements using a test setup discussed in Chapter 2 that is comparable to the setup in Fig. 3.4, differential phase fluctuations below $\pi/20$ at Ramsey probe durations as long as 12 s are observed which is well below the invertable range of Ramsey fringes. This residual noise is likely limited by the short, out-of-loop, open-air paths such as those before the ion traps. When running the experiment, a frequency counter monitors the in-loop beat-note to check for cycle slips in the phase-lock loop.

3.3.2 Differential magnetic field noise minimization

Another effect that can limit the atom-atom coherence of the two systems is fluctuations of the local magnetic fields. To minimize the corresponding Zeeman shifts in each clock, we servo the magnetic field based on measurements with multiple fluxgate magnetometers placed close to the vacuum chamber and oriented along the clock quantization axis. A linear combination of these measurements is used to estimate the magnetic field at the ion and corrections are made using a set of Helmholtz coils mounted around each optical table. Using active stabilization, we reduce the magnetic field noise amplitude to below $20 \mu\text{G}$ for averaging times as long as 10^3 s as seen in Fig 3.5.

Both the 1S_0 and 3P_0 states in $^{27}\text{Al}^+$ have a total angular momentum quantum number

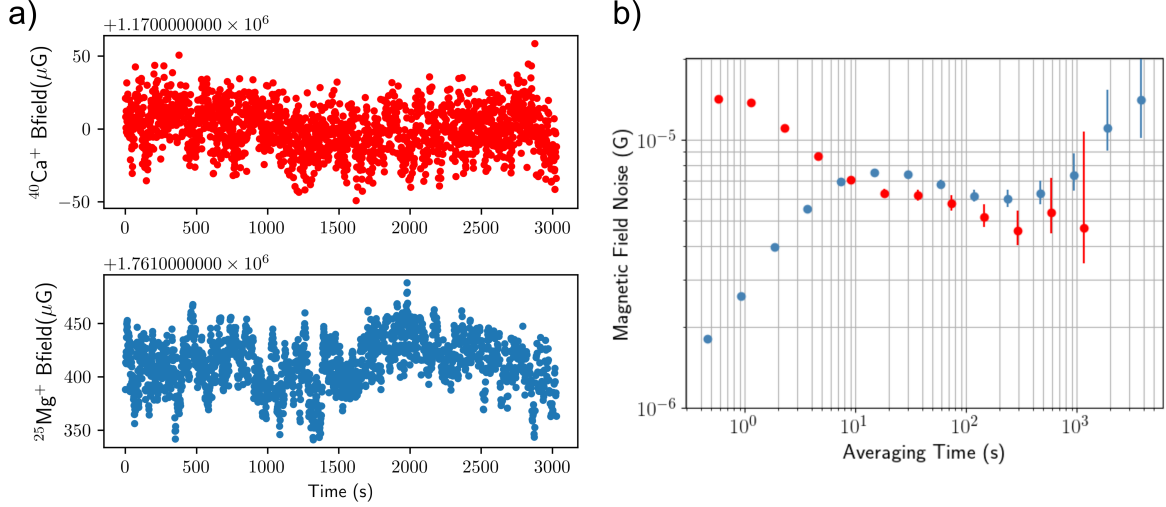


Figure 3.5: a) Time series of measurements of the magnetic fields local to the two systems taken at the same time. This provides representative magnetic field noise data which can be used to accurately model the effect of differential magnetic field noise in our systems. b) Allan deviation of the measured magnetic field amplitude along the quantization axis, simultaneously sampled in the $^{25}\text{Mg}^+ / ^{27}\text{Al}^+$ system (red) and in the $^{40}\text{Ca}^+ / ^{27}\text{Al}^+$ system (blue).

$F = 5/2$ due to the nuclear spin. Initial correlation spectroscopy experiments were performed on the $|^1S_0, m_F = 5/2\rangle \leftrightarrow |^3P_0, m_F = 5/2\rangle$ transition, which has a sensitivity to magnetic fields of -4.2 kHz/G ($1 \text{ G} = 10^{-4} \text{ T}$). When using this transition for correlation spectroscopy an optimum measurement instability is found at $\approx 2 \text{ s}$. Measurements of the stabilized magnetic field noise local to the two vacuum systems seen in Fig 3.5 were then performed to determine if residual magnetic field noise was still limiting the probe duration when using this transition. By using this data in a numerical simulation of the parity measurement the effect of the magnetic field noise on the parity amplitude can be determined.

Representative magnetic field noise is obtained for the two systems by making an in-situ measurement with the logic ions in the two systems. In the $^{25}\text{Mg}^+$ system we lock a frequency-doubled DDS source to the $|^2S_{1/2}, F = 3, m_F = 3\rangle \leftrightarrow |^2S_{1/2}, F = 2, m_F = 2\rangle$ microwave transition that has a sensitivity to magnetic fields of 2.3 MHz/G and monitor the drift in the frequency to infer the change in the magnetic field as a function of time. In the $^{40}\text{Ca}^+$ system we use Ramsey spectroscopy on a superposition of the $|^2D_{5/2}, m_F = -5/2\rangle$ and $|^2D_{5/2}, m_F = 3/2\rangle$ Zeeman states,

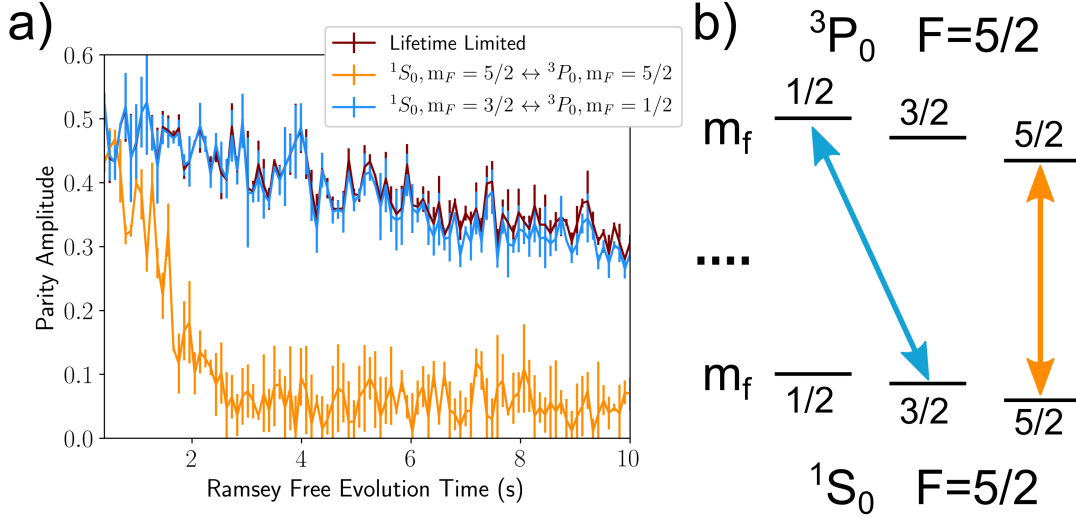


Figure 3.6: Simulated parity amplitude vs. Ramsey free evolution time using random laser phase noise and the measured differential magnetic field noise and simplified level diagram. a) Here, the red trend neglects the effects of the differential magnetic field noise and only takes into account the lifetime limit of the excited state, while the dark orange and light blue includes differential magnetic phase noise determined using the magnetic field sensitivities of the $|^1S_0, m_F = 5/2\rangle \leftrightarrow |^3P_0, m_F = 5/2\rangle$ and $|^1S_0, m_F = 3/2\rangle \leftrightarrow |^3P_0, m_F = 1/2\rangle$ transitions, respectively. When probing the $|^1S_0, m_F = 3/2\rangle \leftrightarrow |^3P_0, m_F = 1/2\rangle$ transition we expect to measure a parity amplitude consistent with the parity amplitude due to the lifetime limit. b) Half of the clock manifold for $^{27}\text{Al}^+$ is shown, where the two transitions used in these experiments are depicted. The two transitions are the $|^1S_0, m_F = 5/2\rangle \leftrightarrow |^3P_0, m_F = 5/2\rangle$ which was initially used for experiments and $|^1S_0, m_F = 3/2\rangle \leftrightarrow |^3P_0, m_F = 1/2\rangle$ which is used to minimize the impact of differential magnetic field noise in correlation spectroscopy measurements.

discussed in Chapter 2, to increase the sensitivity of the magnetic field measurement and reduce the impact of laser frequency noise on the measurement. Using this choice of Zeeman states a sensitivity to magnetic fields of 6.72 MHz/G is obtained. This superposition state is generated by first driving a $\pi/2$ -pulse on the $|^2S_{1/2}, m_F = -1/2\rangle \rightarrow |^2D_{5/2}, m_F = -5/2\rangle$ transition, then driving a π -pulse on the $|^2S_{1/2}, m_F = -1/2\rangle \rightarrow |^2D_{5/2}, m_F = 3/2\rangle$ transition. By locking the phase of the second $\pi/2$ -pulse to the peak of the Ramsey fringe we can track changes in the magnetic field by converting the determined phase correction into a magnetic field. With this data the effect of magnetic field noise on the correlation spectroscopy measurements can be estimated.

The effect of differential first order Zeeman shifts are modeled between the ground and excited

state of the clock transition due to magnetic field noise using

$$\Delta f_{\text{Al}}(B) = \mu_{\text{B}} B (g_{\text{P}} m_F(^3P_0) - g_{\text{S}} m_F(^1S_0)), \quad (3.17)$$

where $g_{\text{P}} = -0.00197686(21)$, $g_{\text{S}} = -0.00079248(14)$, μ_{B} is the Bohr magneton, and B is the instantaneous applied magnetic field [98]. To simulate the parity fringes we begin with the single atom $\hat{\sigma}_{z,i}$ observable where $\langle \hat{\sigma}_{z,i} \rangle = \langle \cos(\phi_{\text{L}} - \phi_{\text{diff},i} - \phi_i) \rangle$ and i labels which atomic clock is being measured. In this equation, ϕ_{L} is the laser phase noise common to both systems, $\phi_{\text{diff},i}$ is the differential phase noise present in system i , and ϕ_i is used to scan the phase in one system and held constant in another to scan the relative phase between the two systems. The probe time is assumed to be much longer than the laser coherence time such that the laser phase can be modeled as a uniformly-distributed random number on the interval $\phi_{\text{L}} \in [0, 2\pi)$. The time series of the measured magnetic fields of the two systems is converted into a phase shift, which is inserted into the model as $\phi_{\text{diff},i}$. The simulated $\langle \hat{\sigma}_{z,i} \rangle$ time series for each system is then used to determine the parity $\langle \hat{\Pi} \rangle = \langle \hat{\sigma}_{z,1} \rangle \langle \hat{\sigma}_{z,2} \rangle$ which is averaged for each value of $(\phi_1 - \phi_2)$ and a fringe is fit to extract the contrast. Because the phase noise grows with T_{R} the effect of this measured magnetic field noise becomes more significant at longer Ramsey free evolution times as seen in Fig. 3.6. This simulation suggests that switching to interrogating the inner manifold transition ($|^1S_0, m_F = 3/2\rangle \leftrightarrow |^3P_0, m_F = 1/2\rangle$) is necessary to achieve lifetime limited contrast of the parity fringe. Preparing the state of the $^{27}\text{Al}^+$ ion to be in an inner manifold ground-state is accomplished using the π -polarized state preparation techniques outlined in Chapter 2. This transition has a sensitivity to magnetic fields of 0.28 kHz/G, a factor of ≈ 15 reduction in sensitivity compared to the typical clock transition.

3.3.3 Experimental sequence

When running the experimental sequence, synchronization between the two experimental control systems is achieved in a transmit/receive configuration. The $^{25}\text{Mg}^+ / ^{27}\text{Al}^+$ system takes the role of the transmitter and supplies the $^{40}\text{Ca}^+ / ^{27}\text{Al}^+$ system with triggering pulses; the exper-

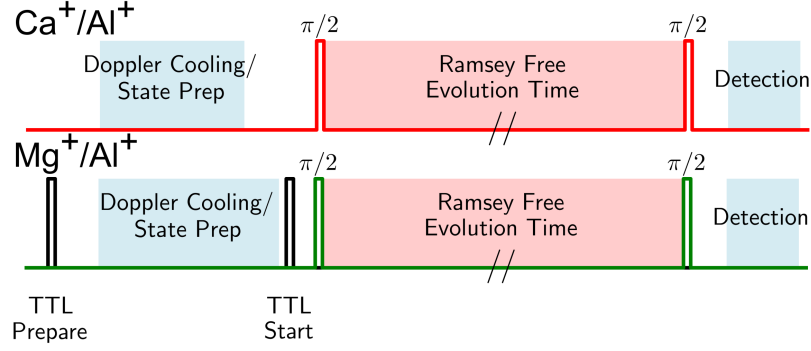


Figure 3.7: A simplified timing diagram of the experimental pulse sequence. These clocks are synchronized with a transmit/receive configuration where one clock transmits the timing pulses and the other receives and reacts accordingly. Time is properly allocated to allow for sufficient cooling, state preparation, and state detection.

Experimental sequence can be seen in Fig. 3.7(b). The sequence is as follows:

- (1) To begin the experiment, the $^{25}\text{Mg}^+ / ^{27}\text{Al}^+$ system sends a “prepare” TTL pulse to the $^{40}\text{Ca}^+ / ^{27}\text{Al}^+$ system, which initiates the laser cooling and state preparation sequences required before interrogating the clock transition.
- (2) The $^{40}\text{Ca}^+ / ^{27}\text{Al}^+$ system (which requires less time for preparation) then waits for a “start” TTL indicating that the $^{25}\text{Mg}^+ / ^{27}\text{Al}^+$ system is finished with its cooling and state preparation.
- (3) After the “start” TTL each clock waits for a (different) predefined time, which is used to manually account for a constant communication lag between the two systems.
- (4) Subsequently, the two systems drive the first of the two $\pi/2$ Ramsey pulses on the corresponding atomic clocks.
- (5) The clocks’ states evolve for the Ramsey period T_R , with continuous sympathetic Doppler cooling applied to the qubit ion [98].
- (6) Following the Ramsey probe duration the second $\pi/2$ pulse is applied to each clock.

- (7) The relative phase of the second $\pi/2$ pulse between the two systems is adjusted to scan over the parity fringe in many iterations of this sequence.
- (8) Finally, the state of the atom is measured using quantum-logic-based readout and recorded for post-processing calculations of the parity.

During a measurement run, we use the measurement outcome of the previous experimental cycle as projective state preparation for the next such that $|\downarrow\rangle$ can be either the 1S_0 or 3P_0 state. Parity measurements are made by observing if a transition in each ion state has occurred since the previous interrogation. A parity of +1 corresponds to both atoms making a transition or both not making a transition, whereas a parity of -1 corresponds to only one of the two ions making a transition. To generate the parity fringes seen in Fig. 3.8 and Fig. 3.9, the $^{40}\text{Ca}^+ / ^{27}\text{Al}^+$ clock is interrogated with a constant Ramsey phase ϕ_1 , while the $^{25}\text{Mg}^+ / ^{27}\text{Al}^+$ clock scans its phase ϕ_2 relative to the $^{40}\text{Ca}^+ / ^{27}\text{Al}^+$ clock. By scanning the relative phase between the two systems' second $\pi/2$ -pulses, ϕ_- can be scanned allowing the coherence between the two systems to be observed. Each point on the correlation spectroscopy fringe is probed $\gtrsim 50$ times to average down the quantum projection noise.

3.4 Experimental Results

In these parity phase scans, we observe atom-atom coherence well beyond the coherence time of the laser (460 ± 30 ms), which is shown in Fig. 3.1. Periodic interruptions, from ion loss and other effects, are filtered from the data in post processing and in real time. Data that is flagged in real time consists of collision events and missed experiment triggers. An added benefit of Doppler cooling over the interrogation period is that background gas collision events can be observed as either a loss in fluorescence from the cooling ion or as a change in the order of the two ions [55]. Both of these signals are continuously monitored and collision events are filtered by removing the data point coincident with the event and the one immediately preceding. The total percentage of useful data was as small as 24% for short T_R and as large as 71% for longer T_R . At short

probe durations the loss of data is primarily a result of timing synchronization errors. Timing jitters can be minimized by using one control computer as an NTP time server for the other so the polling computer will follow the server as it drifts and data points can be matched by using time windowing to match the timestamps. Large jitters push the timestamps outside of this relative time window but for a percentage of the data the timestamps can be matched properly. Filtering the data in this way significantly reduces the mean duty-cycle for probing the clock transitions, but improves the contrast of the parity signal. For long interrogations, events filtered in post processing are primarily formation of an an $\text{Al} - \text{H}^+$ molecule or excitations of the $^{27}\text{Al}^+$ -ion to a different metastable state which could be either a different Zeeman level of the 3P_0 manifold or excitation to the 3P_2 excited state. Hydride formation events can only occur when $^{27}\text{Al}^+$ is in its 3P_0 excited state and a H_2 molecule collides with energy greater than the reaction barrier needed to form $\text{Al} - \text{H}^+$. Collision events can also result in the ion being excited to a metastable internal state that is not addressable by any of the experimental pulses. The likely metastable states for $^{27}\text{Al}^+$ are $|^3P_2\rangle$ ($\tau = 298.5$ s) and any Zeeman sublevel of $|^3P_0\rangle$ not addressed by the clock probe. Both of these types of collision events are filtered in post processing by checking for long measurement periods where no transitions are detected on one of the clocks. In future experiments the data loss due to background gas collisions can be reduced by reducing the background pressure. The collision rate is proportional to the vacuum pressure so by reducing the vacuum pressure by an order of magnitude the data loss due to collision events can be reduced below 10%.

After filtering the data for errors, the data accumulated from multiple runs spanning a total measurement duration as long as 4 hours can be averaged resulting in the fringes shown in Figs. 3.8 and 3.9. The fringe contrast thus represents all atom-atom decoherence mechanisms that act on timescales of seconds as well as long-term frequency drifts that act on timescales of hours. To maintain the laser frequency near resonance for the Ramsey $\pi/2$ pulses between these runs, common-mode adjustments to the laser frequency were made as feed forward correction to the laser offset frequency. Fits of the function $\langle \hat{\Pi}(\phi_2) \rangle = C \cos(\phi_2 - \phi_0)$ to the parity data in Fig. 3.9 and Fig. 3.8 are used to extract the contrast C , phase ϕ_0 , and their associated uncertainties. The uncertainties

Data Filtering			
Ramsey Evo. Time (s)	Free	Total # of meas.	% data used
0.5		2224	24
1.0		1035	71
1.5		1317	50
2.0		944	42
3.0		706	66
4.0		1040	63
6.0		594	44
8.0		791	43

Table 3.1: Number of measurements taken at each Ramsey free evolution time for experiments performed with the $|^1S_0, m_F = 3/2\rangle \leftrightarrow |^3P_0, m_F = 1/2\rangle$ transition and the percent of data remaining following filtering. Total # of meas. is the total length of the data array before filtering and % data used is the data remaining following filtering for data affected by collisions and asynchronous probes. At short probe durations the loss of data is primarily a result of timing synchronization errors.

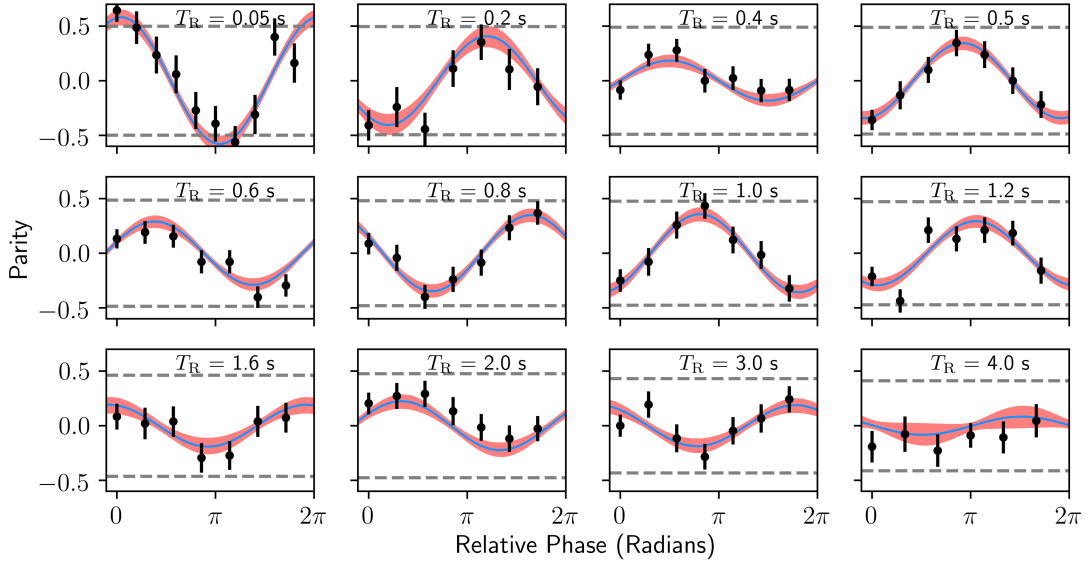


Figure 3.8: Parity fringes obtained for Ramsey probe durations between 0.05 s and 4 s (upper right labels). Here, the transition used for correlation spectroscopy is the $|^1S_0, m_F = 5/2\rangle \leftrightarrow |^3P_0, m_F = 5/2\rangle$ transition. Experimental data (black dots) are shown with error bars dominated by quantum projection noise. Fits to these parity fringes (blue lines) and their 1σ confidence intervals (red shading) are determined by re-sampling the data using non-parametric bootstrapping methods. The maximum obtainable parity amplitude (gray dashed lines) due to the finite lifetime of the two $^{27}\text{Al}^+$ ions is calculated using Eq. (3.13).

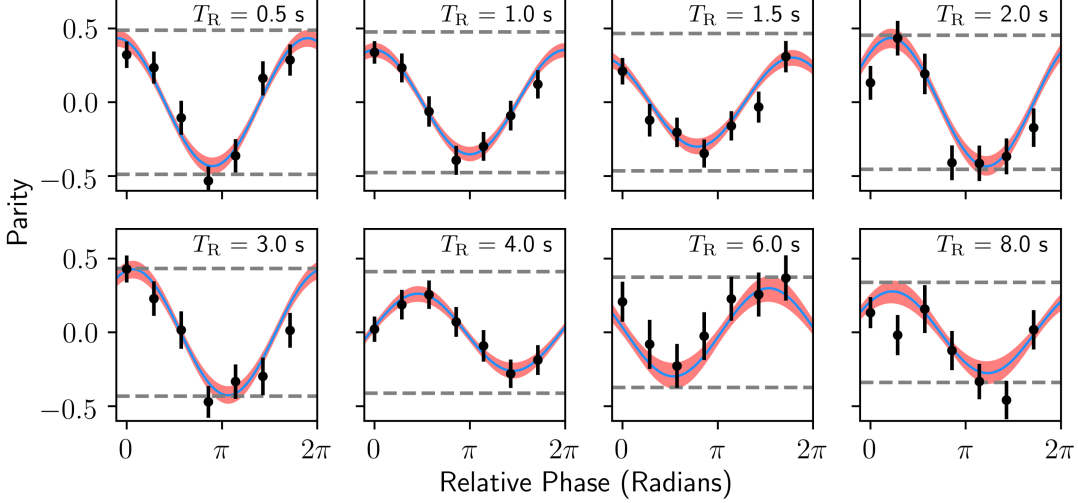


Figure 3.9: Parity fringes obtained for Ramsey probe durations between 0.5 s and 8 s (upper right labels). Here, the transition used for correlation spectroscopy is the $|^1S_0, m_F = 3/2\rangle \leftrightarrow |^3P_0, m_F = 1/2\rangle$ transition. Experimental data (black dots) are shown with error bars dominated by quantum projection noise. Fits to these parity fringes (blue lines) and their 1σ confidence intervals (red shading) are determined by re-sampling the data using non-parametric bootstrapping methods. The maximum obtainable parity amplitude (gray dashed lines) due to the finite lifetime of the two $^{27}\text{Al}^+$ ions is calculated using Eq. (3.13).

are obtained by a bootstrapping method which resamples the experimentally determined binomial distributions [99]. A plot of the measured contrast as a function of the Ramsey probe duration can be seen in Fig. 3.10, showing data taken on the less magnetically sensitive $|^1S_0, m_F = 3/2\rangle \leftrightarrow |^3P_0, m_F = 1/2\rangle$ transition as well as initial data taken on the $|^1S_0, m_F = 5/2\rangle \leftrightarrow |^3P_0, m_F = 5/2\rangle$ transition. The noise suppression due to the magnetic field servo is comparable in both of these data sets and the improvement in the contrast is due to the reduced magnetic sensitivity of the $|^1S_0, m_F = 3/2\rangle \leftrightarrow |^3P_0, m_F = 1/2\rangle$ transition. The decay time of the contrast for experiments on the $|^1S_0, m_F = 3/2\rangle \leftrightarrow |^3P_0, m_F = 1/2\rangle$ transition is measured to be $t_d = 19 \pm 11$ s. This value is much longer than the measured laser coherence time of 460 ± 30 ms and is consistent with the decay time of 20.6 s expected due to the finite excited-state lifetime. However, we observe a 20(8)% reduction in the contrast from the ideal value of 0.5 set by Eq. (3.13). We attribute this primarily to errors in the $^{27}\text{Al}^+$ state preparation and π -pulse infidelity when driving the clock transition. Experimental optimization of the state preparation sequence using Rabi spectroscopy results in

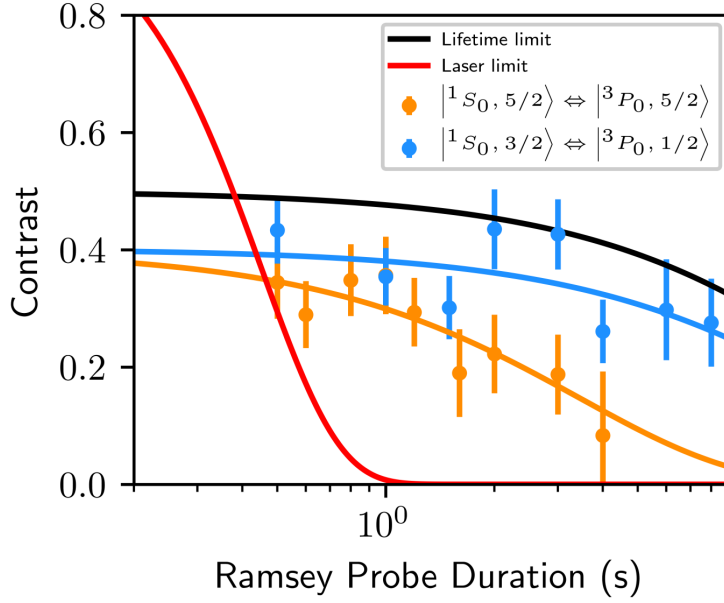


Figure 3.10: Contrast as a function of the probe duration. The measured contrast (solid points) and associated uncertainty come from fits to the parity fringes. For comparison, a fit to the laser-coherence-limited Ramsey spectroscopy contrast (red line) and the calculated upper bound on the correlation spectroscopy contrast set by the lifetime limit (black line) are plotted. A fit to the experimental points using the model function $A \exp^{-T_R/t_d}$ is determined, where A is the contrast and t_d is the decay time. Fitting with this function gives $A = 0.4 \pm 0.04$ and $t_d = 19 \pm 11$ s for $|^1S_0, m_F = 3/2\rangle \leftrightarrow |^3P_0, m_F = 1/2\rangle$ and $A = 0.4 \pm 0.06$ and $t_d = 4 \pm 2$ s for $|^1S_0, m_F = 5/2\rangle \leftrightarrow |^3P_0, m_F = 5/2\rangle$.

5%–10% state preparation infidelity in a single system and we observe $\approx 5\%$ π -pulse infidelity. This results in a 10% – 15% reduction in the maximum achievable contrast when performing correlation spectroscopy on two clocks. One possible cause for the reduction in parity fringe contrast in longer datasets (e.g. 4 s) is long term drifts in the 3P_1 laser frequency. The contrast of the fringes can be used to estimate the measurement instability for correlation spectroscopy comparisons between the two clocks [85], using

$$\sigma_{est} = \frac{1}{\omega_0 C(T_R) \sqrt{T_R}}. \quad (3.18)$$

The contrast of all of the parity measurements are displayed in Fig. 3.10 where trends for the lifetime limit and the contrast considering laser phase noise are plotted. From the measured contrasts the

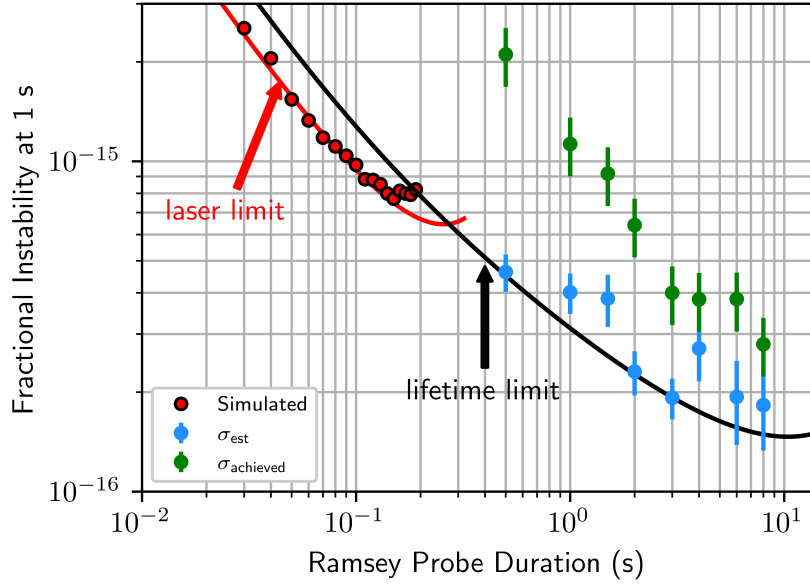


Figure 3.11: Comparison of the instability calculations and measurements as a function of probe duration. The instability σ_{upper} , calculated using Eq. (3.19), is shown with green dots. This can be compared with the instability σ_{est} determined with Eq. (3.18) shown with blue dots. A lower bound on the instability is given by the lifetime limit (black line, Eq. (3.15)), which assumes a randomized laser phase at all probe durations. Also included is an estimate of the instability at the laser-noise limit both from the analytical estimate (red line, Eq. (3.7)) and a numerical simulation (red points) assuming a flicker frequency noise floor at $4.4 \times 10^{-16} \sqrt{\tau/s}$. Numerical simulations stop at a probe duration of ≈ 200 ms due to fringe hops occurring in our numerical simulation. For all theoretical estimates we assume a dead time of only 0.1 s (the average single-cycle dead time of our clocks), which has negligible impact at longer probe durations.

instability is as low as $\sigma_{\text{est}} = (1.8 \pm 0.5) \times 10^{-16} / \sqrt{\tau/s}$ at $T_R = 8$ s, and corresponds to the achievable instability given the observed contrast if there is no dead time in the measurement and all probes were made at the relative phases where the parity slope is the highest. In our experiment, for the longer probe durations, we have negligible overhead due to state preparation and measurement, but suffer from frequent interruptions due to collisions with background gas. An upper estimate of the achievable measurement instability assumes a total averaging time τ_{tot} including all dead time during the measurement runs, and the phase uncertainty σ_ϕ determined from the fit of the parity

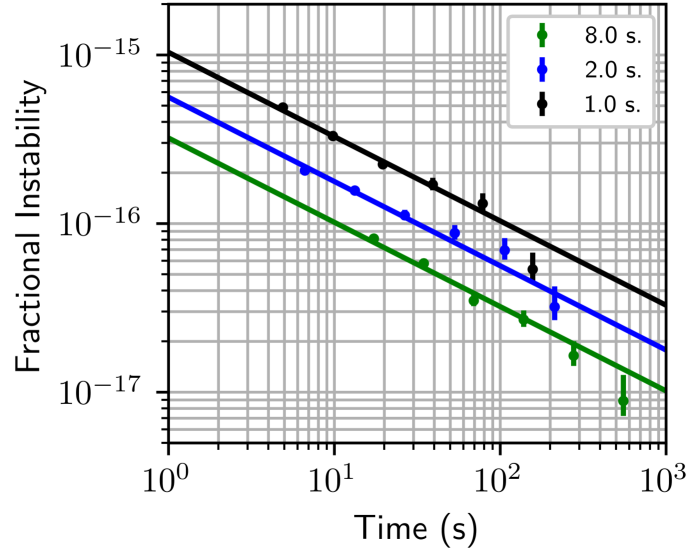


Figure 3.12: Allan Deviation of the correlation spectroscopy frequency ratio measurement at Ramsey precession times of 1, 2, and 8 s. The instabilities extrapolated to a 1 s averaging time are $1.04(3) \times 10^{-15} \sqrt{\tau/s}$, $5.61(19) \times 10^{-16} \sqrt{\tau/s}$, and $3.21(12) \times 10^{-16} \sqrt{\tau/s}$ respectively. These values match closely to the corresponding green points in Fig. 3.11 which are derived from sinusoidal fits to the same data.

fringe,

$$\sigma_{\text{upper}} = \frac{\sigma_{\phi} \sqrt{T_{\text{tot}}}}{T_{\text{R}} \omega_0}. \quad (3.19)$$

This equation is used to determine the measurement instabilities of the green dots plotted in Fig 3.11 which reach as low as $(2.8 \pm 0.6) \times 10^{-16} / \sqrt{\tau/s}$ for $T_{\text{R}} = 8$ s. Alternatively, an Allan deviation can be obtained from this data by converting the parity time series into an error signal. This data is plotted in Fig 3.12 which results in instabilities comparable to those obtained for the instability calculation which includes measurement deadtime. Using correlation spectroscopy between two ions held in separate traps we have demonstrated atomic coherence at probe durations as long as 8 s. The contrast $1/e$ decay time of $t_{\text{d}} = 19 \pm 11$ s is consistent with the 20.6 s excited state lifetime and with this atom-atom coherence ratio measurement instability below $2.8 \times 10^{-16} / \sqrt{\tau/s}$ for averaging times $\tau \gg T_{\text{R}}$ can be reached [56]. With this stability it is possible to compare these separated atomic clocks with a fractional statistical uncertainty of 1×10^{-18} in a single day of

averaging.

Chapter 4

Differential Spectroscopy

Differential spectroscopy is another differential comparison technique that enables probes times beyond the laser coherence time for one or both clocks and therefore allows faster frequency comparisons between atomic clocks. In contrast to correlation spectroscopy, however, the two clocks can operate at vastly different frequencies. Differential spectroscopy allows for interrogation between different species beyond the laser coherence limit but requires that one of the atomic clocks in the frequency comparison must have a single shot measurement uncertainty that is accurate enough to estimate of the variation of the laser phase over the interrogation period. This technique was first proposed in Ref. [100] which details how this method can be implemented between a high-stability and a low-stability clock or between two high stability clocks. For the case of a comparison between two high stability atomic clocks i.e. optical lattice clocks, the measurement instability of the two clocks can be reduced by performing a simultaneous Ramsey interrogation where a maximum likelihood analysis is use to unambiguously determine the evolved laser phase based on the independent measurements of the two atomic clocks. However, in this thesis we focus on differential spectroscopy between a single-ion optical clock and an optical lattice clock. In this procedure a simultaneous Ramsey interrogation is performed between a lower frequency optical lattice clock and a higher frequency ion clock which is based on a single spectroscopy ion. The phase measurement attained by the lower frequency optical lattice clock can be used to narrow the laser phase noise distribution of the higher frequency laser to the quantum projection noise level of the lattice clock, allowing the interrogation period to be extended to the period used for the

lower frequency clock. We also demonstrate an extension of this technique which makes use of a zero deadtime interrogation sequence with two high-stability optical lattice clocks to further extend the interrogation period. Results of this work were published in Ref. [57], where further details on specifics of the ^{171}Yb system can be found.

4.1 Theoretical Discussion

During a typical Ramsey interrogation period the phase of the local oscillator will wander with a behavior dependent on the spectrum of noise. If the free evolution period is within the laser coherence time, the phase of the local oscillator will remain in the invertible region of the Ramsey fringe. This means that evolved laser phase can be unambiguously determined and used as an error signal to correct the local oscillator phase. This method for stabilizing the local oscillator to the atomic reference is the typical Ramsey method of interrogation. The phase evolution over the Ramsey free evolution period can be described by [100]

$$\Delta\phi_i = \int_0^T [\omega_0 - \omega_{L,i}(t)]dt = (\omega_0 - \bar{\omega}_{L,i})T, \quad (4.1)$$

where $\bar{\omega}_{L,i}$ is the mean frequency of laser i over the probe duration T and ω_0 is the atomic reference frequency. Over the interrogation period the laser must remain within the range of $[-\pi/2, \pi/2]$ for the laser to remain locked to the atomic reference, which will be referred to as the invertible range. If the Ramsey interrogation period is longer than the coherence time of the local oscillator then the phase excursion of the local oscillator will have some probability of being outside the invertible range. Incorrect phase determination can cause the phase corrections to move the laser phase further away from the central Ramsey fringe causing the laser to un-lock from the atomic frequency reference. The basic idea behind differential spectroscopy is that if the phase can be unwrapped when it has wandered outside of the invertible range then the lock to the central Ramsey fringe can continue beyond the typical laser coherence time. To perform differential spectroscopy between a high-stability clock and a low-stability clock, the high-stability clock needs to be based on an oscillator which has a frequency lower than the low-stability clock. The other requirement is that

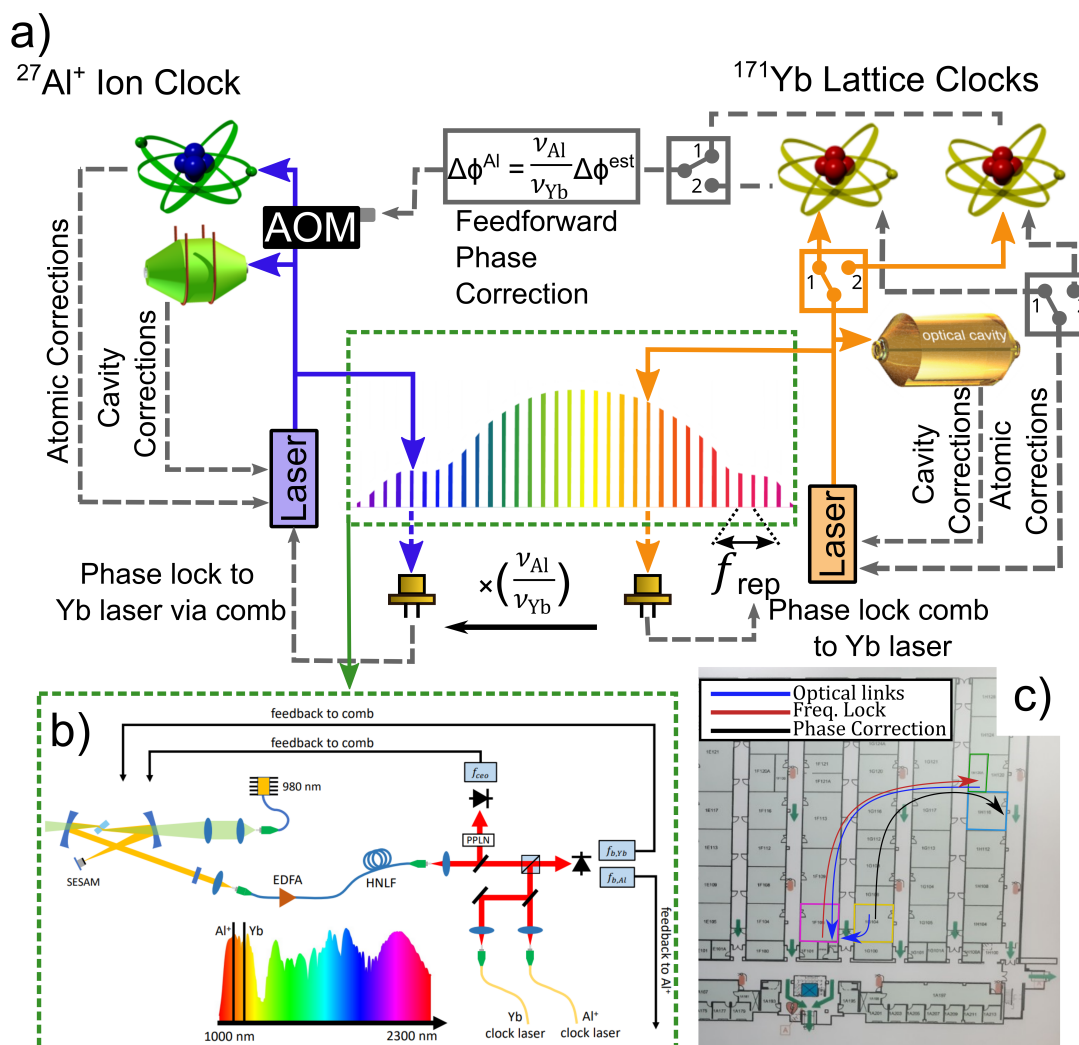


Figure 4.1: a) Overview of the experimental setup used for simple differential spectroscopy and ZDT differential spectroscopy. For both setups the laser systems are stabilized to an optical cavity. In the ^{171}Yb setup this laser is used to interrogate an optical lattice clock or two clocks for the case of ZDT differential spectroscopy. Following these interrogation(s) a phase correction(s) is fedforward and frequency corrections to the local oscillator are applied. a,b) A frequency comb provides a link between the two local oscillators and multiplies the ^{171}Yb local oscillator frequency up to a frequency near the $^{27}\text{Al}^+$ transition frequency. An interferometric measurement between the frequency comb and the $^{27}\text{Al}^+$ laser is then used to lock the $^{27}\text{Al}^+$ laser to the ^{171}Yb laser. Grey lines represent frequency feedback from clocks 1 and 2 as well as phase corrections applied to the $^{27}\text{Al}^+$ system from clocks 1 and 2. b) A more detailed schematic of the Er/Yb-doped glass femtosecond optical frequency comb. This setup further details how the beatnotes are generated between the different lasers. c) Map of NIST building 81 depicting the distances and connections between the labs involved. In this picture the magenta box is the frequency comb lab, the yellow box is the ^{171}Yb clock lab, the green box is the $^{27}\text{Al}^+$ cavity lab, the blue box is the $^{27}\text{Al}^+$ clock lab. The type of connections between the labs are detailed in the figure.

the local oscillators have correlated phase noise which is achieved via a phase lock of the lower frequency oscillator to the higher frequency oscillator through a frequency comb. The reason for this is that the high stability clock will provide a coherent measurement of the evolved phase of both oscillators because the phase evolution scales with the oscillator frequency. A Gaussian phase noise distribution is described by the equation

$$P(\phi_i) = \frac{1}{\sigma_{\phi_i} \sqrt{2\pi}} e^{-\phi_i^2 / 2\sigma_{\phi_i}^2}. \quad (4.2)$$

with the standard deviation of the phase noise distribution $\sigma_{\phi_i} = \sigma_0 \omega_i T_R$ at the specific oscillator frequency ω_i . From this we can see that if both oscillators share the same fractional noise standard deviation σ_0 then the phase noise variance for the lower frequency local oscillator (ω_1) will be a factor of $R = \omega_2 / \omega_1$ smaller than the phase noise distribution of the higher frequency local oscillator ω_2 . In Fig. 4.2(a) the correlated phase wander for the two local oscillators can be seen and Fig. 4.2(b) shows the phase noise distribution for the $^{27}\text{Al}^+$ and ^{171}Yb lasers assuming that they have the same fractional noise. Since the laser phase wanders proportionally for the two lasers a measurement of the evolved laser phase noise with the higher stability atomic clock can be used to determine the phase evolution of the higher frequency laser. To take advantage of this correlated phase wander, the clocks can be operated in a synchronized Ramsey interrogation method. The ^{171}Yb atomic clock would operate with a shorter Ramsey free evolution period to allow time for it to make a measurement of the evolved laser phase before the $^{27}\text{Al}^+$ system is measured. This measured laser phase is then sent to the other system where it can be fed-forward to the higher frequency laser as a phase correction. The $^{27}\text{Al}^+$ atomic clock can use this measurement of the evolved laser phase scaled by R to correct the phase error of the higher frequency atomic clock. Following the correction, these lasers now have the same fractional noise so the higher frequency atomic clock can operate with a interrogation period that is a factor of R larger than the previously attainable probe duration of this system and reduces the measurement instability by a factor of \sqrt{R} . With this improvement it now becomes possible to compare the two atomic clocks at a higher precision in less time. Also, this technique varies from correlation spectroscopy in its ability to still allow

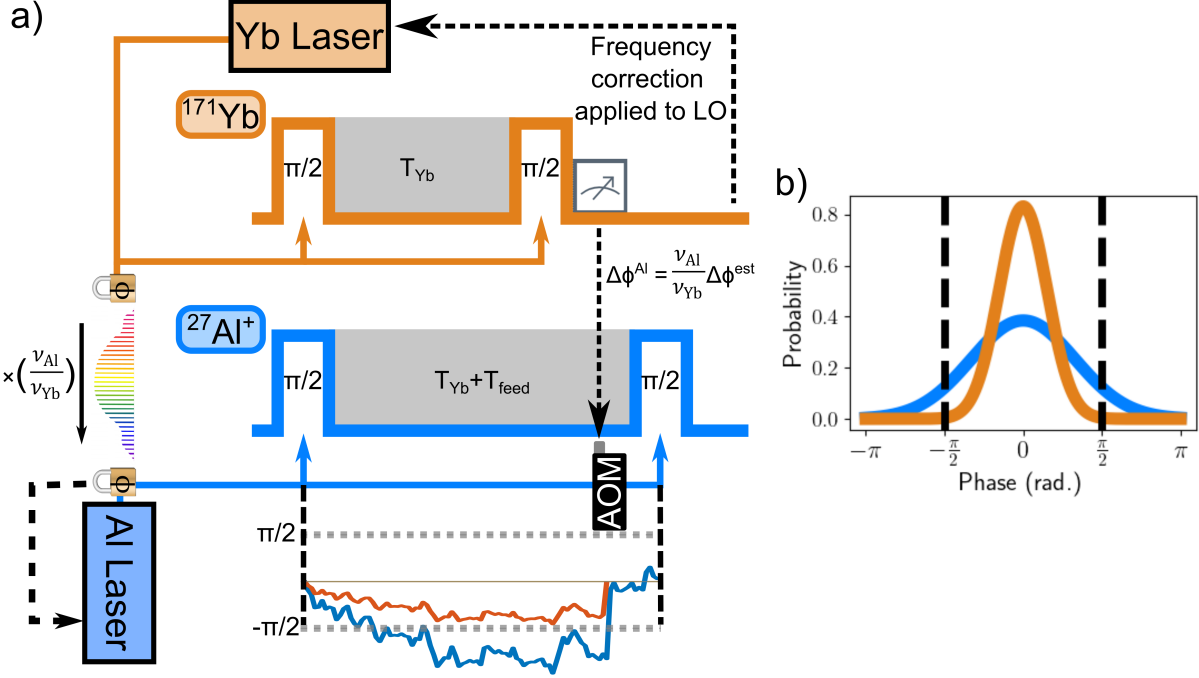


Figure 4.2: a) Pulse sequence for basic differential spectroscopy. The $\pi/2$ -pulses in Ramsey spectroscopy are depicted by the orange (blue) square pulses for the ^{171}Yb ($^{27}\text{Al}^+$) clock. The grey shaded regions represent the Ramsey free-evolution periods. The two clocks start their interrogation at the same time, after which the relative phase between the OLO and the atoms evolves for the two clocks. After the ^{171}Yb clock makes a measurement of the atom-laser phase, the phase information is fed forward to the $^{27}\text{Al}^+$ clock so that it can complete the interrogation on the ion with the phase corrected by the ^{171}Yb clock. An example of the phase wander over the interrogation period and following the phase feedforward is depicted. b) Example phase noise distribution scaling from Eq. 4.2 for the two clocks is shown with $\sigma_0 = 1 \times 10^{-15}$ and $T_R = 150$ ms.

feedback to the local oscillator since the absolute frequency measurement is still preserved, albeit now the total phase correction of the local oscillator is a combination of the phase measurements from the two atomic clocks.

This technique can be further extended by introducing a second high-stability optical lattice clock which can be used with the other lattice clock in a zero deadtime (ZDT) configuration to make a continuous coherent measurement of the evolved laser phase. For discussion of this technique the clocks used in the ZDT configuration will be referred to as clocks 1 and 2 and will refer to the phase corrected clock as clock 3. The total interrogation period of clock 3 can be divided into subsections

for each of the interrogation periods for the two atomic clocks used in the ZDT configuration and can be described by $T_{\text{tot}} = t_{\text{feed}} + \sum_i (t_i + t_{\pi/2})$ with t_{feed} being the time required to correct the laser phase, $t_{\pi/2}$ is the time required for each $\pi/2$ pulse of the Ramsey interrogation for clocks 1 and 2, and t_i is the evolution period of the sub-interrogations. Because the interrogations are interleaved, the interrogations for clock 1 are even values of i and odd for clock 2. This method again utilizes a synchronous Ramsey interrogation followed by a correction of the local oscillator phase to extend the interrogation time of clock 3. One difference between the simple differential spectroscopy method and the ZDT differential spectroscopy method is that the ZDT method can be used with any combination of atomic clocks because the interrogation period increase for clock 3 is not dictated by the frequency ratio R . For this technique to work, the sub-interrogations of the total ZDT operation must be coherent measurements of the evolved laser phase thus limiting the value of t_i for the sub-interrogations. Additionally, much like correlation spectroscopy, differential noise between the three atomic clocks will introduce errors in the laser phase that is used to correct the local oscillator and cause a reduction in fringe contrast.

4.2 Differential spectroscopy experimental details

This section will discuss the experimental setup and technical details of differential spectroscopy, including operation with ZDT measurements. In these experiments we use a $^{40}\text{Ca}^+ / ^{27}\text{Al}^+$ clock which was described in Chapter 2, ^{171}Yb lattice clocks, and a Er/Yb-doped glass femtosecond optical frequency comb which are displayed in Fig 4.1. The ^{171}Yb optical lattice clocks used in these experiments use one-dimensional optical lattices, which are operated near the magic wavelength, to trap atoms in the Lamb-Dicke regime and use the ultra-narrow $^1S_0 \rightarrow ^3P_0$ clock transition at 578 nm. Both of the ^{171}Yb optical lattice clocks operate with $\approx 10,000$ atoms and previous ZDT operation of these two systems resulted in a measurement instability below $1 \times 10^{-16} / \sqrt{\tau}$ [101]. More information on these systems can be found in Ref. [25].

To begin the experimental sequence, the ^{171}Yb control system sends out an initiation pulse to the $^{27}\text{Al}^+$ system. To account for lag and state preparation between the systems a predefined

wait time elapses before each system applies the first $\pi/2$ pulse. Following the evolution period of the ^{171}Yb system the final ^{171}Yb $\pi/2$ pulse is applied and the phase evolution of the laser is measured. The phase estimation is performed in ^{171}Yb by measuring the transition probably following the Ramsey interrogation period. Measurement of the transition probability is done with a destructive fluorescence detection method. When the detection laser is applied fluorescence from atoms in the ground-state is collected and the scattered light causes these atoms to dissipate from the optical lattice. After this, the atoms in the excited clock state are driven to the ground-state and the measurement is repeated. This measurement method allows for an accurate measurement of the bright and dark state fractions independent of the shot to shot atom number that can vary between individual experiments. By dividing the fluorescence in the dark state n_D by sum of the fluorescence in the bright and dark state $n_{tot} = n_B + n_D$ the excitation ratio $r = n_D/n_{tot}$ can be determined. The fringe contrast for the ^{171}Yb system follows the equation

$$r(\Delta\phi_{\text{Yb}}) = \frac{A}{2} \sin(\Delta\phi_{\text{Yb}}) + \frac{r_0}{2} \quad (4.3)$$

where r_0 and A are experimentally determined parameters which are used to account for imperfections in the average and the amplitude of the Ramsey fringe of the ^{171}Yb system, respectively, which can come about from decoherence or improper state preparation of the ^{171}Yb atoms. The excitation ratio is then used with the inverted equation

$$\Delta\phi_{\text{Yb}}^{\text{est}} = \sin^{-1}((2r - r_0)/A) \quad (4.4)$$

to determine the evolved laser phase. Both of the ^{171}Yb lattice clocks used in these experiments operate with approximately 10,000 atoms. From measurements of the Ramsey fringe we find that these parameters are near their ideal values of $r_0 \approx 0.5$ and $A \approx 1$. This estimation of the evolved laser phase can then be sent to the $^{27}\text{Al}^+$ system to correct the local oscillator at the $^{27}\text{Al}^+$ clock transition frequency. After the phase correction is applied to the $^{27}\text{Al}^+$ laser and the final $^{27}\text{Al}^+$ $\pi/2$ -pulse is applied, a frequency correction is then applied the ^{171}Yb local oscillator of $\Delta\phi_{\text{Yb}}^{\text{est}}/(2\pi T_{\text{Yb}})$ to keep the local oscillator locked to the ^{171}Yb optical clock. The correction to the local oscillator

is applied after the $^{27}\text{Al}^+$ Ramsey sequence is complete to avoid causing deviations in the laser phase from the previously measured value of $\Delta\phi_{\text{Yb}}^{\text{est}}$.

To apply the phase correction to the Al system, a 10 MHz signal is supplied by the Yb system on which the scaled phase shift is written. To properly apply this phase shift to the Al system it has to be scaled by the frequency ratio of the Al and Yb clock transition frequencies as well as factors from any other frequency multiplication in the chain. In total, the phase shift sent to the Al system on the 10 MHz signal is $\Delta\phi_{\text{Al}} = \frac{1}{2} \frac{10 \text{ MHz}}{f_{\text{AOM}}} R^{-1} \Delta\phi_{\text{Yb}}^{\text{est}}$ with the additional factor of $\frac{1}{2}$ accounting for the fact that the phase correction is applied to the 534 nm light before it is doubled to 266 nm, the factor f_{AOM} comes from multiplying the 10 MHz signal up to AOM frequency used to apply the phase shift, and R comes from the frequency ratio. For convenience we apply this phase shift using the same electronics which are used for the PNC setup by using the 10 MHz signal as the clock for the PLL used to correct the phase noise from path length variations. The entirety of the length between the atoms and the cavities is stabilized with PNCs. Following the phase correction on the $^{27}\text{Al}^+$ local oscillator, the final $^{27}\text{Al}^+$ system $\pi/2$ pulse is applied. The $^{27}\text{Al}^+$ system then measures the laser phase and further corrects the local oscillator. The phase correlations between the different lasers is made possible by an optical frequency comb which is used to phase lock the higher frequency laser to the lower frequency laser.

Phase-coherent transfer of the stability of the Yb local oscillator is provided by an optical frequency comb. In this experiment a self referenced optical frequency comb based on an Er/Yb-doped glass gain medium shown in Fig. 4.1(b) is used [18]. This comb operates by pumping the gain medium with 980 nm light and via nonlinear processes emits light at 1550nm into a free-space cavity with a 500 MHz free-spectral range. A semiconductor saturable absorption mirror labeled SESAM in the figure, which is one end of the optical cavity, preferentially passes high-intensity light and absorbs low-intensity light in order to mode-lock the laser and provide stable pulse trains. Because of the low loss of the optical cavity (roughly 2%) a very narrow intrinsic free-running laser linewidth less than 5 kHz is realized. This narrow linewidth is imperative for the comb to reliably transfer the stability to the second laser with low phase noise. This laser is amplified from about

70mW to 300mW using an Er-doped fiber amplifier (EDFA) and is then sent through a highly-nonlinear fiber (HLNF) for access to the carrier-envelope offset frequency which requires spectral power for components an octave apart. The comb is then phase locked to the 1156 nm ^{171}Yb clock laser and the 1068 nm $^{27}\text{Al}^+$ clock laser is then locked to the comb using beatnotes between these lasers and the comb allowing for transfer of the phase information between these lasers.

The ^{171}Yb experimental sequence is extended to include a second ^{171}Yb -lattice clock to operate in a ZDT configuration. These systems are labeled Yb-1 and Yb-2 for discussion of ZDT differential spectroscopy. Fig. 4.3 shows the pulse sequence for operating ZDT differential spectroscopy. The beginning of the experiment will start in the same way as the sequence for basic differential spectroscopy but after the clock sequence is triggered the state preparation for Yb2 will begin. A delay to the start of the preparation is added since the entirety of the Ramsey interrogation period isn't needed for state preparation. Yb-1 and Al start their Ramsey interrogations at the same time but the evolution period for Yb-1 is shorter because the clock needs to make a coherent measurement of the evolved laser phase. The ^{171}Yb control system then switched to interrogating Yb-2 and the interleaved interrogation continues for the two ^{171}Yb optical lattice system. After each Yb interrogation, the LO phase is adjusted for the Al clock and following the final correction, the $^{27}\text{Al}^+$ clock completes its interrogation after n cycles on the Yb clocks. Alternatively the phase measurements can be collected and applied as a single correction before the final $^{27}\text{Al}^+$ $\pi/2$ pulse is applied. Measurements of the complementary Zeeman transitions (Δm) are performed back to back to reduce the impact of differential magnetic field noise in the two systems effecting the phase correction. Further details on the ZDT pulse sequence can be found in Ref. [57] where information regarding the optimum π -pulse synchronization is discussed.

In this experiment $t_{feed} = 50$ ms. To minimize the effect of differential magnetic field noise between the Yb lattice clocks each of the clocks alternate between probing the $m_F = 1/2 \rightarrow m_{F'} = 1/2$ and $m_F = -1/2 \rightarrow m_{F'} = -1/2$ transitions. To further minimize the impact of differential noise between the Yb lattice clocks each transition is measured on each clock at least once for every $^{27}\text{Al}^+$ interrogation. This reduction of differential noise occurs when an integer multiple of the

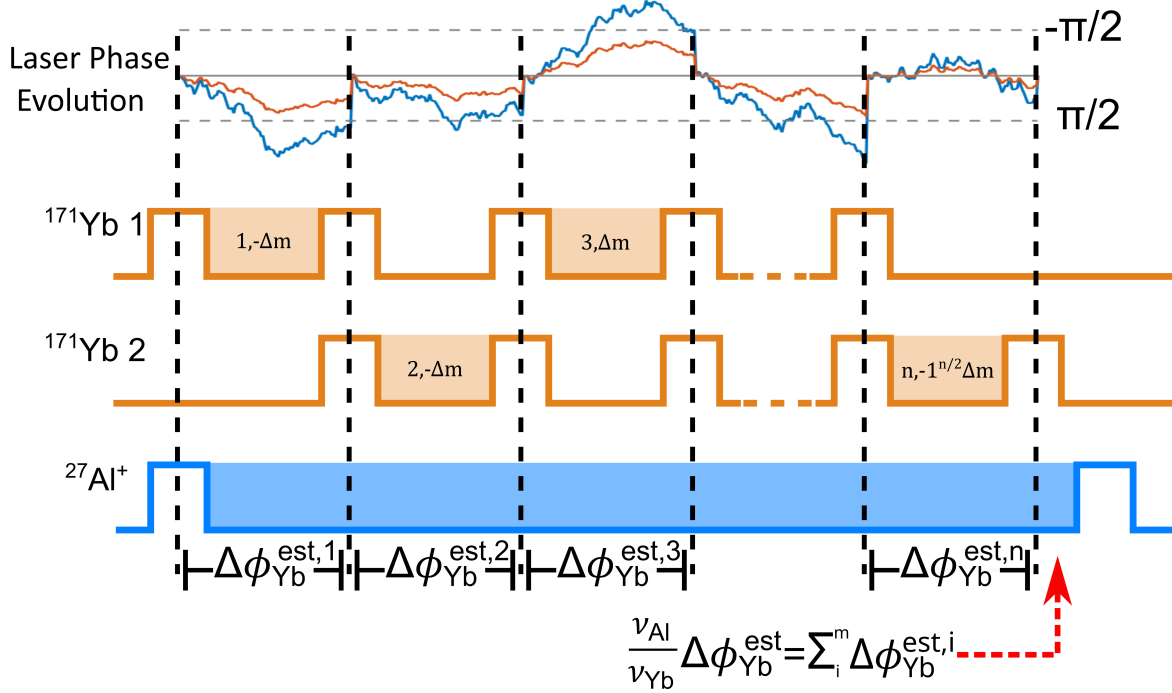


Figure 4.3: Figure detailing the pulse sequence for ZDT differential spectroscopy. The $\pi/2$ -pulses in Ramsey spectroscopy are depicted by the orange (blue) square pulses for the ^{171}Yb ($^{27}\text{Al}^+$) clock. The orange (blue) shaded regions represent the Ramsey free-evolution periods. A representative illustration of wandering and correction of the laser phase is shown at the top of the figure.

4 ^{171}Yb measurements are performed per single $^{27}\text{Al}^+$ measurement. In characterization of ZDT differential spectroscopy and later simulations it can be seen that when multiples of 4 measurements are used the effect of differential noise is minimized due to even probing of both sides of the Zeeman manifold on both systems. Similarly, for the $^{27}\text{Al}^+$ system the interrogation is switched between the $m_F = 3/2 \rightarrow m_{F'} = 1/2$ and $m_F = 3/2 \rightarrow m_{F'} = 1/2$ transitions to average the first order Zeeman shift. The clock transitions used in this experiment are chosen to minimize the sensitivity to magnetic field noise and specifics of the $^{27}\text{Al}^+$ system are discussed in Chapter 3.

4.3 Experimental Results

Initial measurements were performed with a single ^{171}Yb lattice clock and tests were performed to see if the phase measured by the ^{171}Yb lattice clock is representative of the phase

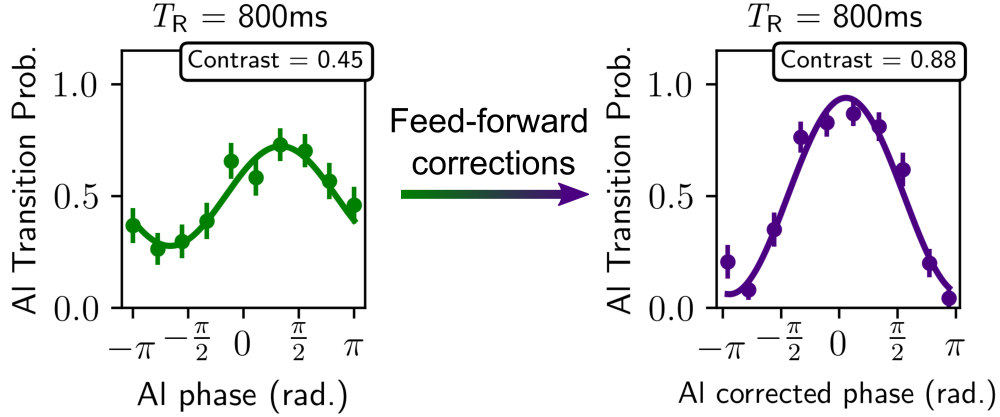


Figure 4.4: Data from an initial test of differential spectroscopy where the interrogation time for the $^{27}\text{Al}^+$ and ^{171}Yb systems are identical. The phase corrections in this plot are applied in post processing to determine if the phase measured by the ^{171}Yb system is representative of the phase of the laser in the $^{27}\text{Al}^+$ system. The plot on the left shows the Ramsey fringe measured by the $^{27}\text{Al}^+$ system with its laser locked to the ^{171}Yb laser. The plot on the right displays the revival of the fringe contrast following correction in post-processing.

excursion of the $^{27}\text{Al}^+$ laser. Measurements of $^{27}\text{Al}^+$ Ramsey fringe were obtained and phase measurements from the ^{171}Yb system were used in post-processing to unwrap the phase noise in the measurements. An example of this post processing is shown in Fig. 4.4 where a Ramsey interrogation is performed on the Al system with the Al laser stabilized to the Yb laser through the frequency comb. This figure demonstrates a significant increase in the fringe contrast following post-processing with a free evolution period of 800 ms. These interrogations were implemented in a fully synchronized experiment where the feedforward and corresponding time gap is not included. These measurements verified that direct feedforward measurements were ready to be implemented.

The experiments started by locking the two systems to their corresponding fringe to determine the two system measurement instability. Both the case where the feedforward was applied and where the feedforward was not applied were performed to determine if there is a significant improvement in the measurement stability. As seen in Fig. 4.5 Ramsey free evolution periods from 150 ms to 950 ms are measured to determine how much the measurement instability is improved from correction of the evolved laser phase. The maximum probe duration for Ramsey interrogation and differential spectroscopy are roughly a factor of the frequency ratio R different from each other, confirming the

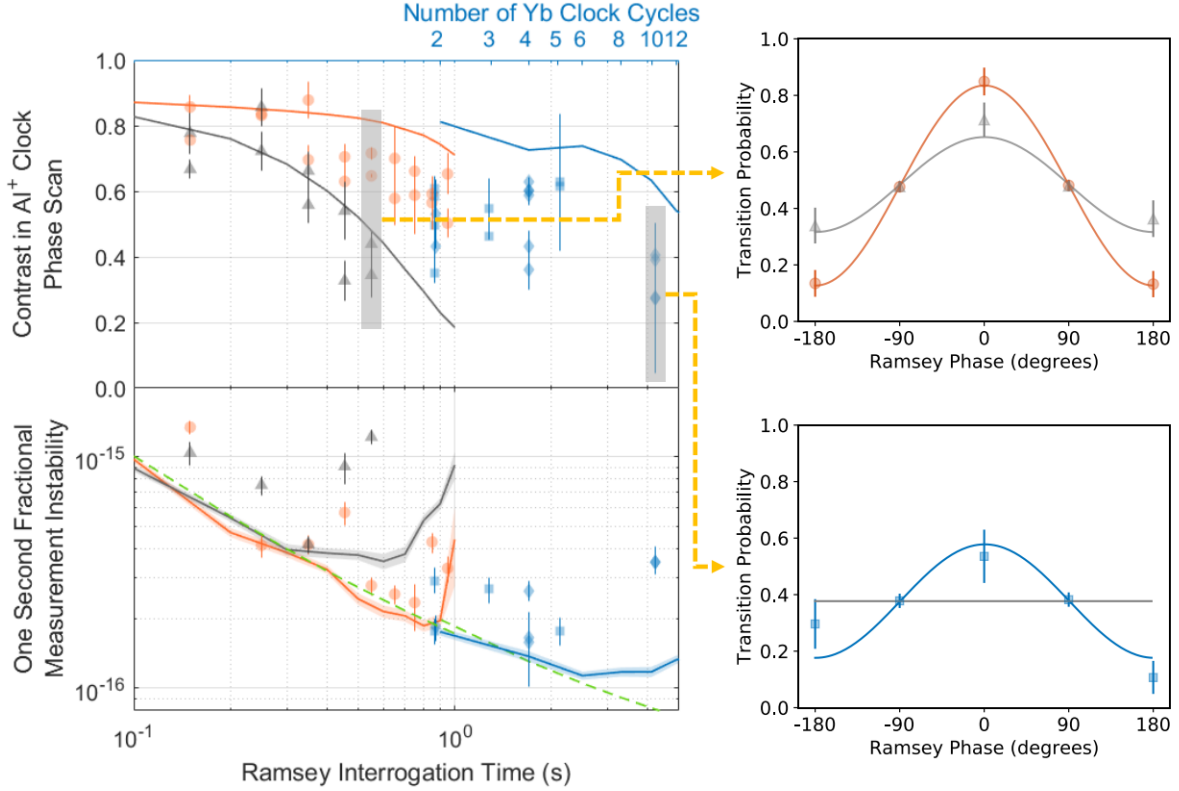


Figure 4.5: Differential spectroscopy clock comparison results for various T_{Al} for the single Yb ensemble case (orange circles) and varying the number of the Yb clock interrogation cycles for the ZDT case (blue squares). Also shown are the results of $^{27}\text{Al}^+$ spectroscopy without phase feedforward corrections (grey triangles). Numerical simulations are shown for single Yb ensemble with corrections (orange line), single Yb ensemble without corrections (grey line), and ZDT (blue line) cases for $m \in \{2, 3, 4, 5, 6, 8, 10, 12\}$ with 1 sigma standard deviation error given by the shaded regions. The green dashed line represents the quantum projection noise limit of the ratio measurement instability. The boxes on the right show the Ramsey fringe (atomic transition probability as a function of the relative phase between the two Ramsey pulses) of the $^{27}\text{Al}^+$ spectroscopy with (orange curve for single Yb ensemble and blue curve for the ZDT) and without (grey curve for both top and bottom) phase feedforward from the Yb clock for two different values of T_{Al} . The maximum slope points are used for feedback to the AOM while the other points are interrogated once every 10 cycles to gather information on the contrast of the Ramsey fringe.

model for the phase noise scaling.

Following the demonstration of basic differential spectroscopy, the full ZDT differential spectroscopy was implemented. A Ramsey free evolution period of 404 ms was chosen to ensure that interrogations of the two ^{171}Yb lattice clocks would proceed without a fringe hop. The number of ^{171}Yb interrogations per $^{27}\text{Al}^+$ interrogation was varied from 2 to 10 to optimize the frequency

ratio measurement stability. Results from these measurements can be seen in Fig. 4.5. The turn up in the 1 s stability at times longer than 2 seconds is likely due to differential noise between the systems which was determined from estimates and simulations. The solid lines plotted in Fig. 4.5 show the simulated effect of laser phase noise and magnetic field noise for both versions of differential spectroscopy. Representative data from the three setups was used for the simulations which resemble those discussed in Chapter 3. This differential noise limits the accuracy of the phase noise estimate from the ^{171}Yb systems thus limiting the ability to extend the interrogation time further. Regardless, with this demonstration we see that we can now reach measurement instabilities close to $1.6 \times 10^{-16}/\sqrt{\tau}$ which is a major instability reduction from previous $^{171}\text{Yb}/^{27}\text{Al}^+$ comparisons which had an instability of $1.3 \times 10^{-15}/\sqrt{\tau}$. Following this initial characterization, ZDT differential spectroscopy was used to average down for a continuous 36 hour period. In this measurement campaign a duty cycle of 68% and a total uptime of 88.8% was achieved. In order to average down over this measurement duration corrections for the ^{171}Yb blackbody radiation (BBR) shift had to be applied to the $^{27}\text{Al}^+$ error signal in post-processing since the frequency offset was transferred to this system through the locks between the two systems lasers. The differential BBR corrections between Yb-1 and Yb-2 can be seen in Fig. 4.6. It was found from the characterization of ZDT differential spectroscopy that the best stability of $1.9 \times 10^{-16}/\sqrt{\tau}$ was achieved with 4 ^{171}Yb measurements for every $^{27}\text{Al}^+$ measurement. This results in an $^{27}\text{Al}^+$ Ramsey interrogation period of 1.72 s. The results of the 36 hour measurement period can be seen in Fig. 4.6. In this figure it can also be seen that there is an apparent fractional frequency noise floor of 3×10^{-18} in the Allan deviation for the full 36 hour campaign. The source of this long-term noise was not yet identified, however all three clocks were not operated in a configuration with a low systematic uncertainty. It is likely that in future measurements when these clocks are operated with low systematic uncertainty that this noise floor will no longer limit the measurements. These results can be compared against previous inter-species frequency comparisons to put the improvement in the measurement stability into context. Typically comparisons between clocks with higher atom number have better measurement instability. These clocks are commonly optical lattice clocks but efforts to scale up

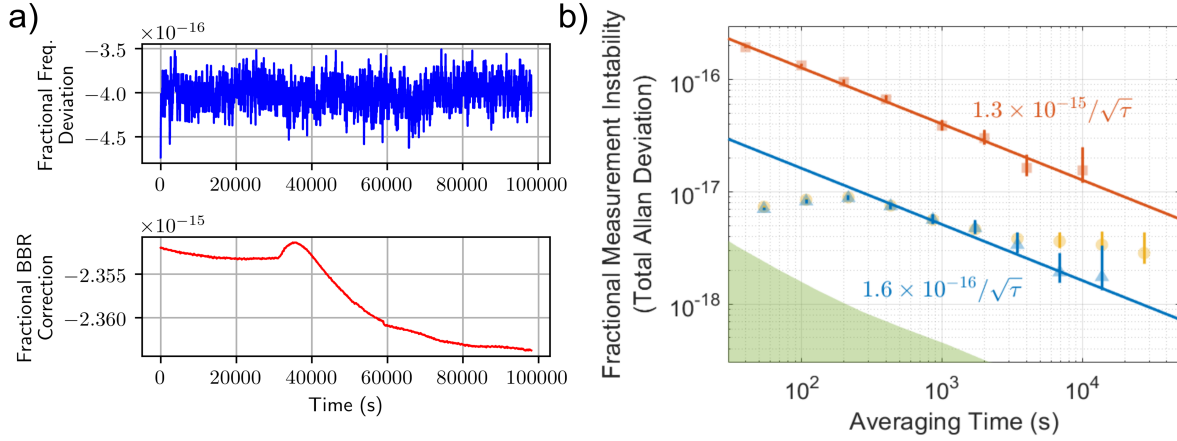


Figure 4.6: a) Time series of the corrected fractional frequency deviation for a 36 hour long ZDT differential spectroscopy clock comparison taken on 5-6 November 2020 and the associated BBR correction used to correct the fractional frequency deviation time series. b) Stability of the 36 hour long ZDT differential spectroscopy run with $n = 4$ Yb clock interrogations corresponding to a single $^{27}\text{Al}^+$ clock interrogation cycle for the full run (yellow circles) and an 8 hour selection of the total run (blue triangles). Our previous result compared ^{171}Yb and $^{27}\text{Al}^+$ (orange squares) using a conventional optical clock comparison technique. The solid lines are error-weighted, least-squares fits to the asymptotic region of the instability curves. The green shaded region represents a bound on the frequency transfer instability introduced by the frequency comb.

the number of atoms in ion clocks is currently in progress [104, 105]. In the past, comparisons between lattice-ion and ion-ion clocks have had measurement instabilities that limited the statistical uncertainty of the frequency ratio above the systematic uncertainty of the independent systems. A figure displaying a sample of frequency comparisons between independent clocks operating at different frequencies can be seen in Fig. 4.7. Using ZDT differential spectroscopy we show that clock comparisons with trapped ions can have measurement instabilities exceeding even the best comparisons between different species lattice clocks.

With basic differential spectroscopy and ZDT differential spectroscopy, two techniques have been demonstrated that reduce the measurement instability for frequency comparisons. With basic differential spectroscopy the probe duration can be extended to the maximum probe duration of the lower frequency high-stability clock used to correct the local oscillator phase. This technique is limited by the phase noise of the lower frequency local oscillator but still results in a frequency comparison measurement instability at the low $10^{-16} / \sqrt{\tau}$ level. By adding a second high-stability

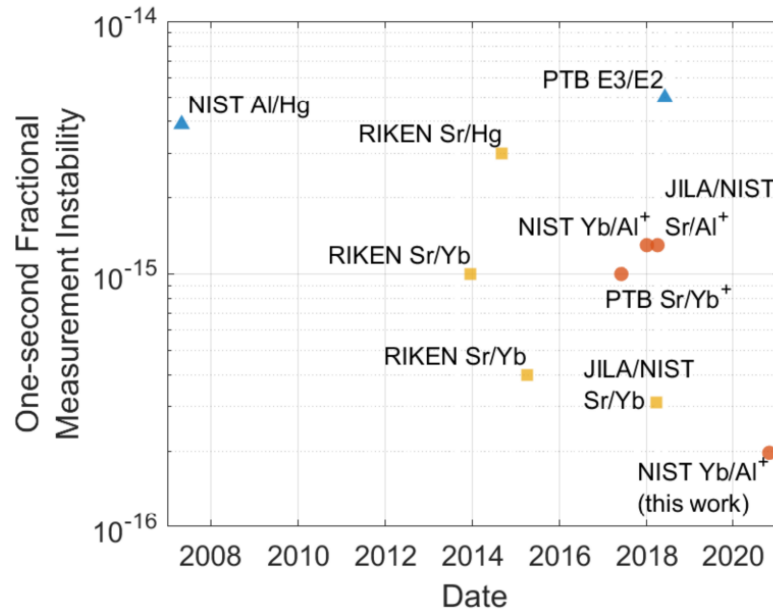


Figure 4.7: One-second instability of various interspecies optical clock comparisons plotted by their publication date. Displayed are: comparisons between an optical lattice clock with another optical lattice clock (yellow squares), an ion clock with another ion clock (blue triangles), and an optical lattice clock with an ion clock (orange circles). Note that this is not an exhaustive list of all previous interspecies comparisons but does include the most competitive results. Each measurement is marked with the laboratories involved in the measurement, as well as the species of optical clocks participating [35, 36, 102, 42, 103]

lattice clock ZDT differential spectroscopy can be employed where the limit to the technique is no longer set by the phase noise of the local oscillator. In practice differential noise between the atomic clocks limits the ability to accurately estimate the evolved laser phase which limits the attainable probe duration. With ZDT differential spectroscopy the clocks operating in a ZDT configuration to correct the local oscillator are not required to be at a lower frequency in contrast to non-ZDT differential spectroscopy. Both of these techniques can be thought of as ways to create a compound optical clock which allows for the ability to reach measurement instabilities below what is attainable for the individual clocks. In the future this technique may also be useful for comparisons with optical clocks that utilize entanglement since laser dephasing is no longer a major limitation. With this technique we demonstrate the ability to quickly compare different species atomic clocks with a fractional statistical uncertainty at the level of 1×10^{-18} .

Chapter 5

Systematic Effects

In this chapter I will detail progress toward characterizing the systematic uncertainty of the $^{40}\text{Ca}^+ / ^{27}\text{Al}^+$ quantum logic clock. I will focus on systematic effects which vary in either magnitude or evaluation method when compared to the evaluation of the $^{25}\text{Mg}^+ / ^{27}\text{Al}^+$ quantum logic clock in Ref. [28]. In Appendix C a table of systematic shifts and their uncertainties is given for the $^{25}\text{Mg}^+ / ^{27}\text{Al}^+$ system is given. In the previous evaluation the 4 leading sources of systematic uncertainty in order from largest to smallest are from second-order Doppler shift due to excess micromotion, the blackbody radiation shift, the quadratic Zeeman shift, and second-order Doppler shift due to secular motion. We will discuss each of these shifts but measurements of the $^{40}\text{Ca}^+ / ^{27}\text{Al}^+$ system have primarily focused on reducing the shift which creates the leading systematic uncertainty in the past system, the shift from excess micromotion, and quantifying the Quadratic Zeeman shift in the new system. These are the initial experimental focus because the new system differs in the ability to further compensate the micromotion because the diamond wafer wheel trap was redesigned and a lack of a first-order magnetic field insensitive transition in $^{40}\text{Ca}^+$ to measure the AC quadratic Zeeman shift [106]. These will be the primary focus of the chapter but progress on sideband cooling the $^{40}\text{Ca}^+ / ^{27}\text{Al}^+$ crystal and measurements of the system temperature for determining the blackbody radiation shift will also be discussed. The measurements for these effects are very similar but we discuss differences we have encountered in the $^{40}\text{Ca}^+ / ^{27}\text{Al}^+$ system.

5.1 Second order Doppler shift

In this section I will discuss progress towards characterizing second order Doppler shifts arising from the motion of the ion due to secular motion and excess micromotion (EMM). The second order Doppler shift from secular motion is minimized by using sideband cooling [66, 24, 107] to cool the ions to their motional ground-state and the shift from EMM is minimized by displacing the ions in the trap and applying RF compensation fields. I will discuss methods used to characterize these effects, the current status of quantifying these shifts, and limitations we are currently facing.

5.1.1 Ground-state cooling

Sideband cooling of single $^{40}\text{Ca}^+$ or the $^{40}\text{Ca}^+ / ^{27}\text{Al}^+$ crystal in our system is performed by sequentially cooling each secular mode. A quantum of motion is removed from a secular mode by applying a 729 nm red sideband pulse at a given mode frequency and applying an 854 nm repumper pulse to quench the ion as described in Chapter 2. We apply multiple pulses and vary the pulse duration to match the Rabi-rate dependence on the Fock state. By varying the pulse duration we can efficiently cool the ion to the motional ground-state. This sideband cooling procedure is repeated for each mode after which we can run a clock sequence or characterize the ion temperature or heating rate. We measure the ion temperature using techniques described in Ref. [24]. Fits to the Rabi time scan when driving a Δn motional sideband pulse are performed by using the equation

$$P_{\uparrow}^{(\Delta n)}(t) = \sum_n \frac{1}{2} (1 - e^{-\gamma t} \cos(2\Omega_{n,n+\Delta n} t)) P_{th}(n) \quad (5.1)$$

which describes the transition probability summed over all of the n to $n+\Delta n$ transitions weighted by the population in each Fock state where γ is a factor accounting for decoherence in the measurement, and $\Omega_{n,n+\Delta n}$ is the Rabi rate between Fock states n and $n+\Delta n$ for a specific secular mode. Fitting to this equation $P_{th}(n)$ can be extracted which describes the population in a Fock state $|n\rangle$ in thermal equilibrium. The equation describing a thermal Fock state distribution, $P_{th}(n)$, is given

by

$$P_{th}(n) = \frac{1}{1 + \bar{n}} \left(\frac{\bar{n}}{\bar{n} + 1} \right)^n. \quad (5.2)$$

Using this with Eq. 5.1 we can write the functions representing the transition probabilities for the red and blue sidebands as

$$P_b = \frac{\bar{n} + 1}{\bar{n}} \sum_{n=1}^{\infty} \frac{1}{2(1 + \bar{n})} [1 - \cos(2\Omega_{n,n+1}t)] \left(\frac{\bar{n}}{\bar{n} + 1} \right)^n, \quad (5.3)$$

$$P_r = \sum_{n=1}^{\infty} \frac{1}{2(1 + \bar{n})} [1 - \cos(2\Omega_{n,n+1}t)] \left(\frac{\bar{n}}{\bar{n} + 1} \right)^n. \quad (5.4)$$

Taking the ratio of these two functions we can determine the value of \bar{n} with

$$\frac{P_b}{P_r} = \frac{\bar{n} + 1}{\bar{n}}, \quad (5.5)$$

$$\bar{n} = \frac{1}{P_b/P_r - 1}. \quad (5.6)$$

When the ions are in a thermal distribution, fits to the sidebands are used to estimate $P_{th}(n)$ and with ratios of a blue and red sideband Rabi time scan we can measure \bar{n} . We use these functions in this section to measure \bar{n} following Doppler cooling, sideband cooling, and to measure heating rates in this system.

Before sideband cooling we first Doppler cool $^{40}\text{Ca}^+$. We test the effectiveness of Doppler cooling by using sideband thermometry to determine the ion temperature where we are confident that following Doppler cooling the ion will be in a thermal distribution. In Fig. 5.1 we plot the red and blue sideband time scans following doppler cooling. These time scans result in $\bar{n} = (3.15(12), 3.17(13), 2.85(10))$ for $(\omega_z, \omega_x, \omega_y)$ following Doppler cooling [108, 109]. This matches with expected values of $\bar{n} = (3.9, 2.6, 2.8)$ for $(\omega_z, \omega_x, \omega_y)$ which are determined using the linewidth of the Doppler cooling lineshape. Following, Doppler cooling we implement sideband cooling on $^{40}\text{Ca}^+$ and obtain $\bar{n} = (0.408(18), 0.0000(1), 0.008(1))$ for $(\omega_z, \omega_x, \omega_y)$. To determine these values we model the initial ion temperature with a thermal distribution with \bar{n} given by theoretical Doppler cooling limit for the modes labeled \bar{n}_{th} in Fig. 5.2. The value of \bar{n} is determined from the fits using $\bar{n} = (1 - P_0)\bar{n}_{th}$ where P_0 describes the probability of being in the motional ground-state considering a thermal distribution.

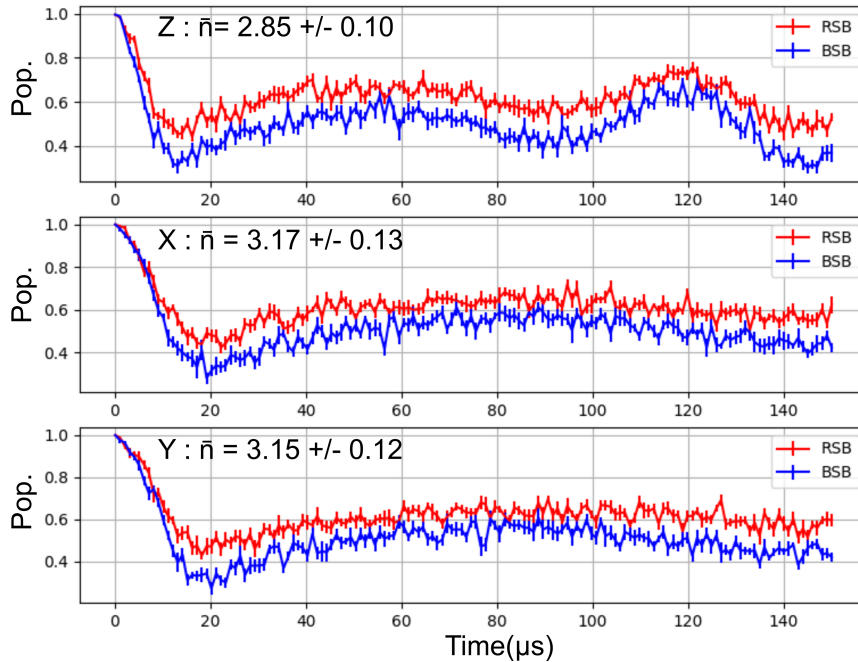


Figure 5.1: Sideband thermometry following Doppler cooling of single $^{40}\text{Ca}^+$. The population of the red and blue sidebands are used with 5.5. We measure $\bar{n} = (3.15(12), 3.17(13), 2.85(10))$ for $(\omega_z, \omega_x, \omega_y)$ which is roughly in line with what we expect from our measured Doppler cooling lineshape in Fig. 2.6. The expected Doppler cooling limit from the figure is $\bar{n} = (3.9, 2.6, 2.8)$ for $(\omega_z, \omega_x, \omega_y)$.

We are currently in the process of implementing sideband cooling on the two-ion $^{40}\text{Ca}^+ / ^{27}\text{Al}^+$ crystal where we are encountering difficulties in the radial COM mode stability. The instability is exacerbated by the low $^{40}\text{Ca}^+$ mode amplitude of these modes which causes long pulse times at our laser intensities. To minimize the instability we replaced our Rogers based resonator board with an alumina resonator board for better thermal stability. Additionally, we are implementing active stabilization of the modes by measuring a secular mode frequency and using this to feedback to the RF amplitude sent to the resonator. We can also increase the mode amplitude of the radial COM modes by reducing ratio of the radial confinement to axial confinement [110]. In Fig. 5.3 we plot the previous mode spectrum and a potential mode spectrum. Additionally, we lowered the quantization field to minimize degeneracy with other $^{40}\text{Ca}^+$ Zeeman transitions. We are working on determining the best trapping parameters to operate the system at and once this is determined

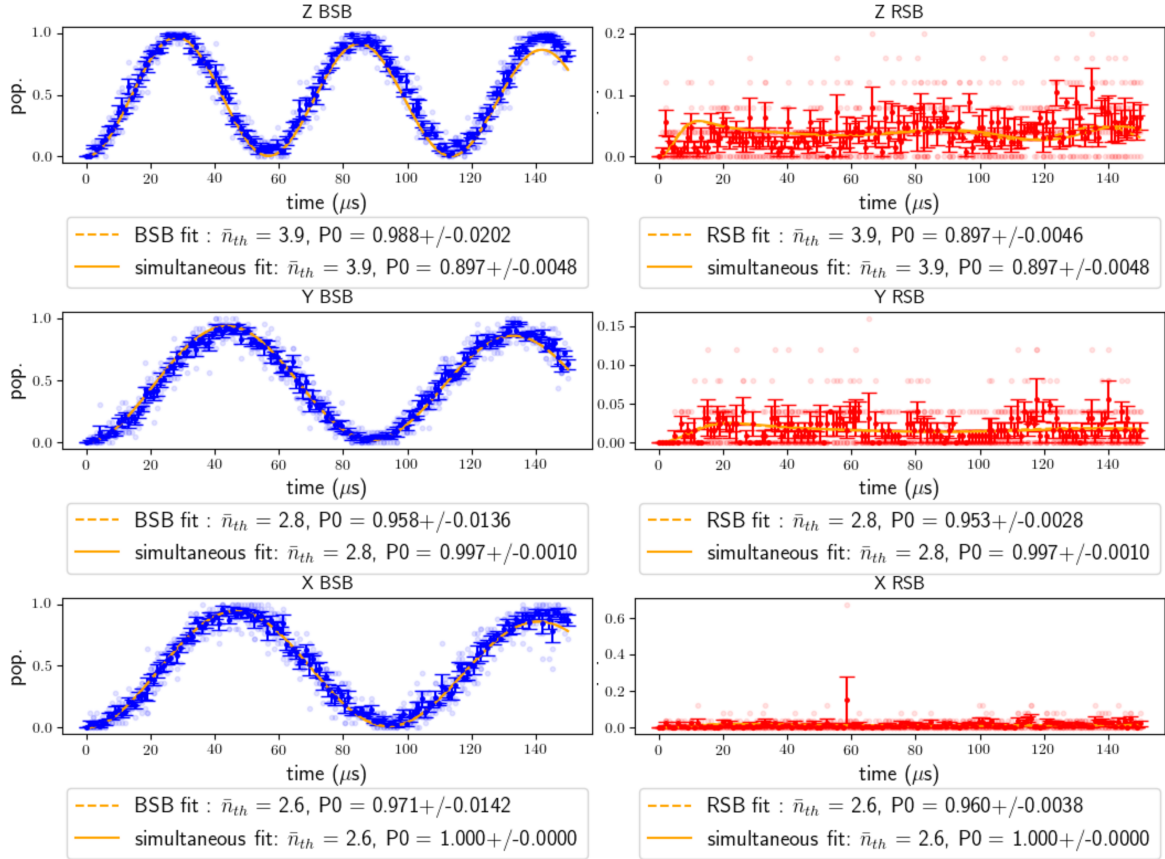


Figure 5.2: Sideband thermometry following Doppler cooling of single $^{40}\text{Ca}^+$. The population of the red and blue sidebands are used with Eq. 5.5 to determine the motional mode occupation. We measure $\bar{n} = (0.408(18), 0.0000(1), 0.008(1))$ for $(\omega_z, \omega_x, \omega_y)$ using the fitted values of $P0$ and the assumed starting thermal distribution given by the Doppler cooling limit.

full 3D ground-state cooling can be characterized.

Characterization of heating rates in our system can be determined without optimized sideband cooling. These heating rates are caused by electric field noise which is always present but other possible sources of heating include recoil induced heating and off-resonant coupling to electronic transitions [111, 54]. Recoil induced heating and off-resonant coupling to electronic transitions will only heat the ion crystal when cooling pulses are applied. We plot the heating rates measured at the old trapping parameters in Fig. 5.4. When compared against the previous system [54], we see a factor of ≈ 5 reduction in the electric field noise heating rates of the radial COM modes. This will help to minimize the second-order Doppler shift uncertainty at long probe durations. In future

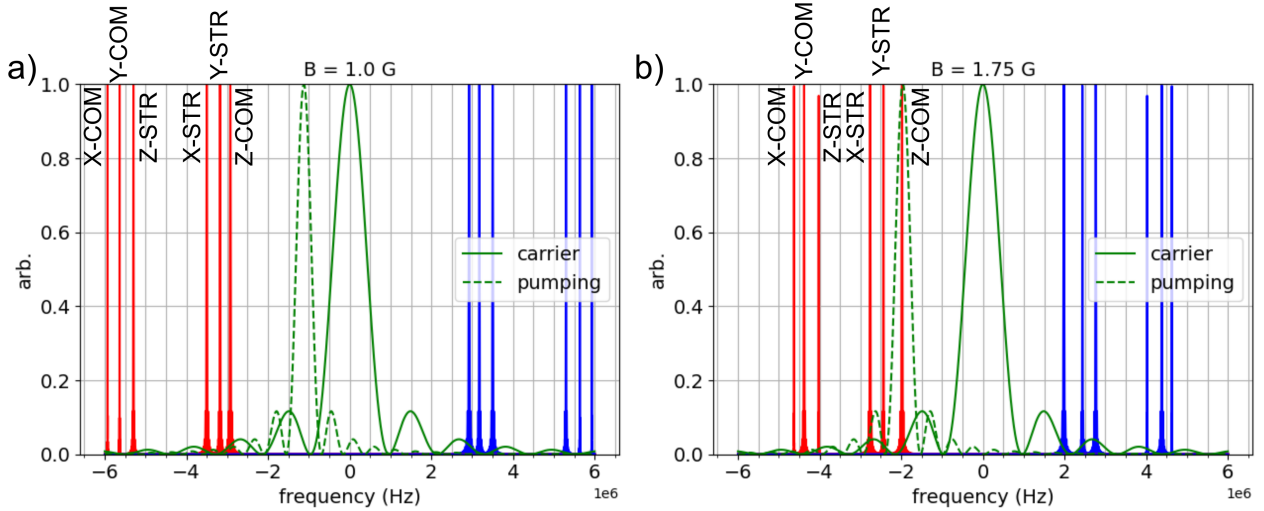


Figure 5.3: Secular frequency spectrum of $^{40}\text{Ca}^+ / ^{27}\text{Al}^+$. We plot the red and blue secular frequency sidebands of the $|4^2S_{1/2}, m_J = -1/2\rangle \leftrightarrow |3^2D_{5/2}, m_J = -5/2\rangle$ carrier transition shown with the solid green line and also pictured is the $|4^2S_{1/2}, m_J = 1/2\rangle \leftrightarrow |3^2D_{5/2}, m_J = -3/2\rangle$ transition which is used for $^{40}\text{Ca}^+$ state preparation. We show two plots, one with a quantization field of 1 G and the other with a quantization field of ≈ 1.7 G. We were initially operating at ≈ 1.7 G but moved to operating at 1 G and also increased our axial confinements and lowered our radial confinement to increase the mode amplitude of the radial COM modes.

differential comparisons using long probe durations the heating will become a significant systematic effect. To deal with the impact of heating rates, these future comparisons will require a continuous cooling sequence or a recoiling procedure during the clock interrogation period.

5.1.2 Micromotion minimization

In the previous $^{27}\text{Al}^+$ quantum logic clock the leading systematic uncertainty in the error budget was a second order Doppler shift from excess micromotion. Micromotion along the vertical direction was the primary contributor to the total systematic shift and was unable to be fully compensated because of a phase imbalance between the electric fields generated by the RF electrodes. The uncertainty in quantifying the EMM shift arises from uncertainty in the probe beam directions used to make a measurement of the orthogonal components and ambiguity in the relative phase of the excess micromotion components [28]. We expect that the ability to better control and minimize

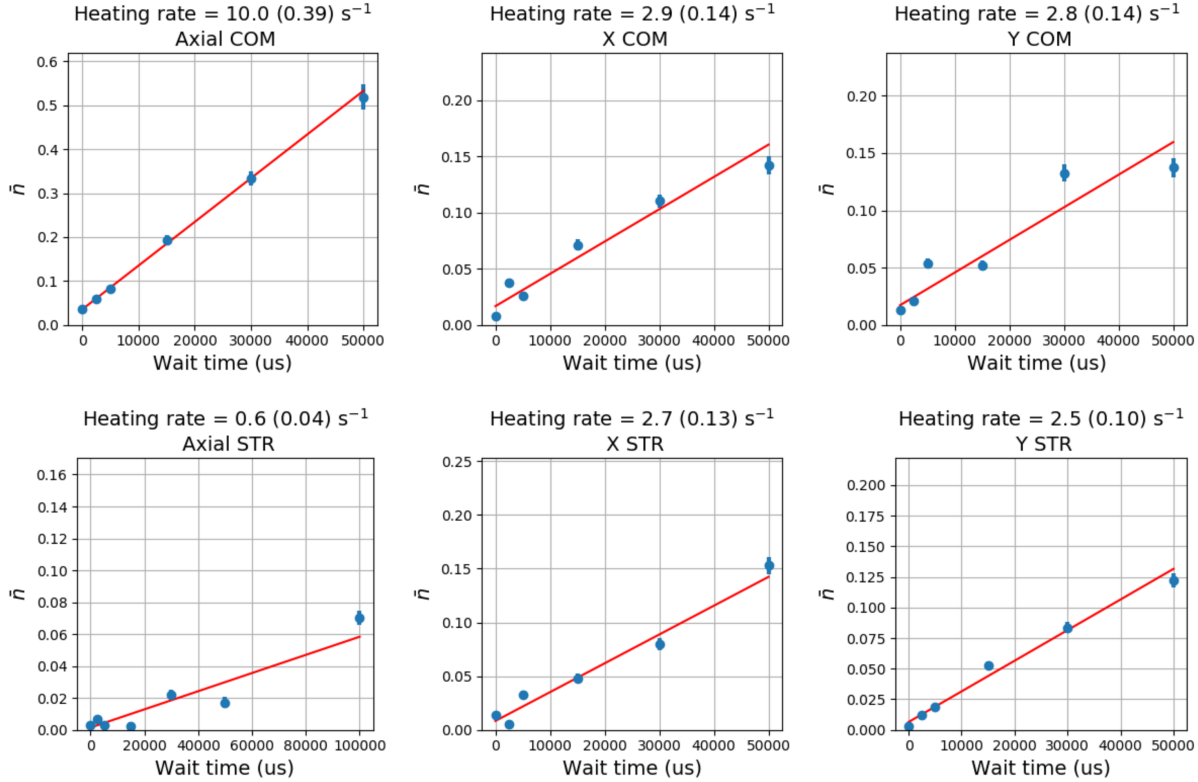


Figure 5.4: Measured heating rates for each of the $^{40}\text{Ca}^+ / ^{27}\text{Al}^+$ secular modes. Using sideband thermometry we measure the average mode occupation as a function of a delay between the cooling pulses and the temperature measurement. When compared to the previous $^{27}\text{Al}^+$ quantum logic clock [54, 28] we observe a factor ≈ 5 reduction in the heating rates of the radial COM modes.

the magnitude of micromotion will result in a reduction in the uncertainty of the micromotion shift in this system. The diamond wafer wheel trap was redesigned to balance the capacitance between electrodes to better cancel the RF electric field at the center of the trap, reducing the magnitude of the vertical micromotion. Previously, due to the large magnitude of vertical micromotion there wasn't motivation to use RF compensation to minimize the residual axial micromotion. In our system, we explore the ability to further null the micromotion by applying an RF electric field and varying the phase and amplitude of the applied field. When this field is applied, the residual RF electric field along the axial direction can be nulled.

We measure Excess micromotion in the $^{40}\text{Ca}^+ / ^{27}\text{Al}^+$ system by using the resolved sideband method. In Chapter 2 I detailed how micromotion sidebands arise in the laser spectrum due to a

phase modulation of the laser in the reference frame of the ion [112, 113]. When the modulation index of this effect is small such that $\beta_{\text{EMM}} \ll 1$ it can be measured by using a ratio of the Rabi rate of the first order micromotion sideband and the carrier Rabi rate. This relation to the modulation index is written as

$$\frac{\Omega_{\pm 1}}{\Omega_0} \approx \frac{\beta_{\text{EMM}}}{2}, \quad (5.7)$$

where $\Omega_{\pm 1}$ is the first order micromotion sideband Rabi rate of the red (-1) and blue (1) sidebands and Ω_0 is the carrier Rabi rate. In these measurements we use the first order red micromotion sideband for the micromotion measurement. Phase modulation amplitude from micromotion is dependent on the probe beam direction so we measure in three probe directions to measure the micromotion vector magnitude and direction. We probe along the axial, vertical, and pi port. Because these directions are not completely orthogonal, the vertical and pi ports measure a component of the axial micromotion. The component is accounted for by multiplying the measured sideband Rabi rate by $\cos(\theta)$ where θ is the angle between \vec{k} and the basis vectors of the micromotion components. To extract the Rabi rates for the carrier and sideband transitions we fit to Rabi time scans. Example fits for the three directions can be seen in Fig. 5.5. In these time scans our contrast is limited at long probe times by decoherence effects due to line noise and decoherence of the 729 nm laser. However, these scans demonstrate a major reduction in the magnitude of the fractional micromotion shift in the axial direction to an order of magnitude smaller than the magnitude of the fractional micromotion shift measured in the vertical direction. The micromotion shift for $^{27}\text{Al}^+$ can be determined from β_{mm} measured using $^{40}\text{Ca}^+$ with the equation [28, 112]

$$\frac{\Delta\nu}{\nu} = -\left(\frac{M_{\text{Ca}} \Omega_{\text{RF}}}{M_{\text{Al}} \omega_L}\right)^2 \left(\frac{\beta_{\text{mm}}}{2 \cos(\theta)}\right)^2, \quad (5.8)$$

where ω_L is the probe laser frequency, M_{Ca} is the mass of $^{40}\text{Ca}^+$, M_{Al} is the mass of $^{27}\text{Al}^+$ and θ is the angle between \vec{k} and the measurement axis. Using this equation we can determine the micromotion shift from the Rabi time scans. From the plotted Rabi time scan we can determine a second order Doppler shift from EMM for $^{27}\text{Al}^+$ of -1.7×10^{-20} for the pi direction, -3.9×10^{-19} for the vertical direction, and we can bound the magnitude of the shift in the axial direction to be

smaller in magnitude than -6×10^{-21} . By performing the error propagation for uncertainties in the parameters β_{mm} and θ we can see what effect the lower total shift has on the shift uncertainty. The expression for the micromotion shift uncertainty is

$$\sigma_{mm} = 2 \frac{\Delta\nu}{\nu} \sqrt{\frac{\sigma_{\beta}^2}{\beta_{\text{mm}}^2} + \sigma_{\theta}^2 \tan^2(\theta)}, \quad (5.9)$$

where σ_{mm} , σ_{β} and σ_{θ} are the uncertainties in the fractional frequency shift due to micromotion, β_{mm} , and θ respectively. This shows that with the reduction in the total shift the uncertainty will also decrease if we obtain uncertainties in β_{mm} , and θ comparable to the $^{25}\text{Mg}^+ / ^{27}\text{Al}^+$ system. It will still be important to estimate the uncertainty of these parameters well but with a lower shift we will likely see a reduction in uncertainty of the second order Doppler shift from micromotion.

We minimize EMM by displacing the ion in the radial potential and applying a compensation RF field in the axial direction. To compensate micromotion in the pi and vertical directions we vary the compensation voltages E_V and E_H respectively. Using these voltages we can displace the ion and position it at the center of the RF pseudo-potential, minimizing the RF electric field. We displace the ion axially by applying a differential voltage to the endcaps and minimize the axial micromotion by using a Holzworth digital synthesizer to apply phase stable RF on one endcap at the trap RF frequency (71.53 MHz). By scanning the amplitude and phase of the RF compensation signal we can null the micromotion along the axial direction by destructive interference with the axial RF field arising from misalignment of the trap axis and the endcaps. Previously in Ref. [28], the ion was just displaced along the axial direction to find the axial micromotion null. Because micromotion along the axial direction arises from misalignment of the wheel trap axis and the endcap axis the axial minimum does not necessarily correspond the center of the trap in the axial direction. To determine if there was a spatial micromotion null in the axial direction in the new wheel trap we performed a survey of the micromotion along the axial direction. Also we wanted to determine if there was a region where the gradient of the axial micromotion was small. This survey is plotted in Fig. 5.6. To perform this survey we displaced the ion by applying a differential voltage to the endcaps to displace the ions axially $\pm 300 \mu\text{m}$ from the unbiased position. This

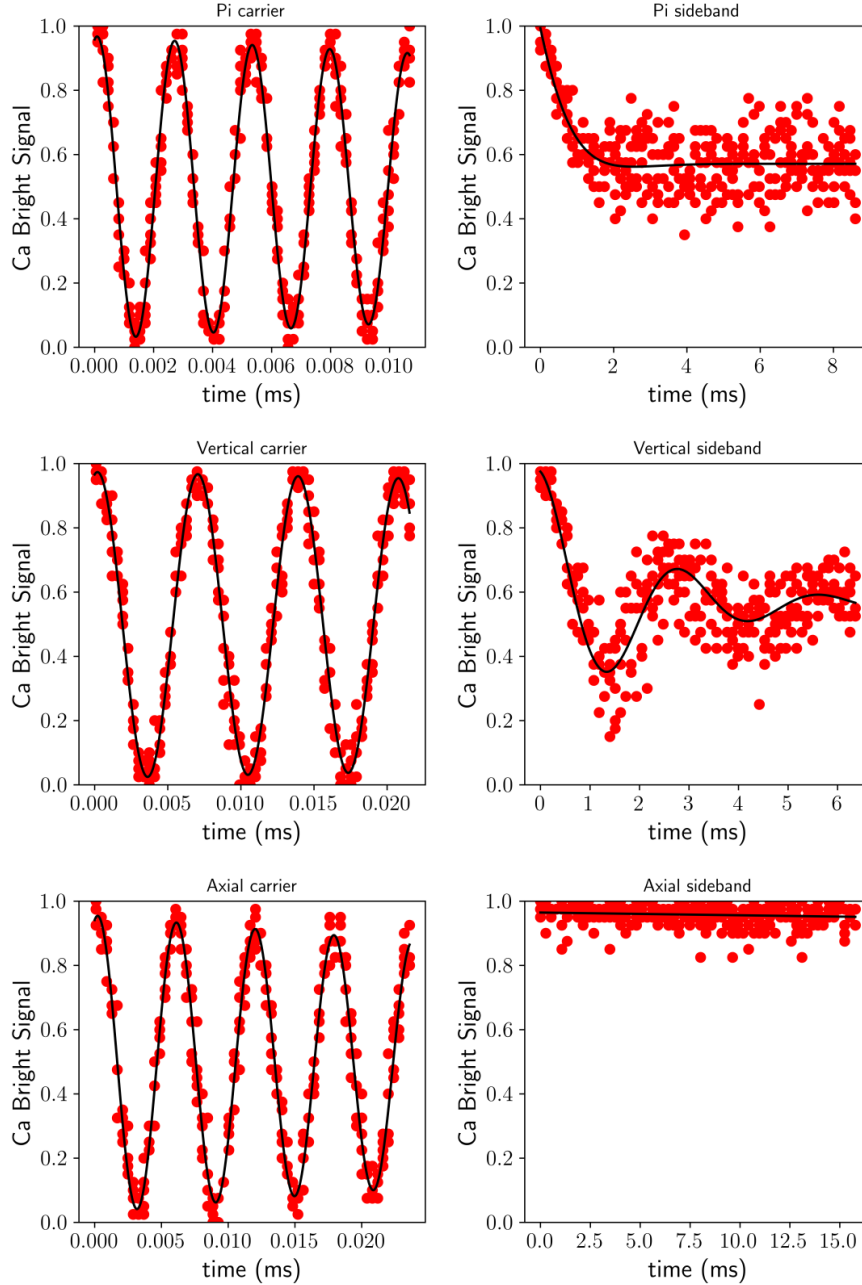


Figure 5.5: Rabi time scans of the carrier transition and the micromotion sideband along the Pi, Vertical and Axial directions. In the Pi direction we use the $|4^2S_{1/2}, m_J = -1/2\rangle \leftrightarrow |3^2D_{5/2}, m_J = -5/2\rangle$ transition, in the vertical direction we use the $|4^2S_{1/2}, m_J = -1/2\rangle \leftrightarrow |3^2D_{5/2}, m_J = -3/2\rangle$ transition, and in the axial direction we use the $|4^2S_{1/2}, m_J = -1/2\rangle \leftrightarrow |3^2D_{5/2}, m_J = -1/2\rangle$ transition. Using fits to the scans we can estimate the modulation index of these transitions as 7×10^{-4} for the pi direction, 4.8×10^{-3} in the vertical direction, and bound it below 3×10^{-4} for the axial direction.

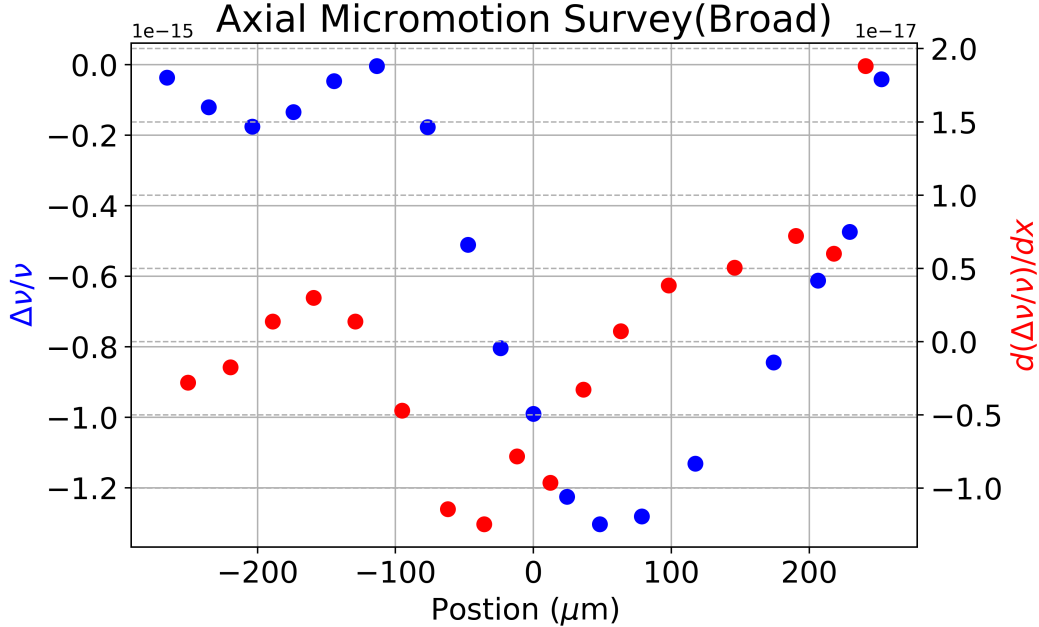


Figure 5.6: Spatial survey of the axial micromotion where the micromotion shift (Blue) and the micromotion shift gradient (Red) is plotted. Zero on this plot corresponds to the ion position when no voltage bias is applied to the endcaps. We observe a micromotion minimum at a position of $\approx -120 \mu\text{m}$ and a minimal gradient position at $\approx 50 \mu\text{m}$.

distance was calibrated using a CCD camera to measure the distance the ion was displaced given a bias voltage. By realigning the 397, 866, 854, and 729 nm lasers to the $^{40}\text{Ca}^+$ ion as it was displaced we measured the micromotion along the length of the trap axis. We found the spatial axial micromotion minimum at a displacement from the unbiased position of $\simeq -120 \mu\text{m}$ where the unbiased position is the the position of the $^{40}\text{Ca}^+$ ion when equal voltages are applied to the endcaps. A finer survey of this minimum is seen in Fig. 5.7. From this survey we have a region of $\approx 6 \mu\text{m}$ with a EMM shift magnitude below 1×10^{-18} . Alternatively, we found a region with a small gradient in the EMM shift that is $\simeq 50 \mu\text{m}$ away from the unbiased position. We apply RF compensation to minimize the micromotion at the position where the gradient of the EMM shift is small which results in a larger region where the magnitude of the shift due to EMM is $< 10^{-18}$. The low gradient position where the micromotion is minimize is seen in Fig 5.8. This shows that at this position we have a region of $\simeq 16 \mu\text{m}$ where the magnitude of the micromotion shift is below

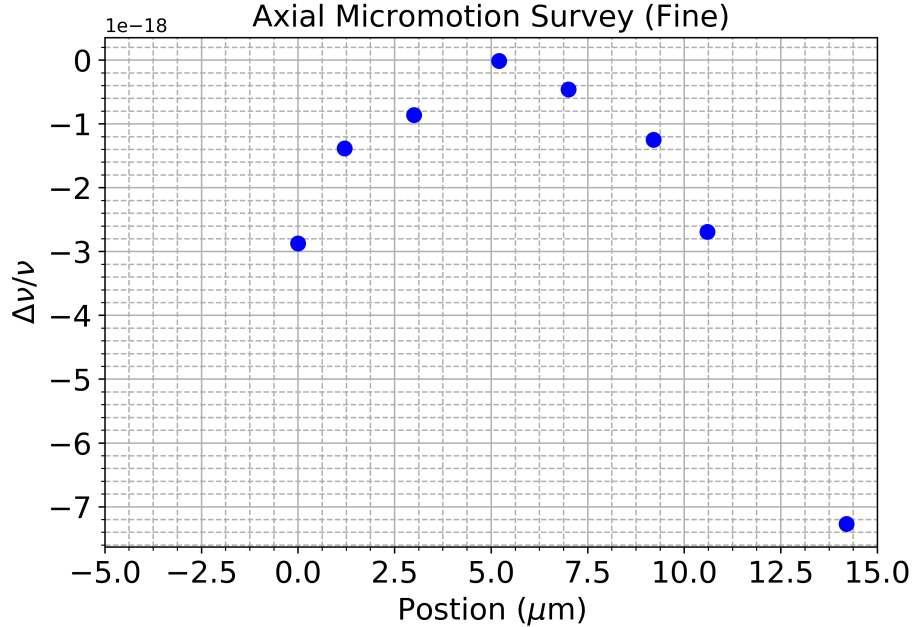


Figure 5.7: Fine survey of the spatial micromotion minimum at $-120 \mu\text{m}$ which corresponds to zero on this plot. This shows that there is a region of $\approx 6 \mu\text{m}$ with a EMM second order doppler shift magnitude below 1×10^{-18} .

1×10^{-18} which will be useful in future experiments where more clock ions [105] are used and will result in an axial ion chain of ≈ 10 ions having a micromotion shift is below 1×10^{-18} which could potentially fit ≈ 10 ions in future experiments.

We measure the long term stability of the micromotion shift by minimizing and measuring the micromotion and over a week timescale. These initial measurements were performed when using a Rogers based resonator board to drive the trap RF. In future measurements replacement with a alumina based resonator will likely improve the stability the micromotion shift further. Throughout this time period we did not vary the values of E_V and E_H but did adjust the phase of the axial RF compensation to minimize the micromotion in the axial direction over the week. Plots of the micromotion shift in each direction and the total micromotion are plotted in Fig. 5.9 as well as the phase required to compensate the micromotion along the axial direction. The second order Doppler shift is stable on the week long timescale but going forward it would be useful to obtain data more measurements to determine a reliable statistical uncertainty of the micromotion modulation index.

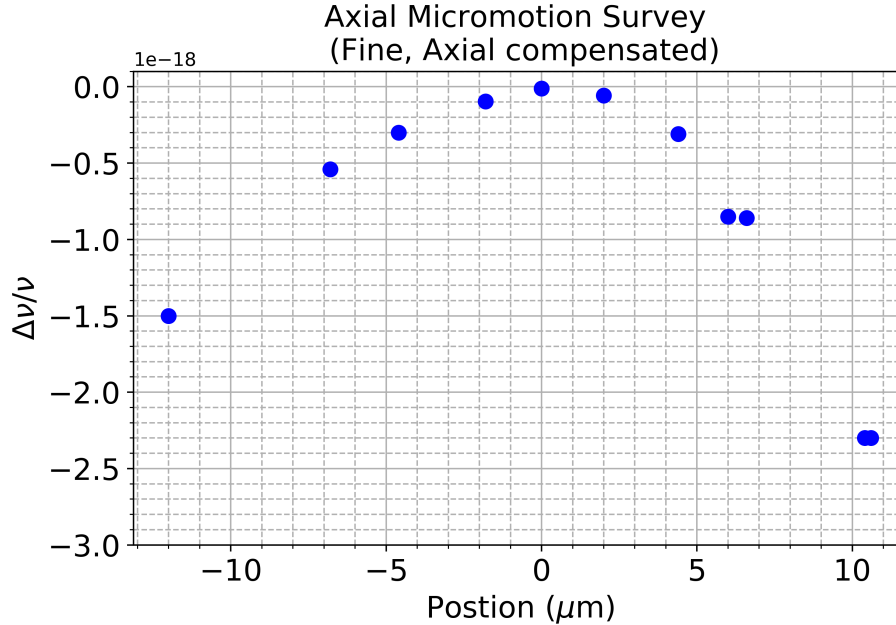


Figure 5.8: Survey of the low gradient position along the trap axis with RF compensation applied to the endcaps. Zero on this plot corresponds to 50 μm on the broad survey plot. At this position there is a span of $\simeq 16 \mu\text{m}$ where the EMM second order Doppler shift is below 1×10^{-18} .

We observe a total fractional second-order Doppler shift from excess micromotion of -4.1×10^{-19} dominated by micromotion in the vertical direction. Further characterization considering beam pointing errors and more measurements are needed to determine the uncertainty of the effect.

After this characterization we began measurements of the AC magnetic field in our system at the trap drive frequency and found that it will generate sidebands that are significant enough to impact the measured modulation index. This will be further discussed later in the chapter but we measure AC magnetic field amplitudes up to $\approx 3 \mu\text{T}$ which will result in a modulation index of ≈ 0.002 . We can estimate the resulting second-order Doppler shift error from the AC magnetic field modulation index to obtain an erroneous shift of $\approx -6 \times 10^{-20}$. The total error in the fractional shift will depend on the Zeeman transition used and the size of β_{EMM} but this gives us an estimate of the potential error. The impact of the AC magnetic field on the sideband spectrum of $^{40}\text{Ca}^+$ can be minimized by using measurements with carriers that have smaller magnetic field shifts or sideband measurements can be performed using resolved sideband spectroscopy of the 3P_1

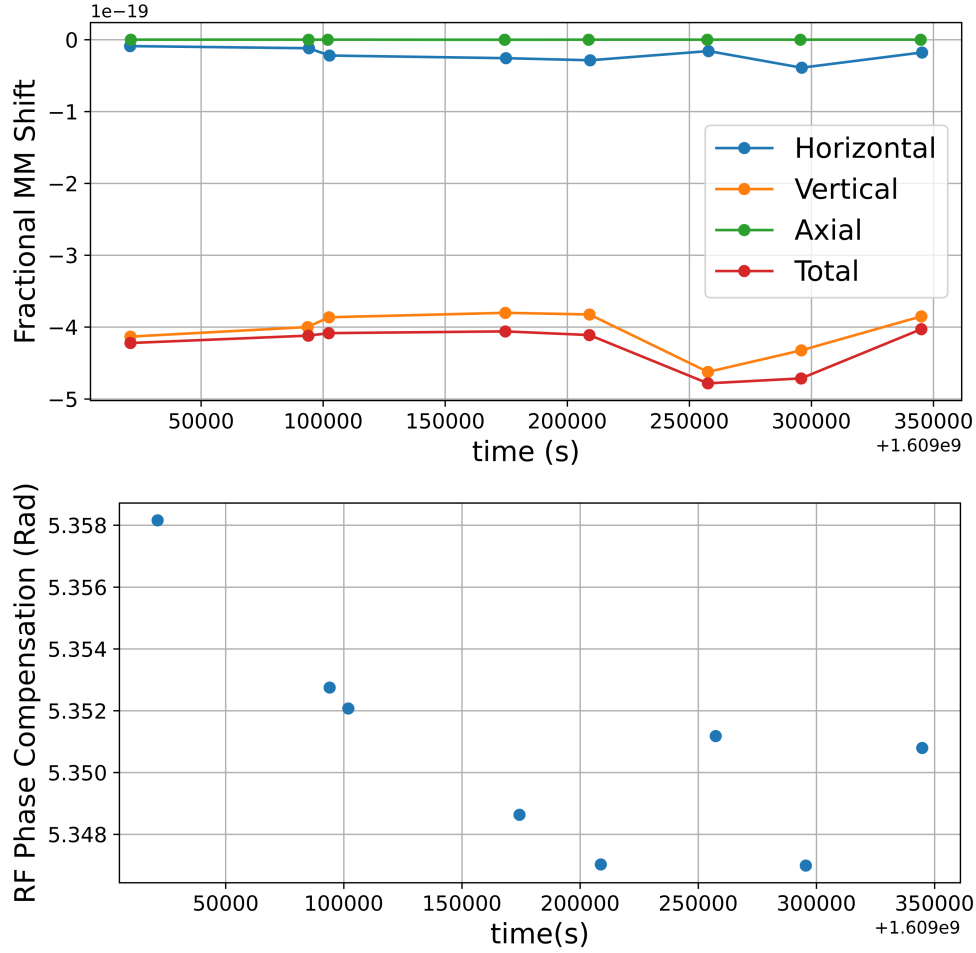


Figure 5.9: Week long characterization of the EMM time dilation shift. We plot the phase needed to compensate the axial micromotion and a measurement of the EMM second order Doppler shift for each direction. The shift remains stable over a week long timescale but could be further stabilized by periodic minimization of the shift.

transition in $^{27}\text{Al}^+$ which has a ≈ 2.8 times smaller first-order Zeeman shift when comparing the Lande g -factor of 3P_1 to the Lande g -factor of $D_{5/2}$ in $^{40}\text{Ca}^+$ [76]. Additionally, averaging over the sidebands of different Zeeman transitions at the trap drive frequency can be used to remove the impact of the AC magnetic fields [114]. However, based on the measurements here the micromotion shift is stable on the week timescale and can be reduced below previous results [28].

5.2 Quadratic Zeeman shift

The quadratic Zeeman shift is a second-order magnetic field shift [106] from both static and oscillating magnetic field amplitudes and modifies the clock frequency according to the equation

$$\Delta f = C_2 \langle B \rangle^2 = C_2 (B_{\text{DC}}^2 + \langle B_{\text{AC}}^2 \rangle). \quad (5.10)$$

where the static component is labeled by B_{DC} and the oscillating component is labeled by B_{AC} . Previous experiments measured the value of C_2 for $^{27}\text{Al}^+$ by using a frequency comparison between $^{27}\text{Al}^+$ and ^{171}Yb and varying B_{DC} of the $^{27}\text{Al}^+$ clock to determine the scaling factor [106]. In Ref. [106] the value of C_2 was determined to be $-71.944(24)$ MHz/T² which resulted in a fractional quadratic Zeeman shift uncertainty of 3.7×10^{-19} . The quadratic Zeeman shift uncertainty measured in Ref. [106] is also a result of the uncertainty in the measured values of B_{DC} and B_{AC} . The value of B_{DC} can be determined by measuring the frequency splitting of the transitions between different Zeeman levels of the $|^1S_0\rangle$ and $|^3P_0\rangle$ manifolds in $^{27}\text{Al}^+$. Measurement of the two sides of the Zeeman manifold in $|^3P_0\rangle$ are routinely used in clock operation where frequency locks are used for both sides of the manifold and in post-processing are averaged so the laser is locked the unperturbed atomic transition frequency making. Operating the clock in this way also provides a measurement of B_{DC} which can be used to quantify the static portion of the quadratic Zeeman shift, but measuring the value of B_{AC} requires a different measurement procedure. I will discuss two method which we studied to measure this effect with $^{40}\text{Ca}^+$ a resolved sideband method and a method based on the Autler-Townes effect.

5.2.1 Resolved sideband method for measuring oscillating magnetic fields

In our system we have targets to load both $^{40}\text{Ca}^+$ and $^{25}\text{Mg}^+$ in case we need to load $^{25}\text{Mg}^+$ to measure the AC magnetic field with a method similar to what was used in Ref. [106]. Loading $^{25}\text{Mg}^+$ would require significant modification to the experimental setup so we first study methods that use $^{40}\text{Ca}^+$ to measure the AC magnetic field. In previous measurements locks to this first order insensitive transition were used to measure the shift from $\langle B \rangle^2$ where the portion of the shift

from B_{DC} can be removed with secondary measurements of the field. $^{40}\text{Ca}^+$ does not have a first order magnetic field insensitive transition for this measurement so instead we attempted to measure the sidebands generated by the AC magnetic field at the RF drive frequency. This effect was first observed in Refs. [115, 114] and was discussed in the context of accurate micromotion minimization.

The total oscillating magnetic field in our system could have many frequency components, but here we consider the case where the primary frequency component is at the trap drive frequency (Ω_{RF}) and the power of sources at other frequencies are many dB below the primary component. This technique can also be used to measure oscillating magnetic fields at frequencies different from the trap drive but here we focus on the case where the micromotion sidebands and the AC magnetic field sidebands are overlapped. The AC magnetic field arises from currents in the ion trap used to generate the trapping RF pseudo-potential. Due to the symmetry of the RF electrodes used in RF Paul traps components of B_{AC} should cancel to a high degree at the center of the pseudo-potential much like E_{RF} . However, fields can arise from the wires connected to the RF electrodes. In the case of the diamond wafer wheel trap, capacitance between RF electrodes will give rise to AC magnetic fields. These capacitive sources will generate fields $\propto \Omega_{\text{RF}} C V r^{-1}$ where C is the capacitance, V is the voltage, and r is the distance from the ion to the capacitive source. Possible capacitive sources are marked in Fig. 5.10. The magnetic field generated by these sources could also have a phase that is different from the RF electric field. Including the possibility of there being a phase lag, we write the AC magnetic field as

$$\mathbf{B}_{\text{AC}}(t) = \mathbf{B}_{\text{AC}} \cos(\Omega_{\text{RF}}t + \phi), \quad (5.11)$$

where the phase relative to E_{RF} is described by ϕ . The oscillating magnetic field perturbs the ion's electronic energy levels. The frequency shift to a electronic energy level is given by

$$\Delta\omega_i = \frac{\mu_B g_i m_i}{\hbar} \mathbf{B}_{\text{AC}} \cdot \hat{q} = \frac{\mu_B g_i m_i}{\hbar} B_{q,\text{AC}}, \quad (5.12)$$

where μ_B is the Bohr magneton, g_i is the Lande g -factor for the state i , and m_i is the magnetic quantum number of the state. The perturbation to the resonance frequency of $|4^2S_{1/2}\rangle \leftrightarrow |3^2D_{5/2}\rangle$

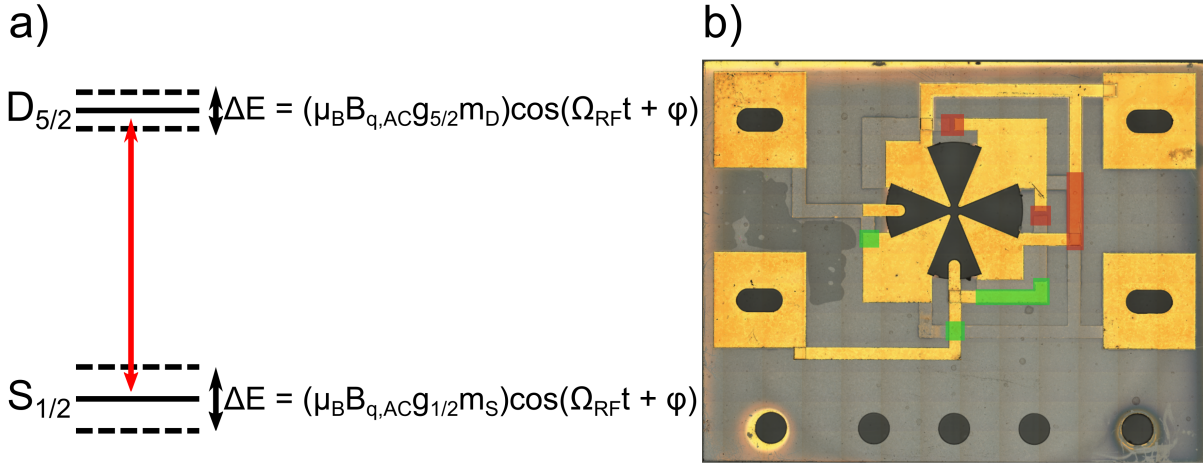


Figure 5.10: a) Energy level diagram of the $^{40}\text{Ca}^+$ qubit transition where the transition at $\approx 729 \text{ nm}$ is labeled by a red arrow. The energy modulation to the electronic states is labeled by the dashed line and the modulation amplitude is written next to the energy levels. b) Diamond wafer wheel trap where possible capacitive sources are marked. Picture of the diamond wafer wheel trap where the highlighted regions show where trap features overlap and capacitive sources could be present. The green sections mark places where the voltage across the traces is set by a DC line and an RF line and the red sections show where two RF lines overlap.

is found using Eq. 5.12 and is written as

$$\delta\omega_{AC}(t) = \frac{\mu_B}{\hbar} B_{q,AC} (g_{1/2} m_S - g_{5/2} m_D) \cos(\Omega_{RF} t + \phi), \quad (5.13)$$

where $g_{1/2}$ and $g_{5/2}$ are the Lande g -factors of the $|4^2S_{1/2}\rangle$ and $|3^2D_{5/2}\rangle$ states respectively. The first order Zeeman shift from the AC magnetic field produces a frequency shift of the internal state of the ion which appears as a phase modulation relative to the laser. This is similar to how sidebands appear from first-order Doppler shifts from ion micromotion [113]. The modulation index is defined by $\beta = \frac{\delta\omega}{\Omega_{RF}}$ where $\delta\omega$ is the frequency shift for the given effect. Using Eq. 5.13, the modulation index produced by B_{AC} is given by

$$\beta_{AC} = \frac{\mu_B}{\hbar \Omega_{RF}} B_{q,AC} (g_{1/2} m_S - g_{5/2} m_D) \quad (5.14)$$

and the modulation index from micromotion is labeled by β_{mm} . In Fig 5.10(a) the modulation to the relevant energy levels in $^{40}\text{Ca}^+$ is shown. From this we can write the frequency modulation as

$$\delta\omega(t) = \Omega_{RF} \beta_{AC} \cos(\Omega_{RF} t + \phi) + \Omega_{RF} \beta_{mm} \cos(\Omega_{RF} t), \quad (5.15)$$

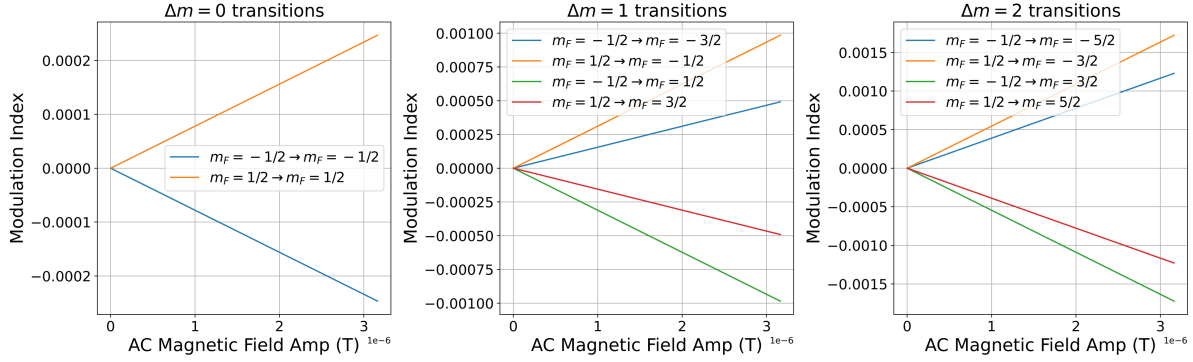


Figure 5.11: Modulation index from the AC magnetic field is shown for different magnetic field sensitivity transitions between the $S_{1/2}$ and $D_{5/2}$ manifolds in a $^{40}\text{Ca}^+$ ion as a function of the AC magnetic field amplitude. In the experiment if there was no micromotion then $|\beta_{\text{AC}}|$ would be measured for these transitions because the measured modulation index is strictly positive for the resolved sideband method. Here the sign of the sensitivity remains to illustrate the relative change in the total modulation index.

and the laser electric field in the ion rest frame as

$$\vec{E} = \vec{E}_0 e^{i\omega_L t} e^{i\beta_{mm} \cos(\Omega_{RF} t)} e^{i\beta_{AC} \cos(\Omega_{RF} t + \phi)}, \quad (5.16)$$

where ω_L is the laser frequency. The exponential that contains the phase modulation can be rewritten using the Jacobi-Anger expansion resulting in a sum of Bessel functions for each of the sources of modulation, where the Jacobi-Anger expansion is

$$e^{i(z \cos(\theta))} \equiv \sum_{n=-\infty}^{\infty} i^n J_n(z) e^{in\theta}. \quad (5.17)$$

Using the Jacobi-Anger expansion to rewrite Eq. 5.16 we obtain the expression

$$e^{i\delta\omega(t)/\Omega_{RF}} = \left(\sum_{n=-\infty}^{\infty} i^n J_n(\beta_{mm}) e^{in(\Omega_{RF} t)} \right) \left(\sum_{n=-\infty}^{\infty} i^n J_n(\beta_{AC}) e^{in(\Omega_{RF} t + \phi)} \right) \quad (5.18)$$

For both β_{mm} and β_{AC} we assume $\beta \ll 1$ which limits the expansion up to $n = 1$. Expanding the sums to $n = 1$ we obtain

$$e^{i\delta\omega(t)/\Omega_{RF}} = \left(J_0(\beta_{mm}) + iJ_1(\beta_{mm})e^{i(\Omega_{RF} t)} - iJ_{-1}(\beta_{mm})e^{-i(\Omega_{RF} t)} \right) \times \left(J_0(\beta_{AC}) + iJ_1(\beta_{AC})e^{i(\Omega_{RF} t + \phi)} - iJ_{-1}(\beta_{AC})e^{-i(\Omega_{RF} t + \phi)} \right). \quad (5.19)$$

Limiting this equation to terms that only evolve with frequency $\leq |\Omega_{RF}|$ we obtain

$$\begin{aligned}
e^{i\delta\omega(t)/\Omega_{RF}} &= J_0(\beta_{mm})J_0(\beta_{AC}) + J_1(\beta_{mm})J_{-1}(\beta_{AC})e^{-i\phi} + J_{-1}(\beta_{mm})J_1(\beta_{AC})e^{i\phi} \\
&\quad + iJ_1(\beta_{mm})J_0(\beta_{AC})e^{i(\Omega_{RF}t)} + iJ_1(\beta_{AC})J_0(\beta_{mm})e^{i(\Omega_{RF}t+\phi)} \\
&\quad - iJ_{-1}(\beta_{mm})J_0(\beta_{AC})e^{-i(\Omega_{RF}t)} - iJ_{-1}(\beta_{AC})J_0(\beta_{mm})e^{-i(\Omega_{RF}t+\phi)}
\end{aligned} \tag{5.20}$$

Simplifying the Bessel functions by considering $\beta \ll 1$ and only considering blue sidebands we obtain

$$e^{i\delta\omega(t)/\Omega_{RF}} \approx 1 + \frac{\beta_{mm}\beta_{AC}(e^{-i\phi} + e^{i\phi})}{4} + \frac{i\beta_{mm}}{2}e^{i\Omega_{RF}t} + \frac{i\beta_{AC}}{2}e^{i(\Omega_{RF}t+\phi)} \tag{5.21}$$

This can then be reinserted into the expression for the electric field

$$\vec{E} = Re \left[\vec{E}_0 e^{i(\omega t)} \left(1 + \frac{\beta_{mm}\beta_{AC}(e^{-i\phi} + e^{i\phi})}{2} + \frac{i\beta_{mm}}{2}e^{i(\Omega_{RF}t)} + \frac{i\beta_{AC}}{2}e^{i(\Omega_{RF}t+\phi)} \right) \right] \tag{5.22}$$

In this equation the static term that is proportional to $\beta_{mm}\beta_{AC}$ modifies the carrier Rabi rate but it can be neglected since $\beta_{mm}\beta_{AC} \ll 1$. Focusing on terms that oscillate at Ω_{RF} we can determine the magnitude of the modulation index measured by the ion using Ref. 2.40 which will result in a sideband Rabi rate that is proportional to βE_0 . Then, by dividing the sideband Rabi rate by the carrier Rabi rate we can determine the modulation index using the relation

$$\frac{\Omega_1}{\Omega_0} \approx \frac{|\beta|}{2} = \frac{\sqrt{\beta\beta^*}}{2} = \frac{1}{2} \sqrt{\beta_{mm}^2 + \beta_{AC}^2 + 2\beta_{mm}\beta_{AC} \cos(\phi)}. \tag{5.23}$$

The modulation index due to the AC magnetic field can be isolated by using measurements with Zeeman transitions that have different frequency shifts. We choose sets of Zeeman transitions where the magnitude of the frequency shift is equal but opposite in sign which is true when the ground and excited state magnetic quantum number of the transitions used are the same but are opposite in sign. For example we would use two sets with the same magnitude of sensitivity such as $\{|4^2S_{1/2}, m_J = 1/2\rangle \leftrightarrow |3^2D_{5/2}, m_J = 3/2\rangle, |4^2S_{1/2}, m_J = -1/2\rangle \leftrightarrow |3^2D_{5/2}, m_J = -3/2\rangle\}$ and $\{|4^2S_{1/2}, m_J = 1/2\rangle \leftrightarrow |3^2D_{5/2}, m_J = -3/2\rangle, |4^2S_{1/2}, m_J = -1/2\rangle \leftrightarrow |3^2D_{5/2}, m_J = 3/2\rangle\}$ and we label these two sets $\{\Delta m, -\Delta m\}$ and $\{\Delta m', -\Delta m'\}$ where prime and non-primed sets differentiate

transitions with the same magnitude of Zeeman shift. The sign difference in the frequency shift acts as a π phase shift for the oscillating magnetic field which can be used to remove the phase dependence in the measured total modulation index while leaving the square of β_{AC} unaffected. When adding the square of the two equal sensitivity modulation indices we obtain

$$\begin{aligned} & \frac{1}{4}(\beta_{\Delta m}^2 + \beta_{-\Delta m}^2) = \\ & \frac{1}{4} \left(\beta_{mm}^2 + \beta_{AC}^2 + 2\beta_{mm}|\beta_{AC}|\cos(\phi) + \beta_{mm}^2 + \beta_{AC}^2 - 2\beta_{mm}|\beta_{AC}|\cos(\phi) \right) = \quad (5.24) \\ & \frac{1}{2}(\beta_{mm}^2 + \beta_{AC,|\Delta m|}^2) \end{aligned}$$

Alternatively, the phase dependence can be isolated by taking the difference in these two measurements

$$\beta_{\Delta m}^2 - \beta_{-\Delta m}^2 = 4\beta_{mm}\beta_{AC,|\Delta m|}\cos(\phi) \quad (5.25)$$

It is also interesting to note that a measurement of the g -factor ratio of the different atomic transitions can be obtained by taking a ratio of the isolated phase dependent portions. We then isolate β_{AC} by taking the difference between two sets of modulation index measurements with different Zeeman shifts since the component due to β_{mm} is identical but magnitude of B_{AC} is different for Zeeman transitions resulting in

$$\frac{1}{4} \left((\beta_{\Delta m}^2 + \beta_{-\Delta m}^2) - (\beta_{\Delta m'}^2 + \beta_{-\Delta m'}^2) \right) = \frac{1}{2} \left((\beta_{AC,|\Delta m|}^2 - \beta_{AC,|\Delta m'|}^2) \right) \quad (5.26)$$

Now plugging in Eq. 5.14 we obtain a relation between the magnetic field and the modulation index

$$\begin{aligned} & \frac{1}{2}(\beta_{AC,|\Delta m|}^2 - \beta_{AC,|\Delta m'|}^2) = \\ & \frac{1}{2} \left(\left(\frac{\mu_B}{\hbar\Omega_{RF}} B_q \right)^2 \left((g_{S,1/2}m_{S,1/2} - g_{D,5/2}m_{D,3/2})^2 - (g_{S,1/2}m_{S,1/2} + g_{D,3/2}m_{D,3/2})^2 \right) \right). \quad (5.27) \end{aligned}$$

This can be used for any sets of transitions which might have lower or higher susceptibility to other systematic effects like the electric quadrupole shift [116]. This choice happens to be insensitive to the electric quadrupole shift since all transitions would observe a common mode shift due to the same $|m_J|$ being used for the D state. In Fig. 5.11 we plot β_{AC} for transitions with different magnetic field sensitivities.

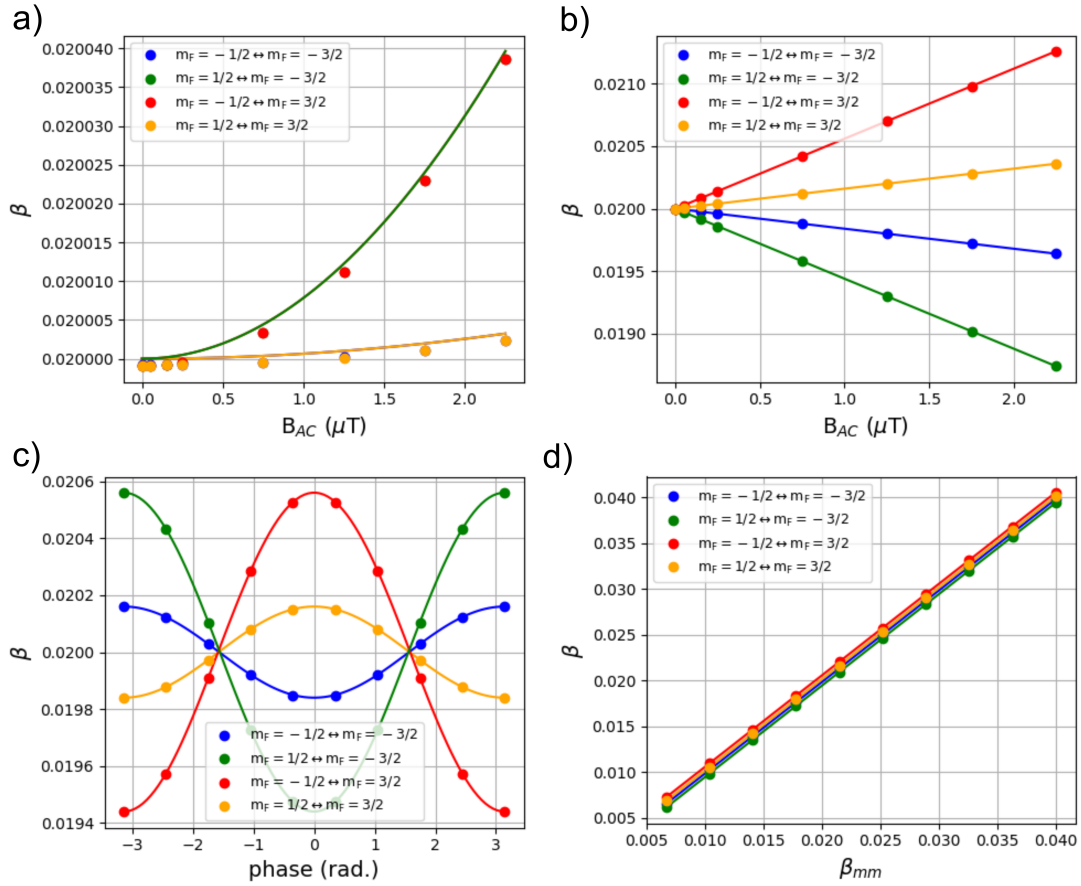


Figure 5.12: Comparison of the analytical model developed to describe the total modulation index and a simulation of the system taking into account micromotion and the AC magnetic field. a) Figure showing the quadratic dependence of the magnetic field when the phase dependent term is removed by setting $\phi = \pi/2$. b) Scaling with B_{AC} when $\phi = 0$, the effect is much more noticeable because the phase dependent term is multiplied by β_{mm} . c) Modulation index dependence on ϕ with $B_{AC} = 1 \mu\text{T}$ and $\beta_{mm} = 0.02$. d) Model dependence on β_{mm} with $B_{AC} = 1 \mu\text{T}$ and $\phi = 0$. Transitions used are listed in the legends of the plot.

The validity of this model is tested using a master equation solver in qutip where the effect of micromotion and the AC magnetic field are modeled. The Hamiltonian of this system with \hbar set

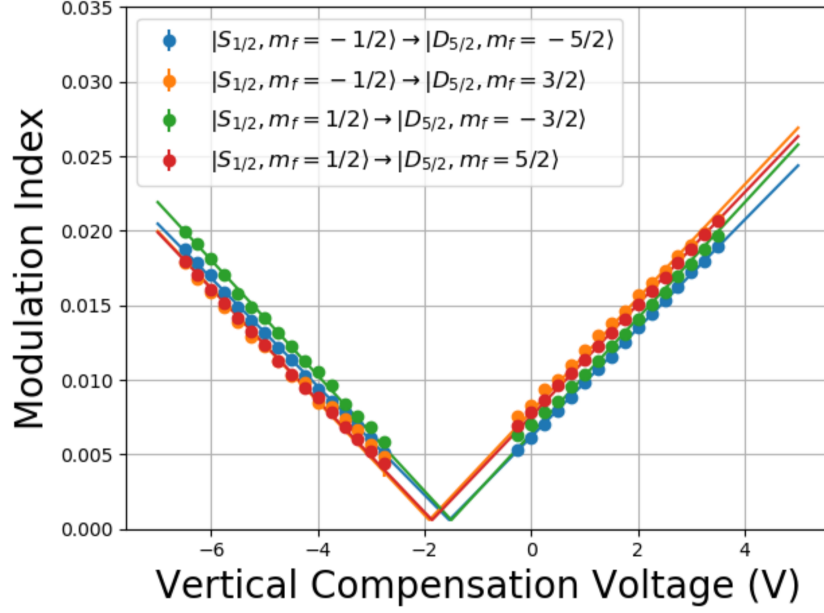


Figure 5.13: Current experimental sideband measurement result along the Pi direction. In this plot we can see a noticeable difference in the null position indicating that the modulation index from B_{AC} should be measurable. The solid lines were added to aid the eye but are not fits to the data. It is likely that some systematic effect is impacting the measured data; understanding of the error is need to extract the correct modulation index.

to 1 is described by

$$H(t) = H_0 + H_1(t) + H_2(t), \quad (5.28)$$

$$H_0 = \sum_i E_i |i\rangle \langle i|, \quad (5.29)$$

$$H_1(t) = \sum_i \sum_j \frac{\Omega_{L,i,j}}{2} \epsilon_{i,j} |i\rangle \langle j| \cos(\omega_L t + 2\pi\beta_{mm} \cos(\Omega_{RF} t)), \quad (5.30)$$

$$H_2(t) = \sum_i \Omega_{RF} \beta_{AC} |i\rangle \langle i| \cos(\Omega_{RF} t + \phi), \quad (5.31)$$

where i and j are both indices describing the $S_{1/2}$ and $D_{5/2}$ states, E_i Zeeman shifted atomic state energy, $\Omega_{L,i,j}$ is the laser Rabi rate for a specific transition between states i and j , $\epsilon_{i,j}$ is a factor accounting for the selection rules, Ω_{RF} is the trap RF frequency, β_{AC} is the modulation index from the AC magnetic field described in this section, and β_{mm} is the micromotion modulation index. Further, the term H_0 describes the state energies, H_1 describes the laser ion interaction and the

phase modulation of the laser due to micromotion, and H_2 describes the modulation of the state energies due to the magnetic fields. Using these simulations we see good agreement with the model. In Fig. 5.12 we can see agreement in scaling of the AC magnetic field amplitude and dependence on the magnetic field phase as well as good agreement with phase and micromotion amplitude variation. In Fig. 5.12(a) we can observe the scaling of the total modulation index with the AC magnetic field amplitude when the phase dependent component is removed by setting $\phi = \pi/2$. In Fig. 5.12(b) we can see the splitting of the total modulation index for different Zeeman transitions with increasing AC magnetic field magnitude when the phase dependent component is included ($\phi = 0$). The effect of the total modulation index when the AC magnetic field phase is varied can be seen in Fig. 5.12(c) where $B_{AC} = 1 \mu\text{T}$. When β_{mm} is increased the total modulation index for all of the transitions linearly increases shown in Fig. 5.12(d). This suggests that under the assumptions of $\beta \ll 1$ and the magnetic field being primarily at a frequency of Ω_{RF} the model is representing the system well.

We have measured the sideband at the trap RF frequency for different Zeeman transitions in the $^{40}\text{Ca}^+ / ^{27}\text{Al}^+$ system and we see a deviation in the modulation index between different transitions indicating a resolved sideband method can be used to measure this effect. An example of a measurement where the ion is displaced through the micromotion null is seen in Fig 5.13, displaying the change in the modulation index when measuring with different Zeeman transitions. We see a deviation from the expected behavior when compared to the modeling and the simulation described in this section indicating there is an error in how the data is taken or a systematic effect which we have not yet considered. We will continue to work on understanding this discrepancy but we have also used a different measurement method to independently determine the AC magnetic field amplitude to later compare with the field measured with the resolved sideband method.

5.2.2 Autler-Townes method for measuring oscillating magnetic fields

Measurement of the AC magnetic field magnitude using the Autler-Townes effect has been demonstrated in previous experiments with $^{138}\text{Ba}^+$ [117] and $^{171}\text{Yb}^+$ [118]. The Autler-Townes

effect describes the modification of a spectral lineshape from a transition between two states when these states are coupled to a third by an oscillating electromagnetic field. For Autler-Townes based measurements in our system we apply a first-order Zeeman shift that is strong enough to make the frequency splitting of the $|S_{1/2}\rangle$ Zeeman sub-states equal to the oscillating frequency of interest. Because this requires magnetic fields on the order of 2.6 mT for our RF frequency we use large permanent magnets to generate the field. In this section I will provide background on how the Autler-Townes effect is used and present measurements of the AC magnetic field at our trap frequency.

The Autler-Townes effect modifies the $S_{1/2}$ states of $^{40}\text{Ca}^+$ through coupling with the oscillating magnetic field. It is convenient to use the dressed state picture to describe this effect where a “pump” field and a “probe” field interact with the ion. The “pump” field is the AC magnetic field which couples $|S_{1/2}, m_J = 1/2\rangle$ and $|S_{1/2}, m_J = -1/2\rangle$ and is assumed to be linearly polarized and perpendicular to the quantization axis. Fields parallel to the quantization axis are not included in the derivation because these fields will not have the correct polarization need to drive population between the two ground-states of $^{40}\text{Ca}^+$. We define the quantization axis as $\vec{B} = B_0 \hat{z}$, and the AC magnetic field as

$$\vec{B}_{AC}(t) = B_x \hat{x} \cos(\Omega_{\text{RF}} t) \quad (5.32)$$

where Ω_{RF} is RF trap frequency. The Hamiltonian describing the $S_{1/2}$ manifold is

$$H_0 = E_{+1/2} | +1/2\rangle \langle +1/2| + E_{-1/2} | -1/2\rangle \langle -1/2| = \frac{\hbar\omega_0}{2} \sigma_z \quad (5.33)$$

where σ_i are the Pauli matrices and ω_0 is the frequency difference between the two S states. The interaction Hamiltonian of the oscillating magnetic field is written as

$$H_I = -\vec{\mu} \cdot \vec{B} = -\mu \sigma_x B_x(t) \quad (5.34)$$

where $\mu = g_s m_{1/2} \mu_B$, and μ_B is the Bohr magneton. Decomposing σ_x into $\sigma_+ + \sigma_-$ where $\sigma_+ = \frac{\sigma_x + i\sigma_y}{2}$ and $\sigma_- = \frac{\sigma_x - i\sigma_y}{2}$ and inserting this into Eq. 5.34 we obtain the expression

$$H_I = -\mu B_x (\sigma_+ + \sigma_-) \cos(\Omega_{\text{RF}} t) = \hbar\Omega (\sigma_+ + \sigma_-) \cos(\Omega_{\text{RF}} t) \quad (5.35)$$

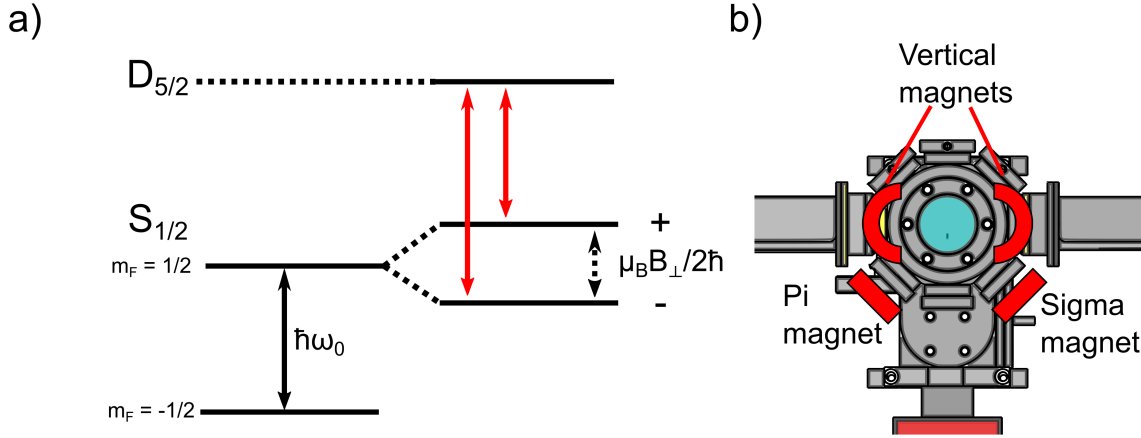


Figure 5.14: Level structure used to measure the Autler-Townes effect (a) and a diagram detailing the placement of the magnets used to make the frequency difference between the states in the $S_{1/2}$ manifold equal to $\approx 72\text{MHz}$ (b). In (a) we show the dressed-state picture for the $m_J = 1/2$ state and label the dressed states as $+$ and $-$. We probe these states by coupling the laser to the same m_J state in the $D_{5/2}$ manifold, shown by the red arrows. In (b) the magnets are highlighted in red and when probing one axis we remove the magnets along the other directions. This is the same overhead view shown in Fig. 2.12 and the labeling of the magnets follows how the ports are labeled.

where we define the frequency $\Omega = -\frac{\mu B_x}{\hbar}$. We can use the Euler identity to write H_I as

$$H_I = \frac{\hbar\Omega}{2}(\sigma_+ + \sigma_-)(e^{i\Omega_{\text{RF}}t} + e^{-i\Omega_{\text{RF}}t}) \quad (5.36)$$

Using the rotating wave approximation (RWA) we can simplify this equation to obtain

$$H_I^{\text{RWA}} = \frac{\hbar\Omega}{2}(\sigma_+ e^{i(\Omega_{\text{RF}} - \omega)t} + \sigma_- e^{-i(\Omega_{\text{RF}} - \omega)t}) \quad (5.37)$$

$$H_0^{\text{RWA}} = \frac{\hbar(\omega_0 - \omega)}{2}\sigma_z \quad (5.38)$$

where ω is the frequency of the interacting field. Finding the eigenstates for $H = H_0 + H_I$ and redefining $(\omega_0 - \omega) = \Delta$ we obtain an energy for the new states $|+\rangle, |-\rangle$ of

$$E_{\pm} = -\frac{\hbar\Delta}{2} \pm \frac{\hbar\sqrt{\Omega^2 + \Delta^2}}{2}. \quad (5.39)$$

We measure the splitting of these two states using a “probe” field which in $^{40}\text{Ca}^+$ couples the dressed $|S_{1/2}\rangle$ manifold to $|D_{5/2}\rangle$. Using this probe we can measure the frequency splitting of these two dressed states $\Delta\omega_{\text{AT}}$. Because the atomic frequency difference ω_0 and the “pump” field ω are

both equal to Ω_{RF} , $\Delta = 0$. This results in

$$\Delta\omega_{\text{AT}} = \frac{\Omega}{2} = \frac{\mu B_x}{2\hbar} = \frac{\mu_B g_{1/2} m_{1/2} B_{\perp}}{2\hbar} \quad (5.40)$$

where we have relabeled $B_x = B_{\perp}$ to be any field perpendicular to the quantization axis. For our system $g_{1/2} \approx 2$ and $m_{1/2} = 1/2$ which will result in

$$\Delta\omega_{\text{AT}} = \frac{\mu_B B_{\perp}}{2\hbar}. \quad (5.41)$$

This equation which matches the results in Ref. [117] where $^{138}\text{Ba}^+$ was used. With this result we can now determine the magnitude and orientation of the magnetic field in our system. By orienting the quantization axis in three orthogonal directions we can determine the total magnetic field vector magnitude. However, each of these measurements will contain components along our orthogonal basis so we will have to solve the system of equations to determine the magnitude along each independent direction.

In the experiment, we use rare-earth magnets to generate the required ≈ 2.6 mT field needed to make the frequency splitting of the two $|S_{1/2}\rangle$ ground-states equal to 72 MHz. We orient these along the Pi, Sigma, and Vertical ports which are labeled in Fig. 5.14. By adjusting the spacing of the magnets from the vacuum system we can get the frequency splitting close the required value and use sets of shim coils oriented along the three directions to finely scan the magnetic field splitting through the resonance. An example of the avoided crossing of the resonance peaks from the dressed states can be seen in Fig. 5.15. We determine $B_{\perp,i}$ along each axis by measuring the splitting of the peaks near the zero crossing. We use the labels $i = \sigma, \pi, V$ to label the measurements along the three ports. There was some difficulty in orienting a magnet along the vertical direction because it interferes with the imaging system but we resolve this by cutting a circular magnet in half and placing the two halves around the imaging system. To obtain an estimate of the AC magnetic field amplitude we use measurements where the compensation RF is < -45 dBm, plots of this representative data is seen in Fig. 5.16. From the frequency splitting in these plots we measure magnetic fields of $B_{\perp,\pi} = 3.38(1) \mu\text{T}$, $B_{\perp,\sigma} = 1.31(1) \mu\text{T}$ and $B_{\perp,V} = 5.02(2) \mu\text{T}$. Using these

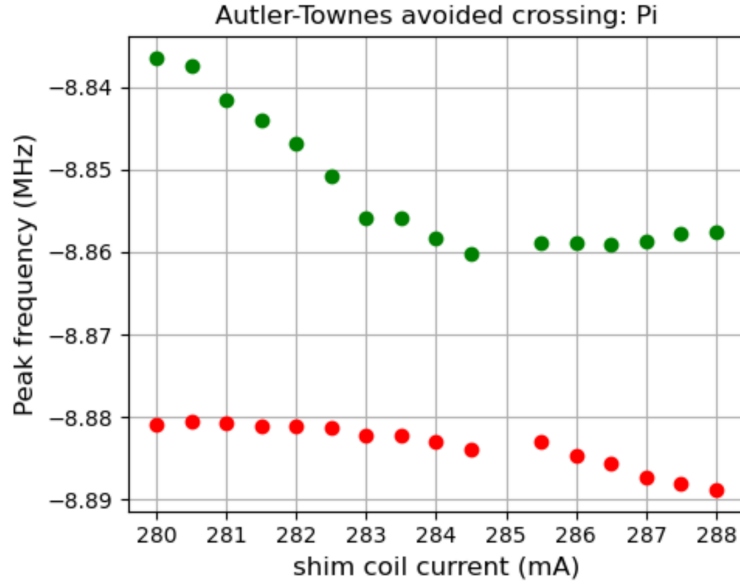


Figure 5.15: Avoided crossing observed along the pi direction. When making measurements of B_{\perp} the field is scanned through the resonance to find the smallest separation which corresponds to the $S_{1/2}$ splitting being equal to Ω_{RF} .

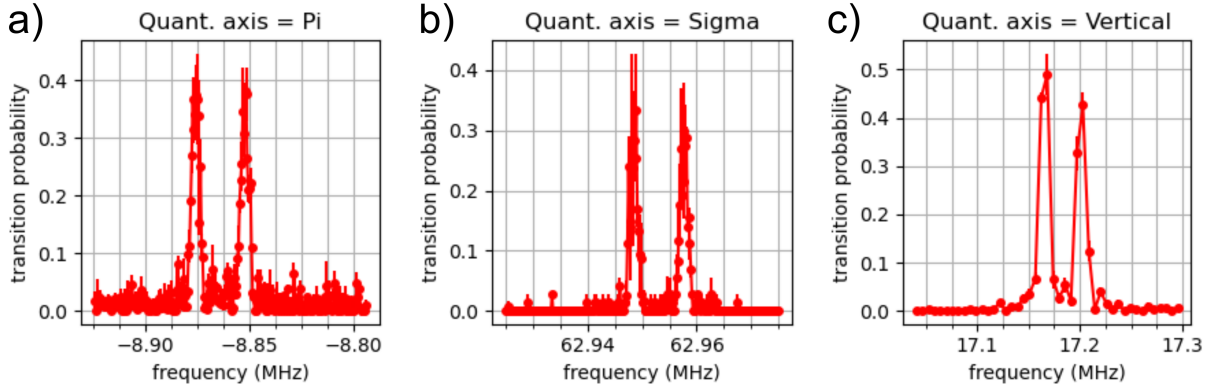


Figure 5.16: Representative measurements of B_{\perp} along the pi, sigma and vertical directions when the axial RF micromotion compensation field is below -45 dBm. From the frequency splittings seen in these plots we measure magnetic fields of $B_{\perp,\pi} = 3.38(1) \mu\text{T}$, $B_{\perp,\sigma} = 1.31(1) \mu\text{T}$ and $B_{\perp,V} = 5.02(2) \mu\text{T}$.

values and the relations

$$B_{\pi} = \frac{1}{2}(B_{\perp,\sigma} - B_{\perp,\pi} + B_{\perp,V}) \quad (5.42)$$

$$B_{\sigma} = \frac{1}{2}(-B_{\perp,\sigma} + B_{\perp,\pi} + B_{\perp,V}) \quad (5.43)$$

$$B_V = \frac{1}{2}(B_{\perp,\sigma} + B_{\perp,\pi} - B_{\perp,V}) \quad (5.44)$$

we determine the AC magnetic field amplitude along the Pi, Sigma, and Vertical directions to be $B_\pi = 1.47(3) \mu\text{T}$, $B_\sigma = 3.54(3) \mu\text{T}$, and $B_V = -0.16(3) \mu\text{T}$. When specifying a final value for a systematic uncertainty these values need to be remeasured at the parameters used for micromotion compensation and RF confinement. With the values stated we can estimate a systematic shift for the quadratic Zeeman effect using $\langle B_{\text{DC}} \rangle^2 = 1 \times 10^{-8} \text{ T}^2$, $\langle B_{\text{AC}} \rangle^2 = 1.48(2) \times 10^{-11} \text{ T}^2$, and $C_2 = -7.1944(24) \times 10^7$ [106] to obtain

$$\frac{\delta\nu}{\nu} = \frac{C_2}{\nu} (\langle B_{\text{DC}}^2 \rangle + \langle B_{\text{AC}}^2 \rangle) = -6433(2) \times 10^{-19}, \quad (5.45)$$

where there is minimal contribution to the uncertainty from B_{DC} because this can be measured with uncertainty below $1 \times 10^{-8} \text{ T}$. The shifts from the AC and DC components separately are $-9.4(1) \times 10^{-19}$ and $-6423(2) \times 10^{-16}$ respectively. This estimate is similar to the one obtained in Ref. [28] and is again limited by uncertainty in C_2 . We also used the Autler-Townes method to determine if there is an effect on B_{AC} when using different trapping fields. The measurements were performed along the sigma and pi quantization axes and we record the effect on the magnitude of $B_{\perp,\sigma}$ and $B_{\perp,\pi}$ in Fig 5.17. It was found that the DC voltages have no noticeable effect on the magnetic field or magnetic field orientation but the RF applied to the endcaps for micromotion compensation and the trap RF amplitude did. For the final systematic evaluation of this system characterizing B_{AC} at the final trapping parameters will be important when determining the shift and shift uncertainty.

5.3 Black-body radiation shift

The BBR shift is characterized by measuring the thermal environment of the $^{40}\text{Ca}^+ / ^{27}\text{Al}^+$ system and using the range of the temperatures across the trap to estimate the uncertainty of this shift. The presence of blackbody radiation in the system will lead to a AC Stark on shift of the clock transition and the magnitude of this shift depends on the sensitivity of the species to thermal radiation and the environment temperature. The sensitivity for a species depends on the static differential polarizability of the clock transition. The static differential polarizability for

AC Zeeman Summary, Trap electrodes

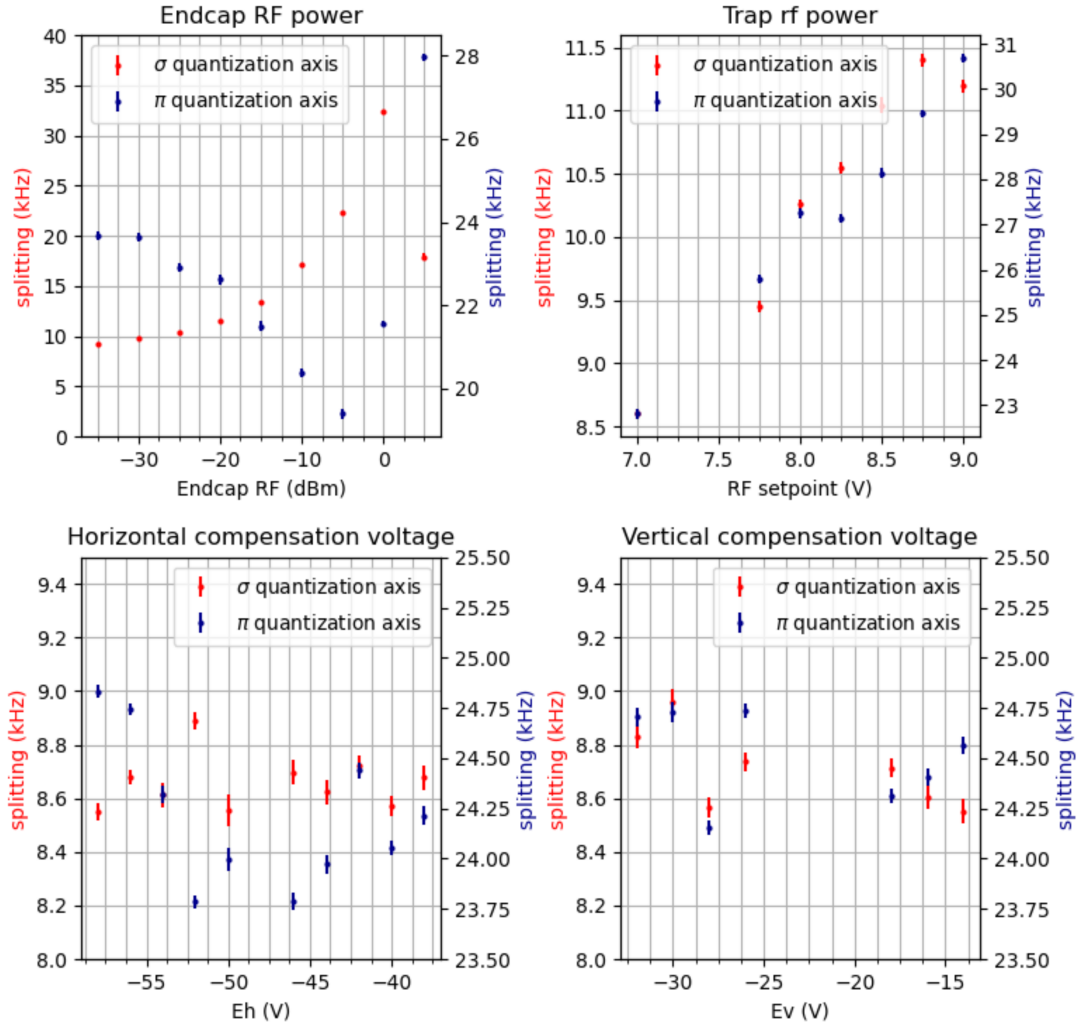


Figure 5.17: Measurement of the Autler-Townes splitting when changing the AC and DC electrode voltage amplitudes. It appears that the DC voltages have no noticeable effect on the value of B_{AC} but varying the RF compensation voltage applied on the endcaps and the trap RF amplitude do have a noticeable impact on the magnitude and direction of the AC magnetic field. While varying these parameters effects the overall shift the uncertainty in the measurement will be insensitive to the measured magnetic field since the frequency of the laser will be unaffected.

$^{27}\text{Al}^+$ is $\Delta\alpha_{\text{clock-}} = (7.02 \pm 0.95) \times 10^{-42} \text{J m}^2/\text{V}^2$ which is insensitive when compared to other systems [119]. This insensitivity makes it less crucial to fully characterize the thermal environment or tightly constrain the uncertainty of the differential polarizability [28]. In our system we measure

with 7 k-type thermocouples located around the setup, with two sensors located on the trap post in vacuum, one hanging from the trap wafer, and 4 sensors attached externally. With these sensors we measure temperatures in the range of 25.95-30.17 C. Using the equation [28]

$$\Delta\nu_{\text{clock}}^{\text{Stark}} = \frac{-\pi\Delta\alpha_{\text{clock}}^{(T)}}{60\epsilon_0c^3} \left(\frac{k_B T}{\hbar}\right)^4, \quad (5.46)$$

where $\Delta\alpha_{\text{clock}}^{(T)}$ is the differential polarizability for the BBR at a temperature T . At room temperature (≈ 300 K), $\Delta\alpha_{\text{clock}}^{(T)} \simeq \Delta\alpha_{\text{clock}}(10 \mu\text{m}) = 7.03(94) \times 10^{-42}$ where $\alpha_{\text{clock}}(10 \mu\text{m})$ is measured by applying an intense laser field at $10 \mu\text{m}$ and measuring the resulting frequency shift [28]. The uncertainty of the shift is given by the equation

$$\sigma_{\Delta\nu_{\text{clock}}^{\text{Stark}}} = \left(\frac{\pi k_B^4}{60\hbar^4\epsilon_0c^3}\right) \sqrt{(T^4\sigma_{\Delta\alpha_{\text{clock}}^{(T)}})^2 + (4\Delta\alpha_{\text{clock}}^{(T)}T^3\Delta T)^2}, \quad (5.47)$$

where $\sigma_{\Delta\alpha_{\text{clock}}^{(T)}}$ is the uncertainty of the differential polarizability and ΔT is the temperature range measured in the system. Using these equations we obtain an estimate of the systematic frequency shift from the average temperature and an uncertainty from the temperature range resulting in a shift of $\delta\nu/\nu = (-33.3 \pm 4.8) \times 10^{-19}$. This effect is likely to be the leading effect in this uncertainty budget but a longer temperature time series at the final RF trap drive power needs to be measured to determine the final systematic shift. Future measurements can reduce the uncertainty of this shift by better characterizing the thermal environment to obtain a better constraint on T , operating the clock at cryogenic temperatures, or measuring the value of $\Delta\alpha_{\text{clock}}(10\mu\text{m})$ with higher precision. It is likely that some combination of these methods will be the best way forward.

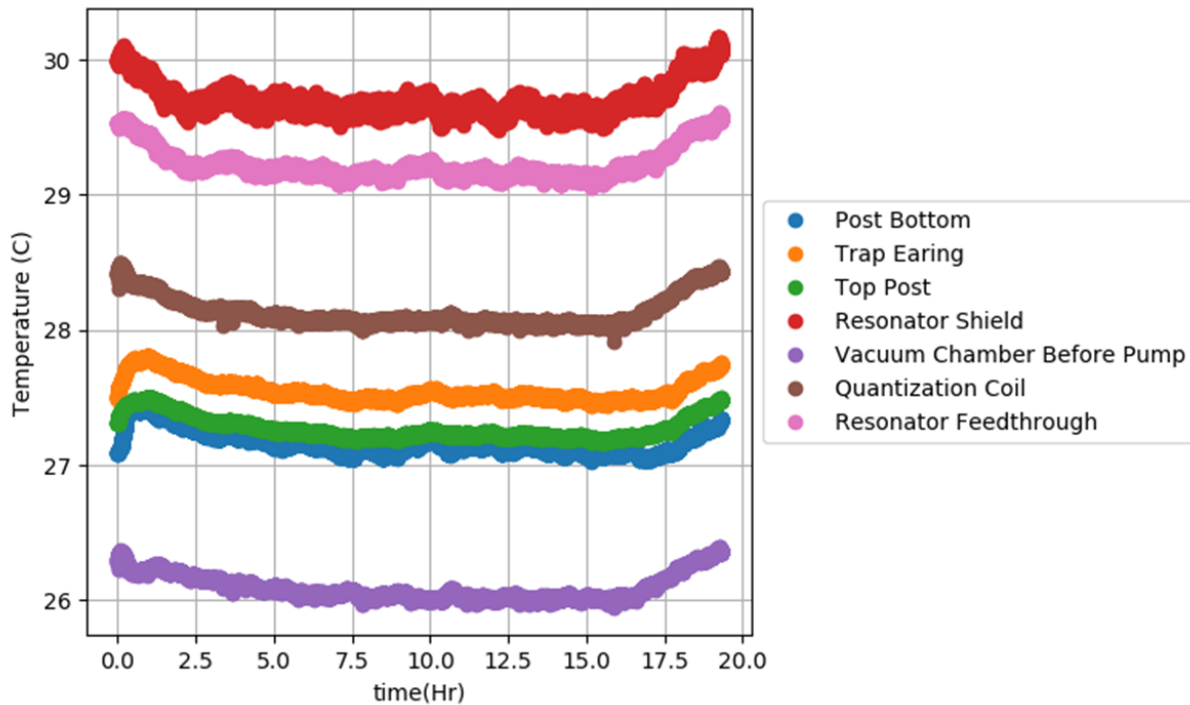


Figure 5.18: Time series of the temperatures measured in our system with k-type thermocouples for a 20 hr. period. The temperature is measured using three in-vacuum sensors located at the bottom of copper trap post, at the top of the trap post, and attached to a copper ribbon mounted to the trap wafer (trap earing). The temperature is also measured outside of the vacuum system on the resonator shield, on the ion pump neck, on the quantization axis coil, and on the conflat feedthrough for the resonator. Measuring at these locations gives us a representative range of the thermal environment seen by the ion. With the measurements we observe a temperature range of 25.95-30.17 C over this period. Data over longer timescales is needed to measure the long term behavior of the thermal environment.

Chapter 6

Conclusion

In this thesis, I have described the $^{40}\text{Ca}^+ / ^{27}\text{Al}^+$ experimental system, demonstrated two differential comparison techniques correlation and differential spectroscopy, and discussed the current status of the systematic evaluation of the $^{40}\text{Ca}^+ / ^{27}\text{Al}^+$ clock. With each of these topics I will summarize the results and present an outlook for future experiments.

Improvements to our experimental setup include: building a vacuum system with parts primarily made of titanium, improved wheel trap design to better balance the capacitance between trap electrodes, and an improved meander line resonator design to reach quality factors of 170. We load both $^{40}\text{Ca}^+$ and $^{27}\text{Al}^+$ from a single Ca/Al alloy target and have implemented state preparation procedures to prepare the $^{27}\text{Al}^+$ ion in the inner 1S_0 manifold allowing clock interrogations with lower magnetic field sensitivity transitions. In the titanium vacuum system we have observed a reduction in AlH^+ formation rates in correlation spectroscopy when compared to the $^{25}\text{Mg}^+ / ^{27}\text{Al}^+$ system. In correlation spectroscopy the $^{25}\text{Mg}^+ / ^{27}\text{Al}^+$ experiment limited the up-time of the measurements due to the system forming an AlH^+ molecule on an average timescale of ≈ 30 min where the $^{40}\text{Ca}^+ / ^{27}\text{Al}^+$ system would only form an AlH^+ molecule once a day. In the 36 hour comparison using ZDT differential spectroscopy we only formed 2 AlH^+ molecules over the course of the measurements. However, when comparing the pressures of the $^{25}\text{Mg}^+ / ^{27}\text{Al}^+$ and $^{40}\text{Ca}^+ / ^{27}\text{Al}^+$ systems, we do not see a proportional reduction in the total background pressure [55] which indicates some other gas besides H_2 is limiting the background pressure in the $^{40}\text{Ca}^+ / ^{27}\text{Al}^+$ system. In future experiments the vacuum can be improved with increased conductance to the ion pump. The

impact of AlH^+ on the clock duty cycle could alternatively be reduced by photo-dissociating the molecule [120]. With the current reduction in the AlH^+ formation rate we expect higher uptime in future clock comparisons. With improvements in trap design we also observe better control over the axial micromotion which results a reduction of the total micromotion shift in our system. The improvements in resonator board design allow for high radial confinement and a better filtered RF trap frequency. With the use of alumina as the resonator PCB substrate we also see better thermal stability of the resonator board which will lead to more stable trap frequencies. The hardware improvements used in this version of the $^{27}\text{Al}^+$ quantum logic clock will be helpful for the operation of the clock and will have a significant effect on the systematic evaluation.

Using correlation and differential spectroscopy we demonstrate differential frequency comparisons with maximum probe durations of 8 s and 1.7 s. We demonstrate correlation spectroscopy between a $^{40}\text{Ca}^+ / ^{27}\text{Al}^+$ and a $^{25}\text{Mg}^+ / ^{27}\text{Al}^+$ quantum logic clock and observe frequency comparison measurement instabilities of $\approx 2.8 \times 10^{-16} / \sqrt{\tau}$ with Ramsey free evolution periods of 8 s [56]. With this measurement instability we can reach frequency comparison statistical uncertainties of 1×10^{-18} with a few day measurement campaign. In future measurements of fundamental atomic parameters, for example the quadratic Zeeman coefficient [106] or the differential polarizability [28], correlation spectroscopy can be used to make a more precise measurement of the differential shifts induced in these systems which will allow for better constraints of the atomic properties. Also, the measurement stability of correlation spectroscopy could be improved further by using entanglement between the two clocks [121] or by using compound oscillators which have matching frequencies. For instance, if a clock operating at ω_1 is compared against an atomic clock based on a species with oscillator frequency $\omega_1/2$, then a Greenberger–Horne–Zeilinger (GHZ) state [122] of two atoms can be used to make the oscillator phase evolution equivalent. This would allow correlation spectroscopy to be used with atomic clocks that have species with very different oscillator frequencies. Correlation spectroscopy with GHZ states also has the benefit of being insensitive to atom-laser dephasing because it is a relative frequency measurement. Correlation spectroscopy between unentangled atoms is useful in testing the accuracy of similar frequency clocks but the technique could

also be useful for measurements that don't require comparisons between different clock species like relativistic geodesy [7, 123, 49] and tests of Lorentz invariance [11, 12, 13]. A GHZ state is just one example of a useful entangled state and it would be interesting to study how different entangled states interact with differential comparison techniques. Additionally, this correlation spectroscopy could be useful for mobile atomic clocks because the laser stability is not as important for comparisons. This would minimize the technical challenge of stabilizing the laser system remotely. Correlation spectroscopy is a technique which is useful in circumventing limits imposed by the local oscillator stability or other correlated noise effects and is useful in characterizing systemic shifts within systems [124] and in the future between systems.

We demonstrate differential spectroscopy with a $^{40}\text{Ca}^+ / ^{27}\text{Al}^+$ quantum logic clock and a ^{171}Yb optical lattice clock and extend this technique by operating two ^{171}Yb optical lattice clocks in a zero deadtime (ZDT) configuration. With these two techniques we observe a measurement instability of $2.5 \times 10^{-16} / \sqrt{\tau}$ for a probe duration of 750 ms with differential spectroscopy and a measurement instability of $1.9 \times 10^{-16} / \sqrt{\tau}$ for a probe time of 1.7 s with ZDT differential spectroscopy [57]. Differential spectroscopy is a technique which is used between different frequency atomic clocks but requires one atomic clock to have a low enough single shot measurement uncertainty to correct the local oscillator phase [100]. This technique can also improve the frequency comparison measurement instability for two clocks with small single shot measurement uncertainty by using a maximum likelihood phase estimation algorithm to allow for phase inversion beyond the laser coherence time [100]. Differential spectroscopy can be extended by operating two ^{171}Yb optical lattice clocks in a ZDT configuration where the evolved laser phase can be continuously measured and does not require a difference in the atomic clock frequencies to improve the measurement instability in long clock interrogations. Because the third atomic clock is still performing an absolute phase measurement this technique can still be used to stabilize the local oscillator which is not possible with the relative phase measurements of correlation spectroscopy. Differential spectroscopy offers the possibility of improving constraints on various tests of fundamental physics, relativistic geodesy and tests of Lorentz invariance and can offer a comparison technique to further

constrain the variation of the fine structure constant [125, 126, 127, 128] and bound coupling of scalar dark matter fields to the systems [129] where the improved measurement instability would allow for higher frequencies variations and smaller shifts to be measured. Much like correlation spectroscopy, differential spectroscopy could be useful when comparing clocks using entangled states since local oscillator dephasing can be accounted for. Lastly, differential spectroscopy will allow for even lower frequency ratio measurement uncertainty which will be important in future frequency ratio closures [35, 36] needed for redefining the second in terms of an optical frequency.

The evaluation of the $^{40}\text{Ca}^+ / ^{27}\text{Al}^+$ quantum logic clock is well underway and the results are encouraging. After fixing the capacitive imbalances of the wheel trap electrodes, micromotion can be better compensated where we observe the ability to reduce shifts to the range of 10^{-19} fractionally. This lower shift should translate into a lower systematic uncertainty which will likely lead to the BBR shift being the leading source of systematic uncertainty. However, the micromotion shift needs to be further evaluated by making resolved sideband measurements with $^{27}\text{Al}^+$ to decouple this shift from the impact of oscillating magnetic fields [114] and performing more measurements to constrain the beam pointing error and obtain measurements of the long term stability of the compensation parameters. We have performed preliminary measurements where an RF compensation field is applied along the vertical direction. The vertical compensation field resulted in further reduction in the magnitude of the vertical micromotion shift but we found the circuit used to couple in the RF was thermally unstable. Better circuit design for the coupling circuit will result in a thermally stable RF signal that will result in further cancellation of micromotion. By measuring the magnetic field oscillating at the trap RF frequency with the Autler-Townes effect we measure the total magnetic field to be $\langle B_{\text{AC}} \rangle^2 = 1.48(2) \times 10^{-11} \text{ T}^2$. This should result in a total quadratic Zeeman shift of $\delta\nu/\nu = -6433(2) \times 10^{-19}$. The final trap and quantization field parameters are still being determined for the system so the total shift and uncertainty will vary but will likely remain at this magnitude. We are in the process of developing a second method to measure the AC magnetic field which uses a resolved sideband method similar to how micromotion measurements are performed. This technique offers a second check on the AC magnetic field and a way to measure the effect with

optical transitions and does not require large quantization fields. Sideband cooling has been used in the system to measure the heating rates due to electric field noise but characterization of the second order Doppler shift from secular motion is still underway. With the development of the new comparison techniques an uncertainty budget will need to be developed for longer interrogation times which will be impacted by background gas collisions [55] and the ion secular modes heating over the evolution period.

I am excited to see how the systematic evaluation progresses and hope to see a further reduction in systematic uncertainty when compared to the previous $^{27}\text{Al}^+$ quantum-logic clock. Final characterization of the ion crystal temperature and micromotion shifts need to be made before this is done. Most of all, I am eager to see the use of differential comparison techniques like these to improve the performance when testing fundamental physics and constraining possible extensions to our understanding of physics. Optical atomic clocks are platforms that can both improve metrology and explore new ideas in physics and it will be exciting to see these areas progress in the future.

Bibliography

- [1] F. Riehle. Towards a redefinition of the second based on optical atomic clocks. Comptes Rendus Physique, 16(5):506–515, 2015.
- [2] A. Bauch. Caesium atomic clocks: function, performance and applications. Measurement Science and Technology, 14(8):1159, 2003.
- [3] R. Wynands and S. Weyers. Atomic fountain clocks. Metrologia, 42(3):S64, 2005.
- [4] B. Jaduszliwer and J. Camparo. Past, present and future of atomic clocks for GNSS. GPS Solutions, 25(1):1–13, 2021.
- [5] V. Martin, J. P. Brito, C. Escribano, M. Menchetti, C. White, A. Lord, F. Wissel, M. Gunkel, P. Gavignet, N. Genay, et al. Quantum technologies in the telecommunications industry. EPJ Quantum Technology, 8(1):19, 2021.
- [6] E. L. English, A. Ashkhasi, and P. Whibberley. Distributing time by fibre. Contemporary Physics, pages 1–15, 2021.
- [7] T. E. Mehlstäubler, G. Grosche, C. Lisdat, P. O. Schmidt, and H. Denker. Atomic clocks for geodesy. Reports on Progress in Physics, 81(6):064401, 2018.
- [8] A. Derevianko and M. Pospelov. Hunting for topological dark matter with atomic clocks. Nature Physics, 10(12):933–936, 2014.
- [9] A. Arvanitaki, J. Huang, and K. Van Tilburg. Searching for dilaton dark matter with atomic clocks. Physical Review D, 91(1):015015, 2015.
- [10] P. Wcisło, P. Ablewski, K. Beloy, S. Bilicki, M. Bober, R. Brown, R. Fasano, R. Ciuryło, H. Hachisu, T. Ido, et al. New bounds on dark matter coupling from a global network of optical atomic clocks. Science Advances, 4(12):eaau4869, 2018.
- [11] R. Lange, N. Huntemann, J. Rahm, C. Sanner, H. Shao, B. Lipphardt, C. Tamm, S. Weyers, and E. Peik. Improved limits for violations of local position invariance from atomic clock comparisons. Physical Review Letters, 126(1):011102, 2021.
- [12] R. Shaniy, R. Ozeri, M. S. Safronova, S. G. Porsev, V. A. Dzuba, V. V. Flambaum, and H. Häffner. New methods for testing Lorentz invariance with atomic systems. Physical Review Letters, 120(10):103202, 2018.

- [13] C. Sanner, N. Huntemann, R. Lange, C. Tamm, E. Peik, M. S. Safronova, and S. G. Porsev. Optical clock comparison for Lorentz symmetry testing. *Nature*, 567(7747):204–208, 2019.
- [14] F. Riehle, P. Gill, F. Arias, and L. Robertsson. The cipm list of recommended frequency standard values: guidelines and procedures. *Metrologia*, 55(2):188, 2018.
- [15] A. D. Ludlow, M. M. Boyd, J. Ye, E. Peik, and P. O. Schmidt. Optical atomic clocks. *Reviews of Modern Physics*, 87(2):637, 2015.
- [16] M. A. Martin-Delgado. The new SI and the fundamental constants of nature. *European Journal of Physics*, 41(6):063003, 2020.
- [17] H. Leopardi, J. Davila-Rodriguez, F. Quinlan, J. Olson, J. A. Sherman, S. A. Diddams, and T. M. Fortier. Single-branch Er:fiber frequency comb for precision optical metrology with 10^{-18} fractional instability. *Optica*, 4(8):879–885, 2017.
- [18] N. V. Nardelli, T. M. Fortier, M. Pomponio, E. Baumann, C. Nelson, T. R. Schibli, and A. Hati. 10 GHz generation with ultra-low phase noise via the transfer oscillator technique. *APL Photonics*, 7(2):026105, 2022.
- [19] D. Matei, T. Legero, S. Häfner, C. Grebing, R. Weyrich, W. Zhang, L. Sonderhouse, J. Robinson, J. Ye, F. Riehle, et al. 1.5 μm lasers with Sub-10 mHz linewidth. *Physical review letters*, 118(26):263202, 2017.
- [20] T. Fortier and E. Baumann. 20 years of developments in optical frequency comb technology and applications. *Communications Physics*, 2(1):1–16, 2019.
- [21] D. R. Leibbrandt, M. J. Thorpe, M. Notcutt, R. E. Drullinger, T. Rosenband, and J. C. Bergquist. Spherical reference cavities for frequency stabilization of lasers in non-laboratory environments. *Optics express*, 19(4):3471–3482, 2011.
- [22] S. Stein and R. Filler. Kalman filter analysis for real time applications of clocks and oscillators. In *Proceedings of the 42nd Annual Frequency Control Symposium, 1988.*, pages 447–452. IEEE, 1988.
- [23] K. G. Mishagin, V. A. Lysenko, and S. Y. Medvedev. A practical approach to optimal control problem for atomic clocks. *IEEE Transactions on Ultrasonics, Ferroelectrics, and Frequency Control*, 67(5):1080–1087, 2019.
- [24] J.-S. Chen, S. M. Brewer, C. Chou, D. Wineland, D. Leibbrandt, and D. Hume. Sympathetic ground state cooling and time-dilation shifts in an $^{27}\text{Al}^+$ optical clock. *Physical Review Letters*, 118(5):053002, 2017.
- [25] W. McGrew, X. Zhang, R. Fasano, S. Schäffer, K. Beloy, D. Nicolodi, R. Brown, N. Hinkley, G. Milani, M. Schioppo, et al. Atomic clock performance enabling geodesy below the centimetre level. *Nature*, 564(7734):87–90, 2018.
- [26] T. Bothwell, D. Kedar, E. Oelker, J. M. Robinson, S. L. Bromley, W. L. Tew, J. Ye, and C. J. Kennedy. JILA SrI optical lattice clock with uncertainty of 2.0×10^{-18} . *Metrologia*, 56(6):065004, 2019.

- [27] I. Ushijima, M. Takamoto, M. Das, T. Ohkubo, and H. Katori. Cryogenic optical lattice clocks. *Nature Photonics*, 9(3):185–189, 2015.
- [28] S. Brewer, J.-S. Chen, A. Hankin, E. Clements, C. Chou, D. Wineland, D. Hume, and D. Leibbrandt. $^{27}\text{Al}^+$ quantum-logic clock with a systematic uncertainty below 10^{-18} . *Physical Review Letters*, 123(3):033201, July 2019.
- [29] N. Huntemann, C. Sanner, B. Lipphardt, C. Tamm, and E. Peik. Single-Ion Atomic Clock with 3×10^{-18} Systematic Uncertainty. *Physical Review Letters*, 116(6), February 2016.
- [30] S. Falke, N. Lemke, C. Grebing, B. Lipphardt, S. Weyers, V. Gerginov, N. Huntemann, C. Hagemann, A. Al-Masoudi, S. Häfner, et al. A strontium lattice clock with inaccuracy 3×10^{-17} and its frequency. *New Journal of Physics*, 16(7):073023, 2014.
- [31] J. Cao, P. Zhang, J. Shang, K. Cui, J. Yuan, S. Chao, S. Wang, H. Shu, and X. Huang. A compact, transportable single-ion optical clock with 7.8×10^{-17} systematic uncertainty. *Applied Physics B*, 123(4):1–9, 2017.
- [32] S. Hannig, L. Pelzer, N. Scharnhorst, J. Kramer, M. Stepanova, Z. Xu, N. Spethmann, I. Leroux, T. Mehlstäubler, and P. Schmidt. Towards a transportable aluminium ion quantum logic optical clock. *Review of Scientific Instruments*, 90(5):053204, 2019.
- [33] N. Ohmae, K. Yamanaka, I. Ushijima, M. Takamoto, and H. Katori. Frequency ratio measurement of Hg and Sr optical lattice clocks. In *European Quantum Electronics Conference*, page ED_3.2. Optical Society of America, 2015.
- [34] A. W. Young, W. J. Eckner, W. R. Milner, D. Kedar, M. A. Norcia, E. Oelker, N. Schine, J. Ye, and A. M. Kaufman. Half-minute-scale atomic coherence and high relative stability in a tweezer clock. *Nature*, 588(7838):408–413, 2020.
- [35] B. A. C. O. N. Collaboration. Frequency ratio measurements at 18-digit accuracy using an optical clock network. *Nature*, 591(7851):564–569, 2021.
- [36] M. Takamoto, I. Ushijima, M. Das, N. Nemitz, T. Ohkubo, K. Yamanaka, N. Ohmae, T. Takano, T. Akatsuka, A. Yamaguchi, et al. Frequency ratios of Sr, Yb, and Hg based optical lattice clocks and their applications. *Comptes Rendus Physique*, 16(5):489–498, 2015.
- [37] H. Leopardi, K. Beloy, T. Bothwell, S. M. Brewer, S. L. Bromley, J.-S. Chen, S. A. Diddams, R. J. Fasano, Y. S. Hassan, D. B. Hume, et al. Measurement of the $^{27}\text{Al}^+$ and ^{87}Sr absolute optical frequencies. *Metrologia*, 58(1):015017, 2021.
- [38] S. Bilicki, E. Bookjans, G. Vallet, M. Abgrall, R. Le Targat, and J. Lodewyck. Contributing to TAI with Sr optical lattice clocks. In *2017 Joint Conference of the European Frequency and Time Forum and IEEE International Frequency Control Symposium (EFTF/IFCS)*, pages 815–816. IEEE, 2017.
- [39] P. Wolf, G. Petit, E. Peik, C. Tamm, H. Schnatz, B. Lipphardt, S. Weyers, R. Wynands, J. Richard, S. Bize, et al. Comparing high accuracy frequency standards via TAI. In *Proceedings of the 20th European Frequency and Time Forum*, pages 476–485. IEEE, 2006.
- [40] H. Hachisu, F. Nakagawa, Y. Hanado, and T. Ido. Months-long real-time generation of a time scale based on an optical clock. *Scientific Reports*, 8(1):1–12, 2018.

- [41] R. Tyumenev, M. Favier, S. Bilicki, E. Bookjans, R. Le Targat, J. Lodewyck, D. Nicolodi, Y. Le Coq, M. Abgrall, J. Guéna, et al. Comparing a mercury optical lattice clock with microwave and optical frequency standards. New Journal of Physics, 18(11):113002, 2016.
- [42] N. Nemitz, T. Ohkubo, M. Takamoto, I. Ushijima, M. Das, N. Ohmae, and H. Katori. Frequency ratio of Yb and Sr clocks with 5×10^{-17} uncertainty at 150 seconds averaging time. Nature Photonics, 10(4):258–261, 2016.
- [43] N. Ohmae, F. Bregolin, N. Nemitz, and H. Katori. Direct measurement of the frequency ratio for hg and yb optical lattice clocks and closure of the hg/yb/sr loop. Optics Express, 28(10):15112–15121, 2020.
- [44] W. M. Itano, J. C. Bergquist, J. J. Bollinger, J. Gilligan, D. Heinzen, F. Moore, M. Raizen, and D. J. Wineland. Quantum projection noise: Population fluctuations in two-level systems. Physical Review A, 47(5):3554, 1993.
- [45] C. Cecilia, C. Davide, F. Matteo, M. Alberto, and L. Filippo. A fiber link for the remote comparison of optical clocks and geodesy experiments. In 2015 Joint Conference of the IEEE International Frequency Control Symposium & the European Frequency and Time Forum, pages 579–582. IEEE, 2015.
- [46] J. Grotti, S. Koller, S. Vogt, S. Häfner, U. Sterr, C. Lisdat, H. Denker, C. Voigt, L. Timmen, A. Rolland, et al. Geodesy and metrology with a transportable optical clock. Nature Physics, 14(5):437–441, 2018.
- [47] S. Koller, J. Grotti, A. Al-Masoudi, S. Dörscher, S. Häfner, U. Sterr, C. Lisdat, et al. Transportable optical lattice clock with 7×10^{-17} uncertainty. Physical review letters, 118(7):073601, 2017.
- [48] M. Takamoto, I. Ushijima, N. Ohmae, T. Yahagi, K. Kokado, H. Shinkai, and H. Katori. Test of general relativity by a pair of transportable optical lattice clocks. Nature Photonics, 14(7):411–415, 2020.
- [49] T. Bothwell, C. J. Kennedy, A. Aeppli, D. Kedar, J. M. Robinson, E. Oelker, A. Staron, and J. Ye. Resolving the gravitational redshift across a millimetre-scale atomic sample. Nature, 602(7897):420–424, 2022.
- [50] B. M. Roberts, P. Delva, A. Al-Masoudi, A. Amy-Klein, C. Baerentsen, C. Baynham, E. Benkler, S. Bilicki, S. Bize, W. Bowden, et al. Search for transient variations of the fine structure constant and dark matter using fiber-linked optical atomic clocks. New Journal of Physics, 22(9):093010, 2020.
- [51] G. D. Cole, W. Zhang, B. J. Bjork, D. Follman, P. Heu, C. Deutsch, L. Sonderhouse, J. Robinson, C. Franz, A. Alexandrovski, et al. High-performance near-and mid-infrared crystalline coatings. Optica, 3(6):647–656, 2016.
- [52] T. Kessler, C. Hagemann, C. Grebing, T. Legero, U. Sterr, F. Riehle, M. Martin, L. Chen, and J. Ye. A sub-40-mHz-linewidth laser based on a silicon single-crystal optical cavity. Nature Photonics, 6(10):687–692, 2012.

- [53] J. M. Robinson, E. Oelker, W. R. Milner, W. Zhang, T. Legero, D. G. Matei, F. Riehle, U. Sterr, and J. Ye. Crystalline optical cavity at 4 k with thermal-noise-limited instability and ultralow drift. Optica, 6(2):240–243, 2019.
- [54] J.-S. Chen. Ticking near the zero-point energy: Towards 1×10^{-18} accuracy in Al^+ optical clocks. PhD Thesis, University of Colorado at Boulder, 2017.
- [55] A. M. Hankin, E. Clements, Y. Huang, S. M. Brewer, J.-S. Chen, C.-W. Chou, D. Hume, and D. Leibbrandt. Systematic uncertainty due to background-gas collisions in trapped-ion optical clocks. Physical Review A, 100(3):033419, 2019.
- [56] E. R. Clements, M. E. Kim, K. Cui, A. M. Hankin, S. M. Brewer, J. Valencia, J.-S. Chen, C.-W. Chou, D. R. Leibbrandt, and D. B. Hume. Lifetime-limited interrogation of two independent $^{27}\text{Al}^+$ clocks using correlation spectroscopy. Physical review letters, 125(24):243602, 2020.
- [57] M. E. Kim, W. F. McGrew, N. V. Nardelli, E. R. Clements, Y. S. Hassan, X. Zhang, J. L. Valencia, H. Leopardi, D. B. Hume, T. M. Fortier, et al. Optical coherence between atomic species at the second scale: improved clock comparisons via differential spectroscopy. arXiv preprint arXiv:2109.09540, 2021.
- [58] D. J. Wineland, C. Monroe, W. M. Itano, D. Leibfried, B. E. King, and D. M. Meekhof. Experimental issues in coherent quantum-state manipulation of trapped atomic ions. Journal of research of the National Institute of Standards and Technology, 103(3):259, 1998.
- [59] J. B. Wübbena, S. Amairi, O. Mandel, and P. O. Schmidt. Sympathetic cooling of mixed-species two-ion crystals for precision spectroscopy. Physical Review A, 85(4):043412, 2012.
- [60] H. Kurisu, T. Muranaka, N. Wada, S. Yamamoto, M. Matsuura, and M. Hesaka. Titanium alloy material with very low outgassing. Journal of Vacuum Science & Technology A: Vacuum, Surfaces, and Films, 21(5):L10–L12, September 2003.
- [61] M. Minato and Y. Itoh. Vacuum characteristics of titanium. Journal of Vacuum Science & Technology A: Vacuum, Surfaces, and Films, 13(3):540–544, May 1995.
- [62] R. F. Berg. Hydrogen traps in the outgassing model of a stainless steel vacuum chamber. Journal of Vacuum Science & Technology A: Vacuum, Surfaces, and Films, 32(3):031604, 2014.
- [63] C. Roos, T. Zeiger, H. Rohde, H. Nägerl, J. Eschner, D. Leibfried, F. Schmidt-Kaler, and R. Blatt. Quantum state engineering on an optical transition and decoherence in a Paul trap. Physical Review Letters, 83(23):4713, 1999.
- [64] D. Berkeland and M. Boshier. Destabilization of dark states and optical spectroscopy in Zeeman-degenerate atomic systems. Physical Review A, 65(3):033413, 2002.
- [65] D. Allcock, T. Harty, M. Sepiol, H. Janacek, C. Ballance, A. Steane, D. Lucas, and D. Stacey. Dark-resonance Doppler cooling and high fluorescence in trapped Ca-43 ions at intermediate magnetic field. New Journal of Physics, 18(2):023043, 2016.
- [66] A. Rasmusson, M. D’Onofrio, Y. Xie, J. Cui, and P. Richerme. Optimized pulsed sideband cooling and enhanced thermometry of trapped ions. Physical Review A, 104(4):043108, 2021.

- [67] Q. Mechanics. by c. cohen-tannoudji, b. diu, f. laloe, 1977.
- [68] D. James. Quantum dynamics of cold trapped ions with application. Quantum Computation and Quantum Information Theory: Reprint Volume with Introductory Notes for ISI TMR Network School, 12-23 July 1999, Villa Gualino, Torino, Italy, 66:345, 2000.
- [69] G. Tommaseo, T. Pfeil, G. Revalde, G. Werth, P. Indelicato, and J. Desclaux. The g_j -factor in the ground state of Ca^+ . The European Physical Journal D-Atomic, Molecular, Optical and Plasma Physics, 25(2):113–121, 2003.
- [70] M. M. Chwalla. Precision spectroscopy with $^{40}\text{Ca}^+$ ions in a Paul trap. PhD thesis, Universität Innsbruck, 2009.
- [71] C.-w. Chou, C. Kurz, D. B. Hume, P. N. Plessow, D. R. Leibbrandt, and D. Leibfried. Preparation and coherent manipulation of pure quantum states of a single molecular ion. Nature, 545(7653):203–207, 2017.
- [72] J. I. Thorpe, K. Numata, and J. Livas. Laser frequency stabilization and control through offset sideband locking to optical cavities. Optics express, 16(20):15980–15990, 2008.
- [73] D. R. Leibbrandt and J. Heidecker. An open source digital servo for atomic, molecular, and optical physics experiments. Review of Scientific Instruments, 86(12):123115, 2015.
- [74] E. A. Donley, T. P. Heavner, F. Levi, M. Tataw, and S. R. Jefferts. Double-pass acousto-optic modulator system. Review of Scientific Instruments, 76(6):063112, 2005.
- [75] M. Guggemos. Precision spectroscopy with trapped $^{40}\text{Ca}^+$ and $^{27}\text{Al}^+$ ions. PhD thesis, Universität Innsbruck, 2017.
- [76] M. Guggemos, M. Guevara-Bertsch, D. Heinrich, O. Herrera-Sancho, Y. Colombe, R. Blatt, and C. Roos. Frequency measurement of the $^1\text{S}_0, F = 5/2 \leftrightarrow ^3\text{P}_1, F = 7/2$ transition of $^{27}\text{Al}^+$ via quantum logic spectroscopy with $^{40}\text{Ca}^+$. New Journal of Physics, 21(10):103003, 2019.
- [77] P. O. Schmidt, T. Rosenband, C. Langer, W. M. Itano, J. C. Bergquist, and D. J. Wineland. Spectroscopy using quantum logic. Science, 309(5735):749–752, 2005.
- [78] B. Young, F. Cruz, W. Itano, and J. Bergquist. Visible lasers with subhertz linewidths. Physical Review Letters, 82(19):3799, 1999.
- [79] L.-S. Ma, P. Jungner, J. Ye, and J. L. Hall. Delivering the same optical frequency at two places: accurate cancellation of phase noise introduced by an optical fiber or other time-varying path. Optics Letters, 19(21):1777, November 1994.
- [80] J. Ye, J.-L. Peng, R. J. Jones, K. W. Holman, J. L. Hall, D. J. Jones, S. A. Diddams, J. Kitching, S. Bize, J. C. Bergquist, et al. Delivery of high-stability optical and microwave frequency standards over an optical fiber network. JOSA B, 20(7):1459–1467, 2003.
- [81] F. Wolf, Y. Wan, J. C. Heip, F. Gebert, C. Shi, and P. O. Schmidt. Non-destructive state detection for quantum logic spectroscopy of molecular ions. Nature, 530(7591):457–460, 2016.
- [82] P. Micke, T. Leopold, S. King, E. Benkler, L. Spieß, L. Schmoeger, M. Schwarz, J. Crespo López-Urrutia, and P. Schmidt. Coherent laser spectroscopy of highly charged ions using quantum logic. Nature, 578(7793):60–65, 2020.

- [83] M. Chwalla, K. Kim, T. Monz, P. Schindler, M. Riebe, C. Roos, and R. Blatt. Precision spectroscopy with two correlated atoms. Applied Physics B, 89(4):483–488, 2007.
- [84] S. Olmschenk, K. C. Younge, D. L. Moehring, D. N. Matsukevich, P. Maunz, and C. Monroe. Manipulation and detection of a trapped Yb^+ hyperfine qubit. Physical Review A, 76(5):052314, November 2007.
- [85] C.-W. Chou, D. Hume, M. J. Thorpe, D. J. Wineland, and T. Rosenband. Quantum coherence between two atoms beyond $Q = 10^{15}$. Physical review letters, 106(16):160801, 2011.
- [86] T. R. Tan, R. Kaewuam, K. J. Arnold, S. R. Chanu, Z. Zhang, M. Safronova, and M. D. Barrett. Suppressing inhomogeneous broadening in a lutetium multi-ion optical clock. Physical Review Letters, 123(6):063201, 2019.
- [87] R. Shaniv, N. Akerman, T. Manovitz, Y. Shapira, and R. Ozeri. Quadrupole shift cancellation using dynamic decoupling. Physical Review Letters, 122(22):223204, 2019.
- [88] T. Manovitz, R. Shaniv, Y. Shapira, R. Ozeri, and N. Akerman. Precision measurement of atomic isotope shifts using a two-isotope entangled state. Physical Review Letters, 123(20):203001, 2019.
- [89] G. E. Marti, R. B. Hutson, A. Goban, S. L. Campbell, N. Poli, and J. Ye. Imaging optical frequencies with 100 μHz precision and 1.1 μm resolution. Physical review letters, 120(10):103201, 2018.
- [90] X. Zheng, J. Dolde, V. Lochab, B. N. Merriman, H. Li, and S. Kolkowitz. Differential clock comparisons with a multiplexed optical lattice clock. Nature, 602(7897):425–430, 2022.
- [91] E. Riis and A. G. Sinclair. Optimum measurement strategies for trapped ion optical frequency standards. Journal of Physics B: Atomic, Molecular and Optical Physics, 37(24):4719–4732, December 2004.
- [92] I. D. Leroux, N. Scharnhorst, S. Hannig, J. Kramer, L. Pelzer, M. Stepanova, and P. O. Schmidt. On-line estimation of local oscillator noise and optimisation of servo parameters in atomic clocks. Metrologia, 54(3):307, 2017.
- [93] J. B. Dick. Local oscillator induced instabilities in trapped ion frequency standards. Proc. Precise Time and Time Interval Meeting, pages 133–147, 1987.
- [94] Norman F. Ramsey. Molecular Beams. Oxford University Press, London, 1956.
- [95] J. E. Gray and D. W. Allan. A method for estimating the frequency stability of an individual oscillator. In 28th Annual Symposium on Frequency Control, pages 243–246. IEEE, 1974.
- [96] D. Wineland, J. Bergquist, J. Bollinger, R. Drullinger, and W. Itano. Quantum computers and atomic clocks. In Frequency Standards and Metrology, pages 361–368. World Scientific, 2002.
- [97] Y. Colombe, D. H. Slichter, A. C. Wilson, D. Leibfried, and D. J. Wineland. Single-mode optical fiber for high-power, low-loss UV transmission. Optics express, 22(16):19783–19793, 2014.

- [98] T. Rosenband, P. Schmidt, D. Hume, W. Itano, T. Fortier, J. Stalnaker, K. Kim, S. Diddams, J. Koelemeij, J. Bergquist, and D. Wineland. Observation of the $^1S_0 \rightarrow ^3P_0$ Clock Transition in $^{27}\text{Al}^+$. *Physical Review Letters*, 98(22):220801, May 2007.
- [99] B. Efron. Bootstrap Methods: Another Look at the Jackknife. In S. Kotz and N. L. Johnson, editors, *Breakthroughs in Statistics: Methodology and Distribution*, Springer Series in Statistics, pages 569–593. Springer, New York, NY, 1992.
- [100] D. B. Hume and D. R. Leibbrandt. Probing beyond the laser coherence time in optical clock comparisons. *Physical Review A*, 93(3):032138, 2016.
- [101] M. Schioppo, R. C. Brown, W. F. McGrew, N. Hinkley, R. J. Fasano, K. Beloy, T. Yoon, G. Milani, D. Nicolodi, J. Sherman, et al. Ultrastable optical clock with two cold-atom ensembles. *Nature Photonics*, 11(1):48–52, 2017.
- [102] T. Rosenband, D. Hume, P. Schmidt, C.-W. Chou, A. Brusch, L. Lorini, W. Oskay, R. E. Drullinger, T. M. Fortier, J. E. Stalnaker, et al. Frequency ratio of Al^+ and Hg^+ single-ion optical clocks; metrology at the 17th decimal place. *Science*, 319(5871):1808–1812, 2008.
- [103] S. Dörscher, N. Huntemann, R. Schwarz, R. Lange, E. Benkler, B. Lipphardt, U. Sterr, E. Peik, and C. Lisdat. Optical frequency ratio of a $^{171}\text{Yb}^+$ single-ion clock and a ^{87}Sr lattice clock. *Metrologia*, 58(1):015005, 2021.
- [104] N. Herschbach, K. Pyka, J. Keller, and T. E. Mehlstäubler. Linear paul trap design for an optical clock with coulomb crystals. *Applied Physics B*, 107(4):891–906, 2012.
- [105] K. Cui, K. Boyce, D. Leibbrandt, and D. Hume. Scalable quantum logic spectroscopy using a schrödinger cat interferometer. *Bulletin of the American Physical Society*, 66, 2021.
- [106] S. Brewer, J.-S. Chen, K. Beloy, A. Hankin, E. Clements, C. Chou, W. McGrew, X. Zhang, R. Fasano, D. Nicolodi, et al. Measurements of $^{27}\text{Al}^+$ and $^{25}\text{Mg}^+$ magnetic constants for improved ion-clock accuracy. *Physical Review A*, 100(1):013409, 2019.
- [107] K.-f. Cui, J.-j. Shang, S.-j. Chao, S.-m. Wang, J.-b. Yuan, P. Zhang, J. Cao, H.-l. Shu, and X.-r. Huang. Sympathetic sideband cooling of a $^{40}\text{Ca}^+ \text{-} ^{27}\text{Al}^+$ pair toward a quantum logic clock. *Journal of Physics B: Atomic, Molecular and Optical Physics*, 51(4):045502, 2018.
- [108] W. M. Itano, J. C. Bergquist, J. J. Bollinger, and D. J. Wineland. Cooling methods in ion traps. *Physica Scripta*, 1995(T59):106, 1995.
- [109] J. Eschner, G. Morigi, F. Schmidt-Kaler, and R. Blatt. Laser cooling of trapped ions. *JOSA B*, 20(5):1003–1015, 2003.
- [110] D. B. Hume. *Two-species ion arrays for quantum logic spectroscopy and entanglement generation*. PhD thesis, University of Colorado at Boulder, 2010.
- [111] Q. Turchette, C. Myatt, B. King, C. Sackett, D. Kielpinski, W. Itano, C. Monroe, and D. Wineland. Decoherence and decay of motional quantum states of a trapped atom coupled to engineered reservoirs. *Physical Review A*, 62(5):053807, 2000.
- [112] J. Keller, H. L. Partner, T. Burgermeister, and T. Mehlstäubler. Precise determination of micromotion for trapped-ion optical clocks. *Journal of Applied Physics*, 118(10):104501, 2015.

- [113] D. Berkeland, J. Miller, J. C. Bergquist, W. M. Itano, and D. J. Wineland. Minimization of ion micromotion in a paul trap. Journal of applied physics, 83(10):5025–5033, 1998.
- [114] Z. Meir, T. Sikorsky, R. Ben-shlomi, N. Akerman, M. Pinkas, Y. Dallal, and R. Ozeri. Experimental apparatus for overlapping a ground-state cooled ion with ultracold atoms. Journal of Modern Optics, 65(5-6):501–519, 2018.
- [115] Z. Meir. Dynamics of a single, ground-state cooled and trapped ion colliding with ultracold atoms: a micromotion tale. PhD thesis, The Weizmann Institute of Science (Israel), 2017.
- [116] F. W. Knollmann, A. N. Patel, and S. C. Doret. Part-per-billion measurement of the $4^2S_{1/2} \rightarrow 3^2D_{5/2}$ electric-quadrupole-transition isotope shifts between $^{42,44,48}\text{Ca}^+$ and $^{40}\text{Ca}^+$. Physical Review A, 100(2):022514, 2019.
- [117] K. J. Arnold, R. Kaewuam, S. R. Chanu, T. R. Tan, Z. Zhang, and M. D. Barrett. Precision measurements of the $^{138}\text{Ba}^+ 6s^2S_{1/2} - 5d^2D_{5/2}$ clock transition. Physical Review Letters, 124(19):193001, 2020.
- [118] H. Gan, G. Maslennikov, K.-W. Tseng, T. Tan, R. Kaewuam, K. Arnold, D. Matsukevich, and M. Barrett. Oscillating-magnetic-field effects in high-precision metrology. Physical Review A, 98(3):032514, 2018.
- [119] M. S. Safronova, M. G. Kozlov, and C. W. Clark. Blackbody radiation shifts in optical atomic clocks. IEEE transactions on ultrasonics, ferroelectrics, and frequency control, 59(3):439–447, 2012.
- [120] C. M. Seck, E. G. Hohenstein, C.-Y. Lien, P. R. Stollenwerk, and B. C. Odom. Rotational state analysis of AlH^+ by two-photon dissociation. Journal of Molecular Spectroscopy, 300:108–111, 2014.
- [121] R. Srinivas, B. Nichol, D. Nadlinger, P. Drmota, D. Main, G. Araneda, C. Ballance, and D. Lucas. A quantum network of entangled optical atomic clocks. Bulletin of the American Physical Society, 2022.
- [122] E. M. Kessler, P. Komar, M. Bishof, L. Jiang, A. S. Sørensen, J. Ye, and M. D. Lukin. Heisenberg-limited atom clocks based on entangled qubits. Physical review letters, 112(19):190403, 2014.
- [123] C.-W. Chou, D. B. Hume, T. Rosenband, and D. J. Wineland. Optical clocks and relativity. Science, 329(5999):1630–1633, 2010.
- [124] T. R. Tan, R. Kaewuam, K. J. Arnold, S. R. Chanu, Z. Zhang, M. Safronova, and M. D. Barrett. Suppressing inhomogeneous broadening in a lutetium multi-ion optical clock. Physical Review Letters, 123(6):063201, 2019.
- [125] V. Dzuba and V. Flambaum. Atomic optical clocks and search for variation of the fine-structure constant. Physical Review A, 61(3):034502, 2000.
- [126] T. M. Fortier, N. Ashby, J. Bergquist, M. Delaney, S. Diddams, T. Heavner, L. Hollberg, W. Itano, S. R. Jefferts, K. Kim, et al. Precision atomic spectroscopy for improved limits on variation of the fine structure constant and local position invariance. Physical Review Letters, 98(7):070801, 2007.

- [127] E. Peik, B. Lipphardt, H. Schnatz, T. Schneider, C. Tamm, and S. G. Karshenboim. New limit on the present temporal variation of the fine structure constant. In AIP Conference Proceedings, volume 770, pages 103–111. American Institute of Physics, 2005.
- [128] M. S. Safronova, S. G. Porsev, C. Sanner, and J. Ye. Two clock transitions in neutral Yb for the highest sensitivity to variations of the fine-structure constant. Physical review letters, 120(17):173001, 2018.
- [129] M. Safronova, D. Budker, D. DeMille, D. F. J. Kimball, A. Derevianko, and C. W. Clark. Search for new physics with atoms and molecules. Reviews of Modern Physics, 90(2):025008, 2018.

Appendix A

Optimization of the magnetic field servo

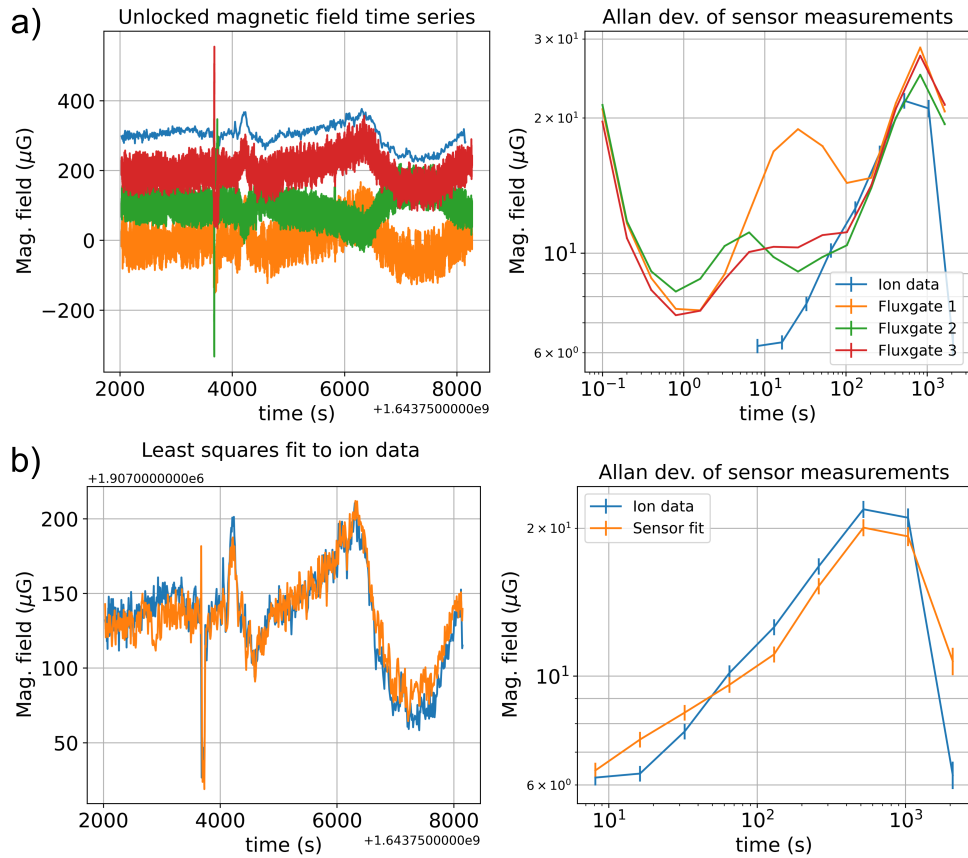


Figure A.1: a) Data showing the time series and Allan deviation of the unservoed magnetic field data when measured with 3 fluxgate magnetometer and a $^{40}\text{Ca}^+$ ion. One fluxgate sensor is aligned anti-parallel the others to better account for magnetic field gradients. b) Time series and Allan deviation of the fluxgate data fit to the magnetic field measured with $^{40}\text{Ca}^+$. The unservoed data is averaged to remove high frequency noise and following fitting we see good agreement in the Allan deviation of the two time series.

We calibrate the magnetic servo by comparing in-situ magnetic field measurements with $^{40}\text{Ca}^+$ to measurements of the magnetic field with fluxgate magnetometers mounted outside the vacuum chamber. During calibration the feedback is disengaged to get an accurate measurement of the environmental magnetic field variations where uncorrected measurements are seen in Fig. A.1(a). A least squares fit of the fluxgate data to the ion based measurement is performed to determine the proper coefficients that will be applied to the fluxgates to get an accurate estimate of the magnetic field at the ion. We describe the relation of the fluxgate measurements to the ion measurement with the equation

$$B_{ion} = a B_{f,1} + b B_{f,2} + c B_{f,3} \quad (\text{A.1})$$

where all the magnetic field measurements here are magnetic field magnitudes, B_{ion} is the magnetic field measured with $^{40}\text{Ca}^+$, $B_{f,i}$ is the magnetic field measured with fluxgate magnetometer i where we have three, and $a, b,$ and c are the weighting coefficients applied to each fluxgate magnetometer measurement. We use the Ramsey method described by Eq. 2.45 to determine the magnetic field with $^{40}\text{Ca}^+$. The fluxgate data is first averaged to minimize higher frequency noise and the ion data is averaged to obtain a comparable bin, which is shown in Fig. A.1(b). The data is then fit and the coefficients are modified in the servo software. Fits to the data can be seen in Fig. A.1(b). The new coefficients are then tested by again by measuring the magnetic field with $^{40}\text{Ca}^+$. The measurement of the magnetic field stability is shown in Fig. A.2 which is data taken following the calibration shown in Fig. A.1(b). Depending on the outcome of the stability measurement we will perform the calibration again to determine the proper coefficients.

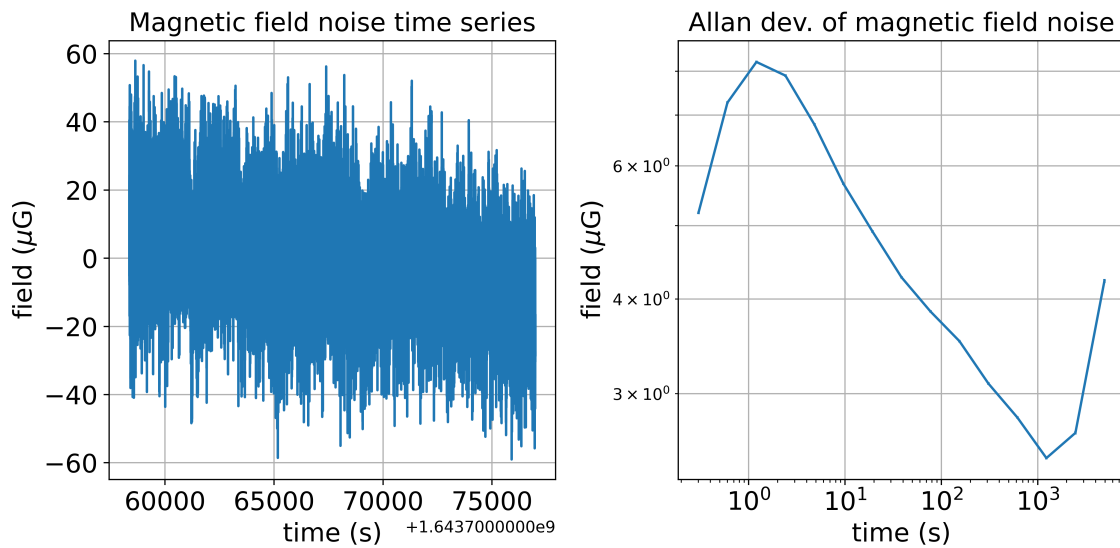


Figure A.2: Time series and Allan deviation of the magnetic field measured with $^{40}\text{Ca}^+$ where the servo is reengaged following re-calibration of the scaling coefficients. We can see from the Allan deviation the the magnetic field noise has been stabilize at long time scales where we have stabilized the magnetic field noise magnitude below $10\mu\text{G}$ out to 10^3 s. The initial bump in the Allan deviation at 1 s is due to the gain of the laser phase lock to the Ramsey fringe.

Appendix B

Sphere cavity box temperature control

Drifts of the $^{40}\text{Ca}^+$ lasers frequencies are reduced in our lab by temperature stabilizing the volume of the sphere cavity laser table seen in Fig. 2.10. This is implemented by using a thermoelectric cooler (TEC) to pump heat out of a box surrounding the cavity table where the heat is then dissipated into the lab with a second heatsink. We constructed a box made of insulating foam where the cooling (heating) heatsink is mounted to the inner (outer) side of the insulating foam. Thermal contact between the heatsink and the TEC is made via an aluminum adapter plate on either side of the insulating walls that is pressed in between two heatsinks. Thermal grease is applied to each interface to ensure good thermal conductivity. The TEC is driven using a BK precision linear power supply where we adjust the current from 0–5 A using a computer control script. Temperature of the air in the box and at the surface of the heatsinks is measured using Pt-100 resistance temperature detectors and a Pico-logger. We then use a servo script to stabilize the air temperature of the box below the temperature of the room to ensure enough cooling range is available since the current driver is not bi-directional. The bandwidth of the temperature servo is improved by linearizing the TEC and heatsink by implementing a fast servo to make the heatsinks quickly reach the desired temperature which is determined by a secondary slow servo loop which servos to stabilize the air temperature in the box. We calibrate these servos by using a step response method from which we determine the proportional, integral, and derivative gain. A simplified schematic of the temperature control system is shown in Fig. B.1.

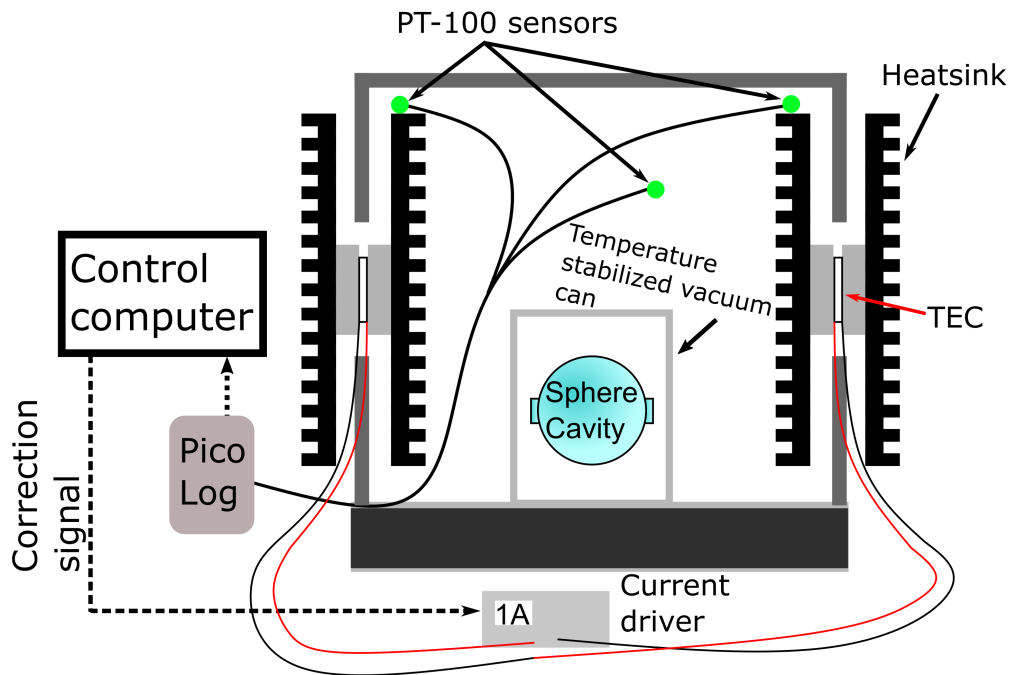


Figure B.1: Diagram of the temperature control box used to stabilize the air temperature surrounding the sphere cavity. Heatsinks and adapter plates clamp around a TEC which is used to pump heat from inside the box out into the lab. PT-100 temperature sensors are used to measure the temperature of the heatsinks and the air inside the sphere cavity box where this data is used by a servo script to stabilize the temperature a couple of degrees below room temperature. The correction signal is applied to the current driver which controls the current sent to the two TECs that are wired in series. Inside the box there is also a vacuum can which houses the sphere cavity. The temperature of this can is separately stabilized by a PTC10 Stanford Research Systems temperature control which controls a TEC mounted between the vacuum can and the optical breadboard. With these two stages of temperature control we can minimize the drifts of the lasers locked to the sphere cavity.

Appendix C

Previous $^{27}\text{Al}^+$ clock uncertainty budget

Table C.1: Systematic fractional frequency shifts ($\Delta\nu/\nu$) and associated uncertainties for the previous $^{27}\text{Al}^+$ quantum-logic.

Effect	Shift (10^{-19})	Uncertainty (10^{-19})
Excess micromotion	-45.7	5.9
Quadratic Zeeman	-9241.6	3.7
Blackbody radiation	-26.2	3.2
Secular motion	-17.3	2.9
Background gas collisions	-0.7	2.5
First-order Doppler	0	2.2
Clock laser Stark	0	2.0
AOM phase chirp	0	< 1
Electric quadrupole	0	< 1
Total	-9331.5	9.1